Study of Transverse Collective Beam Dynamics in the J-PARC MR Synchrotron

Nobuyuki Yoshimura

High Energy Physics Group
Division of Physics and Astronomy
Graduate School of Science
Kyoto University

Abstract

The origin of the matter-antimatter asymmetry in the Universe remains an unresolved problem. While CP violation is necessary to generate this asymmetry, the contribution from the quark sector is insufficient to explain the observed baryon asymmetry. Leptonic CP violation, probed through neutrino oscillations, therefore provides a possible explanation. Long-baseline accelerator experiments, such as T2K and Hyper-Kamiokande, investigate this by comparing neutrino and antineutrino oscillation probabilities. Due to the weak interaction of neutrinos with matter, precise measurements require large statistical samples. Since these neutrino beams are generated by proton beams, the neutrino flux is directly determined by the primary proton beam intensity. Therefore, an upgrade of the J-PARC Main Ring to increase the proton beam power is required for the operation of these experiments at the intended sensitivity.

Achieving such beam power is constrained by beam instabilities arising from electromagnetic interactions between the beam and its surrounding environment. In high-intensity proton beams, space charge forces, resulting from Coulomb repulsion, induce a significant incoherent tune spread comparable to the synchrotron tune. Under these conditions, conventional perturbative approaches are insufficient for describing intra-bunch dynamics. This thesis addresses this issue by establishing a framework for high-intensity beam dynamics that integrates macroparticle simulations, extended theoretical models, and experimental measurements.

The primary contribution of this work is an improved understanding of the interplay between wakefield and space charge forces that govern the threshold beam intensity for instability. Macroparticle simulations demonstrate that direct space charge forces enhance instability by modifying the potential well, whereas indirect space charge forces, originating from image currents in the beam pipe, suppress instability by shifting coherent mode frequencies. This finding clarifies the suppression mechanism of Transverse Mode Coupling Instability at beam intensities dominated by space charge and resolves discrepancies in conventional theoretical predictions studies the role of space charge.

Furthermore, the linear dependence of the bunch oscillation frequency on chromaticity, a fundamental feature exploited in beam diagnostics, is confirmed to persist in high-intensity beams. The recoherence period, which characterizes the recovery of coherent beam motion after phase mixing within a bunch, is found to saturate nonlinearly with increasing beam intensity. This behavior is attributed to space charge induced modifications of the head-tail mode spectrum, which governs characteristic intra-bunch oscillation patterns. These findings are validated by beam measurements at the J-PARC Main Ring and consistently reproduced by macroparticle simulations. Consequently, this study provides a comprehensive picture of intra-bunch motion, demonstrating the impact of strong space charge on the eigenvalues and eigenfunctions of head-tail modes.

The physical framework established in this study provides a consistent description of high-intensity beam dynamics, addressing the constraints imposed by beam instabilities. By enabling a quantitative evaluation of instability thresholds and intra-bunch dynamics, this framework supports stable high-power operation of proton accelerators and provides

guidance for the design of feedback and mitigation systems. Moreover, these findings are applicable to the design of future MW-class proton synchrotrons. As a result, these results contribute to upgrades of the J-PARC Main Ring and to the reliable delivery of neutrino beams for long-baseline experiments, including T2K and Hyper-Kamiokande.

Acknowledgement

Over the course of my six-year research journey, I encountered numerous challenges. However, it is only through the unwavering support and guidance of many individuals that I have been able to reach this milestone. I would like to express my deepest gratitude to everyone who supported me throughout this period.

I would like to express my profound gratitude to Professor Tsuyoshi Nakaya for his invaluable guidance and support throughout my doctoral studies. I am sincerely grateful for his critical and constructive feedback, which significantly improved the quality of this thesis. Furthermore, his recommendation during my doctoral program to pivot my research focus toward J-PARC accelerator science was a pivotal moment that enabled me to continue my academic pursuit in this laboratory.

I am deeply grateful to Professor Takeshi Toyama for his comprehensive mentorship since the earliest stages of this research. His expert guidance in navigating the complexities of the J-PARC beam system, a domain that was entirely new to me, was indispensable for the successful progression of my work.

Special thanks are also due to Dr. Yoshihiro Shobuda for the extensive discussions regarding beam dynamics and the strategic direction of this research. His profound theoretical insights into the space charge effect served as a fundamental guiding principle for my studies.

I would like to express my appreciation to the J-PARC beam operation team, a collaboration of KEK and JAEA. I am particularly grateful to Dr. Aine Kobayashi and Masashi Okada of the monitor group for their assistance with BPM adjustments, data acquisition systems, and numerous fruitful discussions. I wish to thank Professor Takeshi Nakamura for sharing his expertise on feedback systems and for our in-depth discussions on intra-bunch beam dynamics. My gratitude also extends to the MR commissioning group, including Professor Yoichi Sato and Dr. Takaaki Yasui, for coordinating beam conditions and experimental schedules. I am also thankful to Dr. Fumihiro Tamura, Dr. Yasuyuki Sugiyama, and Dr. Hidefumi Okita of the RF group for their technical support regarding RF matching, and Professor Kazuhito Ohmi for his essential contributions to the early direction of this research.

I am indebted to the members of the T2K experiment. I thank Dr. Tatsuya Kikawa for his consistent guidance and support. Professor Atsuko Ichikawa inspired me to approach physics with passion and sincerity. I also appreciate the expert insights provided by Professor Ken Sakashita, Dr. Megan Friend, and Dr. Kiseki Nakamura regarding the primary and secondary beamlines. My research life was greatly enriched by past and present student members of the Kyoto T2K Group, including Dr. Soichiro Kuribayashi, Dr. Takahiro Odagawa, Shunta Arimoto, Naoto Onda, Naoki Otani, Koki Hayashi, Kotaro Indo, and Koichi Hasegawa.

I would like to extend my gratitude to all members of the High Energy Physics Group at Kyoto University The coffee breaks in Room 305 were more than just a respite; they were sessions of creativity that played a vital role in my research. I am especially thankful to the faculty members: Professor Osamu Tajima, Professor Roger Wendell, Dr. Shion

Chen, Dr. Junya Suzuki, and Dr. Miho Katsuragawa. I also cherish the time spent with my peers, Masaki Kawaue, Hironobu Nakata, and Takane Sano.

Finally, I would like to express my most heartfelt gratitude to my father and mother. This thesis would not have been possible without their lifelong support and encouragement.

Contents

1 Introduction **7**
- 1.1 Overview of Accelerator Science . . . 7
  - 1.1.1 Fundamentals of Particle Accelerators . . . 7
  - 1.1.2 The Energy and Intensity Frontiers . . . 8
  - 1.1.3 Intensity Frontier Facilities in Japan . . . 8
- 1.2 Challenges in High-Intensity Proton Synchrotrons . . . 9
  - 1.2.1 Beam Instability . . . 9
  - 1.2.2 Performance Limitations by Beam Loss . . . 11
- 1.3 Previous Studies . . . 12
  - 1.3.1 Structural Design . . . 13
  - 1.3.2 Operational Optimization . . . 14
  - 1.3.3 Feedback Control . . . 15
- 1.4 Outline of This Thesis . . . 16

2 J-PARC **17**
- 2.1 Overview of J-PARC . . . 17
  - 2.1.1 Time Structure of Beams . . . 18
- 2.2 LINAC . . . 19
- 2.3 3 GeV Rapid-Cycling Synchrotron . . . 19
- 2.4 30 GeV Main Ring . . . 21
  - 2.4.1 Lattice Design . . . 23
  - 2.4.2 Beam Injection . . . 23
  - 2.4.3 Magnet System . . . 24
  - 2.4.4 Radio Frequency Cavity . . . 24
  - 2.4.5 Collimator and Beam Dump . . . 24
  - 2.4.6 Beam Extraction . . . 26
- 2.5 Beam Diagnosis . . . 26
  - 2.5.1 Beam Position Monitor . . . 26
  - 2.5.2 Beam Profile Monitor . . . 27
  - 2.5.3 Beam Current Monitor . . . 30
- 2.6 Experimental Facilities . . . 30
  - 2.6.1 Neutrino Experimental Facility . . . 30
  - 2.6.2 Hyper-Kamiokande Experiment . . . 31
  - 2.6.3 Primary Beamline . . . 32

3 Basic Dynamics and Intensity Effects in Synchrotron **34**
- 3.1 Transverse Motion . . . 34

3.1.1 Equation of Motion and Coordinate System . . . 34
3.1.2 Betatron Oscillation and Phase Space . . . 35
3.1.3 Betatron Tune and Resonance . . . 36
3.1.4 Effect of Momentum Deviation . . . 36
3.2 Longitudinal Motion . . . 37
3.2.1 Synchronized Particles and Coordinate System . . . 37
3.2.2 Principles of RF Acceleration and Phase Stability . . . 38
3.2.3 Synchrotron Oscillation . . . 38
3.2.4 RF Buckets and Bunches . . . 39
3.3 Space Charge . . . 39
3.3.1 Beam Self-Field . . . 40
3.3.2 Incoherent Tune Shift and Tune Spread . . . 40
3.3.3 Image Effects and Coherent Tune Shift . . . 41
3.3.4 Consequences of Space Charge . . . 41
3.4 Wakefield and Impedance . . . 41
3.4.1 Physical Image of Wakefield . . . 41
3.4.2 Classification of Wakefields . . . 42
3.4.3 Impedance: A Frequency Domain Perspective . . . 43
3.4.4 Sources of Impedance . . . 43
3.5 Beam Instability Mechanism . . . 44
3.5.1 Instability Analysis . . . 45
3.5.2 Competition Between Driving and Damping . . . 46
3.5.3 Classification of Major Instabilities . . . 47
3.6 Feedback System . . . 49
3.6.1 Feedback System Components . . . 49
3.6.2 Operating Principle . . . 50
3.6.3 Types of Feedback Systems . . . 50

4 Transverse Decoherence without Intensity Effects 51
4.1 Theoretical Derivation . . . 51
4.2 Analysis of Intra-Bunch Motion . . . 52
4.2.1 Recoherence and Signal Sharpness . . . 52
4.2.2 Intra-Bunch Frequency . . . 52
4.2.3 Global Beam Centroid . . . 53

5 Definition of Head-tail Modes 54
5.1 Air-Bag Square-well potential model . . . 54
5.1.1 Head-tail Modes with Space Charge Forces . . . 54
5.1.2 Oscillation Amplitude with Weak Space Charge Force . . . 59
5.2 Air-Bag Harmonic potential model . . . 61
5.2.1 Head-tail Modes with Space Charge Forces . . . 61
5.2.2 Oscillation Amplitude with Weak Space Charge Force . . . 62
5.3 Oscillation Amplitude for the Gaussian Beam with Weak Space Charge Force 64

6 Macroparticle Tracking Simulation 66
6.1 Kinematic Framework . . . 66
6.2 Longitudinal Wakefield Model . . . 69

6.3 Transverse Wakefield Model . . . 71
6.4 Space Charge Model . . . 74
6.5 Feedback System Model . . . 75

7 Validation of the Simulation **77**
7.1 Validation of Simulation Parameters . . . 77
7.2 Consistency Check with the Linear Decoherence Scenario . . . 79

8 Analysis of the Simulation in the Frequency Domain **82**
8.1 Analysis of ABS Model . . . 82
8.1.1 Weak Space Charge Force . . . 82
8.1.2 Without Indirect Space Charge Force . . . 84
8.1.3 With Indirect Space Charge Force . . . 88
8.2 Analysis of Gaussian Bunch . . . 90
8.2.1 Weak Space Charge Force . . . 90
8.2.2 Without Indirect Space Charge Force . . . 93
8.2.3 With Indirect Space Charge Force . . . 95

9 Comparison with Conventional Study **99**

10 Time-Domain Analysis of Simulation Results **103**
10.1 Typical Results of the Simulation . . . 103
10.2 Modeling of Head-tail Mode Reflecting Simulation . . . 104
10.3 Head-tail Eigenfunction at Gaussian Bunch . . . 106

11 Experimental Validation with Beam Measurements **109**
11.1 Conditions of Measurements . . . 109
11.2 Typical Results of the Measured Intra-Bunch Motion . . . 111
11.3 Synchrotron Period Dependence . . . 111
11.3.1 Simulation Predictions and Measurement Results . . . 113
11.3.2 Comparison and discussion . . . 113
11.4 Beam Intensity Dependence . . . 117
11.4.1 Simulation Predictions and Measurement Results . . . 117
11.4.2 Comparison and discussion . . . 118
11.5 Chromaticity Dependence . . . 122
11.5.1 Simulation Predictions and Measurement Results . . . 122
11.5.2 Comparison and discussion . . . 122

12 Conclusion and Outlook **126**

References **128**

A Applications of Accelerators in Science **141**

B J-PARC Facility Overview **143**
B.1 Control and Safety Systems . . . 143
B.1.1 Control System . . . 143
B.1.2 Custom Application System . . . 144

B.2 Description of the LINAC . . . 145
B.2.1 Ion Source . . . 145
B.2.2 Linac . . . 145
B.2.3 MEBT1: Chopper . . . 146
B.2.4 L3BT: Debuncher . . . 147
B.2.5 L3BT: Scraper . . . 147
B.3 Description of the RCS . . . 147
B.3.1 Lattice Design . . . 147
B.3.2 Beam Injection . . . 148
B.3.3 Electromagnetic System . . . 150
B.3.4 Radio Frequency Cavity . . . 151
B.3.5 Vacuum Chamber . . . 152
B.3.6 Beam Extraction . . . 153
B.4 Description of the Beam Diagnosis System . . . 153
B.4.1 Beam Positon Monitor . . . 153
B.4.2 Beam Profile Monitor . . . 155
B.4.3 Beam Current Monitor . . . 158
B.4.4 Beam Loss Monitor . . . 158
B.5 Description of the Experimental Facility . . . 159
B.5.1 Material and Life Science Experimental Facility . . . 159
B.5.2 Hadron Experimental Facility . . . 161
B.5.3 Neutrino Experimental Facility . . . 162

C Vlasov Formalism for Head-Tail Modes 168
C.1 Sacherer's Integral Equation . . . 168
C.2 General Solution Method . . . 170
C.3 Air-Bag Model . . . 171
C.4 Gaussian Distribution . . . 172
C.5 Sinusoidal Model . . . 172

D Space Charge Effects in the Elliptical Chamber 174
D.1 Potential in the Rest Frame . . . 174
D.2 Electric Field in the Laboratory Frame . . . 175
D.3 Approximation for Small Beam Size . . . 175

E Reconstruction of Intra-bunch Beam Position from BPM Signals 176
E.1 Hardware Configuration and Signal Acquisition . . . 176
E.2 Position Calculation Algorithm . . . 176
E.3 Extraction of Intra-bunch Motion . . . 177
E.4 Digital Filtering for Feedback . . . 177

List of Acronyms 178

List of Symbols 183

List of Figures 188

List of Tables 195

Chapter 1

Introduction

1.1 Overview of Accelerator Science

1.1.1 Fundamentals of Particle Accelerators

Particle accelerators are essential tools in modern science for investigating the subatomic structure of matter. These devices accelerate charged particles, such as electrons or protons, to high velocities, often approaching the speed of light. The motion of these particles is governed by the Lorentz force $\boldsymbol{F} = q(\boldsymbol{E} + \boldsymbol{v} \times \boldsymbol{B})$, which describes the interaction between charged particles and electromagnetic fields.

Specifically, electric fields are employed to increase the kinetic energy of particles, while magnetic fields are used to control their trajectories and maintain beam focus. This combined manipulation enables the stable transport of particle beams over long distances.

Accelerators are broadly classified into two types: linear and circular. Linear accelerators (linacs) accelerate particles along a straight path using Radio Frequency (RF) electric fields applied to a sequence of resonant cavities. The fields are synchronized with the particle motion to provide continuous acceleration. Linacs are especially effective for low-mass particles, such as electrons, as they avoid energy loss due to synchrotron radiation, which arises when charged particles move along curved trajectories. Consequently, linacs are adopted for proposed next-generation electron-positron colliders and serve as injector stages for larger circular accelerators.

Circular accelerators, such as synchrotrons, confine particles within a closed orbit using a lattice of dipole magnets for bending and quadrupole magnets for focusing. RF cavities placed at specific sections in the ring provide periodic energy increments. Synchrotrons achieve high particle energies efficiently by repeatedly circulating particles and incrementally increasing their energy with each pass. This approach is particularly effective for heavy particles like protons, for which synchrotron radiation loss is negligible. During the acceleration ramp, the magnetic field strength and RF frequency are increased in synchronization with the particle energy to maintain a stable orbit.

This study specifically focuses on high-intensity proton synchrotrons, which play a central role in modern particle physics. In these machines, increasing the number of particles introduces complex collective effects that challenge stable operation. Therefore, mastering these dynamics is key to addressing current performance limitations.

1.1.2 The Energy and Intensity Frontiers

The advancement of particle accelerator technology is driven by the quest to resolve fundamental questions in physics. Two major strategic directions define the current research landscape: the Energy Frontier and the Intensity Frontier. Both approaches aim to test the validity of the Standard Model (SM) and to search for evidence of new physics beyond it.

The Energy Frontier focuses on achieving the highest possible collision energies to probe subatomic structures at the smallest scales. High-energy collisions can produce new particles not included in the SM, replicating conditions similar to the early universe immediately after the Big Bang. Since the de Broglie wavelength of the colliding particles decreases with increasing energy, this approach enables probing matter with higher spatial resolution. The Large Hadron Collider (LHC) at European Organization for Nuclear Research (CERN) exemplifies this strategy, leading to the discovery of the Higgs boson in 2012. [1] Future Energy Frontier programs aim to directly produce particles predicted by models such as Supersymmetry (SUSY) and to investigate the nature of Dark Matter (DM).

In contrast, the Intensity Frontier pursues a complementary approach. Rather than pushing for higher energies, it focuses on generating large quantities of particles to achieve extremely high beam luminosities. This strategy enables the detection of rare processes and decay modes that occur with infinitesimal probabilities in the SM. Small deviations from theoretical expectations in these processes may signal the influence of undiscovered particles or interactions. Studies at this frontier are essential for exploring neutrino oscillations, searching for forbidden decays, and improving the precision of fundamental constants. These experiments are highly sensitive to quantum loop corrections, offering a window into the virtual effects of new physics.

The Energy and Intensity Frontiers are deeply synergistic. Discoveries at the Energy Frontier identify new particles, whose detailed properties must then be characterized through the high-statistics measurements of the Intensity Frontier. Conversely, anomalies observed in precision measurements can suggest the energy scales relevant for future direct searches.

This thesis situates itself firmly within the context of the Intensity Frontier. The research presented in this thesis addresses the technical challenges of generating and stabilizing high-intensity proton beams, which are critical for experiments seeking to uncover rare phenomena beyond the SM.

1.1.3 Intensity Frontier Facilities in Japan

Japan hosts world-leading accelerator complexes that play a central role in global Intensity Frontier research. Notably, High Energy Accelerator Research Organization (KEK) in Tsukuba, Ibaraki and Japan Proton Accelerator Research Complex (J-PARC) in Tokai, Ibaraki, operate dedicated high-intensity facilities designed to explore the fundamental structure of matter. These laboratories exemplify the scientific progress enabled by sustained high-intensity beam operation.

Among these, J-PARC forms the cornerstone of Japan's Intensity Frontier program. One of its primary scientific objectives is the investigation of Charge-Parity (CP) violation in the lepton sector through long-baseline neutrino oscillation experiments. These experiments require a highly stable and intense proton beam to generate a sufficient neutrino flux for accurate measurements. As a result, the physics sensitivity is directly constrained by the accelerator performance. Increasing beam power while suppressing beam loss and mitigating beam instabilities is, therefore, an absolute necessity. This requirement provides the primary motivation for the beam dynamics studies presented in this thesis.

In parallel, the SuperKEKB collider at KEK serves as a leading facility for electron-positron physics. Optimized for ultra-high luminosity, SuperKEKB collides 7 GeV electrons with 4 GeV positrons to produce many B meson pairs. The Belle II detector analyzes these collisions to investigate CP violation in the quark sector. Although the Standard Model includes a mechanism for CP violation, it fails to fully account for the observed matter-antimatter asymmetry in the universe. By analyzing a large dataset of B meson decays, Belle II aims to detect deviations from predictions that could indicate new physical interactions. Just as with J-PARC, achieving this goal requires maintaining high beam currents and stable accelerator performance.

1.2 Challenges in High-Intensity Proton Synchrotrons

High-intensity proton synchrotrons constitute critical infrastructure for advancing Intensity Frontier physics. However, realizing megawatt-class beam power requires overcoming fundamental physical limitations that are negligible in low-intensity machines. The challenges can be broadly divided into two interconnected categories: collective beam instabilities that degrade beam quality, and beam loss which limits hardware performance through radio-activation. This section outlines these mechanisms and the operational constraints they impose.

1.2.1 Beam Instability

Compressing large numbers of charged particles into a small volume generates collective effects where particles no longer behave as independent entities. In low-intensity regimes, particle trajectories are primarily determined by external electromagnetic fields from dipole and quadrupole magnets. However, as beam intensity rises to the level of 10^{13}–10^{14} proton per bunch (ppb), as required at facilities like J-PARC, the beam transitions into a dense, non-neutral plasma. In this state, self-generated electromagnetic fields rival external fields in magnitude.

These collective effects are the primary obstacles to high-intensity operation and are categorized into two mechanisms:

- Space Charge Effects: Direct repulsive interactions among particles within the beam.
- Impedance and Wakefields: Indirect interactions mediated by the vacuum chamber and accelerator components.

Accurate modeling and suppression of these effects are prerequisites for achieving high beam power while maintaining beam quality.

Space Charge Effects

The space charge effect arises from the Coulomb repulsion between particles (protons) within a high-density bunch. This force acts as a defocusing lens that counteracts the external focusing force provided by quadrupole magnets. Unlike external fields, the space charge force is non-uniform; it is strongest at the high-density core of the bunch and weaker at the periphery.

This non-linear force alters the betatron tune, defined as the number of transverse oscillations a particle undergoes per revolution. Since the force varies depending on the particle's position within the bunch, the extent of the tune shift differs for each particle. This phenomenon results in an "incoherent tune spread," a condition where particles with a wide range of oscillation frequencies coexist within a single bunch.

In circular accelerators, lattice resonances occur when the betatron tune satisfies specific integer or fractional conditions, causing oscillation amplitudes to grow uncontrollably. For low-intensity beams with negligible tune spread, the operating point (bare tune) can be set safely away from these resonance lines. However, in high-intensity beams, the tune spread becomes large enough that the "footprint" of the beam in tune space inevitably overlaps with resonance lines. Particles crossing these boundaries experience resonant growth in amplitude and eventually hit the physical aperture, resulting in beam loss.

The magnitude of this incoherent tune shift can be evaluated using the Laslett formula scaling. [2] Based on this scaling law, the severity of space charge effects depends on four key parameters:

- Beam Energy: The tune shift is inversely proportional to the cube of the relativistic Lorentz factor (γ^3) and the square of the velocity (β^2). Consequently, space charge effects are most severe at low energies, making the injection period the most critical phase in the acceleration cycle.
- Beam Intensity: The shift is directly proportional to the number of particles per bunch (N_B). Higher beam intensities linearly increase repulsive forces, leading to larger tune spreads.
- Transverse Emittance: The shift is inversely proportional to the transverse emittance (ϵ), which represents the phase-space area occupied by the beam. By intentionally increasing the physical cross-section of the beam (thereby reducing charge density), the repulsive force can be mitigated. At J-PARC, this is technically achieved using "painting injection," which uniformly fills the phase space.
- Bunch Factor: The shift is inversely proportional to the bunch factor (B_f). The bunch factor is defined as the ratio of the average current to the peak current within a bunch. A small B_f indicates a short, peaked bunch with high charge density. Increasing B_f by lengthening and flattening the longitudinal bunch distribution reduces the peak current and mitigates the space charge effect. At J-PARC, this is realized by superimposing a second-harmonic RF voltage to flatten the bunch shape.

Impedance and Wakefields

Indirect collective effects originate from the electromagnetic interaction between the beam and its environment. As a charged bunch travels through the vacuum chamber, it induces image currents and electromagnetic fields in the surrounding structures. Discontinuities in the vacuum chamber, such as RF cavities, bellows, kickers, or beam monitors, act as impedance sources that excite wakefields. These wakefields persist after the head of the bunch has passed and act back on the trailing particles (intra-bunch) or subsequent bunches (inter-bunch).

Beam coupling impedance quantifies the accelerator structure's tendency to resist the beam current and generate these disruptive fields. If the interaction amplifies particle oscillations, it leads to coherent instabilities:

- Transverse Head-Tail Instability: Oscillations propagate from the head to the tail of the bunch, potentially leading to rapid beam loss.
- Longitudinal Microwave Instability: High-frequency wakefields distort the energy distribution of the beam, degrading longitudinal beam quality.

While complete elimination of impedance is unfeasible, minimizing impedance through smooth vacuum chamber design and suppressing instabilities using active feedback systems are standard strategies in modern synchrotrons.

1.2.2 Performance Limitations by Beam Loss

While collective instabilities represent the dynamical limits of the beam, their most severe consequence is particle loss. In high-power proton accelerators, beam loss is not merely a matter of transmission efficiency but the defining factor for the facility's maintainability and maximum achievable power. This section examines these limitations through three critical aspects: the radio-activation of machine components caused by direct loss, the degradation of experimental performance due to emittance growth, and the mechanism of chronic loss driven by beam halo formation.

Beam Loss and Machine Activation

Beam loss refers to the phenomenon where particles deviate from the stable orbit and strike accelerator components. In electron accelerators, losses primarily result in heat, but in proton accelerators, the consequences are fundamentally different due to nuclear interactions. When GeV-energy protons strike the vacuum chamber or magnets, they induce nuclear spallation reactions, transforming stable structural materials into radioactive isotopes.

This radio-activation poses a critical safety hazard. Activated equipment emits radiation even after the beam is turned off, creating a harsh environment for personnel. If residual radiation levels exceed safety limits, manual "hands-on" maintenance becomes impossible. Replacing or repairing failed components would then require prolonged cooling times for decay or the use of remote-handling systems, drastically reducing the facility's availability. Thus, the operational limit of a high-intensity proton accelerator is often determined not

by RF power or magnet strength, but by the capacity to keep beam losses below the threshold for safe maintenance (typically ∼1 W/m).

To manage this, a collimation system is employed to localize losses. Collimators are heavy shielding blocks with apertures narrower than the rest of the ring. They actively intercept the beam halo, particles diffusing away from the core, before they can strike sensitive equipment. By concentrating unavoidable losses into these heavily shielded and remote-handling-capable regions, the rest of the machine remains accessible for maintenance.

Emittance Growth and Beam Quality Degradation

Even when instabilities do not result in immediate beam loss, they degrade performance through emittance growth. Emittance is a measure of the beam's quality, representing the volume it occupies in position-momentum phase space. For experimental users, a low-emittance (compact and parallel) beam is crucial.

Instabilities perturb the orderly motion of particles, effectively "heating" the beam and expanding its phase-space volume. This dilution has two negative consequences. First, a larger beam requires larger physical apertures, increasing the risk of loss at restrictions like extraction septa. Second, it reduces the efficiency of secondary particle production. For example, in the J-PARC neutrino experiment, the proton beam must be tightly focused onto a target rod. Increased emittance enlarges the focal spot size, reducing the efficiency of pion capture and directly decreasing the resulting neutrino flux.

Beam Halo Formation and Chronic Loss

A specific manifestation of emittance growth is the formation of a beam halo. Non-linear space charge forces and lattice mismatches can drive a fraction of particles into large-amplitude oscillations, forming a tenuous "halo" surrounding the dense beam core. Although the halo contains only a small fraction of the total beam intensity, its large envelope continuously grazes the vacuum chamber walls. This results in chronic, slow beam loss that is difficult to detect but serves as a primary source of long-term machine activation. Mitigating halo formation requires precise matching of the injection beam to the ring optics and effective removal of halo particles via the collimation system described previously.

1.3 Previous Studies

Since the early development of accelerator technology, collective beam instabilities have presented fundamental limitations to high-intensity operation. Addressing these phenomena has driven sustained advancements in beam dynamics and machine design. Historically, a multi-tiered mitigation framework has been established, structured around three principal strategies:

1. Structural Design: Passive suppression through hardware optimization.
2. Operational Optimization: Quasi-static correction of machine parameters.
3. Feedback Control: Active, real-time damping of coherent oscillations.

While each strategy has contributed to the stable operation of existing machines, none offers a universal solution. The limitations of these conventional approaches highlight the critical need for improved predictive models and more effective control methods. The research described in this thesis directly addresses these gaps by investigating intra-bunch dynamics and developing advanced mitigation techniques for high-intensity proton synchrotrons.

1.3.1 Structural Design

The first line of defense consists of structural design choices that inherently suppress instability sources. These passive measures aim to create a beam environment with minimal electromagnetic perturbations. This subsection reviews the primary design strategies: minimizing geometric and resistive wall impedance, and mitigating electron cloud effects.

Geometric Impedance

The core objective of structural design is to minimize the "impedance budget" defined by the cumulative interactions between the beam and its surroundings. Geometric impedance arises from discontinuities in the vacuum chamber profile. Modern design practice aims to maintain smooth, continuous conducting boundaries for image currents. Transitions between components are shaped with gradual tapers to avoid abrupt steps. A representative example is the use of RF-shielded bellows, which accommodate mechanical tolerances while preserving electrical continuity through flexible metallic fingers. Similar impedance minimization is applied to Beam Position Monitor (BPM), vacuum ports, septa, and kicker modules, with designs optimized via three-dimensional electromagnetic simulation tools such as CST Studio Suite.

Resistive Wall Impedance

Resistive wall impedance results from the finite conductivity of the beam pipe material. This effect, prominent at low frequencies, can drive slowly growing coupled-bunch instabilities. To suppress this, high-conductivity materials such as copper or aluminum are used to construct or coat the vacuum chamber, even when mechanical considerations might suggest alternative materials like stainless steel.

Electron Cloud

Another passive concern is the electron cloud effect, especially in proton and positron machines. Stray electrons emitted from the chamber wall are accelerated by the beam and produce secondary electrons, leading to exponential amplification. Preventive measures include applying low Secondary Electron Yield (SEY) coatings, such as amorphous carbon or titanium nitride, to the vacuum chamber interior.[3]

Limitations of Structural Design

Although these passive strategies are essential for enabling stable MW-class beam operation, they have intrinsic limitations. First, impedance cannot be eliminated entirely; certain devices like RF cavities inherently present impedance. Second, passive components are

fixed at construction and cannot adapt to changes in beam conditions. Most critically, these methods primarily target impedance and electron cloud effects, offering limited mitigation for the space charge effect. These residual issues necessitate a second layer of defense: operational optimization.

1.3.2 Operational Optimization

The second tier involves the precise adjustment of machine operating parameters. Even with perfectly designed hardware, real accelerators exhibit deviations due to magnetic field imperfections and alignment errors. This subsection describes quasi-static correction schemes used to compensate for these imperfections, focusing on closed orbit correction and working point tuning.

Closed Orbit Correction

One of the fundamental procedures involves correcting the Closed Orbit Distortion (COD), which arises from dipole field errors and misaligned magnets. A large COD reduces the physical aperture and enhances nonlinear field effects. To compensate, the beam orbit is monitored by an array of BPMs. Corrections are applied via steering magnets, whose strengths are computed using algorithms based on measured response matrices. This feedback loop typically operates on a timescale of seconds to minutes, correcting slow drifts but not fast, turn-by-turn oscillations. [4]

Working Point and Chromaticity Control

A critical aspect of operational optimization is the selection of the accelerator's "working point," defined by the horizontal and vertical betatron tunes (ν_x, ν_y). In a circular accelerator, if these tunes satisfy specific integer or fractional resonance conditions, particles accumulate energy from magnetic field errors, leading to amplitude growth and beam loss. To prevent this, the main quadrupole currents are precisely adjusted to place the working point in a stable region of the tune diagram, sufficiently distant from destructive resonance lines.

Simultaneously, the chromaticity (ξ_x, ξ_y), the dependence of the betatron tune on momentum deviation, must be controlled. Natural chromaticity, induced by the strong focusing quadrupoles, is typically negative and can lead to instabilities. It is corrected using families of sextupole magnets. However, simply zeroing the chromaticity is not always ideal. A slightly non-zero chromaticity is often intentionally maintained to introduce a controlled tune spread based on the beam's momentum spread. This frequency spread disrupts the coherence of collective oscillations, a stabilization mechanism known as Landau damping.

Proper management of the working point and chromaticity is thus a balancing act: avoiding resonances while ensuring sufficient Landau damping to suppress coherent instabilities.

Limitations of Operational Optimization

While these static corrections establish a globally stable operating condition, they possess inherent limitations in time response and granularity. Since they rely on averaged

measurements, they cannot mitigate instabilities that evolve on microsecond timescales. These constraints underscore the necessity for a third class of active systems: real-time feedback control.

1.3.3 Feedback Control

When passive designs and static correction schemes fall short, the final strategy involves real-time diagnostics and active control. High-speed feedback loops detect beam motion and apply corrective kicks to damp developing instabilities. This subsection discusses the standard implementation of these systems and identifies the remaining challenges that motivate this thesis.

Standard Bunch-by-Bunch Feedback

The most established implementation is the transverse bunch-by-bunch feedback (BxBFB) system, deployed in major facilities such as the LHC, SuperKEKB, and J-PARC. A typical system consists of a BPM for detection, an Field-Programmable Gate Array (FPGA) for signal processing, and a stripline kicker for actuation. These systems treat each bunch as a rigid macroparticle, correcting the centroid motion on a turn-by-turn basis to mitigate coupled-bunch instabilities caused by long-range wakefield.

Unresolved Challenges

Despite their effectiveness against coupled-bunch modes, conventional feedback systems face two major challenges in the high-intensity frontier.

Intra-Bunch Dynamics Most current systems lack the temporal resolution to detect or correct dynamics within a single bunch. In high-intensity regimes, fast-growing intra-bunch instabilities, such as transverse head-tail modes driven by short-range wakefield, often dominate beam degradation. Suppressing these modes requires feedback bandwidths exceeding the bunch repetition rate, necessitating advancements in wide-band digital processing and kicker technology.

Space Charge Driven Incoherent Effects Standard feedback is designed to damp coherent (center-of-mass) oscillations. It is inherently ineffective against incoherent emittance growth driven by space charge tune spreads. As discussed in Sec 1.2.1, space charge forces shift individual particle frequencies, causing resonance crossings that standard feedback cannot "see" or correct.

The development of wide-band, high-speed feedback architectures is essential for extending the operational limits of next-generation accelerators. The research presented in this thesis aims to bridge this gap. By investigating how space charge effects influence intra-bunch dynamics within the J-PARC parameter space, this work contributes directly to the development of advanced feedback strategies capable of mitigating these complex instabilities.

1.4 Outline of This Thesis

This thesis consists of 12 chapters, organized to guide the reader from foundational principles to original research contributions and their experimental validation. Chapter 1 begins by outlining the scope of accelerator science, identifying the limitations imposed by collective effects in high-intensity proton synchrotrons, reviewing conventional mitigation strategies, and defining the objectives, novelty, and structure of this work. Following this, Chapter 2 introduces the J-PARC complex, the experimental site for this study, describing the overall facility and its key components. Chapter 3 then presents the necessary theoretical background, covering the fundamentals of beam dynamics and the primary collective effects such as space charge, wakefield, and impedance. The theoretical framework is developed in detail across Chapters 4 and 5, which examine analytical models of intra-bunch motion, starting with transverse decoherence and extending to head-tail modes under the influence of space charge. The core of the numerical investigation is detailed in Chapter 6, which describes the development of the macroparticle tracking simulation, and Chapter 7, which establishes the code's credibility through rigorous validation and benchmarking. With the validated code, Chapter 8 analyzes simulation results in the frequency domain, focusing on the dependence of head-tail mode spectra on beam intensity and chromaticity, while Chapter 9 explores the interaction between space charge and wakefield-driven instabilities like Transverse Mode Coupling Instability (TMCI). Chapter 10 shifts the analysis to the time domain, connecting features like the recoherence period to the underlying mode structure. The pivotal experimental validation of these findings is presented in Chapter 11, which offers a direct comparison between beam measurement results from the J-PARC Main Ring (MR) and the predictions given by the simulation. Finally, Chapter 12 concludes the thesis by summarizing the main findings, answering the research questions posed in the introduction, and discussing the outlook for future beam stability enhancement at J-PARC.

Chapter 2

J-PARC

2.1 Overview of J-PARC

J-PARC is a high-intensity proton accelerator facility located in Tokai Village, Ibaraki Prefecture, jointly operated by the Japan Atomic Energy Agency (JAEA) and KEK. The facility aims to conduct a wide range of research, from fundamental physics to industrial applications, by utilizing secondary particle beams, such as neutrons, muons, kaons, and neutrinos, generated by colliding high-energy protons with target materials. [5–8]

Figure 2.1 illustrates the schematic layout of the J-PARC facility. As shown in this figure, the accelerator complex consists of three cascaded accelerators located along the coast:

1. A 400 MeV H^- Linear Accelerator (LInear accelerator (LI))
2. A 3 GeV Rapid-Cycle Synchrotron (RCS)
3. A 30 GeV MR

Experimental facilities utilize beams extracted from these accelerators: the Materials and Life Science Experimental Facility (MLF) receives the 3 GeV beam from the RCS, while the Hadron Experimental Facility and the Neutrino Beam Line utilize the 30 GeV beam from the MR. Currently, J-PARC operates as one of the world's leading sources of high-intensity proton beams.

Detailed descriptions of LI and RCS, along with several Experimental Facilities, are provided in Appendix B.

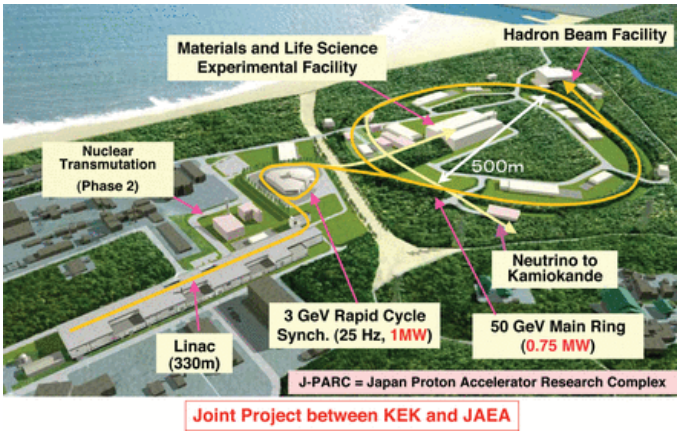

Figure 2.1: Schematic layout of the J-PARC accelerators and experimental facilities. [5]

2.1.1 Time Structure of Beams

The proton beam at J-PARC possesses a hierarchical three-staged time structure, as depicted in Fig. 2.2. This structure consists of micro-pulses (3 ns interval), intermediate-pulses, and macro-pulses (500 μs duration).

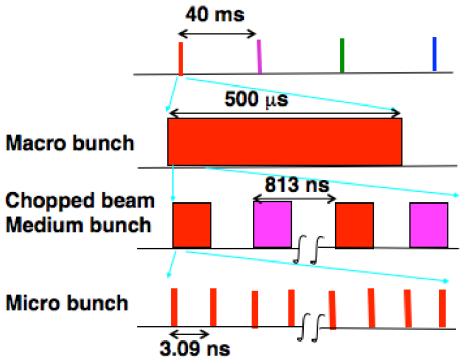

Figure 2.2: Schematic of beam time structure. [8].

Micro-pulse

The finest time structure is the micro-pulse, which is synchronized with the 324 MHz RF frequency of the LI. The continuous beam from the ion source is bunched into a train of short pulses (typically less than 100 ps), spaced at intervals corresponding to the RF wavelength.

Intermediate-pulse

The second tier is the intermediate-pulse, shaped to match the RF buckets of the RCS. Since the RCS captures the beam at a specific revolution frequency, the continuous train of micro-pulses must be chopped to fit into the stable acceleration phase of the RCS. A beam chopper in the LI removes the beam corresponding to the gap between RCS buckets, creating intermediate-pulses with a maximum duration of 456 ns. Additionally, this chopper system allows for precise intensity adjustment by thinning out pulses (a process often referred to as "MABIKI"), capable of reducing intensity down to a 1/128 ratio for commissioning or low-intensity studies. Figure 2.3 illustrates this "thinning" (MABIKI) process. By selectively chopping the intermediate pulses, various bunch patterns, ranging from a full 2-bunch injection to a sparse 1-bunch injection with a 1/128 ratio, can be created to control the total beam intensity injected into the RCS.

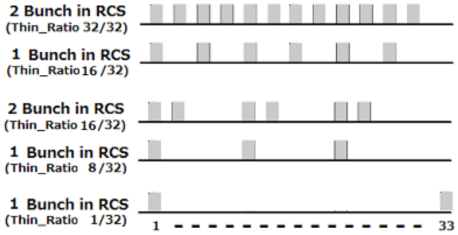

Figure 2.3: Schematic of thinning process (currently implemented with 128 segments)

Macro-pulse

The macro-pulse represents the total duration of the beam injection train from the LI to the RCS. A single macro-pulse has a maximum width of 500 μs and consists of a sequence of intermediate-pulses. During this 500 μs interval, the RCS circulates the beam for approximately 307 turns, accumulating the injected macro-pulse into two distinct bunches via the multi-turn injection method. [8, 9]

2.2 LINAC

The LI serves as the injector for the entire J-PARC complex. It is a 330-meter-long linear accelerator that accelerates negative hydrogen ions (H^-) from the ion source to 400 MeV. The acceleration system comprises four distinct cavity structures arranged in sequence:

- Radio Frequency Quadruple Linac (RFQ)
- Drift Tube Linac (DTL)
- Separated-type Drift Tube Linac (SDTL)
- Annular Coupled Structure Linac (ACS)

The primary design parameters of the LI are summarized in Table 2.1. The LI operates at a repetition rate of 25 Hz, synchronized with the RCS. Through pulse-to-pulse switching, beam characteristics such as the macro-pulse width are dynamically adjusted to match the destination's requirements (e.g., high-intensity beams for MLF users or optimized parameters for MR injection).

Table 2.1: LI parameter [10, 11]

particle	H^-
Energy [MeV]	400
Peak current [mA]	50
Repetition [Hz]	25
Pulse width [ms]	0.5

Stringent control of beam parameters is essential to minimize injection loss in the RCS. In particular, energy stability is critical; momentum fluctuations are suppressed to within $\pm 0.1\%$ (typically 400 MeV $\pm$ 0.7 MeV). Furthermore, to facilitate the painting injection scheme described in the following section, the transverse emittance of the injected beam is strictly maintained below 4π mm mrad. [10, 11]

2.3 3 GeV Rapid-Cycling Synchrotron

The RCS is a circular accelerator that functions as the central hub of J-PARC. It plays two distinct roles: acting as a high-power pulsed neutron driver for the MLF and serving as a booster injector for the MR. The ring has a circumference of 348.3 m and features a three-fold symmetric lattice structure, as shown in the schematic in Fig. 2.4. This figure

highlights the arrangement of key components: the Injection and Collimation section are located in the first straight section, the Extraction section in the second, and the RF Acceleration section in the third. Additionally, the locations of beam diagnostic instruments, indicated in red text, are distributed around the ring to monitor beam status during acceleration.

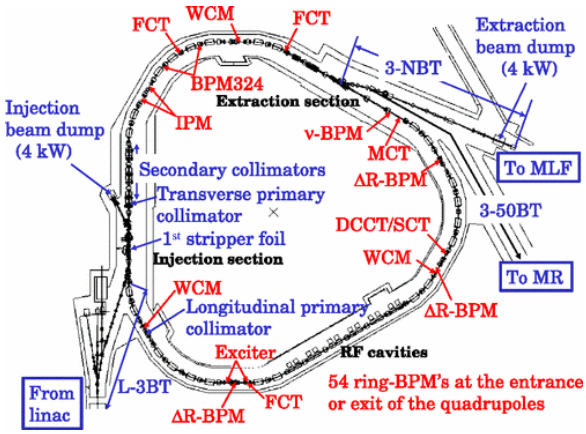

Figure 2.4: Schematic of the Rapid-Cycling Synchrotron, where the red text correspond to the beam diagnostics equipment. [12]

Key machine parameters of the RCS are listed in Table 2.2.

Table 2.2: RCS parameter [12]

Circumference [m]	348.333
Super-periodicity	3
Injection	Multi-turn, charge-exchange
Injection energy [GeV]	0.4
Injection period [ms]	0.5 (307 turns)
Harmonic number	2
Number of Bunches	2
Transition γ_t	10.8
Extraction energy [GeV]	3.0
Repetition rate [Hz]	25
Protons per pulse	8.33×10^{13}
Beam power [MW]	1
RF frequency [MHz]	1.23-1.67

The fundamental cycle of the RCS proceeds as follows, repeating at 25 Hz:

The H^-beam from the LI is injected into the RCS over a 500 μs period (multi-turn injection). Upon entry, the beam passes through a charge stripping foil, converting H^-into protons (H^+). This process occurs while the main magnet field is at its minimum. To mitigate space charge effects, "painting injection" is employed, where the injection orbit is dynamically swept using bump magnets to uniformly fill the transverse phase space.

The captured protons are accelerated from 400 MeV to 3 GeV within 20 ms. The RCS

operates with a harmonic number of 2, meaning the beam forms two bunches within the ring.

Once the beam reaches 3 GeV, it is extracted in a single turn using fast kicker magnets. The extracted beam is transported to either the MLF or the MR. This switching is controlled by pulsed bending magnets in the transport line, synchronized with the MR cycle. Since the MR cycle is typically several seconds long, most RCS pulses are directed to the MLF. When the MR is ready for injection, the pulsed magnets divert the beam to the MR. Typically, four consecutive RCS pulses (injecting $2 \times 4 = 8$ bunches) are required to fill the MR, after which the beam delivery reverts to the MLF. [12–15]

2.4 30 GeV Main Ring

The MR is a large-scale synchrotron with a circumference of 1,567.5 m, located at the downstream end of the J-PARC accelerator complex. It features a three-fold symmetric lattice structure comprising three arc sections and three long straight sections. Each straight section is dedicated to specific functions: Injection and Collimation section, "Slow Extraction" section, and RF Acceleration and "Fast Extraction" section. Figure 2.5 presents the layout of the MR and its associated experimental facilities. The triangular-shaped ring connects to the Hadron Experimental Facility (HD) via the Slow Extraction (SX) section and to the Neutrino Experimental Facility (NU) via the Fast Extraction (FX) section.

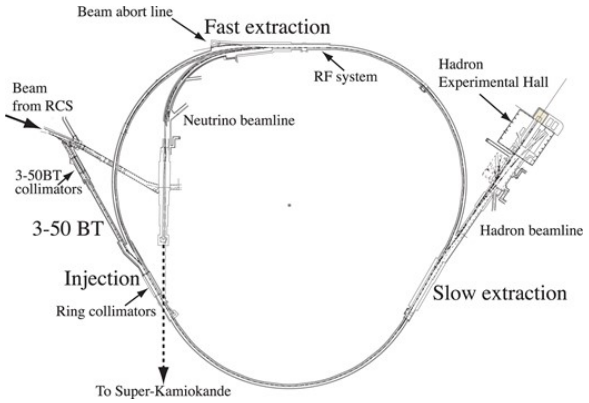

Figure 2.5: Schematic of the Main Ring, the Hadron Experimental Facility, and the Neutrino Experimental Facility. [16]

Designed to accelerate protons to 30 GeV, the MR operates with a cycle consisting of injection, acceleration, and extraction phases. The main parameters of the MR are presented in Table 2.3. The cycle begins with a "flat bottom" phase (P1–P2), where the magnetic field is held constant to circulate the 3 GeV beam injected from the RCS. During this period, the MR receives beams from the RCS four times at 40 ms intervals. Since the RCS provides two bunches per extraction and the MR operates with a harmonic number of 9, a total of 8 bunches are filled, leaving one bucket empty to accommodate the rise time of the extraction kicker. Following injection, the magnetic field is ramped up over typically 1.4 seconds (from P2 to P3) to accelerate the beam to 30 GeV. Synchronously,

the RF frequency is swept from 1.67 MHz to 1.72 MHz to match the increasing velocity of the protons.

Table 2.3: MR parameter [16]

Circumference [m]	1567.5
Super-periodicity	3
Injection	Bunch to bucket
Injection energy [GeV]	3
Injection period [ms]	120
Harmonic number	9
Number of Bunches	8
Transition γ_t	31.6**i**
Extraction energy [GeV]	30
Repetition rate [Hz]	0.4-0.86
Protons per pulse	3.3×10^{14}
Beam power [MW]	0.75-1.3
RF frequency [MHz]	1.67-1.72

The extracted beam is delivered to experimental facilities via two distinct methods depending on the physics requirements:

- Fast Extraction (FX): All 8 bunches are extracted within a single turn (approx. 5 μs) and delivered to NU.
- Slow Extraction (SX): The beam is extracted continuously over several seconds and delivered to HD.

Figure 2.6 contrasts the beam intensity and energy evolution for these modes. In FX shown in Fig. 2.6a, the beam is accelerated to 30 GeV (blue line) and all 8 bunches are extracted instantaneously, resulting in a sharp drop in intensity (red line). Conversely, in SX shown in Fig. 2.6b, the beam intensity decreases gradually over several seconds as the beam is continuously spilled to HD.

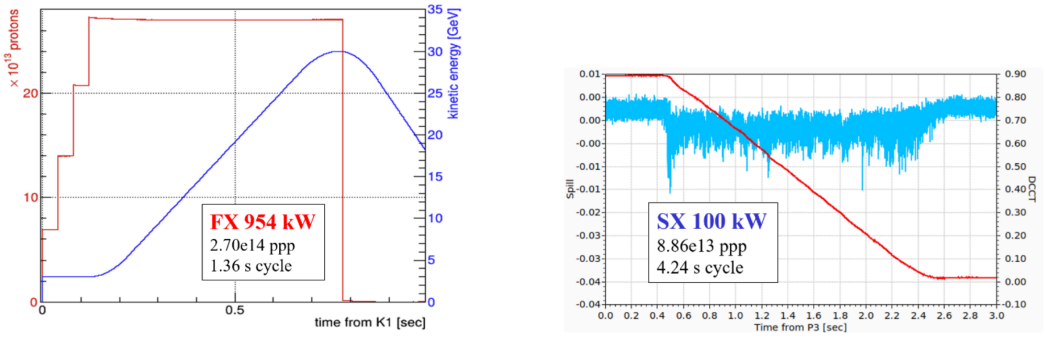

(a) **(b)**

Figure 2.6: (a) Beam intensity (red) and kinetic energy (blue) during the 954 kW FX beam study. (b) Beam intensity (red) and spill structure (blue) during the 100 kW SX beam study. [17]

To maximize the integrated beam power for neutrino experiments, the MR has transitioned to a high-repetition operation scheme at FX. By upgrading the magnet power supplies and RF systems, the repetition cycle has been significantly shortened (to 1.36 (1.28) s or 1.16 s) compared to the original design, prioritizing beam intensity (power) over maximum energy. [16, 18–23]

2.4.1 Lattice Design

The MR employs a FODO-type lattice, a standard structure for beam focusing. A defining feature of the MR design is the use of an imaginary transition energy (γ_t). Generally, when a beam crosses the transition energy during acceleration, it becomes susceptible to instabilities. To avoid this, the MR creates a lattice with a negative momentum compaction factor (α_C), resulting in an imaginary transition energy ($\gamma_t = 1/\sqrt{\alpha}$). This design ensures that the beam never crosses the transition energy throughout the entire acceleration process from 3 GeV to 30 GeV, thereby maintaining stability.

2.4.2 Beam Injection

Proton bunches from the RCS are transported via the 3GeV to 50GeV Beam Transport (3-50BT) line and injected into the MR using a kicker-based injection scheme. This process involves filling the 8 buckets through four separate injection cycles. The injection system comprises three types of electromagnets:

1. Septum Magnets: Two units bend the incoming beam to align it parallel to the circulating orbit.
2. Bump Magnets: Three units create a local orbit distortion (bump) to bring the circulating orbit closer to the injection point, ensuring sufficient physical aperture.
3. Injection Kickers: Fast-response magnets kick the injected bunches onto the central closed orbit.

Figure 2.7 illustrates the schematic of the MR injection section. As depicted, the beam transported from the 3-50BT line is guided into the ring using Septum Magnets and placed onto the circulating orbit by the Injection Kickers. To preserve the quality of the already circulating bunches, a counter-kicker system is employed to cancel out any residual field (reflection) from the main injection kickers. [24]

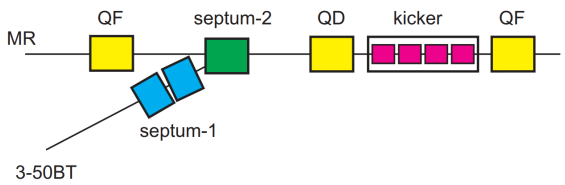

Figure 2.7: Schematic of the MR injection section. [24]

2.4.3 Magnet System

The main magnet system consists of 96 bending magnets (6 families), 216 quadrupole magnets (16 families), and 72 sextupole magnets (3 families), along with 186 steering magnets. The magnet cores are constructed from laminated silicon steel to minimize eddy currents during rapid cycling. The Power Supply (PS) system driving these magnets utilizes a capacitor-bank energy storage system. This advanced design was introduced to enable high-repetition operation (1.3 s cycle or faster) without imposing excessive load fluctuations on the commercial power grid. [25, 26]

2.4.4 Radio Frequency Cavity

The RF system utilizes high-gradient Magnetic Alloy (MA) cavities employing FINEMET FT3L cores. This material offers a high shunt impedance, enabling the generation of high accelerating voltages within a compact footprint. The cavities operate with a low Q-value ($Q \approx 26$) configured by a cut-core structure, which eliminates the need for active frequency tuning loops and passively suppresses transient beam loading. To support the high-power operation, the system currently comprises 11 fundamental frequency cavities and 2 second-harmonic cavities used for bunch shaping. [27]

2.4.5 Collimator and Beam Dump

Beam collimation is essential for localizing beam loss and preventing radio-activation of the accelerator components. The MR employs a two-stage collimation strategy:

1. Pre-collimation: The beam halo is stripped in the 3-50BT line before injection.
2. Ring Collimation: A dedicated collimator section within the MR removes any secondary halo generated during injection or acceleration.

The collimators restrict the aperture to 54–60 π mm·mrad, significantly narrower than the physical aperture of the ring magnets (81 π mm·mrad), ensuring that losses occur exclusively at the collimators. The effectiveness of this localization is demonstrated in Fig. 2.8, which plots the beam loss monitor signals around the ring. The signals are predominantly concentrated in the collimator section (indicated in red), while losses in other regions (blue) are suppressed to negligible levels, even when measured with 24 times higher sensitivity The current system utilizes rotatable tungsten blocks capable of handling high heat loads. While the collimators are designed to absorb up to 3.5 kW of beam loss, operational limits are typically set lower (about 1 kW total loss) to maintain a safe maintenance environment.

For beam aborts and machine tuning, the ring is equipped with a beam dump capable of absorbing 30 kW (after recent upgrades), allowing for safe disposal of the full intensity beam. Figure 2.9 shows the schematic of the beam dump core structure. The core, composed of copper and graphite, is roughly 4 meters long and is installed deep within iron and concrete shielding to safely absorb the full intensity beam energy. [28, 29]

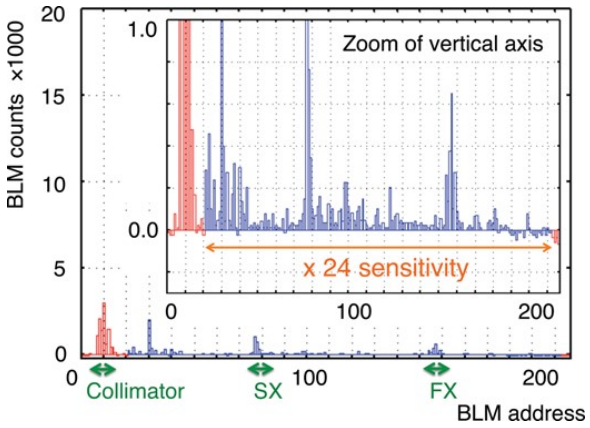

Figure 2.8: Distribution of beam loss monitor signals during high-power beam operation at 1×10^{14} ppp. Signal sensitivity in the blue region is 24 times that in the red region. [16]

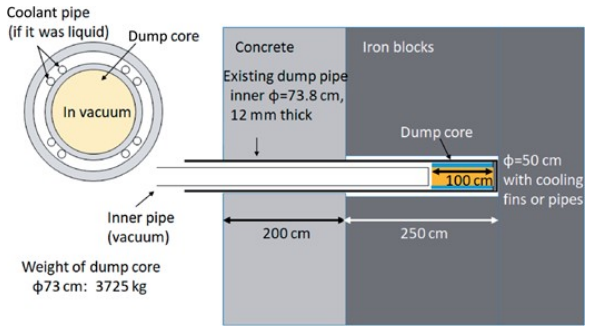

Figure 2.9: Schematic of installed dump core [18]

2.4.6 Beam Extraction

For neutrino experiments, the FX system extracts the entire 30 GeV beam (8 bunches) in a single turn. The system utilizes a bipolar kicker magnet configuration capable of kicking the beam in two directions:

- Inward Kick: Directs the beam to the neutrino experimental beamline.
- Outward Kick: Directs the beam to the abort dump. This path is used for machine tuning and as an emergency abort system to protect hardware in case of failures.

To handle high-intensity beams exceeding 750 kW, the extraction hardware has been upgraded to reduce impedance and heating. The kicker magnets feature water-cooled cores and damping resistors to suppress wakefield heating. Furthermore, the downstream extraction line employs large-aperture magnets, such as the recently developed large-bore quadrupole (QDT), to expand the physical aperture to 60 π mm·mrad, thereby eliminating beam loss bottlenecks in the extraction region.

Figure 2.10a shows the schematic configuration of the FX septum magnets. The beam is deflected sequentially by the low-field eddy current type septa and the high-field septa. A photograph of the installed high-field septum magnets is provided in Fig. 2.10b, showing the actual hardware arrangement in the tunnel. [4, 30–33]

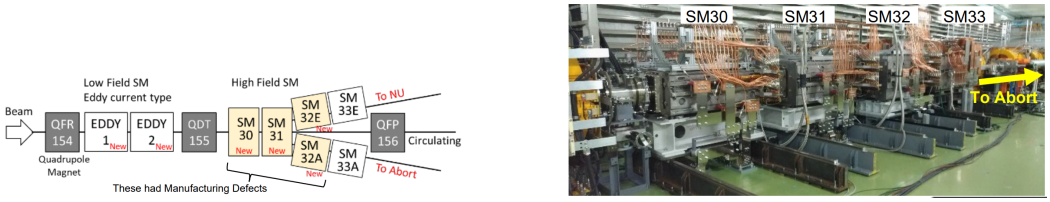

(a) **(b)**

Figure 2.10: (a) Schematic of the FX septum magnet (SM). (b) Photo of the high-field SM. [32]

2.5 Beam Diagnosis

Precise beam diagnostics are essential for maintaining stable operation and achieving high-quality beams in high-intensity proton accelerators like J-PARC. These systems provide real-time information on beam properties such as position, profile, intensity, and temporal structure, serving as the "eyes" of the accelerator. This section describes the key diagnostic instruments employed in the J-PARC MR focusing on their principles, implementation, and roles in beam tuning and machine protection.

2.5.1 Beam Position Monitor

The BPM system is the primary diagnostic tool for measuring the transverse trajectory of the beam center of mass. It plays a critical role in measuring the COD and correcting orbit distortions. The J-PARC BPM system is optimized for each accelerator stage, with

distinct detector structures and signal processing schemes tailored to the specific beam parameters of the LI, RCS, and MR.

The MR is equipped with 186 BPM units, constituting the largest diagnostic subsystem at J-PARC. The detectors employ electrostatic diagonal-cut cylindrical electrodes as illustrated in Fig. 2.11a, made of stainless steel (SUS316L). This diagonal geometry (V_1 to V_4) ensures excellent linearity over a wide aperture (typically 130 mm), which is crucial for handling large-emittance beams.

To maximize radiation resistance, no active electronic components, such as pre-amplifiers, are installed inside the accelerator tunnel. Instead, signals from the four electrodes are transmitted via independent coaxial cables to Beam Position Monitor Circuit (BPMC) units located in radiation-free service buildings. The BPMC incorporates a high-speed Analog to Digital Converter (ADC) (14-bit, 80 MS/s) and an FPGA for digital signal processing. Figure 2.11b outlines the signal processing schematics. The signals pass through calibration switches and attenuators before being digitized, allowing for precise position calculation.

The system provides three distinct measurement modes:

1. COD Mode: Measures the average closed orbit using Fast Fourier Transform (FFT) analysis, providing the input for global orbit correction.
2. Bunch-by-Bunch (BxB) Mode: Detects the peak of each bunch's waveform to measure the position on a bunch-by-bunch and turn-by-turn basis. This mode is essential for analyzing injection oscillations and betatron tunes.
3. Waveform Mode: Records raw voltage waveforms for detailed offline analysis.

To achieve a position accuracy of better than 0.2 mm, advanced calibration techniques utilizing the beam itself are employed. Beam Based Alignment (BBA) is used to determine the offset between the electrical center of the BPM and the magnetic center of the adjacent quadrupole magnet. Additionally, Beam Based Gain Calibration (BBGC) calibrates the gain differences among the four signal channels, including cables and electronics, by using beam signals. This combination ensures high reliability and precision, underpinning the stable operation of the MR.

In this study, BPM was used to detect intra-bunch oscillations per turn. Analysis was performed using Waveform Mode with data stored in the FPGA under shot-by-shot conditions. [34–37]

2.5.2 Beam Profile Monitor

Beam profile monitors measure the transverse spatial distribution (cross-sectional shape) and size of the beam. These measurements are vital for emittance evaluation and for matching the beam optics between accelerators.

Multi-Ribbon and Multi-Wire Profile Monitors

Multi-Ribbon Profile Monitor (MRPM) and Multi-Wire Profile Monitor (MWPM) operate on the principle of secondary electron emission. An array of fine wires or ribbons is inserted

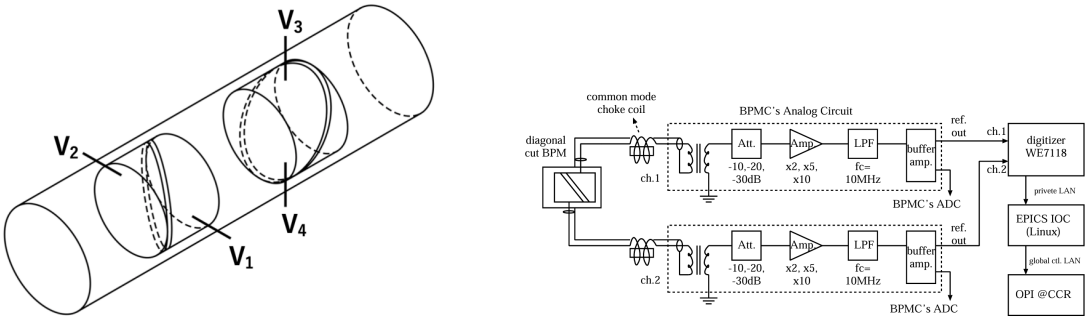

(a) **(b)**

Figure 2.11: (a) Schematic of the BPM of J-PARC MR. [36] (b) Schematic of the signal processing for the BPM of J-PARC MR. [38]

into the beam path, and the profile is reconstructed from the intensity distribution of secondary electrons emitted when the beam strikes the target material. Figure 2.12a shows the schematic of the MRPM .

To accommodate the increasing beam intensity at J-PARC, target materials have been progressively upgraded to minimize thermal damage and beam scattering. Standard tungsten wires have been replaced by titanium ribbons, which offer higher signal strength, and graphite ribbons, which have a low atomic number ($Z = 6$) to minimize beam interaction.

Specific implementations include:

- RCS Injection Line: The choice of monitor depends on the beam species. Upstream of the charge stripping foil, where H^-ions are present, electrons stripped from the ions provide a strong signal, allowing the use of 0.1 mm diameter gold-plated tungsten wires. Downstream, where protons (H^+) are dominant, the signal relies on secondary emission (efficiency ∼1%), necessitating the use of thicker 1 mm titanium ribbons to ensure sufficient signal-to-noise ratio.
- 3-50BT Line: 10 MRPMs utilizing 1 μm thick graphite or titanium ribbons diagnose the beam profile during transport to the MR.
- Injection Point (INJ-MRPM): A specialized monitor at the MR injection point measures both the injected beam and the circulating beam for up to 100 turns. Using ultra-thin targets (3 μm titanium / 1 μm graphite), it enables detailed analysis of injection matching and turn-by-turn oscillations.
- Abort Line (ABT-MRPM): Installed in the beam dump line, this monitor allows for profile measurement at any timing in the acceleration cycle by extracting the beam to the dump. Combined with the "Q-scan" method (varying quadrupole strength), it enables precise emittance measurements. A high-speed DAQ system supports detailed analysis of the beam core and halo structure. Figure 2.12b presents typical measurement results from the ABT-MRPM, displaying the clear beam profiles in both horizontal and vertical planes.

In this study, tests were conducted using ABT-MRPM while confirming that no changes

in emittance occurred. This ensures that no instabilities were occurred. [39, 40]

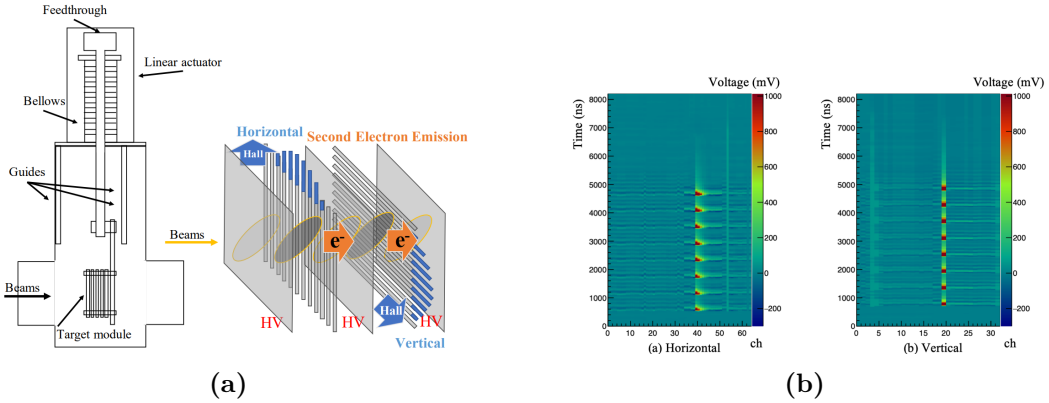

(a) **(b)**

Figure 2.12: (a) Schematic of the multi-ribbon profile monitor. (b) Profing results of MR ABT-MRPM. [40]

Wall Current Monitor

The Wall Current Monitor (WCM) is a non-destructive, wide-band monitor designed to detect the image current flowing along the inner wall of the vacuum chamber. Structurally, a ceramic break insulates a section of the beam pipe, which is bridged by a resistor array. The voltage drop across these resistors, induced by the wall current accompanying the beam, reproduces the beam's longitudinal current profile. A key feature of the WCM is its broad frequency response (from a few hundred kHz to several hundred MHz). This is achieved by loading the monitor with FINEMET cores to provide inductance that cancels the stray capacitance of the ceramic gap. The wide-band capability of the WCM serves multiple critical functions:

- Longitudinal Diagnostics: It enables precise observation of the bunch shape and detailed temporal structure. The "mountain plot" analysis, which stacks waveform traces for each revolution, is indispensable for diagnosing synchrotron oscillations and injection mismatching.
- Beam Loading Compensation: The WCM signal provides the high-frequency beam current input for the RF feedforward system. This system cancels the wakefield voltage induced in the cavities, which is essential for stable high-power acceleration in both the RCS and MR.
- Physics Analysis: WCM data is used to calculate the bunching factor (critical for space charge evaluation) and to verify longitudinal painting efficiency. Furthermore, harmonic analysis of the WCM and cavity voltage signals allows for the experimental evaluation of the machine impedance seen by the beam.

In this study, the synchrotron tune ν_s was confirmed by verifying the increase and decrease in the bunch peak current due to lonfutidinal quadrupole oscillations.It was also used for adjustments to establish the longitudinal phase space matching conditions. [41, 42]

2.5.3 Beam Current Monitor

Current Transformers (CTs) are non-destructive monitors used to measure the total beam intensity (charge) and phase. J-PARC utilizes three types of CTs: Slow Current Transformer (SCT) and Fast Current Transformer (FCT) for Alternating Current (AC) components, and DC Current Transformer (DCCT) for Direct Current (DC) components. To enhance sensitivity, most sensors (excluding the RCS DCCT) employ FINEMET FT3M cores due to their high magnetic permeability.

DC Curent Transformer

The DCCT is the primary instrument for measuring the circulating beam intensity in the RCS and MR with high precision (better than 0.1%). It fulfills two main roles: accurate accounting of the number of accelerated protons and machine protection through real-time beam loss monitoring (by differentiating the intensity signal).

Since standard transformers cannot couple to DC currents, the DCCT employs a parametric modulation technique. Two toroidal cores are driven into magnetic saturation by an external modulator at roughly 1 kHz in opposite phases. Any DC beam current passing through the cores creates a flux imbalance, which is detected as a second-harmonic signal. For AC components (typically 5 Hz to 20 kHz), a separate core functions as a standard transformer. Advanced feedback circuitry integrates these DC and AC signals to drive a compensation current that nulls the magnetic flux in the cores. Measuring this feedback current yields the beam current with high stability, independent of the core's magnetic properties.

The system is designed for high reliability and noise immunity. The detector head is magnetically and electrostatically shielded, and all active electronics are located outside the accelerator tunnel to prevent radiation damage.

In this study, it was used to confirm that no beam loss occurred due to beam instability or longitudinal mismatch. [43, 44]

2.6 Experimental Facilities

The three main experimental facilities at J-PARC utilizing the high-intensity proton beams supplied from the RCS and MR are MLF, HD, and NU. These facilities drive cutting-edge research in diverse fields ranging from materials science to fundamental particle physics. Since the beam dynamics and extraction schemes discussed in this thesis are particularly critical for the high-power operation required by neutrino physics, this section focuses on the primary beamline of the Neutrino Experimental Facility. Detailed descriptions of MLF, HD, and the downstream detector systems of NU are provided in Appendix B. [45]

2.6.1 Neutrino Experimental Facility

T2K Experiment

NU is the host of the Tokai to Kamioka (T2K) experiment, a long-baseline neutrino oscillation experiment designed to probe the fundamental properties of neutrinos. In this

experiment, the 30 GeV proton beam extracted from the MR strikes a graphite target to produce secondary pions, which subsequently decay into muons and muon neutrinos. The resulting intense neutrino beam is directed toward the Super-Kamiokande (SK) detector, located approximately 295 km away in Kamioka, Gifu Prefecture.

The primary physics goal of T2K is to elucidate the mixing parameters of neutrino oscillations, specifically to observe the appearance of electron neutrinos from a muon neutrino beam ($\nu_\mu \rightarrow \nu_e$) and to measure the disappearance of muon neutrinos. By comparing these oscillation patterns between neutrinos and antineutrinos, the experiment aims to constrain the CP-violation phase (δ_{CP}) in the lepton sector, which may provide clues to the matter-antimatter asymmetry of the universe. To achieve statistically significant measurements of these rare events, a high-intensity proton beam is indispensable. The history of beam delivery to the T2K experiment is summarized in Fig. 2.13. The plot shows the steady increase in beam power (right axis) and the accumulated Protons On Target (POT) (left axis) over the years, reflecting the continuous upgrades of the accelerator facility.

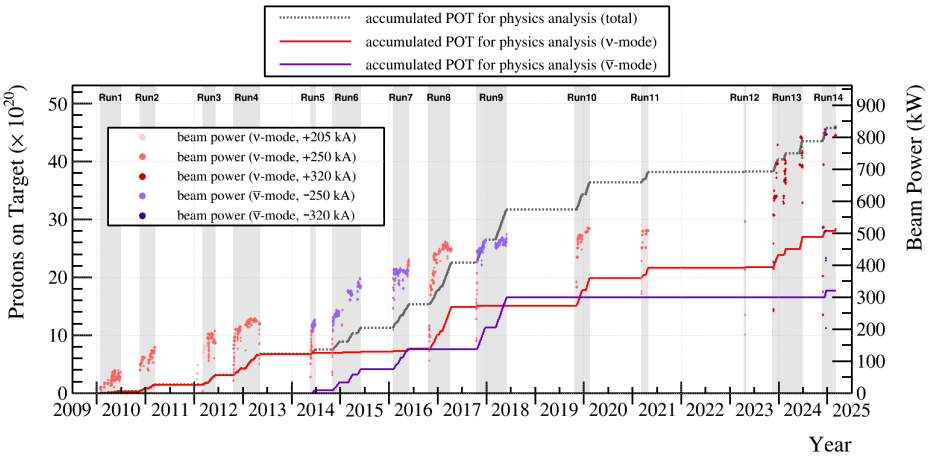

Figure 2.13: History of delivered proton count to the T2K experiment. [46]

2.6.2 Hyper-Kamiokande Experiment

Hyper-Kamiokande is the next-generation ultra-large water Cherenkov detector currently under construction as the successor to SK, with observations scheduled to begin in 2027. The detector will possess an effective volume approximately eight times that of SK and will be equipped with newly developed high-performance photomultiplier tubes. The physics target of Hyper-Kamiokande extends beyond the precision measurement of neutrino oscillation parameters; it aims for the definitive discovery of CP violation in the lepton sector with high statistical significance. To maximize the potential of this massive detector, the J-PARC MR is required to upgrade its beam power to 1.3 MW, delivering an unprecedented flux of neutrinos to Kamioka. The suppression of beam instabilities discussed in this thesis is a prerequisite for achieving this design intensity.

2.6.3 Primary Beamline

The primary proton beamline transports the high-intensity beam from the MR extraction point to the production target. Figure 2.14 illustrates the layout of the primary neutrino beamline, showing the three sections: the Preparation Section, the Arc Section, and the Final Focusing Section. [47–52]

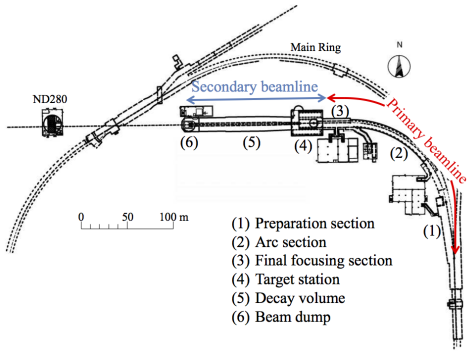

Figure 2.14: Schematic of the neutrino beamline. [47]

Preparation Section

This section is located immediately downstream of the MR extraction point. Its primary function is to match the beam optics to the subsequent arc section and, crucially, to eliminate beam halos. Since the downstream Arc Section employs superconducting magnets, protection against quenching caused by beam loss is paramount. The section comprises 11 normal-conducting magnets and 4 collimators. These collimators scrape off beam halos exceeding a transverse emittance of 60π mm mrad. The system is designed to handle controlled beam losses, with a maximum allowable point loss set to 750 W, thereby ensuring a clean beam enters the superconducting region.

Arc Section

The Arc Section bends the proton beam trajectory by 80.7 degrees to direct it toward Kamioka. Due to site constraints, the radius of curvature is relatively small (approximately 100 m), necessitating the use of strong magnetic fields. To achieve this, 28 Superconducting Composite Function Magnets (SCFMs) are employed. These innovative magnets generate both a dipole field (2.6 T) for bending and a quadrupole field (18.6 T/m) for focusing simultaneously. Physically, they are arranged in a doublet structure, where two SCFMs are housed within a single cryostat. To minimize the risk of quenching, the physical aperture is designed with a large tolerance of 206π mm mrad, keeping uncontrolled beam loss below 1 W/m. [53]

Final Focusing Section

After passing through the Arc Section, the beam enters the Final Focusing Section, which performs the precise targeting irradiation. This section focuses the beam onto the center of the graphite target while simultaneously bending the trajectory downward by approximately 3.65 degrees to aim at SK. It consists of 10 normal-conducting magnets,

including two specialized vertical bending magnets designated as FV1 and FV2. Like the Preparation Section, the acceptance is limited to 60π mm mrad. In this section, the beam optics involve expanding the beam size before final focusing, making it sensitive to optical mismatches. Consequently, relatively high beam loss is anticipated, estimated at a maximum of 250 W point loss.

Chapter 3

Basic Dynamics and Intensity Effects in Synchrotron

This chapter describes the theoretical framework necessary for understanding the beam dynamics discussed in this thesis. While Chapter 1 outlined the operational limitations imposed by collective effects in high-intensity proton synchrotrons from a global perspective, this chapter provides the rigorous mathematical formalism and physical mechanisms governing these phenomena.

While the motion of a single particle in a synchrotron is well-described by linear optics, the behavior of high-intensity beams, which is the central theme of this research, is governed by complex collective effects. As beam intensity increases, the electromagnetic fields generated by the beam itself, specifically space charge fields and wakefield, become comparable to the external guiding fields, acting as significant perturbations that can drive instabilities.

We begin by reviewing the fundamental transverse and longitudinal dynamics of a single particle to define key parameters such as emittance and tune. Subsequently, we introduce the mechanisms of collective effects, focusing on space charge forces and impedance-driven wakefield. Finally, we describe the theory of beam instabilities resulting from these interactions and the feedback systems used to mitigate them. These theoretical concepts provide the basis for the analytical models and simulation studies presented in the subsequent chapters.

3.1 Transverse Motion

In a synchrotron, particles are guided by a magnetic lattice that confines their trajectories near a central design orbit. The motion of these particles in the directions perpendicular to this orbit, defined by the horizontal (x) and vertical (y) planes, is known as transverse motion. A thorough understanding of these dynamics is fundamental to ensuring the stability and preservation of the beam over many revolutions.

3.1.1 Equation of Motion and Coordinate System

To describe a particle's trajectory, we use the Frenet-Serret coordinate system, which moves along the design orbit. This system is defined by the longitudinal path length s and the transverse displacements x (horizontal) and y (vertical). Within this frame, the transverse motion is governed by periodic focusing forces, primarily generated by quadrupole magnets. This motion is described by a second-order linear differential equation known as Hill's

Equation:

$$\frac{d^2}{ds^2}x + K(s)x = 0. \tag{3.1}$$

Here, x represents either the horizontal or vertical coordinate. The function $K(s)$ is the focusing strength, which is periodic with the accelerator lattice ($K(s+L) = K(s)$ for a lattice period L). It represents the magnitude of the focusing (or defocusing) forces acting on the particle at a position s along the ring.

3.1.2 Betatron Oscillation and Phase Space

The solution to Hill's Equation describes a quasi-harmonic motion known as betatron oscillation. Particles oscillate around the central design orbit, but unlike simple harmonic motion, the oscillation's amplitude is modulated by the varying focusing strength $K(s)$. The solution for a particle's position $x(s)$ and angle $x'(s) = dx/ds$ is expressed using a set of parameters known as Twiss parameters (α, β, γ):

$$x(s) = \sqrt{\epsilon\beta(s)}\cos(\phi(s) + \phi_0), \tag{3.2}$$

$$x'(s) = -\sqrt{\frac{\epsilon}{\beta(s)}}(\alpha(s)\cos(\phi(s) + \phi_0) + \sin(\phi(s) + \phi_0)). \tag{3.3}$$

The state of any particle is fully described by its coordinates in phase space, the two-dimensional plane defined by position x and angle x'. A single particle's trajectory in phase space traces an ellipse. Key parameters defining this motion are described below.

Beta function $\beta(s)$

The beta function $\beta(s)$ is a periodic function determined by the magnetic lattice. It describes the envelope (amplitude modulation) of the betatron oscillation. Regions with a small $\beta(s)$ correspond to a tightly focused beam, while regions with a large $\beta(s)$ correspond to a larger beam size.

Phase advance $\phi(s)$

The phase of the oscillation advances along the accelerator according to the integral:

$$\phi(s) = \int_0^s \frac{ds'}{\beta(s')}. \tag{3.4}$$

Emittance ϵ

Emittance ϵ is a constant of motion for a single particle (in the absence of dissipative effects) that defines its maximum oscillation amplitude. It is proportional to the area of the particle's phase space ellipse. This elliptical area is described by the Courant-Snyder invariant:

$$\epsilon = \gamma(s)x^2(s) + 2\alpha(s)x(s)x'(s) + \beta(s)x'^2(s). \tag{3.5}$$

The Twiss parameters themselves are related by the Wronskian condition:

$$\beta(s)\gamma(s) - \alpha(s)^2 = 1. \tag{3.6}$$

For an entire beam of particles, the rms emittance (ϵ_{rms}) is used as a statistical measure of the phase space area occupied by the beam:

$$\epsilon_{\text{rms}} = \sqrt{\sigma_x^2 \sigma_{x'}^2 - \sigma_{xx'}^2}. \tag{3.7}$$

These quantities are given by the central moments of the beam distribution (where σ_x is the rms beam size, $\sigma_{x'}$ is the rms beam divergence, and $\sigma_{xx'}$ is the correlation term):

$$\sigma_x^2 = \overline{x^2} - (\overline{x})^2, \tag{3.8}$$

$$\sigma_{x'}^2 = \overline{x'^2} - (\overline{x'})^2, \tag{3.9}$$

$$\sigma_{xx'}^2 = \overline{xx'} - \overline{x}\,\overline{x'}. \tag{3.10}$$

To compare beam quality across different energy levels, the normalized emittance is used:

$$\epsilon_{\text{norm,rms}} = \beta_{\text{rel}} \gamma_{\text{rel}} \epsilon_{\text{rms}}, \tag{3.11}$$

where β_{rel} and γ_{rel} are the relativistic Lorentz factors (not to be confused with the Twiss parameters β and γ).

3.1.3 Betatron Tune and Resonance

In a circular accelerator, one of the most critical parameters is the betatron tune (ν), defined as the number of betatron oscillations a particle completes per revolution:

$$\nu = \frac{1}{2\pi} \oint \frac{1}{\beta(s)} ds. \tag{3.12}$$

Beam stability is critically dependent on the tune. If the horizontal and vertical tunes (ν_x, ν_y) satisfy a resonance condition:

$$k\nu_x + l\nu_y = n, \tag{3.13}$$

where k, l, n are integers, even small imperfections in the magnetic fields can resonantly drive the oscillation amplitude, leading to particle loss. Figure 3.1 shows a tune diagram with third-order resonance lines, where the fractional part of the tune satisfies the region $0 < \nu_x < 0.5, 0 < \nu_y < 0.5$.

Therefore, the operating tunes must be carefully chosen to avoid these resonance lines on a tune diagram.

3.1.4 Effect of Momentum Deviation

Not all particles in a beam have the design momentum p_0. The behavior of these off-momentum particles, characterized by their relative momentum deviation $\delta = \Delta p/p_0$, is different. The equation of motion for an off-momentum particle, including the effect of bending magnets (with bending radius ρ), is given by the inhomogeneous Hill's equation:

$$\frac{d^2}{ds^2} x + K(s)x = \frac{\delta}{\rho(s)}. \tag{3.14}$$

The solution to this equation is the sum of the betatron oscillation $x_\beta(s)$ and a new stable orbit $\Delta x_\delta(s)$ that depends on the momentum:

$$x(s) = x_\beta(s) + \Delta x_\delta(s). \tag{3.15}$$

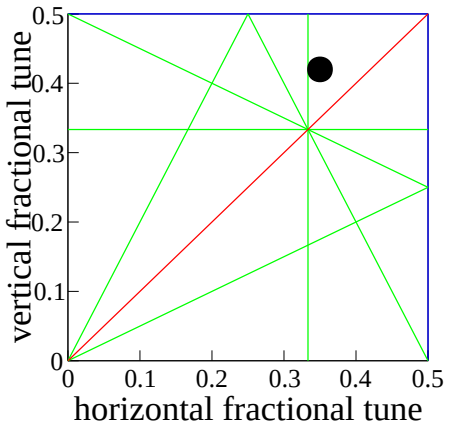

Figure 3.1: Tune diagram with resonance lines ($0 < \nu_x < 0.5, 0 < \nu_y < 0.5$)

Dispersion Function $D(s)$

Particles with higher momentum ($\delta > 0$) are bent less by the dipole magnets, resulting in an outward shift of the closed orbit. The dispersion function $D(s)$ is defined by this relationship,

$$\Delta x_\delta(s) = D(s)\delta, \tag{3.16}$$

and it quantifies the closed orbit shift per unit momentum deviation.

Chromaticity ξ

The focusing strength of a quadrupole magnet is momentum-dependent ($K \propto 1/p$). As a result, the betatron tune shift also depends on momentum. This dependence is called chromaticity (ξ), defined as the change in tune per unit momentum deviation:

$$\Delta\nu = \xi\delta. \tag{3.17}$$

The "natural" chromaticity of an accelerator lattice is typically negative, which can drive beam instabilities. To counteract this, sextupole magnets are strategically placed to correct the chromaticity, usually adjusting it to a small positive or zero value. This chromatic effect is a primary cause of the transverse decoherence phenomena discussed in Chapter 4.

3.2 Longitudinal Motion

In addition to transverse confinement, a mechanism is required to maintain the energy of the particles and to group them into discrete packets known as bunches. This is the domain of longitudinal motion, which describes the dynamics governing the relationship between a particle's energy and its timing relative to the accelerating system.

3.2.1 Synchronized Particles and Coordinate System

We begin by defining an ideal reference particle, the synchronous particle, which has the exact design momentum p_0 and energy E_0. This particle travels on the design orbit

and arrives at each RF accelerating cavity at a precise synchronous phase (ϕ_s). The longitudinal state of any other particle is described by its deviation from this synchronous particle:

- Energy Deviation (ΔE): The difference in energy, $\Delta E = E - E_0$.
- Phase Deviation (ϕ): The difference in RF phase upon arrival at a cavity, which is proportional to the time-of-arrival difference Δt.

3.2.2 Principles of RF Acceleration and Phase Stability

RF cavities are resonant metallic structures that sustain a time-varying, sinusoidal electric field. As particles pass through, they receive an energy gain given by $\Delta E = eV_{\mathrm{RF}} \sin(\phi)$, where V_{RF} is the peak cavity voltage. The synchronous particle arrives at phase ϕ_s to receive the exact energy gain $eV_{\mathrm{RF}} \sin(\phi_s)$ needed to compensate for losses (e.g., from synchrotron radiation) or to achieve net acceleration.

The core concept that allows for stable bunches is the principle of phase stability. For a machine operating below its transition energy ($\gamma < \gamma_T$, or slip factor $\eta < 0$), stability is achieved by choosing a synchronous phase on the rising slope of the RF voltage. The restoring mechanism works as follows:

- A particle arriving earlier ($\phi < \phi_s$) sees a lower voltage and receives less energy. Due to the negative slip factor ($\eta < 0$), lower energy leads to a shorter revolution period (higher velocity dominates). Thus, on the next turn, it arrives later, moving back towards ϕ_s.
- A particle arriving later ($\phi > \phi_s$) sees a higher voltage and receives more energy. This increases its revolution period, causing it to arrive earlier on the next turn, also moving back towards ϕ_s.

This feedback mechanism ensures that particles with small deviations will oscillate stably around the synchronous particle.

3.2.3 Synchrotron Oscillation

The interplay between a particle's energy and phase deviations leads to a slow, oscillatory motion known as synchrotron oscillation. The dynamics are governed by how a particle's revolution frequency changes with its momentum. This relationship is defined by the momentum compaction factor (α_c) and the slippage factor (η):

$$\frac{\Delta C}{C} = \alpha_c \frac{\Delta p}{p_0} \tag{3.18}$$

where

$$\alpha_c = \frac{1}{C} \oint \frac{D(s)}{\rho} ds \tag{3.19}$$

The fractional change in velocity is:

$$\frac{\Delta v}{v_0} = \frac{1}{\gamma^2} \frac{\Delta p}{p_0} \tag{3.20}$$

The change in revolution period ΔT (or frequency $\Delta\omega$) is then given by:

$$\frac{\Delta T}{T_0} = -\frac{\Delta\omega}{\omega_0} = \left(\alpha_c - \frac{1}{\gamma^2}\right)\frac{\Delta p}{p_0} = \eta\frac{\Delta p}{p_0} \tag{3.21}$$

The energy at which $\eta = 0$ is the transition energy, $\gamma_T = 1/\sqrt{\alpha_c}$. These relationships lead to two coupled first-order differential equations:

$$\frac{d(\Delta E)}{dt} = \frac{\omega_0 e V_{\mathrm{RF}}}{2\pi}(\sin\phi - \sin\phi_s) \tag{3.22}$$

$$\frac{d\phi}{dt} = -\frac{h\omega_0\eta}{\beta^2 E_0}\Delta E \tag{3.23}$$

Here, h is the harmonic number. For small phase deviations ($\Delta\phi = \phi - \phi_s \approx 0$), we can linearize the equations: $\sin\phi - \sin\phi_s \approx \Delta\phi\cos\phi_s$. Taking the time derivative of the second equation and substituting the first gives the equation for a simple harmonic oscillator:

$$\frac{d^2(\phi - \phi_s)}{dt^2} + \frac{h\omega_0^2 e V_{\mathrm{RF}}|\eta\cos\phi_s|}{2\pi\beta^2 E_0}(\phi - \phi_s) = 0 \tag{3.24}$$

This is expressed as $d^2(\Delta\phi)/dt^2 + \omega_s^2\Delta\phi = 0$, where the angular synchrotron frequency ω_s is:

$$\omega_s = \omega_0\sqrt{\frac{h e V_{\mathrm{RF}}|\eta\cos\phi_s|}{2\pi\beta^2 E_0}} \tag{3.25}$$

The number of synchrotron oscillations per revolution is the synchrotron tune ($\nu_s = \omega_s/\omega_0$). Typically, $\nu_s \ll 1$, indicating that longitudinal motion is much slower than transverse betatron motion.

3.2.4 RF Buckets and Bunches

The non-linear restoring force from the sinusoidal RF field creates a potential well. Particles with insufficient energy to escape this well remain trapped. This stable region, when visualized in longitudinal phase space (ΔE vs. ϕ), is known as the RF bucket. The boundary of the bucket is called the separatrix. Particles inside the bucket are confined and execute stable synchrotron oscillations. Particles outside the bucket are untrapped and will drift away in phase, eventually being lost from the beam.

The collection of particles trapped within an RF bucket forms a bunch. The distribution of these particles in phase space determines macroscopic properties such as the bunch length and energy spread.

3.3 Space Charge

Since particle beams consist of numerous charged particles, the electromagnetic fields generated by the particles themselves can significantly influence beam dynamics. This collective interaction arises from the direct electromagnetic forces between particles within the bunch and is known as the space charge effect. It is a dominant intensity-dependent effect, particularly pronounced in the low-to-medium energy range where particles are not yet highly relativistic.

3.3.1 Beam Self-Field

A charged particle bunch generates both electric and magnetic fields.

Electric Field

The beam's net charge generates a repulsive electric field radiating outward from the beam center. This field exerts a defocusing force on individual particles, pushing them away from each other and from the central axis.

Magnetic Field

The longitudinal motion of the charged particles constitutes a beam current, which generates an azimuthal magnetic field. According to the Lorentz force law, this magnetic field exerts an inward-directed focusing force on the particles. For a particle moving at a velocity $v = \beta c$, this magnetic focusing force partially opposes the electric defocusing force. The net force remains defocusing but is reduced by the relativistic factor $1/\gamma^2$:

$$F_{\text{total}} \propto \left(1 - \beta^2\right) F_{\text{ele}} = \frac{1}{\gamma^2} F_{\text{ele}}. \tag{3.26}$$

This cancellation mechanism explains why space charge effects become progressively weaker as the beam energy increases.

3.3.2 Incoherent Tune Shift and Tune Spread

The net defocusing force from space charge acts as a distributed lens that weakens the overall focusing provided by the accelerator lattice. This reduction in focusing strength decreases the betatron oscillation frequency of individual particles. This phenomenon is known as the incoherent space charge tune shift ($\Delta\nu_{\text{inc}}$). It is termed "incoherent" because it affects the oscillation of individual particles relative to the beam's center, in contrast to the coherent motion of the center itself.

Quantitatively, the maximum tune shift for a Gaussian beam is described by the Laslett formula:

$$\Delta\nu_{\text{inc}} = -\frac{N_B r_p}{4\pi\epsilon_{\text{norm,rms}}\beta_{\text{ele}}\gamma_{\text{ele}}^2 B_f}, \tag{3.27}$$

where N_B is the number of particles per bunch, r_p is the classical proton radius, $\epsilon_{\text{norm,rms}}$ is the normalized rms transverse emittance, β_{rel} and γ_{rel} are the relativistic factors, and B_f is the bunching factor. This equation highlights that the tune shift is most severe at low energies (scaling with $1/\beta_{\text{rel}}\gamma_{\text{rel}}^2$) and for short, peaked bunches (small B_f).

Furthermore, in a realistic beam with a non-uniform transverse profile (e.g., a Gaussian distribution), the space charge force is non-linear; it is strongest in the high-density core and weakest at the periphery. Consequently, particles with different oscillation amplitudes experience different tune shifts, resulting in a "tune spread" rather than a uniform shift for the entire beam.

3.3.3 Image Effects and Coherent Tune Shift

As a beam passes through a conductive vacuum chamber, its electromagnetic field induces image charges and image currents on the surrounding walls. When the beam is perfectly centered, the forces from these image fields are symmetric and cancel out. However, if the beam's center-of-mass (centroid) is displaced, the image forces become asymmetric, exerting a net force on the entire beam. This force alters the oscillation frequency of the beam's centroid. The resulting shift in the centroid's tune is known as the coherent tune shift ($\Delta\nu_{\text{coh}}$).

It is crucial to distinguish this from the incoherent tune shift. While $\Delta\nu_{\text{inc}}$ affects the relative motion of individual particles (incoherent motion), $\Delta\nu_{\text{coh}}$ affects the collective, center-of-mass motion of the entire beam (coherent motion).

3.3.4 Consequences of Space Charge

The primary consequences of space charge are limitations on beam intensity and quality:

Resonance Excitation

The tune spread caused by space charge can be detrimental. If the spread is sufficiently large, the tunes of individual particles may be pushed onto nearby resonance lines in the tune diagram. This can drive rapid amplitude growth, leading to emittance degradation and particle loss.

Space Charge Limit

For every synchrotron, there exists a maximum beam intensity, known as the space charge limit. Exceeding this limit causes the tune shift to become so large that the beam footprint overlaps with major structural resonances, making stable operation impossible.

3.4 Wakefield and Impedance

A particle beam does not travel through a perfectly smooth and ideal vacuum chamber. It encounters various structures such as RF cavities, bellows, beam monitors, and other discontinuities. As the charged particle bunch passes these elements, it induces electromagnetic fields on the surrounding chamber walls. These fields, collectively called the wakefield, act back on the particles within the bunch, causing intensity-dependent effects and potential instabilities.

3.4.1 Physical Image of Wakefield

The physical origin of wakefield can be understood by analogy: a boat moving through water creates a wakefield that disturbs only the boats following it, not those ahead, as illustrated in the top panel of Fig. 3.2. Similarly, in the ultra-relativistic limit, the electromagnetic fields induced by the "head" of a charged particle bunch persist for a short time and exert forces on the "tail" of the same bunch or on subsequent bunches.

This interaction satisfies causality; the wakefield generated by a particle affects only those trailing it.

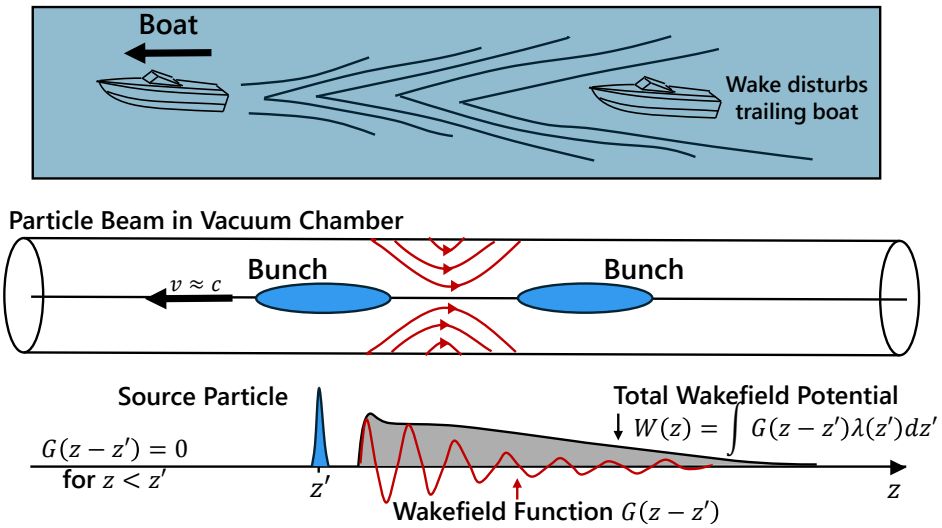

Figure 3.2: Conceptual illustration of the wakefield mechanism. (Top) Analogy using a boat's wake to demonstrate causality, where the disturbance affects only the trailing region. (Bottom) Schematic of electromagnetic wakefield induced by a particle bunch in a vacuum chamber. The graph shows the source particle, the wakefield function $G(z-z')$, and the resulting cumulative total wakefield potential $W(z)$.

This interaction is mathematically described in the time domain by the wakefieldfunction (or Green's function, $G(z)$), which quantifies the force exerted by a single source particle at a distance z behind it. Consistent with causality, $G(z)$ vanishes for $z < 0$ (i.e., ahead of the source). The total wakefield potential $W(z)$ experienced by a test particle at position z is given by the convolution of the wakefield function with the longitudinal bunch distribution $\lambda(z')$:

$$W(z) = \int_{-\infty}^{+\infty} G(z-z')\lambda(z')dz' \tag{3.28}$$

Here, due to the causal nature of $G(z-z')$, the integration effectively sums contributions only from particles z' ahead of the test particle z (i.e., where $z - z' > 0$).

3.4.2 Classification of Wakefields

Wakefields are classified based on the direction of the force they exert.

Longitudinal Wakefield

The longitudinal wakefield, described by the wakefield function $W_L(s)$, causes energy changes in the trailing particles. This leads to two primary effects:

- Parasitic Energy Loss: The entire bunch loses energy as it excites wakefield. This energy loss must be compensated for by the RF acceleration system.

- Bunch Distortion: The energy gain or loss varies along the bunch length, which can distort the bunch's longitudinal profile and modify the potential well (Potential Well Distortion).

Transverse Wakefield

When a leading particle is displaced from the central axis, it excites transverse wakefield. These fields, described by the transverse wakefield function $W_T(s)$, impart a transverse (deflecting) kick to trailing particles. This is a particularly dangerous effect, as it provides a mechanism for the head of the bunch to drive the tail to increasingly larger oscillation amplitudes, leading to coherent instabilities like the head-tail instability.

3.4.3 Impedance: A Frequency Domain Perspective

While wakefield provide an intuitive picture in the time domain, it is often more convenient to analyze collective effects in the frequency domain. The coupling impedance is defined as the Fourier transform of the wakefield. It characterizes the accelerator environment's response to the beam's electromagnetic field at a specific frequency ω:

$$Z_{T,L}(\omega) = \frac{\mathbf{i}}{c}\int_{-\infty}^{+\infty} W_{T,L}(z)\exp\left(-\mathbf{i}\omega\frac{z}{c}\right)dz \tag{3.29}$$

Longitudinal Impedance ($Z_L(\omega)$)

The real part of Z_L corresponds to resistive energy loss, while the imaginary part causes coherent shifts in the synchrotron frequency and distortion of the RF potential well.

Transverse Impedance ($Z_T(\omega)$)

This describes the transverse deflecting force experienced by the beam when oscillating at frequency ω. The imaginary part of Z_T causes coherent shifts in the betatron tune. Since the wakefield $W_T(z)$ is a real-valued function, the transverse impedance satisfies the following symmetry property:

$$-Z_T^*(-\omega) = Z_T(\omega). \tag{3.30}$$

This implies that the real part of the transverse impedance is an odd function of ω, and the imaginary part is an even function.

3.4.4 Sources of Impedance

Impedance in accelerators arises from any deviation from a perfectly smooth, perfectly conductive cylindrical pipe. Primary sources include:

Resistive Wall Impedance

The finite resistivity (ρ_c) of the vacuum chamber walls generates both longitudinal and transverse wakefields. This is a classic example of a long-range wakefield (decaying slowly as $|z|^{-1/2}$) that can cause coupled-bunch instabilities. For a cylindrical pipe of radius b

and length L, the transverse impedance Z_T and its corresponding wakefield W_T are given by:

$$Z_T(\omega) = (1 - \mathbf{i}\mathrm{sgn}(\omega))Z_0\frac{\delta_s L}{\pi b^3} \tag{3.31}$$

$$W_T(z) = -\frac{cL}{\pi b^3}\sqrt{\frac{Z_0\rho_c}{\pi}}\frac{1}{|z|^{1/2}}, \quad \text{for } z < 0 \tag{3.32}$$

where $\delta_s = \sqrt{2\rho_c/(\omega\mu_0)}$ is the skin depth and Z_0 is the vacuum impedance.

Geometric Impedance

This arises from any discontinuity in the chamber geometry, such as RF cavities (especially their Higher-Order Modes (HOMs)), Bellows (used for vacuum connections), BPMs, Flanges and transitions in pipe radius. The sum of all these contributions constitutes the total impedance of the accelerator, which ultimately determines the thresholds for various beam instabilities.

Resonator Impedance

Many geometric discontinuities, especially RF cavities, behave electromagnetically like resonators. This provides a powerful model to describe their impedance. This is not a separate source of impedance, but rather a widely used model for geometric impedances. A resonator is characterized by a resonant frequency ω_r, a shunt impedance R_s, and a quality factor Q. Its transverse impedance is given by:

$$Z_T(\omega) = \frac{c}{\omega}\frac{R_s}{1 + \mathbf{i}Q(\frac{\omega_r}{\omega} - \frac{\omega}{\omega_r})} \tag{3.33}$$

The corresponding wakefield is a damped sinusoid, which can be a strong source of coupled-bunch instabilities if the quality factor Q is high.

$$W_T(z) = \frac{cR_s\omega_r}{Q\overline{\omega}}\exp\left(\alpha\frac{z}{c}\right)\sin\left(\overline{\omega}\frac{z}{c}\right), \quad \text{for } z < 0 \tag{3.34}$$

where $\alpha = \omega_r/2Q$ and $\overline{\omega} = \sqrt{\omega_r^2 - \alpha^2}$.

Figure 3.3 illustrates the frequency dependence of the resonator impedance. The real part (resistive component) exhibits a sharp peak at the resonant frequency ω_r, which contributes to energy loss and instability growth. The imaginary part (reactive component) crosses zero at resonance and affects the coherent tune shift.

3.5 Beam Instability Mechanism

While space charge and impedance describe the forces acting on the beam, beam instabilities are the macroscopic manifestation of these forces. An instability occurs when a small, collective (coherent) oscillation of particles, driven by the beam's interaction with its own self-generated fields, grows exponentially over time. These phenomena constitute some of

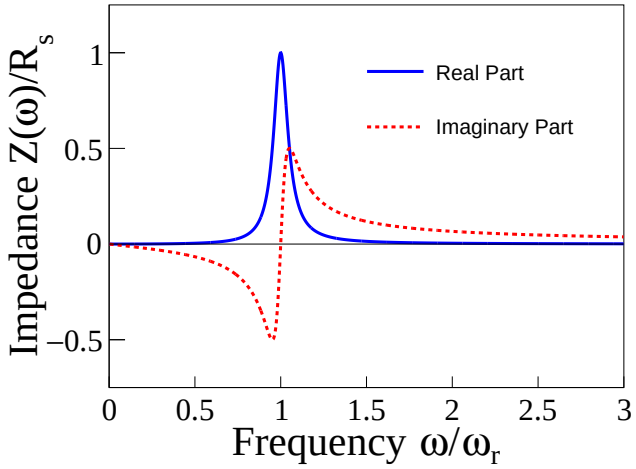

Figure 3.3: Real (solid blue line) and imaginary (dashed red line) parts of the transverse resonator impedance as a function of frequency ratio ω/ω_r

the most significant limiting factors for particle accelerator performance and maximum intensity.

The fundamental mechanism underlying all instabilities is a positive feedback loop. This process begins with an infinitesimal coherent motion in the beam, such as a slight transverse oscillation or a density modulation. This motion generates electromagnetic fields by interacting with the accelerator's impedance. If the phase of these fields is constructive, they exert a force back on the beam, adding energy to the initial oscillation and increasing its amplitude. This amplified oscillation generates even stronger fields, leading to exponential growth that can result in beam degradation or complete beam loss.

3.5.1 Instability Analysis

Theoretical frameworks, such as Sacherer's Vlasov formulation provided in Appendix C, aim to determine the coherent frequency Ω of oscillation modes to assess beam stability. These analytical methods generally reduce the physical problem to a matrix equation, where the coherent frequencies Ω appear as eigenvalues of the interaction matrix. The coherent frequency Ω obtained in this manner is generally a complex number:

$$\Omega = \mathrm{Re}(\Omega) + \mathbf{i}\mathrm{Im}(\Omega). \tag{3.35}$$

Substituting this solution into the phasor $\exp(-\mathbf{i}\Omega t)$, which represents the time evolution of the perturbation, yields:

$$\exp(-\mathbf{i}\Omega t) = \exp(-\mathbf{i}\mathrm{Re}(\Omega)t)\exp(\mathrm{Im}(\Omega)t) \tag{3.36}$$

The physical interpretation of this complex frequency is the key to stability analysis:

- Re(Ω) (Real part): Represents the coherent frequency shift of the mode (i.e., the deviation from its unperturbed frequency, $\omega_\beta + m\omega_s$).

- $\mathrm{Im}(\Omega)$ (Imaginary part): Represents the temporal growth or damping rate of the mode's amplitude.

The stability of the beam is determined by the sign of $\mathrm{Im}(\Omega)$:

1. $\mathrm{Im}(\Omega) > 0$: The term $\exp(\mathrm{Im}(\Omega)t)$ grows exponentially with time. The mode amplitude becomes infinitely large, and the beam is unstable.
2. $\mathrm{Im}(\Omega) < 0$: The amplitude decays exponentially. The instability is suppressed (e.g., by Landau damping), and the beam is stable.
3. $\mathrm{Im}(\Omega) = 0$: The amplitude remains unchanged. The beam is at the instability threshold.

Given the impedance Z_T and beam distribution, Sacherer's theory allows the construction of this matrix equation for Ω. By calculating the eigenvalues, if even one solution (one mode) satisfies $\mathrm{Im}(\Omega) > 0$, the beam will undergo a collective instability. Practically, the mode with the fastest growth rate (the largest positive $\mathrm{Im}(\Omega)$) will dominate the beam's behavior.

3.5.2 Competition Between Driving and Damping

Whether an instability occurs depends on the delicate balance between the driving terms that cause growth and the damping mechanisms that suppress it. The sign of $\mathrm{Im}(\Omega)$ is the net result of this competition.

Driving Terms

These are primarily the forces from wakefield (described by impedance) that are in phase with the oscillation's velocity, thus performing positive work on the beam and causing growth.

Damping Mechanisms

These are forces or processes that remove energy from the coherent oscillation, causing it to decay.

- Landau Damping: This is the most significant natural damping mechanism in hadron accelerators. It arises from a spread in the individual particles' oscillation frequencies (a betatron or synchrotron tune spread). Because particles oscillate at slightly different frequencies, they gradually lose phase coherence with each other (a process called decoherence). This decoherence causes the macroscopic, coherent signal to decay, even as individual particles continue to oscillate. This essential tune spread can arise naturally from space charge forces or be intentionally introduced using chromaticity.
- Radiative Damping: In electron synchrotrons, the emission of synchrotron radiation provides a powerful natural damping effect for oscillations in all three dimensions.

3.5.3 Classification of Major Instabilities

Beam instabilities are typically classified by several criteria, including:

- Direction: Longitudinal (affecting energy/timing) or Transverse (affecting position/angle).
- Scope: Single-Bunch (driven by short-range wakes) or Multi-Bunch (driven by long-range wakes).

Coupled Bunch Instability (Multi-bunch)

This type of instability is driven by long-range wakefield, such as those from the resistive walls or from HOMs in RF cavities. This wakefield persist long enough to affect many subsequent bunches. The wakefield from each bunch drives the motion of the others, causing all bunches in the ring to oscillate coherently, often with a specific phase relationship between them. Quantitatively, the growth rate (or its inverse, the growth time τ) for a specific coupled-bunch mode (m, μ) can be calculated. It is proportional to the sum of the real part of the transverse impedance sampled at the relevant mode frequencies ω_q:

$$\frac{1}{\tau_{m\mu}} = -\frac{1}{1+m}\frac{eMI_bc}{4\pi\nu_\beta E_0}\frac{\sum_q \mathrm{Re}Z_T(\omega_q)h_m(\omega_q - \chi/\tau_L)}{B_f \sum_q h_m(\omega_q - \chi/\tau_L)} \tag{3.37}$$

where M is the number of bunches, I_b is the current per bunch, $B_f = M\tau_L/T_0$ is the bunching factor, and $\chi = \omega_\xi \tau_L$ is the head-tail phase shift. The mode frequencies are defined by the accelerator parameters: $\omega_q = (qM + \mu)\omega_0 + \omega_\beta + m\omega_s$.

Head-Tail Instability (Transverse, Single Bunch)

This is a classic single-bunch instability driven by short-range transverse wakefield. The mechanism is as follows:

1. The "head" of the bunch performs a betatron oscillation.
2. As it passes through an impedance source, it leaves a transverse wakefield.
3. This wakefield then kicks the "tail" of the bunch.

A critical factor determining stability is chromaticity (ξ). Particles within the bunch are also undergoing synchrotron motion, constantly exchanging positions between the head and tail. Chromaticity induces a momentum-dependent betatron phase advance, which creates a phase difference between the oscillation of the head and the arrival of the kick at the tail. For a specific sign of chromaticity (e.g., $\xi > 0$ above transition), this phase shift causes the wakefield's kick to damp the oscillation. For the opposite sign, the kick amplifies the oscillation, causing an instability. The sign of chromaticity required for stability depends on the accelerator's parameters, such as operating above or below the transition energy. The coherent frequency shift Ω_m for a given head-tail mode m (relative to the synchrotron sideband $m\omega_s$) is driven by the interplay of the chromaticity (via the chromatic frequency ω_ξ) and the transverse impedance Z_T:

$$\Omega_m - m\omega_s = -\frac{1}{1+m}\frac{eI_bc}{4\pi\omega_\beta E_0}\int_0^\infty d\omega \mathrm{Re}Z_T(\omega)(h_m(\omega - \omega_\xi) - h_m(\omega + \omega_\xi)) \tag{3.38}$$

Here, $\omega_\xi = \xi\omega_0/\eta$ represents the effective frequency shift induced by chromaticity. An imaginary part of Ω_m arising from this integral indicates instability.

The index m represents the head-tail mode number, describing the standing-wave pattern of the oscillation along the bunch.

- $m = 0$: Rigid-bunch motion (barycenter oscillation).
- $m = 1$: Head and tail oscillate in opposite phases (tilt motion).
- $m \geq 2$: Higher-order modes involving more nodes within the bunch.

Typically, the $m = 0$ mode is dominant, but higher-order modes can be excited depending on the chromaticity and the frequency spectrum of the impedance.

Figure 3.4 visualizes the temporal structure of these modes. Figure 3.4a shows the case with zero chromaticity ($\chi = 0$), where the modes manifest as pure standing waves with fixed nodes. In contrast, Figs. 3.4b and 3.4c illustrate cases with non-zero chromaticity ($\chi \neq 0$). Here, the chromaticity induces a phase shift along the bunch (where the total phase shift is $\chi = \omega_\xi \tau_L$), transforming the oscillations into traveling waves. This phase shift allows the wakefield generated by the head to resonantly drive the tail, leading to instability.

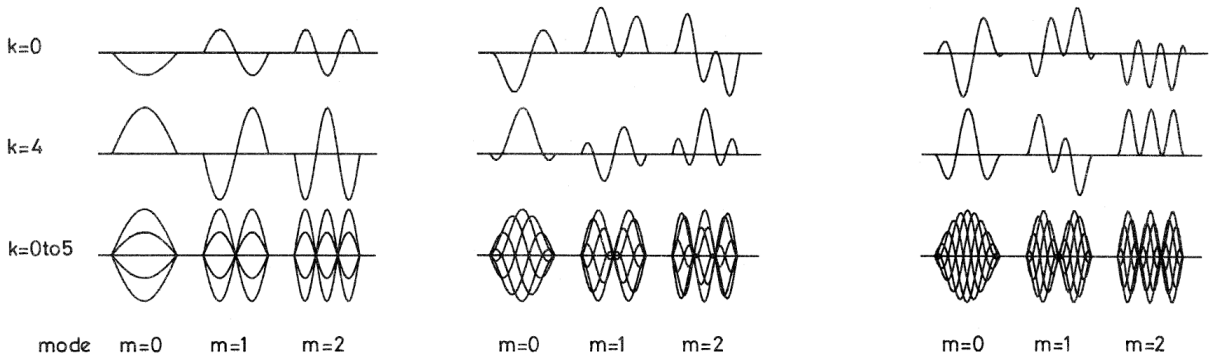

(a) $\chi = 0$ **(b)** $\chi = 5$ **(c)** $\chi = 9$

Figure 3.4: Signal patterns of head-tail modes ($m = 0, 1, 2$) for different chromatic phases χ. The rows display signals at specific turns ($k = 0, 4$) and the superposition of multiple turns ($k = 0$ to 5). (a) represents zero chromaticity ($\chi = 0$), showing standing waves. (b) and (c) represent non-zero chromaticity ($\chi = 5, 9$ rad), showing the traveling wave characteristics driven by the head-tail phase shift.[54]

At very high currents, this instability can evolve into the much faster TMCI, where the tunes of different intra-bunch motion modes shift and merge, causing rapid beam loss. This instability occurs when the coherent tune shift of two adjacent modes (e.g., $m = 0$ and $m = -1$) forces their frequencies to merge. While this is a hard intensity limit in electron machines, in proton synchrotrons, the strong space charge tune spread can alter this coupling mechanism, a phenomenon that will be explored in detail in Chapter 9.

Microwave Instability (Longitudinal, Single Bunch)

This is a longitudinal instability driven by high-frequency impedance. Above a specific intensity threshold, it manifests as an uncontrollable increase in the bunch's energy spread and length. This is caused by microscopic density fluctuations (shot noise) within the bunch being amplified by the longitudinal wakefield.

3.6 Feedback System

Natural damping mechanisms in accelerators are often insufficient to suppress strong, impedance-driven coherent instabilities, particularly at high beam intensities. To overcome this limitation, active (or artificial) damping systems, known as beam feedback systems, are essential technology in modern accelerators. Their purpose is to provide a powerful, artificial damping mechanism by detecting undesirable coherent oscillations and applying corrective forces to cancel them. The principle is similar to a noise-canceling system. The feedback loop detects the undesirable coherent "noise" from a beam oscillation and generates an "anti-noise" signal, a precisely timed kick, to counteract it.

3.6.1 Feedback System Components

A feedback system consists of four main components arranged in a loop that spans a section of the accelerator:

Pickup (Sensor)

A device that detects the coherent motion of the beam. Typically, a BPM is used, which converts the beam's position or phase oscillations into an electronic signal.

Signal Processing Unit

The signal from the pickup is filtered, delayed, and amplified according to specific gain and phase settings. This processing is commonly implemented using high-speed Digital Signal Processors (DSPs) or FPGAs.

Power Amplifier

The small, processed correction signal is amplified by a high-power amplifier to a level sufficient to exert a meaningful force on the high-energy beam.

Kicker (Actuator)

This device applies the corrective force to the beam. A transverse kicker uses electromagnetic fields to apply a deflecting "kick," while a longitudinal kicker is a cavity-like device that modulates the beam's energy.

3.6.2 Operating Principle

For the feedback system to provide damping, the timing and phase of the corrective kick are critical. The process is as follows: A bunch's oscillation is measured by the pickup on a specific turn. The signal is then processed and timed so that the corrective kick is applied precisely when that exact same bunch reaches the kicker's location (which may be on the same or a subsequent turn). Crucially, the kick must have the correct phase relative to the oscillation to remove energy from it. For a transverse oscillation, the ideal damping kick is proportional to the oscillation's velocity, not its position. This means the kick should be applied with a 90-degree phase shift relative to the position error measured at the pickup.

3.6.3 Types of Feedback Systems

Feedback systems are designed and specialized to suppress specific types of instabilities.

Bunch-by-Bunch Feedback

These systems are designed to suppress coupled-bunch instabilities. They possess the necessary bandwidth and processing power to measure and apply a unique corrective kick to each individual bunch in the accelerator.

Intra-Bunch Feedback

These are technically more advanced systems designed to damp instabilities occurring within a single bunch, such as the head-tail instability. They require extremely high-bandwidth components to resolve the internal motion of the bunch, such as the difference in motion between the head and tail.

Classification by Direction

Feedback systems are also classified by the direction of the correction applied, targeting either transverse (betatron) oscillations or longitudinal (synchrotron) oscillations.

Chapter 4

Transverse Decoherence without Intensity Effects

To establish a baseline for understanding the complex intra-bunch dynamics discussed in later chapters, this chapter reviews the linear decoherence model [55, 56]. In this simplified framework, we neglect collective effects such as space charge and wakefield, assuming that the tune shift arises solely from chromaticity. We examine the evolution of a beam injected with a uniform initial transverse offset, exciting coherent betatron oscillations. The subsequent disappearance (decoherence) and reappearance (recoherence) of the oscillation signal reflect the betatron phase spread induced by chromaticity coupled with synchrotron motion.

4.1 Theoretical Derivation

We consider the transverse motion of a particle with longitudinal amplitude z_0 and initial synchrotron phase θ_0. The longitudinal dynamics are described by:

$$z(n) = z_0 \cos\theta, \tag{4.1}$$

$$\delta(n) = \frac{2\pi\nu_s}{\eta C} z_0 \sin\theta = \mathrm{sgn}(\eta)\frac{\sigma_\delta}{\sigma_z} z_0 \sin\theta, \tag{4.2}$$

where $\theta = 2\pi\nu_s n + \theta_0$ is the synchrotron phase at turn n, ν_s is the synchrotron tune, C is the ring circumference, η is the slippage factor, and the ratio $\sigma_\delta/\sigma_z = 2\pi\nu_s/(|\eta|C)$ defines the aspect ratio of the matched bucket.

The betatron phase advance $\phi(n)$ accumulates turn-by-turn according to the momentary tune $\nu(n) = \nu_\beta + \xi\delta(n)$. Integrating over n turns yields:

$$\begin{aligned}
\phi(n) &= 2\pi \int_0^n (\nu_\beta + \xi\delta(n'))dn' \\
&= 2\pi\nu_\beta n - \mathrm{sgn}(\eta)\frac{\sigma_\delta}{\sigma_z}\xi z_0(\cos\theta - \cos(\theta - 2\pi\nu_s n)) \\
&= 2\pi\nu_\beta n - \chi_\sigma \frac{z}{\sigma_z}(1 - \cos(2\pi\nu_s n)) + \mathrm{sgn}(\eta)\chi_\sigma \frac{\delta}{\sigma_\delta}\sin(2\pi\nu_s n),
\end{aligned} \tag{4.3}$$

where we have defined the rms chromatic phase χ_σ as:

$$\chi_\sigma = \frac{2\pi\xi\sigma_z}{\eta C} = \frac{\xi}{\nu_s\eta}\frac{2\pi\nu_s\sigma_z}{C} \approx \frac{|\xi|}{\nu_s}\sigma_\delta. \tag{4.4}$$

To obtain the behavior of the macroscopic beam, we must integrate over the particle distribution. We define the local transverse centroid $\bar{x}(n, z)$ as the average position of

particles at a specific longitudinal slice z at turn n. Assuming the initial condition $\bar{x}(0,z) = X_0$ (rigid displacement) and a Gaussian longitudinal phase space distribution:

$$\rho_\delta(\delta) = \frac{1}{\sqrt{2\pi}\sigma_\delta} \exp\left(-\frac{\delta^2}{2\sigma_\delta^2}\right), \tag{4.5}$$

the local centroid $\bar{x}(n,z)$ can be calculated by convolving the phase factor $\exp(-i\phi(n))$ with the distribution. The integration yields an analytical expression [57, 58]:

$$\bar{x}(n,z) = X_0 \exp\left[-\frac{1}{2}\chi_\sigma^2 \sin^2(2\pi\nu_s n)\right] \exp\left[-\mathbf{i}\left(2\pi\nu_\beta n - 2\chi_\sigma \sin^2(\pi\nu_s n)\frac{z}{\sigma_z}\right)\right]. \tag{4.6}$$

The real part $\mathrm{Re}[\bar{x}(n,z)]$ corresponds to the observable centroid position.

4.2 Analysis of Intra-Bunch Motion

Equation (4.6) reveals the key characteristics of the intra-bunch motion driven by chromaticity.

4.2.1 Recoherence and Signal Sharpness

The amplitude envelope of the local centroid is given by the term:

$$A_{\mathrm{env}}(n) = X_0 \exp\left[-\frac{1}{2}\chi_\sigma^2 \sin^2(2\pi\nu_s n)\right]. \tag{4.7}$$

This indicates that the oscillation amplitude damps (decoheres) as the phases spread out but eventually recovers (recoheres) when $2\pi\nu_s n = m\pi$ (i.e., every half-synchrotron period $n = mN_s/2$). Expanding the envelope around a recoherence point $n = mN_s/2$, we find:

$$A_{\mathrm{env}}(n) \approx X_0 \exp\left[-2(\pi\chi_\sigma\nu_s)^2(n - mN_s/2)^2\right]. \tag{4.8}$$

This approximation shows that the width of the recoherence signal is inversely proportional to the chromatic phase χ_σ. Consequently, a larger chromaticity results in faster decoherence and sharper, more distinct recoherence peaks.

4.2.2 Intra-Bunch Frequency

The instantaneous frequency of the oscillation within the bunch, or the intra-bunch frequency $f_{\mathrm{int}}(n)$, can be defined as the time derivative of the phase term in Eq. (4.6):

$$\begin{aligned} f_{\mathrm{int}}(n) &= \left|\frac{1}{2\pi}\frac{d}{dt}\left[2\pi\nu_\beta n - 2\chi_\sigma \sin^2(\pi\nu_s n)\frac{z}{\sigma_z}\right]\right| \\ &= \left|2f_0\frac{\xi}{\eta}\sin^2(\pi\nu_s n)\right|. \end{aligned} \tag{4.9}$$

Notably, in this linear model, $f_{\mathrm{int}}(n)$ is independent of the longitudinal position z. This implies that the entire bunch oscillates with a coherent frequency modulation pattern.

The maximum intra-bunch frequency occurs at $n = N_s/2$ (half-synchrotron period) and is given by:

$$f_{\max} = f_{\text{int}}\left(\frac{N_s}{2}\right) = \left|2f_0\frac{\xi_x}{\eta}\right|. \tag{4.10}$$

Equation (4.10) provides a crucial diagnostic relation: $f_{\max}$ is directly proportional to the chromaticity ξ. This linear dependence serves as a fundamental benchmark for validating simulation and experimental results in later chapters.

4.2.3 Global Beam Centroid

Finally, the transverse centroid of the entire bunch $X(n)$ is obtained by integrating $\bar{x}(n,z)$ over the longitudinal profile $\rho_z(z)$:

$$X(n) = \int_{-\infty}^{\infty} \bar{x}(n,z)\rho_z(z)dz = X_0 \exp\left(-2\chi_\sigma^2 \sin^2(\pi\nu_s n)\right) \exp\left(-\mathbf{i}2\pi\nu_\beta n\right). \tag{4.11}$$

Thus, the amplitude of this betatron oscillation follows

$$A_{\text{env}}(n) = X_0 \exp(-2\chi_\sigma^2 \sin^2(\pi\nu_s n)). \tag{4.12}$$

Comparing this to the local centroid result, we observe two differences:

1. The damping exponent has a factor of 2 instead of 1/2, indicating faster decoherence for the global sum signal.
2. The recoherence period for the global signal is the full synchrotron period N_s (when $\sin(\pi\nu_s n) = 0$), whereas the local slices rephase every $N_s/2$.

This distinction highlights the importance of resolving intra-bunch motion: simple BPMs measuring the global centroid $X(n)$ may miss the intricate internal dynamics occurring at $N_s/2$, which are only visible when resolving $\bar{x}(n,z)$.

Chapter 5

Definition of Head-tail Modes

The space charge intrinsic eigenmodes, also known as head-tail modes, originally introduced by Blaskiewicz [59], provide a fundamental framework for interpreting the simulation results of intra-bunch motion presented in this thesis. Although head-tail modes are typically assumed to be excited by wakefield, understanding their behavior under strong space charge forces is crucial for high-intensity proton beams.

In this chapter, we delineate the intra-bunch transverse motions with respect to these intrinsic modes. To systematically disentangle the complex dynamics, we employ three progressive analytical models defined as follows:

1. Air-Bag Square-well (ABS) Model: This model assumes that all particles are concentrated at the longitudinal edges of the bunch (an "Air-Bag" distribution) and move within a square-well potential. While the infinite potential walls are an idealization, this model allows for a rigorous analytical solution of the Vlasov equation even under strong space charge forces, providing the baseline eigenvalues and eigenfunctions.
2. Air-Bag Harmonic (ABH) Model: This model retains the air-bag distribution but replaces the square-well potential with a realistic harmonic potential. By introducing sinusoidal synchrotron motion, this model bridges the gap between the idealized ABS model and the actual beam dynamics in a synchrotron.
3. Gaussian Bunch in Harmonic Potential: This model represents the most realistic scenario, where particles follow a Gaussian longitudinal distribution within a harmonic potential. Finally, the airbag distribution will be replaced by a Gaussian distribution, and approximate solutions will be derived under the weak space charge limit.

The derivation in detail is beneficial to understand the space charge intrinsic modes are dynamically excited by the synchrotron motions in the bunch, and qualitatively understand the measurements. The derived formula will be used as a tool for conducting benchmark tests of our simulation code in the followig chapters.

5.1 Air-Bag Square-well potential model

5.1.1 Head-tail Modes with Space Charge Forces

The horizontal motion of a beam particle in the beam obeys the equation of motion as [60]

$$\frac{d^2}{ds^2}x + \frac{4\pi^2}{C^2}(\nu_\beta + \delta\xi)^2 x = \frac{F_{\text{beam}}(x, \bar{x})}{\gamma m_p c^2 \beta^2}, \tag{5.1}$$

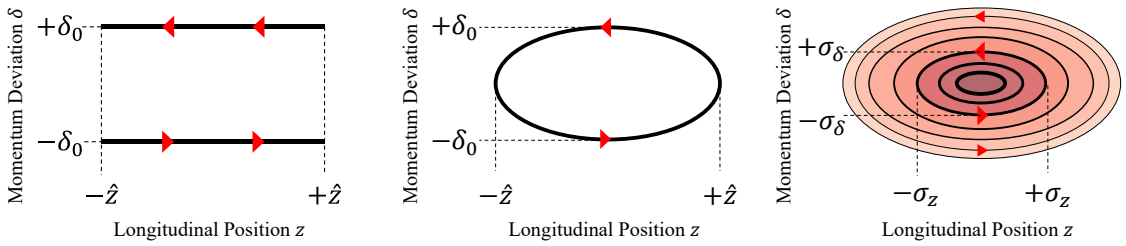

(a) ABS Model **(b)** ABH Model **(c)** Gaussian Bunch

Figure 5.1: Schematic representations of the longitudinal phase space distributions for the three models discussed in this chapter. (a) ABS Model: Particles are concentrated at the bunch edges ($\pm\hat{z}$) and move freely within a square-well potential. (b) ABH Model: Particles are distributed on a ring trajectory (Air-Bag) under a harmonic potential, executing synchrotron oscillation. (c) Gaussian Bunch: Particles are distributed according to a Gaussian profile within a harmonic potential.

where F_{beam} represents the space charge force and wakefield. When the effects of the wakefield can be neglected, Eq. (5.1) simplifies to

$$\frac{d^2}{dn^2}x + 4\pi^2(\nu_\beta + \delta\xi)^2 x = -8\pi^2\nu_\beta(\Delta\nu_{\text{inc}}(x-\bar{x}) + \Delta\nu_{\text{coh}}\bar{x}), \tag{5.2}$$

after transforming the variable s to the turn number n by using the relation $s = Cn$.

This simplified equation of motion, as shown in Eq. (5.2), is realized with the validity of the linear approximation, noting that the transverse beam size must be significantly smaller than the chamber size. Here, we should also note that even an indirect space charge effect can be addressed through the coherent space charge tune shift in Eq. (5.2).

In the ABS model, longitudinal dynamics follow

$$\frac{dz}{dn} = -\eta C\delta, \tag{5.3}$$

$$\delta = \pm\delta_0 = \pm\frac{4\hat{z}\nu_s}{|\eta|C}. \tag{5.4}$$

Let us define the horizontal positions of particles with momentum deviation δ_0 and those with $-\delta_0$ as x_u and x_d, respectively. When $\eta < 0$, we obtain the total derivative with respect to n for x_u and x_d as follows

$$\frac{d}{dn}x_{u,d} = \frac{\partial}{\partial n}x_{u,d} \pm 4\hat{z}\nu_s\frac{\partial}{\partial z}x_{u,d}, \tag{5.5}$$

where the plus and minus signs in front of the second term correspond to the equations for x_u and x_d, respectively.

On the other hand, the equations of motion for particles Eq. (5.2) with positive momentum $\delta = \delta_0$ and negative momentum $\delta = -\delta_0$ are described as follows

$$\frac{d}{dn}x_{u,d} = -\mathbf{i}2\pi\nu_\beta x_{u,d} \mp \mathbf{i}2\pi\delta_0\xi x_{u,d} - \mathbf{i}2\pi\Delta\nu_{\text{inc}}(x_{u,d}-\bar{x}) - \mathbf{i}2\pi\Delta\nu_{\text{coh}}\bar{x}, \tag{5.6}$$

after neglecting the second-order terms for the coherent and incoherent tune shifts. Here, $\bar{x} = (x_u + x_d)/2$ denotes the transverse centroid of the beam. The minus and plus signs in front of the second term in Eq. (5.6) correspond to the equations for x_u and x_d, respectively.

By combining Eqs. (5.5) and (5.6), we obtain

$$4\hat{z}\nu_s \frac{\partial}{\partial z} y_{u,d} = \mp \frac{\partial}{\partial n} y_{u,d} \mp \mathbf{i}2\pi\Delta\nu_{\mathrm{inc}}(y_{u,d} - \bar{y}) \mp \mathbf{i}2\pi\Delta\nu_{\mathrm{coh}}\bar{y}, \tag{5.7}$$

for y_u and y_d after introducing

$$x_{u,d}(n,z) = \exp\left(\mathbf{i}\chi_{\mathrm{ABS}}\frac{z}{\hat{z}} - \mathbf{i}2\pi\nu_\beta n\right) y_{u,d}(n,z). \tag{5.8}$$

Here, the minus and plus signs on the right-hand side correspond to the equations for y_u and y_d, respectively, $\bar{y} = (y_u + y_d)/2$, and the chromatic phase χ_{ABS} in the ABS model is defined by

$$\chi_{\mathrm{ABS}} = 2\pi\frac{\xi}{\eta C}\hat{z}, \tag{5.9}$$

which differs from the definition for the Gaussian beam (refer to Eq. (4.4)).

To solve Eq. (5.7), let us assume that it can be separable for the variables z and n by introducing

$$\frac{\partial}{\partial n} y_{u,d} = -\mathbf{i}2\pi\Delta\nu_x y_{u,d}, \tag{5.10}$$

and solved as

$$y_{u,d}(n,z) = \exp\left(-\mathbf{i}2\pi\Delta\nu_x n\right) y_{u,d}(z). \tag{5.11}$$

Here, we assume that the eigenvalue $\Delta\nu_x$ is identical regardless of the particle's momentum deviation. In this case, the coherent tune shift is generated by the space charge force as $\nu_\beta \to \nu_\beta + \Delta\nu_x$, referring to Eq. (5.8).

Finally, Eq. (5.11) for y_u and y_d is respectively rewritten as

$$\nu_s \frac{d}{d\theta'} y_u(\theta') = -\mathbf{i}\left(\Delta\nu_x - \frac{\Delta\nu_{\mathrm{inc}}}{2} - \frac{\Delta\nu_{\mathrm{coh}}}{2}\right) y_u(\theta') - \mathbf{i}\left(\frac{\Delta\nu_{\mathrm{inc}}}{2} - \frac{\Delta\nu_{\mathrm{coh}}}{2}\right) y_d(\theta'), \tag{5.12}$$

$$\nu_s \frac{d}{d\theta'} y_d(\theta') = +\mathbf{i}\left(\Delta\nu_x - \frac{\Delta\nu_{\mathrm{inc}}}{2} - \frac{\Delta\nu_{\mathrm{coh}}}{2}\right) y_d(\theta') + \mathbf{i}\left(\frac{\Delta\nu_{\mathrm{inc}}}{2} - \frac{\Delta\nu_{\mathrm{coh}}}{2}\right) y_u(\theta'), \tag{5.13}$$

where $\theta' = -\pi/2 \times (z/\hat{z} - 1)$ with $(0 < \theta' < \pi)$.

(i) when $\Delta\nu_x \neq \Delta\nu_{\mathrm{coh}}$, which deals with the higher space charge intrinsic modes, y_u and y_d are solved as

$$\begin{aligned} y_u(\theta') =& A_\alpha \cos\left(\frac{\sqrt{(\Delta\nu_x - \Delta\nu_{\mathrm{inc}})(\Delta\nu_x - \Delta\nu_{\mathrm{coh}})}}{\nu_s}\theta'\right) \\ &+ \mathbf{i}A_\beta \sin\left(\frac{\sqrt{(\Delta\nu_x - \Delta\nu_{\mathrm{inc}})(\Delta\nu_x - \Delta\nu_{\mathrm{coh}})}}{\nu_s}\theta'\right), \end{aligned} \tag{5.14}$$

$$
\begin{aligned}
y_d(\theta') = &\left(A_\alpha \frac{2\Delta\nu_x - \Delta\nu_{\mathrm{inc}} - \Delta\nu_{\mathrm{coh}}}{\Delta\nu_{\mathrm{coh}} - \Delta\nu_{\mathrm{inc}}} + A_\beta \frac{2\sqrt{(\Delta\nu_x - \Delta\nu_{\mathrm{inc}})(\Delta\nu_x - \Delta\nu_{\mathrm{coh}})}}{\Delta\nu_{\mathrm{coh}} - \Delta\nu_{\mathrm{inc}}} \right) \\
&\times \cos\left(\frac{\sqrt{(\Delta\nu_x - \Delta\nu_{\mathrm{inc}})(\Delta\nu_x - \Delta\nu_{\mathrm{coh}})}}{\nu_s} \theta' \right) \\
+\mathbf{i} &\left(A_\beta \frac{2\Delta\nu_x - \Delta\nu_{\mathrm{inc}} - \Delta\nu_{\mathrm{coh}}}{\Delta\nu_{\mathrm{coh}} - \Delta\nu_{\mathrm{inc}}} + A_\alpha \frac{2\sqrt{(\Delta\nu_x - \Delta\nu_{\mathrm{inc}})(\Delta\nu_x - \Delta\nu_{\mathrm{coh}})}}{\Delta\nu_{\mathrm{coh}} - \Delta\nu_{\mathrm{inc}}} \right) \\
&\times \sin\left(\frac{\sqrt{(\Delta\nu_x - \Delta\nu_{\mathrm{inc}})(\Delta\nu_x - \Delta\nu_{\mathrm{coh}})}}{\nu_s} \theta' \right),
\end{aligned}
\tag{5.15}
$$

with arbitrary coefficients A_α and A_β. During synchrotron motion in the square-well potential, the transverse positions do not change abruptly with an instantaneous change in momentum. Hence, the boundary conditions are imposed as

$$
\begin{cases}
y_u\left(\theta' = 0\right) = y_d\left(\theta' = 0\right), \\
y_u\left(\theta' = \pi\right) = y_d\left(\theta' = \pi\right),
\end{cases}
\tag{5.16}
$$

which provides the eigenvalue $\Delta\nu_x$ as

$$
\Delta\nu_{\pm,k} = \frac{\Delta\nu_{\mathrm{inc}} + \Delta\nu_{\mathrm{coh}}}{2} \pm \sqrt{\frac{(\Delta\nu_{\mathrm{inc}} - \Delta\nu_{\mathrm{coh}})^2}{4} + k^2\nu_s^2},
\tag{5.17}
$$

with the condition:

$$
A_\alpha = -\frac{k\nu_s}{\Delta\nu_{\pm,k} - \Delta\nu_{\mathrm{coh}}} A_\beta \equiv A_{\pm,k},
\tag{5.18}
$$

where Eq. (5.17) satisfies $\sqrt{(\Delta\nu_x - \Delta\nu_{\mathrm{inc}})(\Delta\nu_x - \Delta\nu_{\mathrm{coh}})} = k\nu_s$. Notice that the amplitude $A_{\pm,k}$ is independently defined for the respective branches $\pm$ in $\Delta\nu_{\pm,k}$ for the specified $k \in \mathbb{N} = \{1, 2, 3, \cdots\}$, and Eq. (5.17) reproduces the result found in Ref. [59] as $\Delta\nu_{\mathrm{coh}}$ approaches zero neglecting the indirect space charge effect. The case of $k = 0$ must be omitted up to now because $\Delta\nu_x = \Delta\nu_{\mathrm{coh}}$ or $\Delta\nu_x = \Delta\nu_{\mathrm{inc}}$ contradicts the present scope of the assumption.

The concrete calculations demonstrate that the indirect space charge effect is partially incorporated into $\Delta\nu_x$ by neglecting higher-order terms for both the coherent and incoherent tune shifts in the equations of motion: Eq. (5.6). Moreover, we find that the applicability of the space charge parameter q_{sc}, as mentioned in the introduction, is restricted to the region where the linear approximation for the space charge effect is valid: the beam size is much smaller than the chamber radius, and the indirect space charge effect is negligible.

In summary, $y_u(\theta')$ and $y_d(\theta')$ are provided by the set of $y_{u,\pm,k}(\theta')$ and $y_{d,\pm,k}(\theta')$, which are defined as

$$
y_{u,\pm,k}(\theta') = A_{\pm,k}\left(\cos(k\theta') - \mathbf{i}\frac{\Delta\nu_{\pm,k} - \Delta\nu_{\mathrm{coh}}}{k\nu_s} \sin(k\theta') \right),
\tag{5.19}
$$

$$
y_{d,\pm,k}(\theta') = A_{\pm,k}\left(\cos(k\theta') + \mathbf{i}\frac{\Delta\nu_{\pm,k} - \Delta\nu_{\mathrm{coh}}}{k\nu_s} \sin(k\theta') \right),
\tag{5.20}
$$

after Eqs. (5.17) and (5.18) are substituted into Eqs. (5.14) and (5.15).

(ii) when $\Delta\nu_x = \Delta\nu_{\mathrm{coh}}$, the solution for Eqs. (5.12) and (5.13) is given by

$$y_{u,d}(z) = A_0, \tag{5.21}$$

where A_0 is constant. Referring to Eq. (5.17), this case expresses the $m = 0$ mode. Accordingly, let us include $(y_{u,0}, y_{d,0}, \Delta\nu_0)$ into the set of solutions for $(y_u, y_d, \Delta\nu_x)$. Note that $\Delta\nu_x$ has only one branch, unlike in Eq. (5.17).

Finally, referring to Eqs. (5.8) and (5.11), the superposition of these solutions provides the horizontal potions of particles with $+\delta_0$ and $-\delta_0$ as

$$\begin{aligned} x_u(n,z) =& \exp\left(\mathbf{i}\chi_{\mathrm{ABS}}\frac{z}{\hat{z}} - \mathbf{i}2\pi\nu_\beta n\right) A_0 \exp\left(-\mathbf{i}2\pi\Delta\nu_0 n\right) \\ &+ \exp\left(\mathbf{i}\chi_{\mathrm{ABS}}\frac{z}{\hat{z}} - \mathbf{i}2\pi\nu_\beta n\right) \sum_{\pm,k\in\mathbb{N}} A_{\pm,k} \exp\left(-\mathbf{i}2\pi\Delta\nu_{\pm,k} n\right) \\ &\times \left(\cos(k\theta') - \mathbf{i}\frac{\Delta\nu_{\pm,k} - \Delta\nu_{\mathrm{coh}}}{k\nu_s}\sin(k\theta')\right), \end{aligned} \tag{5.22}$$

$$\begin{aligned} x_d(n,z) =& \exp\left(\mathbf{i}\chi_{\mathrm{ABS}}\frac{z}{\hat{z}} - \mathbf{i}2\pi\nu_\beta n\right) A_0 \exp\left(-\mathbf{i}2\pi\Delta\nu_0 n\right) \\ &+ \exp\left(\mathbf{i}\chi_{\mathrm{ABS}}\frac{z}{\hat{z}} - \mathbf{i}2\pi\nu_\beta n\right) \sum_{\pm,k\in\mathbb{N}} A_{\pm,k} \exp\left(-\mathbf{i}2\pi\Delta\nu_{\pm,k} n\right) \\ &\times \left(\cos(k\theta') + \mathbf{i}\frac{\Delta\nu_{\pm,k} - \Delta\nu_{\mathrm{coh}}}{k\nu_s}\sin(k\theta')\right), \end{aligned} \tag{5.23}$$

which produces the transverse centroid of each segment in the bunch as

$$\begin{aligned} \bar{x}(n,\theta') =& \exp\left(\mathbf{i}\chi_{\mathrm{ABS}}\frac{z}{\hat{z}} - \mathbf{i}2\pi\nu_\beta n\right) A_0 \exp\left(-\mathbf{i}2\pi\Delta\nu_0 n\right) \\ &+ \exp\left(\mathbf{i}\chi_{\mathrm{ABS}}\frac{z}{\hat{z}} - \mathbf{i}2\pi\nu_\beta n\right) \sum_{k\in\mathbb{N}} A_{+,k} \exp\left(-\mathbf{i}2\pi\Delta\nu_{+,k} n\right)\cos(k\theta') \\ &+ \exp\left(\mathbf{i}\chi_{\mathrm{ABS}}\frac{z}{\hat{z}} - \mathbf{i}2\pi\nu_\beta n\right) \sum_{k\in\mathbb{N}} A_{-,k} \exp\left(-\mathbf{i}2\pi\Delta\nu_{-,k} n\right)\cos(k\theta') \\ =& X_0 \sum_{m\in\mathbb{Z}} a_{m,\mathrm{ABS}} \exp\left(\mathbf{i}\chi_{\mathrm{ABS}}\frac{z}{\hat{z}} - \mathbf{i}2\pi\nu_m n\right)\cos(m\theta'), \end{aligned} \tag{5.24}$$

where

$$\begin{aligned} \nu_m &= \begin{cases} \nu_0 = \nu_\beta + \Delta\nu_0, \\ \nu_{\pm k} = \nu_\beta + \Delta\nu_{\pm,k}, \end{cases} \\ A_m &= \begin{cases} A_0, \\ A_{\pm k} = A_{\pm,k}, \end{cases} \\ a_{m,\mathrm{ABS}} &= \frac{A_m}{X_0}, \end{aligned} \tag{5.25}$$

and $m \in \mathbb{Z}$ is an integer. Here, the expansion coefficient A_m is normalized to $a_{m,\mathrm{ABS}}$ by dividing by the initial horizontal position of the beam $\bar{x}(n = 0, z) = X_0$ (refer to Chapter 4), where all macroparticles are aligned regardless of z; and the movable region of mode m

in the final expression of Eq. (5.24) is extended to the entire integer region by combining the minus branch with the original mode k. Equations (5.22)-(5.24) also cover the special case of $\Delta\nu_{\mathrm{inc}} = \Delta\nu_{\mathrm{coh}}$ after being derived independently for this case.

Finally, substituting $\theta' = -\pi/2 \times (z/\hat{z} - 1)$ into Eq. (5.24) allows us to expand of the transverse centroid of each segment in the bunch as

$$\begin{aligned}\bar{x}(n,z) =& X_0 \sum_{m\in\mathbb{Z}} a_{m,\mathrm{ABS}} \exp\left(\mathbf{i}\chi_{\mathrm{ABS}}\frac{z}{\hat{z}} - \mathbf{i}2\pi\nu_m n\right)\cos\left(m\frac{\pi}{2}\left(\frac{z}{\hat{z}}-1\right)\right)\\ =& X_0 \sum_{m\in\mathbb{Z}} \tilde{a}_{m,\mathrm{ABS}}(z)\exp\left(-\mathbf{i}2\pi\nu_m n\right),\end{aligned} \tag{5.26}$$

with the space charge intrinsic modes, the head-tail modes m. Here, the relative amplitude $\tilde{a}_{m,\mathrm{ABS}}(z)$ in each segment is defined as

$$\tilde{a}_{m,\mathrm{ABS}}(z) = a_{m,\mathrm{ABS}}\exp\left(\mathbf{i}\chi_{\mathrm{ABS}}\frac{z}{\hat{z}}\right)\cos\left(m\frac{\pi}{2}\left(\frac{z}{\hat{z}}-1\right)\right). \tag{5.27}$$

5.1.2 Oscillation Amplitude with Weak Space Charge Force

In Eqs. (5.22)-(5.24), the amplitudes $A_{\pm,k}$, or A_m are still unknown factors. In general, determining these parameters becomes quite difficult when space charge effects are significant. However, when this effect is neglected or within the minor level, the amplitudes can be explicitly obtained by comparing Eqs. (5.22)-(5.24) with the horizontal positions derived independently, based on the linear decoherence scenario in Chapter 4, after applied to the ABS model.

Let us examine the transverse centroid $\bar{x}(n,z)$ for a group of particles with the same longitudinal position z in a given turn n. As in Chapter 4, the initial condition is set as $\bar{x}(n=0,z) = X_0$ regardless of the longitudinal position of the particles, with an initial betatron phase of $\phi(n=0,z) = 0$.

Since the synchrotron phase is followed as $\theta = 2\pi\nu_s n + \theta_0$ with initial phase θ_0, the equation of motion for a single particle is described as

$$\frac{dz}{d\theta} = \frac{dz}{dn}\frac{dn}{d\theta} = \mp\frac{2\hat{z}}{\pi}. \tag{5.28}$$

Therefore, each particle motion is followed as

$$z(n,\theta_0) = -\frac{2\hat{z}}{\pi}\cos^{-1}(\cos(\theta(n,\theta_0))) + \hat{z}, \tag{5.29}$$

$$\delta(n,\theta_0) = \delta_0\mathrm{sgn}(\sin(\theta(n,\theta_0))). \tag{5.30}$$

Given $z = z_0$ at $n = n_0$, there are two solutions $\theta_{0,u}(n_0,z_0)$ and $\theta_{0,d}(n_0,z_0)$ for the initial synchrotron phase θ_0, as

$$\theta_{0,(u,d)}(n_0,z_0) = \mp\frac{\pi}{2\hat{z}}(z_0-\hat{z}) - 2\pi\nu_s n_0. \tag{5.31}$$

Hence, the betatron phase advance $\phi_u(n_0, z_0)$ and $\phi_d(n_0, z_0)$ can be calculated for the respective $\theta_{0,(u,d)}(n_0, z_0)$ as

$$\begin{aligned}\phi_{u,d}(n_0, z_0) =& 2\pi \int_0^{n_0} dn(\nu_\beta + \xi\delta(n, \theta_0)) \\ =& 2\pi\nu_\beta n_0 - 2\pi\frac{\xi}{\eta C}(z(n_0, \theta_0) - z(0, \theta_0)) \\ =& 2\pi\nu_\beta n_0 - 2\pi\frac{\xi}{\eta C}(z_0 - \hat{z} + \frac{2\hat{z}}{\pi}\cos^{-1}(\cos(\theta_{0,(u,d)}(z_0, s_0)))) \\ =& 2\pi\nu_\beta n_0 - \chi_{\mathrm{ABS}}\left(\frac{z_0}{\hat{z}} - 1 + \frac{2}{\pi}\cos^{-1}(\cos\left(\mp\frac{\pi}{2}\left(\frac{z_0}{\hat{z}} - 1\right) - 2\pi\nu_s n_0\right))\right).\end{aligned} \tag{5.32}$$

Because of the transverse oscillation with initial condition $\bar{x}(n = 0, z) = X_0$, the transverse positions of particles with $\pm\delta_0$ and the transverse centroid of each segment in the bunch are expressed as

$$\begin{aligned}x_{u,d}(n, z) =& X_0 \exp(-\mathbf{i}\phi_{u,d}(n, z)) \\ =& X_0 \exp(-\mathbf{i}2\pi\nu_\beta n)\exp\left(\mathbf{i}\chi_{\mathrm{ABS}}\left(\frac{z}{\hat{z}} - 1\right)\right)\exp\left[\mathbf{i}\frac{2}{\pi}\chi_{\mathrm{ABS}}\cos^{-1}(\cos\left(\mp\frac{\pi}{2}\left(\frac{z}{\hat{z}} - 1\right) - 2\pi\nu_s n\right))\right],\end{aligned} \tag{5.33}$$

$$\begin{aligned}\bar{x}(n, z) =& \frac{1}{2}X_0 \exp(-\mathbf{i}2\pi\nu_\beta n)\exp\left(\mathbf{i}\chi_{\mathrm{ABS}}\left(\frac{z}{\hat{z}} - 1\right)\right) \\ &\times\left(\exp\left[\mathbf{i}\frac{2}{\pi}\chi_{\mathrm{ABS}}\cos^{-1}(\cos\left(-\frac{\pi}{2}\left(\frac{z}{\hat{z}} - 1\right) - 2\pi\nu_s n\right))\right]\right. \\ &+ \left.\exp\left[\mathbf{i}\frac{2}{\pi}\chi_{\mathrm{ABS}}\cos^{-1}(\cos\left(+\frac{\pi}{2}\left(\frac{z}{\hat{z}} - 1\right) - 2\pi\nu_s n\right))\right]\right),\end{aligned} \tag{5.34}$$

respectively.

Now, let us equate Eq. (5.24), the result of the mode expansion method, to Eq. (5.34), the result of the betatron phase tracking method, producing

$$\begin{aligned}&2\sum_{m\in\mathbb{Z}} a_{m,\mathrm{ABS}}\exp\left(\mathbf{i}\chi_{\mathrm{ABS}}\right)\exp(-\mathbf{i}m\varphi)\cos(m\theta') \\ =& \exp\left[\mathbf{i}\frac{2}{\pi}\chi_{\mathrm{ABS}}\cos^{-1}(\cos(+\theta' - \varphi))\right] + \exp\left[\mathbf{i}\frac{2}{\pi}\chi_{\mathrm{ABS}}\cos^{-1}(\cos(-\theta' - \varphi))\right],\end{aligned} \tag{5.35}$$

where $\theta' = -\pi/2 \times (z/\hat{z} - 1)$ with $(0 < \theta' < \pi)$, and $\varphi = 2\pi\nu_s n$.

After multiplying Eq. (5.35) by $\exp(\mathbf{i}m\varphi)$ and then integrating it over φ from 0 to 2π, the coefficient $a_{m,\mathrm{ABS}}$ is expressed as

$$a_{m,\mathrm{ABS}} = (-\mathbf{i})^m \frac{\chi_{\mathrm{ABS}}}{\chi_{\mathrm{ABS}}^2 - (m\frac{\pi}{2})^2}\sin\left(\chi_{\mathrm{ABS}} - m\frac{\pi}{2}\right). \tag{5.36}$$

The transverse centroid of the entire bunch $X(n)$, the average value of Eq. (5.26) over the longitudinal positions of the bunch, is calculated as

$$X(n) = \int_{-\hat{z}}^{\hat{z}} \frac{dz}{2\hat{z}}\bar{x}(n, z) = X_0 \sum_{m\in\mathbb{Z}} |a_{m,\mathrm{ABS}}|^2 \exp\left(-\mathbf{i}2\pi\nu_m n\right), \tag{5.37}$$

where the amplitude is determined by Eq. (5.36).

5.2 Air-Bag Harmonic potential model

5.2.1 Head-tail Modes with Space Charge Forces

Next, let us consider the ABH model under any strength of space charge by replacing the square-well potential with a harmonic potential to more realistically describe the motion of particles in the bunch. Longuitudinal dynamics follow

$$\frac{d\delta}{dn} = \frac{(2\pi\nu_s)^2}{\eta C} z. \tag{5.38}$$

Rigorously, $\Delta\nu_{\mathrm{inc}}$ and $\Delta\nu_{\mathrm{coh}}$ are distributed along the longitudinal direction within the bunch. However, in this model, we simplify the analysis by neglecting the z-dependence of $\Delta\nu_{\mathrm{inc}}$ and $\Delta\nu_{\mathrm{coh}}$, assuming that the space charge effects near the center of the bunch are well described by the waterbag model and the effects are nearly uniform in the entire bunch.

Consequently, the equations corresponding to Eqs. (5.5) and (5.6) are given by

$$\frac{d}{dn}x_{u,d} = \frac{\partial}{\partial n}x_{u,d} - \eta C\delta_{u,d}\frac{\partial}{\partial z}x_{u,d}, \tag{5.39}$$

$$\frac{d}{dn}x_{u,d} = -\mathbf{i}2\pi\nu_\beta x_{u,d} - \mathbf{i}2\pi\delta_{u,d}\xi x_{u,d} - \mathbf{i}2\pi\Delta\nu_{\mathrm{inc}}(x_{u,d} - \bar{x}) - \mathbf{i}2\pi\Delta\nu_{\mathrm{coh}}\bar{x}, \tag{5.40}$$

where x_u and x_d represent the horizontal positions of particles with momentum deviations $\delta_u > 0$ and $\delta_d < 0$, respectively. By combining Eqs. (5.39) and (5.40), we obtain

$$-\eta C\delta_{u,d}\frac{\partial}{\partial z}y_{u,d} = -\frac{\partial}{\partial n}y_{u,d} - \mathbf{i}2\pi\Delta\nu_{\mathrm{inc}}(y_{u,d} - \bar{y}) - \mathbf{i}2\pi\Delta\nu_{\mathrm{coh}}\bar{y}, \tag{5.41}$$

for y_u and y_d after introducing

$$x_{u,d}(n,z) = \exp\left(\mathbf{i}\chi_{\mathrm{ABH}}\frac{z}{\hat{z}} - \mathbf{i}2\pi\nu_\beta n\right) y_{u,d}(n,z), \tag{5.42}$$

replacing Eqs. (5.7) and (5.8) in the ABS model. Here, the chromatic phase χ_{ABH} is defined by

$$\chi_{\mathrm{ABH}} = 2\pi\frac{\xi}{\eta C}\hat{z}, \tag{5.43}$$

which is equivalent to Eq. (5.9), because $\hat{z}$ is the half bunch length at the ABH model.

When we discuss only the case of $\eta < 0$, the momentum deviations δ_u and δ_d are uniquely determined for z and are denoted by

$$\delta_{u,d} = \mp\frac{2\pi\nu_s}{\eta C}\sqrt{\hat{z}^2 - z^2}, \tag{5.44}$$

where the minus and plus signs correspond to δ_u and δ_d, respectively.

Here, by introducing $\theta' = \cos^{-1}(z/\hat{z})$ with $(0 \leq \theta' \leq \pi)$ and applying the formula for Eq. (5.41), we can obtain the same set of equations as Eqs. (5.12) and (5.13) in the ABS model.

Finally, the head-tail mode expansion formula for the transverse centroid of each segment in the bunch is expressed as

$$\bar{x}(n,z) = X_0 \sum_{m\in\mathbb{Z}} a_{m,\mathrm{ABH}} \exp\left(\mathbf{i}\chi_{\mathrm{ABH}}\frac{z}{\hat{z}} - \mathbf{i}2\pi\nu_m n\right)\cos\left(m\cos^{-1}\left(\frac{z}{\hat{z}}\right)\right), \tag{5.45}$$

in the ABH model, after just substituting $\theta' = \cos^{-1}(z/\hat{z})$ into Eq. (5.24). When ν_m is replaced by $\nu_\beta + m\nu_s$, the outcome reproduces the Formula (6.186) in the Chao's textbook [61], which was derived under the assumption that the space charge effects are negligible from the beginning. In this sense, Eq. (5.45) generalizes the previous formula to incorporate the space charge effects.

5.2.2 Oscillation Amplitude with Weak Space Charge Force

In a similar manner explained in Sec. 5.1.2, we need to derive $\bar{x}(n,z)$ to determine $a_{m,\mathrm{ABH}}$ in the weak space charge limit, following the linear decoherence scenario under the harmonic potential. Since the synchrotron phase is followed as $\theta = 2\pi\nu_s n + \theta_0$ with initial phase θ_0, the equations of motion given by Eqs. (5.3) and (5.38) are rewritten as

$$\frac{dz}{d\theta} = \frac{dz}{dn}\frac{dn}{d\theta} = -\frac{\eta C}{2\pi\nu_s}\delta, \tag{5.46}$$

$$\frac{d\delta}{d\theta} = \frac{d\delta}{dn}\frac{dn}{d\theta} = \frac{2\pi\nu_s}{\eta C}z, \tag{5.47}$$

Therefore, each particle motion is followed as

$$z(n,\theta_0) = \hat{z}\cos\theta(n,\theta_0), \tag{5.48}$$

$$\delta(n,\theta_0) = \frac{2\pi\nu_s}{\eta C}\hat{z}\sin\theta(n,\theta_0). \tag{5.49}$$

Given $z = z_0$ at $n = n_0$, there are two solutions $\theta_{0,u}(n_0,z_0)$ and $\theta_{0,d}(n_0,z_0)$ for the initial synchrotron phase θ_0, as

$$\theta_{0,(u,d)}(n_0,z_0) = \pm\cos^{-1}\left(\frac{z_0}{\hat{z}}\right) - 2\pi\nu_s n_0. \tag{5.50}$$

Hence, the betatron phase advance $\phi_u(n_0,z_0)$ and $\phi_d(n_0,z_0)$ can be calculated for the respective $\theta_{0,(u,d)}(n_0,z_0)$ as

$$\phi_{u,d}(n,z) = 2\pi\nu_\beta n - \chi_{\mathrm{ABH}}\left(\frac{z}{\hat{z}} - \cos(\pm\cos^{-1}\left(\frac{z}{\hat{z}}\right) - 2\pi\nu_s n)\right), \tag{5.51}$$

where the plus and minus signs on the right-hand side correspond to ϕ_u and ϕ_d, respectively.

Because of the transverse oscillation with initial condition $\bar{x}(n=0,z)=X_0$, the transverse positions of particles with $\delta_{u,d}$ and the transverse centroid of each segment in the bunch are expressed as

$$x_{u,d}(n,z)=X_0\exp(-\mathbf{i}2\pi\nu_\beta n)\exp\left(\mathbf{i}\chi_{\mathrm{ABH}}\frac{z}{\hat{z}}\right)\exp\left[-\mathbf{i}\chi_{\mathrm{ABH}}\cos(\pm\cos^{-1}\left(\frac{z}{\hat{z}}\right)-2\pi\nu_s n)\right], \tag{5.52}$$

$$\begin{aligned}\bar{x}(n,z)=&\frac{1}{2}X_0\exp(-\mathbf{i}2\pi\nu_\beta n)\exp\left(\mathbf{i}\chi_{\mathrm{ABH}}\frac{z}{\hat{z}}\right)\\&\times\left(\exp\left[-\mathbf{i}\chi_{\mathrm{ABH}}\cos(+\cos^{-1}\left(\frac{z}{\hat{z}}\right)-2\pi\nu_s n)\right]\right.\\&+\quad\left.\exp\left[-\mathbf{i}\chi_{\mathrm{ABH}}\cos(-\cos^{-1}\left(\frac{z}{\hat{z}}\right)-2\pi\nu_s n)\right]\right),\end{aligned} \tag{5.53}$$

respectively.

After equating Eq. (5.53) to Eq. (5.45), we obtain

$$\begin{aligned}&2\sum_{m\in\mathbb{Z}}a_{m,\mathrm{ABH}}\exp(-\mathbf{i}m\varphi)\cos\left(m\theta'\right)\\=&\exp\left[-\mathbf{i}\chi_{\mathrm{ABH}}\cos(+\theta'-\varphi)\right]+\exp\left[-\mathbf{i}\chi_{\mathrm{ABH}}\cos(-\theta'-\varphi)\right],\end{aligned} \tag{5.54}$$

corresponding to Eq. (5.35) in the ABS model, where $\theta'=\cos^{-1}(z/\hat{z})$ with $(0<\theta'<\pi)$, and $\varphi=2\pi\nu_s n$. In the end, the coefficient $a_{m,\mathrm{ABH}}$ is expressed as

$$a_{m,\mathrm{ABH}}=(-\mathbf{i})^m J_m(\chi_{\mathrm{ABH}}), \tag{5.55}$$

where $J_m(x)$ is the Bessel function of the first kind [62]. If we compare Eq. (5.55) of the ABH model with Eq. (5.36) of the ABS model, we observe similar responses of the dominant head-tail modes to a given chromatic phase, χ_{ABH} or χ_{ABS}.

The transverse centroid of the entire bunch $X(n)$, the charge-density-weighted average value of Eq. (5.45) with respect to the airbag distribution over the longitudinal positions of the bunch produces, is calculated as

$$\begin{aligned}X(n)=&\int_{-\hat{z}}^{\hat{z}}\frac{dz}{\pi\sqrt{\hat{z}^2-z^2}}\bar{x}(n,z)\\=&X_0\frac{1}{\pi}\sum_{m\in\mathbb{Z}}(-\mathbf{i})^m J_m(\chi_{\mathrm{ABH}})\exp(-\mathbf{i}2\pi\nu_m n)\int_{-\hat{z}}^{\hat{z}}\frac{dz}{\sqrt{\hat{z}^2-z^2}}\exp\left(\mathbf{i}\chi_{\mathrm{ABH}}\frac{z}{\hat{z}}\right)\cos\left(m\cos^{-1}\left(\frac{z}{\hat{z}}\right)\right)\\=&X_0\frac{1}{\pi}\sum_{m\in\mathbb{Z}}(-\mathbf{i})^m J_m(\chi_{\mathrm{ABH}})\exp(-\mathbf{i}2\pi\nu_m n)\pi\mathbf{i}^m J_m(\chi_{\mathrm{ABH}})\\=&X_0\sum_{m\in\mathbb{Z}}|a_{m,\mathrm{ABH}}|^2\exp(-\mathbf{i}2\pi\nu_m n),\end{aligned} \tag{5.56}$$

where the amplitude is determined by Eq. (5.55).

5.3 Oscillation Amplitude for the Gaussian Beam with Weak Space Charge Force

Now, we consider the transverse centroid of each segment $\bar{x}(n,z)$ in an entire Gaussian bunch by generalizing the ABH model. If the space charge effect is small and there is no interaction between the respective airbags, the calculation can proceed by convolving $\bar{x}(n,z,\delta)$, obtained by replacing $\hat{z}$ in Eq. (5.45) with $\sqrt{z^2+(\eta C/2\pi\nu_s)^2\delta^2}$, with the Gaussian distribution in the momentum direction characterized by the momentum deviation σ_δ, as follows:

$$\bar{x}(n,z)=\int_{-\infty}^{\infty}d\delta\frac{1}{\sqrt{2\pi}\sigma_\delta}\exp\left(-\frac{\delta^2}{2\sigma_\delta^2}\right)\bar{x}(n,z,\delta)=X_0\sum_{m\in\mathbb{Z}}\tilde{a}_{m,b}(z)\exp\left(-\mathbf{i}2\pi\nu_m n\right). \quad (5.57)$$

Since this result must be the same as Eq. (4.6) for the weak space charge limit, the relative amplitude $\tilde{a}_{m,b}(z)$ in each segment is calculated in two different ways as:

$$\begin{aligned}\tilde{a}_{m,b}(z)=&\exp\left(\mathbf{i}\chi_\sigma\frac{z}{\sigma_z}\right)(-\mathbf{i})^m\sum_{l=-\infty}^{\infty}J_{m+2l}\left[\chi_\sigma\frac{z}{\sigma_z}\right](-1)^l\exp\left[-\frac{\chi_\sigma^2}{4}\right]I_l\left[\frac{\chi_\sigma^2}{4}\right]\\ =&\exp\left(\mathbf{i}\chi_\sigma\frac{z}{\sigma_z}\right)(-\mathbf{i})^m\frac{z}{\sqrt{2\pi}\sigma_z}\int_{-\frac{\pi}{2}}^{\frac{\pi}{2}}\frac{d\theta}{\cos^2\theta}J_m\left[\chi_\sigma\frac{z}{\sigma_z}\frac{1}{\cos\theta}\right]\exp\left[-\frac{z^2}{2\sigma_z^2}\tan^2\theta\right]\cos(m\theta).\end{aligned} \quad (5.58)$$

This formula will be compared with the simulation results for the benchmark test of our code in Chapter 7.

Formally, the transverse centroid of the entire bunch $X(n)$ should be calculated by averaging Eq. (5.57) with a charge-density weight over the longitudinal positions of the bunch, resulting in

$$X(n)=\int_{-\infty}^{\infty}dz\frac{1}{\sqrt{2\pi}\sigma_z}\exp\left(-\frac{z^2}{2\sigma_z^2}\right)\bar{x}(n,z)=X_0\sum_{m\in\mathbb{Z}}|a_{m,b}|^2\exp(-\mathbf{i}2\pi\nu_m n). \quad (5.59)$$

Since the straightforward calculation to derive $X(n)$ and $a_{m,b}$ is quite difficult, we bypass it by generalizing Eq. (5.56), treating $\hat{z}$ as a variable, and integrating it with a Rayleigh distribution over $\hat{z}$, resulting in the expression for $X(n)$ as

$$\begin{aligned}X(n)=&\int_0^{\infty}d\hat{z}\frac{\hat{z}}{\sigma_z^2}\exp\left(-\frac{\hat{z}^2}{2\sigma_z^2}\right)X(n,\hat{z})\\ =&X_0\sum_{m\in\mathbb{Z}}\int_0^{\infty}d\hat{z}\frac{\hat{z}}{\sigma_z^2}\exp\left(-\frac{\hat{z}^2}{2\sigma_z^2}\right)J_m^2\left(\chi_\sigma\frac{\hat{z}}{\sigma_z}\right)\exp(-\mathbf{i}2\pi\nu_m n)\\ =&X_0\sum_{m\in\mathbb{Z}}\exp(-\chi_\sigma^2)I_m(\chi_\sigma^2)\exp(-\mathbf{i}2\pi\nu_m n),\end{aligned} \quad (5.60)$$

where $I_m(x)$ is the modified Bessel function of the first kind [62], and the chromatic phase satisfies $\chi_{\mathrm{ABH}}=\chi_\sigma\hat{z}/\sigma_z$. This final result is identical to Eq. (4.11) after m is summed over. Here, we use $\nu_m=\nu_\beta+m\nu_s$, because the space charge is negligible.

The comparison between Eqs. (5.59) and (5.60) leads to

$$|a_{m,b}| = \sqrt{\exp\left(-\chi_\sigma^2\right) I_m(\chi_\sigma^2)}. \tag{5.61}$$

Though Eq. (5.55) features the dominant mode for the chromaticity ξ in the airbag model, they disappear in Eq. (5.61) and there is no longer the dominant mode for the specified chromaticity ξ in the low-intensity beam because the Gaussian bunches fill in the airbag distribution in the $\hat{z}$ direction.

Chapter 6

Macroparticle Tracking Simulation

This chapter details the development of a macroparticle tracking simulation code, named **CHORUS** (**C**hromaticity and **H**ead-tail **O**riented **R**ecoherence **U**nder **S**pace charge), designed to investigate intra-bunch dynamics in high-intensity proton synchrotrons. While analytical models provide essential insights, they are often limited by simplifying assumptions. To capture the complex interplay between chromaticity, wakefield, and space charge forces, a numerical approach is indispensable.

The CHORUS code is constructed by integrating physics models step-by-step. We begin in Sec. 6.1 by establishing the fundamental kinematic framework for transverse and longitudinal motion. In Secs. 6.2 and 6.3, we incorporate the effects of wakefield, modeling the longitudinal and transverse impedance sources characteristic of the J-PARC MR. Section 6.4 introduces a rigorous treatment of space charge effects, accounting for both direct and indirect forces derived from the Poisson equation for an elliptical beam in a realistic vacuum chamber. Finally, Sec. 6.5 describes the implementation of a digital feedback system model, essential for studying active instability mitigation. By unifying these components, CHORUS provides a comprehensive platform for simulating realistic beam behaviors under high-intensity conditions.

6.1 Kinematic Framework

This section establishes the basic kinematic framework of the CHORUS code, initially neglecting collective effects to focus on single-particle dynamics. To simplify the situation, the simulation only deals with 1D transverse (horizontal) and 1D longitudinal motion by tracking macroparticle motions in discrete time steps. In this thesis, only the storage mode, not the acceleration mode, is considered to highlight the feature of the space charge effect on the intra-bunch motion in the following chapters after generalizing this algorithm.

The horizontal coordinate x is defined as the position relative to that of the synchronous particle, and $x' = dx/ds$ is the derivative of x with respect to s, path length along the design trajectory. The horizontal motion terms are calculated as

$$x_{n+1,i} = \cos(\phi_{n,i})x_{n,i} + \beta_x \sin(\phi_{n,i})x'_{n,i}, \tag{6.1}$$

$$x'_{n+1,i} = -\frac{1}{\beta_x}\sin(\phi_{n,i})x_{n,i} + \cos(\phi_{n,i})x'_{n,i}, \tag{6.2}$$

where i is the macroparticle number index, n is the simulation step number index, $x_{n,i}$ is the horizontal position, $x'_{n,i}$ is the horizontal position derivative with respect to $s = \beta c\hat{T}_n$, $\hat{T}_n$ is the n-th time, the betatron phase advance is

$$\phi_{n,i} = 2\pi\left(\nu_{\beta,x} + \xi_x\delta_{n,i}\right)\frac{\Delta T}{T_0}, \tag{6.3}$$

$\Delta T = \hat{T}_{n+1} - \hat{T}_n$, $\delta_{n,i}$ is the longitudinal momentum deviation from the synchronous particle, the bare betatron tune $\nu_{\beta,x} = 21.35$, the circumference $C = 1567.5$ m, the slippage factor $\eta = -0.0578$ for a total energy $E_0 = 3.938$ GeV with Lorentz-$\beta = 0.971$ and Lorentz-$\gamma = 4.198$, the revolution period $T_0 = C/\beta c = 5.384$ μs, and $\beta_x = C/2\pi\nu_{\beta,x}$ is the average value of the beta function along the J-PARC MR.

For the transverse phase space distribution, we adopt a Gaussian distribution with $\sigma_x = 7.5$ mm and $\sigma_{x'} = 0.64$ mrad as its initial condition. The condition for this simulation matches the condition of the J-PARC MR because the beams injected into the ring typically have an unnormalized root mean square (rms) emittance of $\epsilon_x = 4.8\pi$ mm mrad. The horizontal offset position at injection is $X_0 = 0.01$ m.

The longitudinal coordinates z and δ are defined as the position and the momentum deviation relative to those of the synchronous particle, respectively. The longitudinal motion terms are calculated as

$$z_{n+1,i} = z_{n,i} - \eta C \delta_{n,i} \frac{\Delta T}{T_0}, \tag{6.4}$$

$$\delta_{n+1,i} = \delta_{n,i} - \frac{eV_{\mathrm{RF}}}{\beta^2 E_0} \frac{2\pi h}{C} z_{n+1,i} \frac{\Delta T}{T_0}, \tag{6.5}$$

where $z_{n,i}$ is the longitudinal position, the electric charge $e = 1.6 \times 10^{-19}$ C, and the harmonic number $h = 9$. Unless otherwise specified, the RF voltage is $V_{\mathrm{RF}} = 263$ kV.

The small-amplitude bare synchrotron tune ν_s is given by

$$\nu_s = \sqrt{\frac{eV_{\mathrm{RF}} h |\eta|}{2\pi\beta^2 E_0}}, \tag{6.6}$$

which is 0.0024 by the given parameters. The synchrotron period is defined as $N_s = 1/\nu_s (= 410)$.

For the longitudinal phase space distribution, we adopt a Gaussian distribution with $\sigma_z = 10$ m and

$$\sigma_\delta = \frac{2\pi\nu_s}{|\eta| C} \sigma_z, \tag{6.7}$$

as its initial condition.

The bunching factor is defined as

$$B_f = \frac{eN_B}{C\hat{\lambda}}, \tag{6.8}$$

where N_B is the bunch population, $\hat{\lambda}$ is the peak line density of electrical charges, typically featuring $B_f = 0.015$ in this simulation.

Particularly under the ABS model, which is used for the theoretical analysis in the following chapters, Eq. (6.5) is replaced by

$$\delta_{n+1,i} = \begin{cases} \delta_{n,i}, & \text{for } -\hat{z} \le z_{n+1,i} \le \hat{z}, \\ -\delta_{n,i}, & \text{for } z_{n+1,i} < -\hat{z}, \hat{z} < z_{n+1,i}, \end{cases} \tag{6.9}$$

to ensure the consistent longitudinal motion with the momentum deviation at a constant velocity in the region of $-\hat{z} < z < \hat{z}$ ($\hat{z}$ is the half bunch length). We set $\hat{z} = \sqrt{\pi/2}\sigma_z = 12.5$ m to match the peak density of the uniform distribution and that of the Gaussian distribution for the same bunch intensity eN_B, and the momentum is distributed as $\delta = \pm\delta_0 = \pm 0.13\%$ to satisfy

$$\delta_0 = \frac{4\nu_s}{|\eta|C}\hat{z}, \tag{6.10}$$

to guarantee the same synchrotron period as that of the harmonic potential.

The transverse centroid of the entire bunch $\overline{x_n}$ is defined as

$$\overline{x_n} = \frac{1}{N_{\text{particle}}}\sum_i x_{n,i}, \tag{6.11}$$

where N_{particle} is the number of macroparticles in the bunch.

Subsequently, let us divide the ring with the segment length σ_Δ where k-th segment is identified with $z^{(k)} = -C/2h + k\sigma_\Delta$ in the interval $[-C/2h, C/2h]$, and investigate the intra-bunch frequency by calculating the dipole moment $\Delta^{(k)}$ and the charge density $\lambda^{(k)}$ for the k-th segment when the segment is filled with macroparticles comprising the bunch. The number of macroparticles $N^{(k)}$ in k-th segment is calculated as

$$N^{(k)} = \sum_i S_i^{(k)}, \tag{6.12}$$

where (k) and i specify the segment and macroparticle indices, respectively, and the shape function is introduced as follows [63, 64]

$$S_i^{(k)} = \begin{cases} 1 - \frac{|z_i - z^{(k)}|}{\sigma_\Delta}, & \text{for } z^{(k-1)} \le z_i \le z^{(k+1)}, \\ 0, & \text{for } z_i < z^{(k-1)}, z^{(k+1)} < z_i. \end{cases} \tag{6.13}$$

Finally, the dipole moment $\Delta^{(k)}$ and the charge density $\lambda^{(k)}$ of k-th segment are respectively described as

$$\Delta^{(k)} = \frac{q}{\sigma_\Delta}\sum_i x_i S_i^{(k)}, \tag{6.14}$$

$$\lambda^{(k)} = \frac{q}{\sigma_\Delta}\sum_i S_i^{(k)}, \tag{6.15}$$

with $q = eN_B/N_{\text{particle}}$ being the allocated charge for one macroparticle. Accordingly, the transverse centroid $x^{(k)}$ of k-th segment is given by

$$x^{(k)} = \frac{\Delta^{(k)}}{\lambda^{(k)}}. \tag{6.16}$$

In the following simulations concerning the transverse oscillation in the bunch, we will conduct tracking simulations with both the ABS model with Eqs. (6.4) and (6.9), and the harmonic potential bunch model with Eqs. (6.4) and (6.5). The horizontal chamber boundary is set to ± 0.065 m, while the longitudinal bucket size is $\pm C/2h$. We assume that any macroparticles outside this region should be lost.

6.2 Longitudinal Wakefield Model

As we have already seen in Chapter 4, the recoherence time and synchrotron frequency are closely related. In accordance with it, the resistive wall impedance may deform the RF bucket, which can in turn lengthen the synchrotron period. In this chapter, we examine the possibility that the longitudinal resistive wall effect could modulate the recoherence time.

To take into account the nonlinearity of the RF acceleration to the longitudinal amplitude, Eq. (6.5) is replaced by

$$\delta_{n+1,i} = \delta_{n,i} - \frac{eV_{\mathrm{RF}}}{\beta^2 E_0} \sin\left(\frac{2\pi h}{C} z_{n+1,i}\right) \frac{\Delta T}{T_0}. \tag{6.17}$$

The MR, with a circumference of C(=1567.5 m), utilizes SUS316L stainless steel cylindrical chambers with an inner radius of h_C(=0.065 m) and a thickness of d_w (=0.002 m). The longitudinal resistive wall wakefield is given by [65]

$$W_{\mathrm{L0}}(s) = \frac{4cZ_0C}{\pi h_C^2}\left(\frac{e^{-\frac{s}{s_0}}}{3}\cos\frac{\sqrt{3}s}{s_0} - \frac{\sqrt{2}}{\pi}\int_0^\infty dx \frac{x^2 e^{-x^2\frac{s}{s_0}}}{x^6+8}\right), \quad \text{for } s > 0 \text{ m}, \tag{6.18}$$

where $s_0 = (2h_C^2\rho)^{1/3} = 250$ μm.

The potential well distortion is excited by the wakefield potential as

$$W_{\mathrm{L0}}(s) = \int_{-\infty}^{\infty} ds' W_{\mathrm{L0}}(s-s')\rho_z(s'), \tag{6.19}$$

where we assume a Gaussian beam as

$$\rho_z(z) = eN_B \frac{1}{\sqrt{2\pi}\sigma} e^{-\frac{z^2}{2\sigma^2}}. \tag{6.20}$$

Figure 6.1 shows the longitudinal wakefield potential divided by the total charge of bunch: eN_B, in the case of σ=2.72 m, which is used as the initial parameter in the simulation in this chapter.

To compromise this impedance with the space charge calculations in the code, we calculate the wakefield potential only on the mesh grid points in advance and subsequently interpolate it to estimate the kick on the witness particle located between the mesh grid points. The longitudinal kick $kick_z^{(k)}$ at the mesh grid point k is calculated as

$$kick_z^{(k)} = \sigma_\Delta \sum_j W_{\mathrm{L0}}(z_j - z^{(k)})\lambda^{(j)}, \tag{6.21}$$

where the charge density $\lambda^{(j)}$ of j-th segment is given by Eq. (6.15).

Subsequently, the longitudinal kick $kick_{z,i}$ on i-th macroparticle between k-th and $k+1$-th grid points are calculated as

$$kick_{z,i} = \left(1 - \frac{z_i - z^{(k)}}{\sigma_\Delta}\right) kick_z^{(k)} + \frac{z_i - z^{(k)}}{\sigma_\Delta} kick_z^{(k+1)}. \tag{6.22}$$

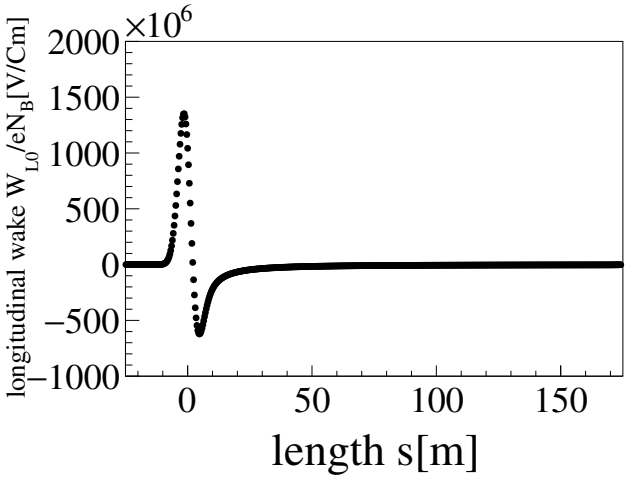

Figure 6.1: Longitudinal resistive wall wakefield potential divided by the total charge of bunch for σ=2.72 m.

Finally, the longitudinal kick at each time step is implemented into the code as

$$\Delta\delta_i = -\frac{1}{E_0} kick_{z,i} \frac{\Delta T}{T_0}. \tag{6.23}$$

Notice that the long-range wakefield effect is neglected in this calculation.

On the other hand, the Hamiltonian formalism theoretically provides the deformation of synchrotron tune through the potential well distortion as follows

$$\nu_s(H_0) = C \left[\oint \frac{d\phi}{2\sqrt{H_0 - U(\phi)}} \right]^{-1}, \tag{6.24}$$

where

$$H_0 = \frac{1}{2} \left(\frac{2\pi h \eta}{C} \right)^2 \delta_i^2 + U(\phi). \tag{6.25}$$

Here, the potential $U(\phi)$ is assumed to be fixed for the given beam distribution as

$$U(\phi) = \frac{2\pi h \eta e V_{\mathrm{RF}}}{C^2 E_0} (\cos\phi - 1) - \frac{2\pi h \eta}{C^2 E_0} \int_{-\infty}^{\phi} d\phi'' \int_{-\infty}^{\infty} d\phi' W_{\mathrm{L0}}(\phi' - \phi'') \lambda(\phi'), \tag{6.26}$$

neglecting the deformation effect on the bunch shape due to the wake, where $\phi = 2\pi h z/C$ is the longitudinal phase and $\lambda(\phi)$ is charge density.

Figure 6.2 shows the theoretical and simulation results only with the longitudinal wakefield potential with $N_B = 3 \times 10^{14}$ ppb for different particle energy represented by H_0. The theoretical and the simulations are in good agreement. The outcome demonstrates that this synchrotron tune distribution is confined in $0.002 < \nu_s < 0.00245$.

On the contrary, we find a significant discrepancy between the theoretical/simulation results only dealing with the wakefield, and the experimental one in the MR: $\nu_s \approx 0.0005$ which is obtained by assuming the recoherence time is determined solely by the synchrotron

tune. Finally, we conclude that the observed longitudinal resistive wall impedance alone cannot explain the lengthened recoherence time, even when the amplitude modulation period due to the wakefield effect is taken into consideration [66].

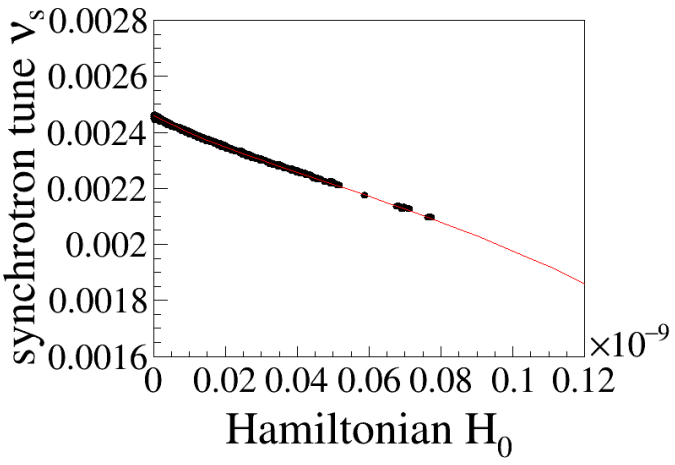

Figure 6.2: Theoretical result of synchrotron tune deviation due to the potential $U'(\phi)$ (red line) and the simulation results (point) in the case of $N_B = 3 \times 10^{14}$ ppb and $\sigma_z = 2.72$ m.

6.3 Transverse Wakefield Model

If the space charge force affects the recoherence time, the wakefield could potentially have an impact on it as well. Since the authors have identified that the effect of the longitudinal impedance on the decoherence time is negligible in Sec. 6.2, this section describes how to implement the horizontal wakefield due to the resistive wall chambers into the code to simulate the impedance source in the J-PARC MR.

The horizontal resistive wall wakefield function $W_{\mathrm{T1}}(s)$ is given by [67–70]

$$\begin{aligned} W_{\mathrm{T1}}(s) &= \frac{LD_{1x}(u_0)}{h_{E_y}^3}\frac{2cZ_0\rho}{\pi d_\omega}\sum_{n=0}^{\infty}\exp\left(-\frac{\pi^2\rho}{d_\omega^2}s\left(n+\frac{1}{2}\right)^2\right) \\ &\approx \begin{cases} \frac{LD_{1x}(u_0)}{h_{E_y}^3}\frac{cZ_0\sqrt{\rho}}{\pi\sqrt{\pi}}\sqrt{\frac{1}{s}}, & \text{for } 0 < s < 500\text{m}, \\ \frac{LD_{1x}(u_0)}{h_{E_y}^3}\frac{2cZ_0\rho}{\pi d_\omega}\exp\left(-\frac{\pi^2\rho}{d_\omega^2}\frac{s}{4}\right), & \text{for } s > 500\text{m}, \end{cases} \end{aligned} \tag{6.27}$$

for an elliptic chamber with the major horizontal axis $2h_{E_x} = 2f\cosh u_0$, the minor vertical axis $2h_{E_y} = 2f\sinh u_0$, ($f = \sqrt{h_{E_x}^2 - h_{E_y}^2}$), a finite thickness d_ω, a length L, SUS316L resistivity $\rho = 1.96 \times 10^{-9}$ m, and the impedance of free space $Z_0 = 120\pi$, where

$$D_{1x}(u_0) = \frac{\sinh^3 u_0}{4\pi}\int_0^{2\pi} dv \frac{Q_{1x}^2(v)}{\sqrt{\sinh^2 u_0 + \sin^2 v}}, \tag{6.28}$$

$$Q_{1x}(v) = 2\sum_{m=0}^{\infty}(-1)^m(2m+1)\frac{\cos(2m+1)v}{\cosh(2m+1)u_0}. \tag{6.29}$$

The factor $D_{1x}(u_0)$ characterizes the asymmetry of the elliptic chamber and approaches one for a cylindrical chamber. Notice that the wakefield function $W_{\mathrm{T1}}(s)$ is proportional to $LD_{1x}/h_{E_y}^3$. As the thickness d_ω goes to infinity, Eq. (6.27) becomes proportional to $1/\sqrt{s}$, which is the typical behavior of the resistive wall impedance. In other words, we can make use of the damping effect due to the chamber thickness in Eq. (6.27) to calculate beam behavior affected by the resistive wall impedance.

In the J-PARC MR, where the cylindrical chamber with an inner radius h_C(=0.065 m) dominates, the thickness of the chamber is d_ω(=0.002 m). The bending magnet region, where the elliptical ducts with a major axis $2h_{E_x}$(= 2 × 0.065 m) and a minor axis $2h_{E_y}$(= 2 × 0.050 m), yielding a geometric factor $D_{1x} = 0.615$, are placed, occupies F(= 0.358) of the total circumference of the ring. Hence, the total resistive wall impedance along the ring, including the effect of the elliptic chambers, is enhanced by the factor $\mathcal{G}$:

$$\mathcal{G} = FD_{1x}\frac{h_C^3}{h_{E_y}^3} + (1 - F) = 1.1, \tag{6.30}$$

compared to the case where the ring is assumed to be effectively composed of cylindrical chambers. This indicates that the assumption that the resistive wall wakefield for the cylindrical chamber:

$$W_{\mathrm{T1}}(s) = \frac{C}{h_C^3}\frac{2cZ_0\rho}{\pi d_\omega}\sum_{n=0}^{\infty}\exp\left(-\frac{\pi^2\rho}{d_\omega^2}s\left(n+\frac{1}{2}\right)^2\right), \tag{6.31}$$

occupies the J-PARC MR, estimates the resistive wall impedance of the ring within about 10% accuracy, which is applied for our formulation.

The resistive wall impedance provides the kick on the witness particle in a similar way as the longitudinal wakefield case. Concretely, the horizontal dipole kick $kick_x^{(k)}$ at the mesh grid point k with a single-turn wakefield is calculated into the code as

$$kick_x^{(k)} = \sigma_\Delta \sum_j W_{\mathrm{T1}}(z_j - z^{(k)})\Delta^{(j)}, \tag{6.32}$$

where the dipole moment $\Delta^{(j)}$ of j-th segment is calculated as Eq. (6.14). Using this kick at each segment, the horizontal dipole kick $kick_{x,i}$ on i-th macroparticle between k-th and $(k+1)$-th grid points are estimated as

$$kick_{x,i} = \left(1 - \frac{z_i - z^{(k)}}{\sigma_\Delta}\right)kick_x^{(k)} + \frac{z_i - z^{(k)}}{\sigma_\Delta}kick_x^{(k+1)}. \tag{6.33}$$

Finally, the horizontal dipole kick at each time step is provided as

$$\Delta x_i' = \frac{1}{E_0}kick_{x,i}\frac{\Delta T}{T_0}. \tag{6.34}$$

Taking into account the thickness of the chamber facilitates dealing with the multi-turn long-range effects on the beams with the rapid decay of the resistive wall impedance, according to Eq. (6.27). To see the convergence of the accumulated multi-turn wake, let

us simply sum the resistive wall impedance up to N_λ, assuming the positions of beams exciting the wakes in the previous turns are identical, as

$$V(N_\lambda) = \sum_{l=1}^{N_\lambda} W_{\mathrm{T1}}(lC). \tag{6.35}$$

Figure 6.3 shows Eq. (6.35) for different N_λ and the deviation of $V(N_\lambda)$ from the analytical estimate of Eq. (6.35) with infinite N_λ, respectively. In the J-PARC MR with circumference C(=1567.5 m), the deviation reduces to nearly 0.1% after $N_\lambda = 4$ turns as already revealed in Ref. [70], because the thickness of the installed chamber is typically d_ω(=0.002 m). Therefore, we conclude that $N_\lambda = 4$ is sufficient to adequately incorporate the accumulation effects of the long-range wakefield in the code.

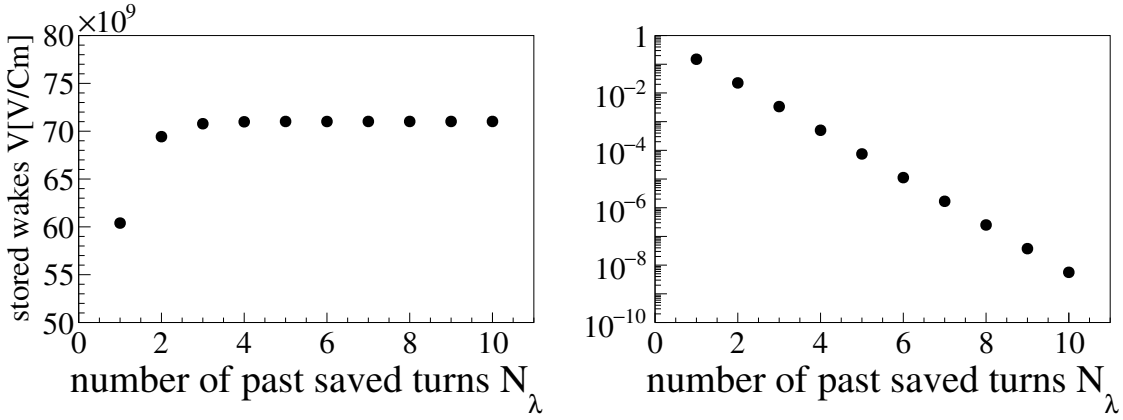

(a) $V(N_\lambda)$ **(b)** $1 - V(N_\lambda)/V(\infty)$

Figure 6.3: Sum of multi-turn wakes for different N_λ(left) and the deviation from the analytical estimate with infinite N_λ(right).

More explicitly, the accumulated horizontal kicks are calculated as

$$\Delta x' = \frac{1}{E_0} kick_x \frac{\Delta T}{T_0}, \tag{6.36}$$

where

$$kick_x = \sum_{l=1}^{4} W_{\mathrm{T1}}(lC)\Delta_{n-l}, \tag{6.37}$$

and the dipole moment of the respective bunches is

$$\Delta_n = q \sum_i x_{n,i} = eN_B \overline{x_n}. \tag{6.38}$$

Here, the transverse centroid of the entire bunch $\overline{x_n}$ in Eq. (6.38) is calculated by averaging the macroparticle positions in the bunch following Eq. (6.11).

As a result, the short-range (Eq. (6.34)) and long-range (Eq. (6.36)) wakes are simultaneously implemented into the code by making use of the feature of resistive wall impedance with chamber thickness.

6.4 Space Charge Model

To investigate the space charge effects on intra-bunch motion, we formulate the electromagnetic forces implemented in our tracking simulation. The model accounts for both direct space charge (self-field) and indirect space charge (image charge) effects derived from the Poisson equation.

We adopt a "2.5D" approach: the beam is sliced perpendicular to the longitudinal direction, and each segment is treated as a two-dimensional elliptical beam with a uniform charge distribution (Kapchinski-Vladimirskij (K-V) distribution) [71]. The horizontal and vertical semi-axes are denoted by a_x and a_y, respectively. While a_y is fixed in this simulation, a_x is dynamically updated at each time step based on the macroparticle distribution. To be consistent with a Gaussian distribution used in other parts of the simulation, we set the effective beam sizes as $a_x = \sqrt{2}\sigma_x$ and $a_y = \sqrt{2}\sigma_y$, which matches the peak charge density of the Gaussian profile.

The electromagnetic fields are calculated by considering the boundary conditions of an elliptical vacuum chamber and the parallel magnetic pole faces of bending magnets. The detailed mathematical derivation, involving the potential theory with Jacobian elliptic functions, is provided in Appendix D.

Based on the derivation in Appendix D, the horizontal equation of motion for a particle at position x is given by summing the electric (F_x^{ele}) and magnetic (F_x^{mag}) forces from both direct (DS) and indirect (im) sources:

$$x'' = \frac{1}{\gamma m_p c^2 \beta^2}\left(F_{x,\mathrm{DS}}^{\mathrm{ele}} + F_{x,\mathrm{DS}}^{\mathrm{mag}} + F_{x,\mathrm{im}}^{\mathrm{ele}} + F_{x,\mathrm{im}}^{\mathrm{mag,AC}} + F_{x,\mathrm{im}}^{\mathrm{mag,DC}}\right) \tag{6.39}$$

Assuming the transverse beam size is sufficiently smaller than the chamber radius (linear approximation), this equation simplifies to a form characterized by the incoherent tune shift $\Delta\nu_{\mathrm{inc}}$ and the coherent tune shift $\Delta\nu_{\mathrm{coh}}$. Consequently, the horizontal kick $\Delta x_i'$ applied to the i-th macroparticle in the k-th longitudinal segment at each time step ΔT is implemented as:

$$\Delta x_i' = -\frac{4\pi}{\beta_x}\left(\Delta\nu_{\mathrm{inc}}^{(k)}(x_i - \bar{x}^{(k)}) + \Delta\nu_{\mathrm{coh}}^{(k)}\bar{x}^{(k)}\right)\frac{\Delta T}{T_0}, \tag{6.40}$$

where $\bar{x}^{(k)}$ is the horizontal centroid of the segment. The incoherent tune shift for the elliptical beam is given by:

$$\Delta\nu_{\mathrm{inc}}^{(k)} = -\frac{r_p C^2}{2\pi^2 e\gamma^3\beta^2\nu_{\beta,x}}\frac{\lambda^{(k)}}{a_x^{(k)}(a_x^{(k)} + a_y)}, \tag{6.41}$$

and the coherent tune shift, which includes the contributions from the image charges, is expressed as:

$$\Delta\nu_{\mathrm{coh}}^{(k)} = -\frac{r_p C^2}{2\pi^2 e\gamma^3\beta^2\nu_{\beta,x}}\lambda^{(k)}\mathcal{F}\frac{\xi_{1,C}}{h_C^2} - \frac{N_B r_p C}{2\pi^2\gamma\nu_{\beta,x}}\mathcal{F}\frac{\xi_{1,C}}{h_C^2}. \tag{6.42}$$

Here, $\lambda^{(k)}$ is the line density of the segment, h_C is the chamber radius, and $\xi_{1,C} = 1/2$ is the coherent image coefficient for a cylindrical chamber. The factor $\mathcal{F}$ accounts for the

filling factor of elliptical chambers along the ring (see Appendix D for the definition of geometric factors).

Finally, the symplectic transformation for the macroparticle tracking is ensured by applying the kick based on the position at the next step, x_{n+1}. The update rule combining the betatron oscillation and the space charge kick is:

$$x_{n+1} = \cos\left(2\pi(\nu_{\beta,x} + \xi_x\delta_n)\frac{\Delta T}{T_0}\right) x_n + \beta_x \sin\left(2\pi(\nu_{\beta,x} + \xi_x\delta_n)\frac{\Delta T}{T_0}\right) x'_n, \tag{6.43}$$

$$\begin{aligned} x'_{n+1} = &-\frac{1}{\beta_x}\sin\left(2\pi(\nu_{\beta,x} + \xi_x\delta_n)\frac{\Delta T}{T_0}\right) x_n + \cos\left(2\pi(\nu_{\beta,x} + \xi_x\delta_n)\frac{\Delta T}{T_0}\right) x'_n \\ &- \frac{4\pi}{\beta_x}\Delta\nu_{\text{inc}}\frac{\Delta T}{T_0}(x_{n+1} - \overline{x_{n+1}}) - \frac{4\pi}{\beta_x}\Delta\nu_{\text{coh}}\frac{\Delta T}{T_0}\overline{x_{n+1}}, \end{aligned} \tag{6.44}$$

where $2\pi(\nu_{\beta,x} + \xi_x\delta_n)$ is the phase advance including chromaticity.

6.5 Feedback System Model

Ideally, a feedback system should damp coherent oscillations without amplifying noise. To model this in CHORUS, we implement a digital Finite Impulse Response (FIR) filter designed using the Tune-Decoupled Least Squares Fitting (TDLSF) method. This method optimizes the filter coefficients to minimize noise transmission while maintaining the target gain and phase at the betatron tune.

In the simulation, the feedback system operation involves three steps: detecting the beam position, processing the signal, and applying the corrective kick. First, the beam position $x(n)$ (representing the bunch centroid $\overline{x_n}$ or a specific slice centroid $x^{(k)}$) is recorded at each turn. The calculated kick signal $y(n)$ is generated from the history of these positions using an N-tap FIR filter:

$$y(n) = \sum_{k=1}^{N} a_k x(n-k) \tag{6.45}$$

Here, a_k are the filter coefficients designed to meet specific response criteria.

The filter design requires the complex response $\tilde{G}(\phi)$ to satisfy three conditions at the target betatron phase advance $\phi_1 = 2\pi\nu_\beta$:

1. Zero DC Gain: $\sum a_k = 0$ to ignore static orbit errors.
2. Target Gain: $|\tilde{G}(\phi_1)| = G_1$.
3. Target Phase: $\arg\tilde{G}(\phi_1) = \psi_1$ (typically $-90°$ for resistive damping).

Using the TDLSF method, we determine the coefficients a_k by solving a constrained minimization problem for the noise power $P = \frac{1}{2}\sum a_k^2$ using Lagrange multipliers. This

leads to a linear system:

$$\begin{pmatrix} N & c_1 & s_1 \\ c_1 & c_2 & u_2 \\ s_1 & u_2 & s_2 \end{pmatrix} \begin{pmatrix} C_0 \\ C_1 \\ S_1 \end{pmatrix} = G_1 \begin{pmatrix} 0 \\ \cos\psi_1 \\ -\sin\psi_1 \end{pmatrix}, \tag{6.46}$$

where $c_1 = \sum \cos(k\phi_1)$, $s_1 = \sum \sin(k\phi_1)$, $c_2 = \sum \cos^2(k\phi_1)$, $s_2 = \sum \sin^2(k\phi_1)$, and $u_2 = \sum \sin(k\phi_1)\cos(k\phi_1)$.

Once the multipliers C_0, C_1, S_1 are found, the coefficients are determined by:

$$a_k = C_0 + C_1 \cos(k\phi_1) + S_1 \sin(k\phi_1). \tag{6.47}$$

For enhanced stability against tune shifts, an additional derivative condition $\partial\tilde{G}/\partial\phi = 0$ can also be imposed.

Finally, the computed correction signal $y(n)$ is applied as a transverse kick to the macroparticles. In the tracking code, this is implemented by modifying the momentum of each particle i in the bunch (or slice) at turn n:

$$\Delta x'_{n,i} = \frac{1}{\sqrt{\beta_m \beta_k}} y(n), \tag{6.48}$$

where β_m and β_k are the beta functions at the monitor (pickup) and kicker locations, respectively (assumed equal in this simplified model). This active damping term competes with the growth mechanisms driven by wakefield and space charge, allowing CHORUS to simulate the threshold behaviors of feedback-controlled beams.

Chapter 7

Validation of the Simulation

Before exploring the complex dynamics governed by collective effects, it is important to establish the numerical reliability and physical accuracy of the CHORUS simulation code developed in Chapter 6. This chapter presents a validation process consisting of two main stages. First, in Sec. 7.1, we perform a systematic scan of critical simulation parameters, specifically the number of macroparticles, time step size, and longitudinal mesh granularity, to determine the conditions necessary for numerical convergence and stability. Second, in Sec. 7.2, we benchmark the code against the analytical linear decoherence model established in Chapter 4. By confirming that the simulation reproduces theoretical predictions for transverse amplitude modulation and intra-bunch frequency in the low-intensity limit, we verify the correct implementation of fundamental beam kinematics and chromaticity effects.

7.1 Validation of Simulation Parameters

The critical parameters in our code dealing with the space charge effects are the number of macroparticles N_{particle}, the advance time per step relative to the revolution time $\Delta T/T_0$, and the longitudinal mesh size σ_Δ. In this section, the required conditions to get reliable simulations are investigated by scanning these three parameters with fixed $\xi = -12.5$ and $N_B = 8.6 \times 10^{12}$ ppb, where the constant wakefield $W_{\text{T1}} = 4 \times 10^{12}$ V/Cm is adopted to streamline the calculation efficiency just for this purpose. This chromaticity is chosen as the worst condition in our simulation because a tiny mesh size is necessary to obtain reliable simulation results for higher chromaticity.

The average transverse amplitudes (Courant-Snyder invariant) of all macroparticles is calculated as

$$\overline{A_n} = \sqrt{\overline{x_n}^2 + \beta_x^2 \overline{x'_n}^2}, \tag{7.1}$$

by assuming the Twiss parameter γ is zero for simplicity, where $\overline{x'_n} = \sum_i x'_{n,i}/N_{\text{particle}}$.

Figures 7.1, 7.2a, and 7.3 represent $\overline{A_n}$ on a turn-by-turn basis in the following cases: (1) scanning N_{particle} with $T_0/\Delta T = 100$ and $\sigma_\Delta = 0.17$ m fixed, (2) scanning $T_0/\Delta T$ with $N_{\text{particle}} = 50000$ and $\sigma_\Delta = 0.17$ m fixed, and (3) scanning σ_Δ with $N_{\text{particle}} = 50000$ and $T_0/\Delta T = 100$ fixed.

The areas marked as $\mathcal{A}$ in Fig. 7.1, $\mathcal{B}$ in Fig. 7.2a, and $\mathcal{C}$ in Fig. 7.3, respectively, illustrate the modulation of the transverse amplitudes caused by the space charge effects, characterizing the intra-bunch motion. The simulations provide a adequate N_{particle}, small step size ΔT, and mesh size σ_Δ to accurately reproduce the phenomena. Figures 7.1, 7.2, and 7.3 indicate that the simulation requires the condition that $N_{\text{particle}} > 5000$, $T_0/\Delta T > 85$, and $C/(h\sigma_\Delta) > 512$ to excite the modulation of the transverse amplitudes

correctly, because we observe the irregular reductions in the transverse amplitude at $T_0/\Delta T = 14, 17, 21, 42, 43$, and 85, as shown in Fig. 7.2a.

Figure 7.2b illustrates the horizontal rms beam size σ_x as a function of $T_0/\Delta T$. We find that the irregular beam size expansion occurs in Fig. 7.2b under the same conditions depicted in Fig. 7.2a. This supports the conclusion that the irregular transverse amplitude reduction in Fig. 7.2a is caused by the beam losses at $T_0/\Delta T = 14, 17, 21, 42, 43$, and 85, resulting from collisions of the macroparticles with the horizontal chamber boundary.

Accordingly, we examined the conditions under which the transverse amplitudes and the beam sizes remain stable up to $T_0/\Delta T = 300$. This analysis determined that $T_0/\Delta T > 85$ is the necessary condition for stability.

After all conditions are taken into consideration, we select $N_{\text{particle}} = 50000$, $\Delta T = T_0/100$, and $\sigma_\Delta = 0.17$ m as the suitable parameter set in the simulations with space charge effects.

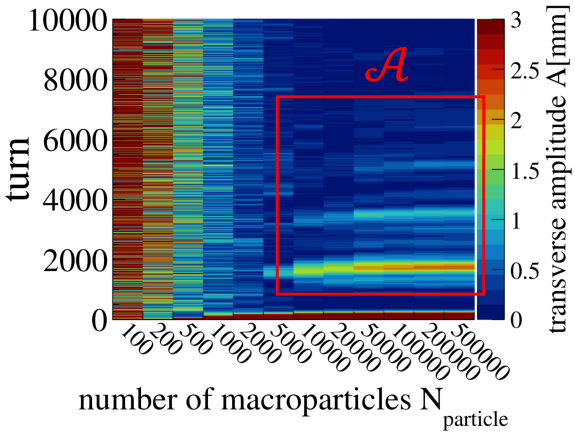

Figure 7.1: Transverse amplitude $\overline{A_n}$ scanned by varying the number of macroparticles N_{particle}.

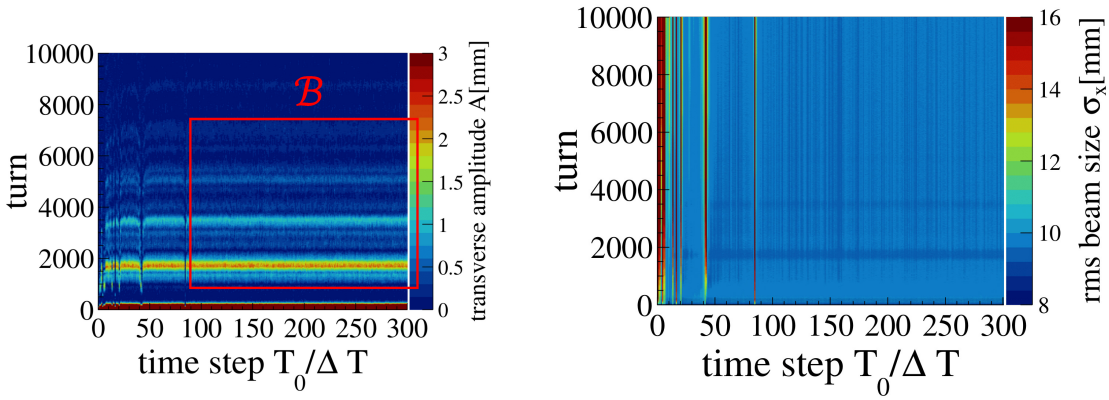

(a) Transverse amplitude $\overline{A_n}$

(b) Horizontal rms beam size σ_x

Figure 7.2: The result of tracking simulation scanned by varying time steps relative to the revolution time $T_0/\Delta T$.

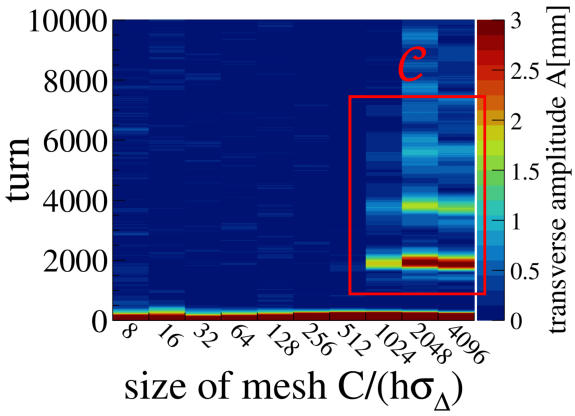

Figure 7.3: Transverse amplitude $\overline{A_n}$ with constant wakefield by varying the size of the mesh that divides the bunch longitudinally as $C/(h\sigma_\Delta)$.

7.2 Consistency Check with the Linear Decoherence Scenario

Linear decoherence scenario described in Chapter 4 is useful for benchmark tests of our code. We investigate the time evolution of the transverse oscillation amplitude of the centroid, of the transverse dipole moment, and of the intra-bunch frequency within the linear approximation of the RF bucket around the bunch.

Tracking simulations are performed under the RF voltages: $V_{\mathrm{RF}} = 110, 263$, and 400 kV and the fixed chromaticity $\xi = -2$. Figure 7.4 compares the theoretical result by Eq. (4.12) of transverse amplitude $\overline{A_n}$ for each turn (Fig. 7.4a) with the simulations (Fig. 7.4b), where the blue, black, and red lines show the cases of $V_{\mathrm{RF}} = 110, 263$, and 400 kV, respectively. Amplitude modulation occurs synchronously with the synchrotron period of $N_s = 330$(red), 410(black), and 630(blue) turns, determined by the RF voltages.

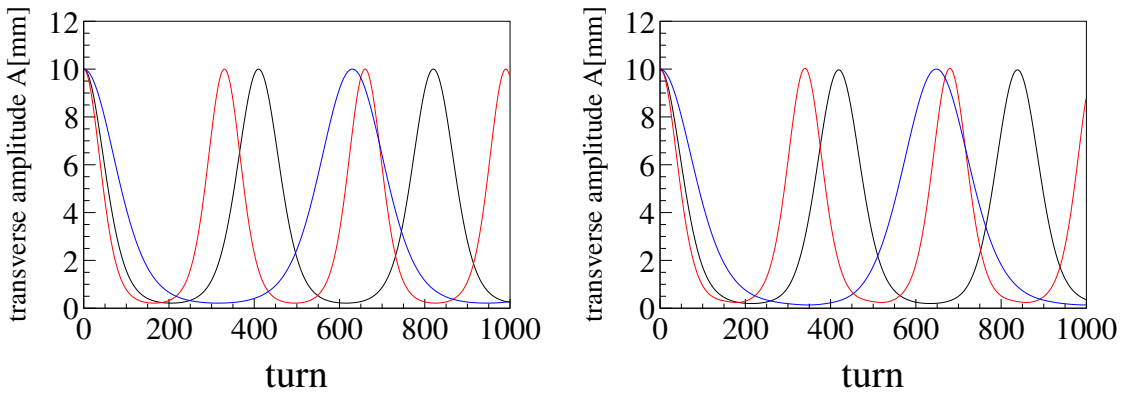

(a) calculated by Eq. (4.12)

(b) tracking simulation

Figure 7.4: Transverse amplitudes of the bunch oscillation calculated by Eq. (4.12) and tracking simulations for $V_{\mathrm{RF}} = 110$kV(blue), $V_{\mathrm{RF}} = 263$kV(black), and $V_{\mathrm{RF}} = 400$kV(red).

For various chromaticity conditions $\xi = -1, -2, -3$, and -8 with fixed $V_{\mathrm{RF}} = 263$ kV, tracking simulations are performed and compared to the theoretical result (Eq. (4.12)). Figures 7.5a and 7.5b show the theoretical and the simulation results, respectively, where the black, red, blue, and green represent the result for $\xi = -1, -2, -3$, and -8, respectively. The simulations reproduce the theoretical results with accuracy and demonstrate the reliability of our code. Notice that the decoherence becomes more clearly identified as the chromaticity increases in the negative direction.

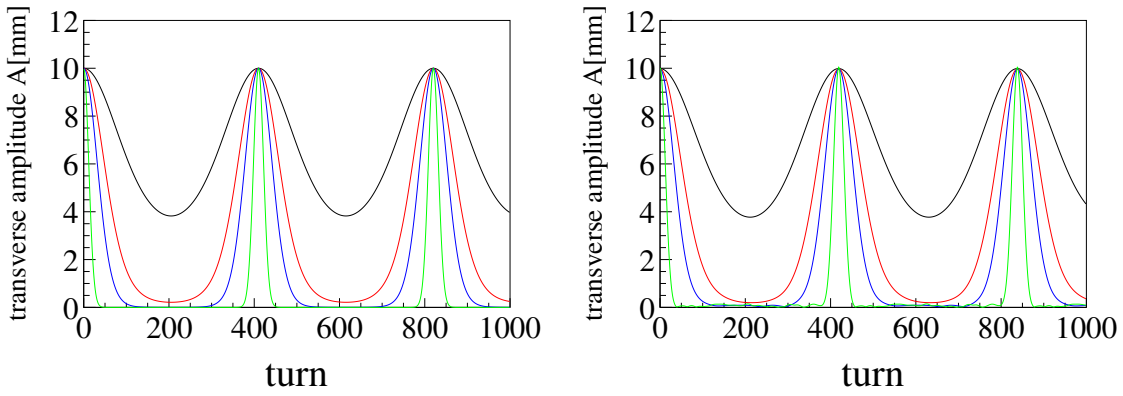

(a) calculate by Eq. (4.12) **(b)** tracking simulation

Figure 7.5: Transverse amplitudes of the bunch oscillation calculated by Eq. (4.12) and tracking simulations for $\xi = -1$ (black), $\xi = -2$ (red), $\xi = -3$ (blue), and $\xi = -8$ (green).

Next, we analyze the frequency component of the bunch per turn after Fourier transforming the dipole moment for each segment. Figures 7.6 and 7.7 represent the simulations illustrating the dipole moments within the bunch and the Fourier components during the beam's circulation in the ring. As the chromaticity increases, the amplitude modulation is suppressed, with the intra-bunch frequency enhanced, which aligns well with theoretical expectations (Eqs. (4.6) and (4.9)).

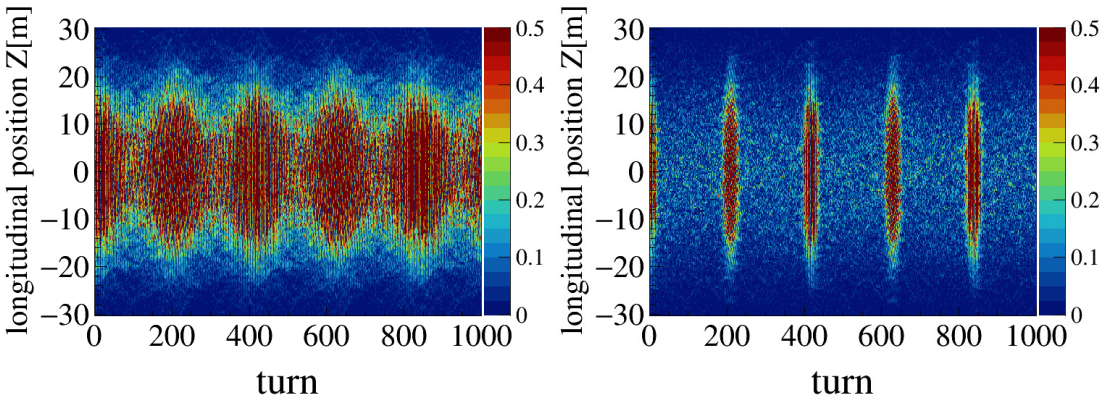

(a) $\xi = -2$ **(b)** $\xi = -8$

Figure 7.6: The dipole moment $|\Delta^{(k)}\sigma_\Delta/q|$ in the bunch by the tracking simulations.

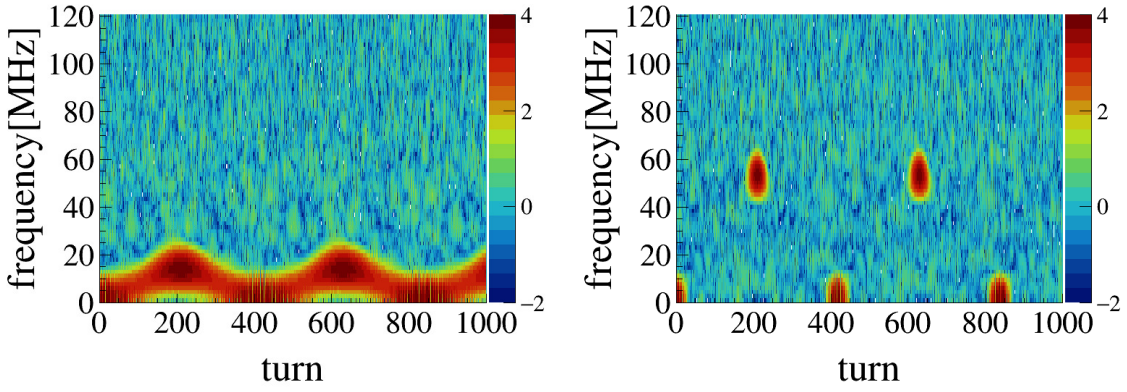

(a) $\xi = -2$ **(b)** $\xi = -8$

Figure 7.7: Frequency components of the dipole moment in the bunch by the tracking simulations.

More closely, let us analyze the maximum intra-bunch frequency $f_{\max}$ against the chromaticity. As illustrated in Fig. 7.8, the simulation's maximum intra-bunch frequency $f_{\max}$ is in good agreement with the theoretical result by Eq. (4.10), showcasing a linear response of the maximum intra-bunch frequency to the chromaticity ξ when excluding the impedance and space charge effects.

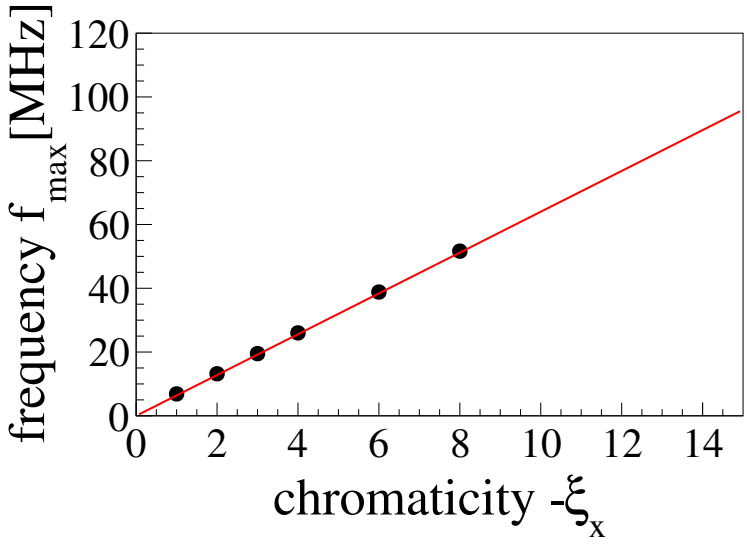

Figure 7.8: The simulations (dots) and the theoretical results by Eq. (4.10) (red line) of the maximum intra-bunch frequency $f_{\max}$ for each chromaticity condition.

Chapter 8

Analysis of the Simulation in the Frequency Domain

The developed tracking simulation code in Secs. 6.1, 6.3, and 6.4 enables us to investigate how the frequency (ν_m), and the amplitudes in the respective segments of the bunch ($\tilde{a}_m^{(k)}$) and in the entire bunch (a_m) of the head-tail modes are affected by the transverse wakefield and space charge effects on the intra-bunch motion unless instabilities are excited after choosing suitable machine parameters.

In this chapter , we will scan the beam intensity and chromaticity in the ABS model, or the Gaussian bunch model under the harmonic potential for the longitudinal distribution to realize the limit of the ABS model and understand the space charge effects on the Gaussian bunch.

The beam sizes assumed to be $\sigma_x = 0.009$ m with fixed $\sigma_y = 0.010$ m, (refer to the final paragraph in Sec. 6.4) and the peak charge density $\hat{\lambda}$ determined by Eq. (6.8) through the bunching factor ($B_f = 0.015$) produce the minimum incoherent tune shift in the bunch:

$$\Delta\nu_{\rm inc} = -157 \times 10^{-4} \times N_B/10^{12}, \tag{8.1}$$

and the minimum coherent tune shift in the bunch:

$$\Delta\nu_{\rm coh} = -7.4 \times 10^{-4} \times N_B/10^{12}, \tag{8.2}$$

for both potential models, after replacing $a_x^{(k)}$, a_y and $\lambda^{(k)}$ by $\sqrt{2}\sigma_x$, $\sqrt{2}\sigma_y$, and $\hat{\lambda}$ in Eqs. (6.41) and (6.42), respectively, though the simulation dynamically changes the horizontal and longitudinal beam sizes.

In both simulations, the tune spectrum, ν_m, and the absolute relative amplitude, $|a_m|$, of the centroid $\overline{x_n}$ (Eq. (6.11)) for the entire bunch oscillation, along with the corresponding values (ν_m, $|\tilde{a}_m^{(k)}|$) for the local segments specified by the centroid $x^{(k)}$ (Eq. (6.16)), are obtained by applying a Fast Fourier Transform (FFT) to the turn-by-turn bunch oscillations from the start of the simulation up to 10000 turns. The results of these simulations will be compared with the theoretical predictions.

8.1 Analysis of ABS Model

8.1.1 Weak Space Charge Force

Now, let us investigate the frequency shifts of the excited betatron oscillation of the particles comprising the low-intensity bunch and the chromaticity dependence of the

oscillation amplitudes. Equation (5.36) suggests that the higher-order head-tail modes can be excited by increasing the chromatic phase ($\chi_{\rm ABS}$) because the dominant mode m is specified as

$$m \simeq \pm\frac{2}{\pi}\chi_{\rm ABS}, \tag{8.3}$$

when the space charge effects are small, where Eq. (5.9) based on the ABS model leads to

$$\chi_{\rm ABS} = 2\pi\frac{\xi}{\eta C}\hat{z} = -0.87\xi, \tag{8.4}$$

in the MR.

Figure 8.1 shows the theoretical relative amplitude $|\tilde{a}_{m,\rm ABS}(z)|$ calculated by Eq. (5.27) for various chromaticity ξ. Figure 8.2 shows the relative amplitude $|\tilde{a}_m^{(k)}|$ in each segment derived from the tracking simulation with the low-intensity $N_B = 1.0\times10^8$ protons per bunch (ppb) corresponding to the weak space charge case. In those figures, the black, red, green, blue, orange, magenta, cyan, dark green, purple, and gray denote the cases of $m = 0, 1, 2, \cdots 9$, respectively. The results of the theory and tracking simulation are in nice agreement at this intensity from these figures.

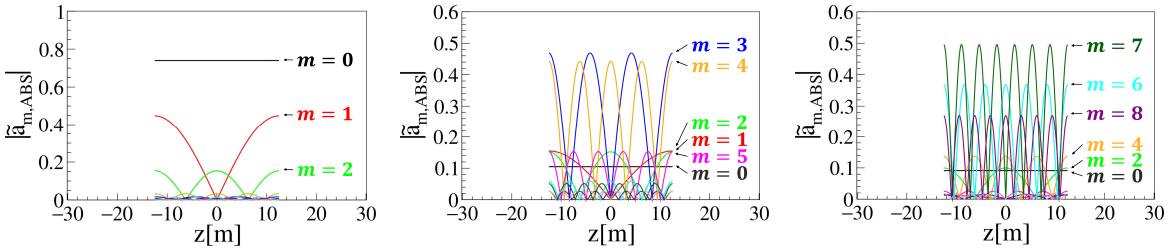

(a) $\xi = -1.5$ **(b)** $\xi = -6.5$ **(c)** $\xi = -12.5$

Figure 8.1: Analytical results of relative amplitudes $|\tilde{a}_{m,\rm ABS}(z)|$ calculated by Eq. (5.27) based on the ABS model with weak space charge force. Here, the black, red, green, blue, orange, magenta, cyan, dark green, purple, and gray denote the cases of $m = 0, 1, 2, \cdots 9$, respectively.

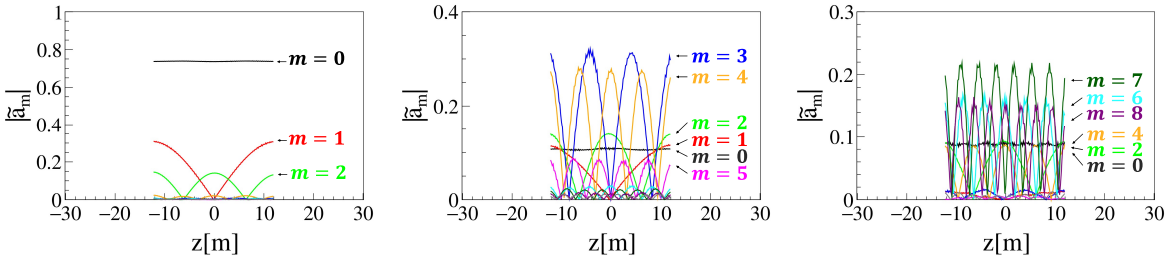

(a) $\xi = -1.5$ **(b)** $\xi = -6.5$ **(c)** $\xi = -12.5$

Figure 8.2: Relative amplitudes $|\tilde{a}_m^{(k)}|$ in tracking simulation based on the ABS model with weak space charge force ($N_B = 1.0\times10^8$ ppb). Here, the black, red, green, blue, orange, magenta, cyan, dark green, purple, and gray denote the cases of $m = 0, 1, 2, \cdots 9$, respectively.

Figure 8.3 shows simulations of the head-tail tune spectra for the ABS model at $N_B = 1.0 \times 10^8$ ppb by scanning the chromaticity from 0 to -15, revealing the higher head-tail modes are enhanced for higher chromaticity, as expected. Equations (8.3) and (8.4) provide a useful guideline for predicting which mode will be excited in the bunch for a given chromaticity.

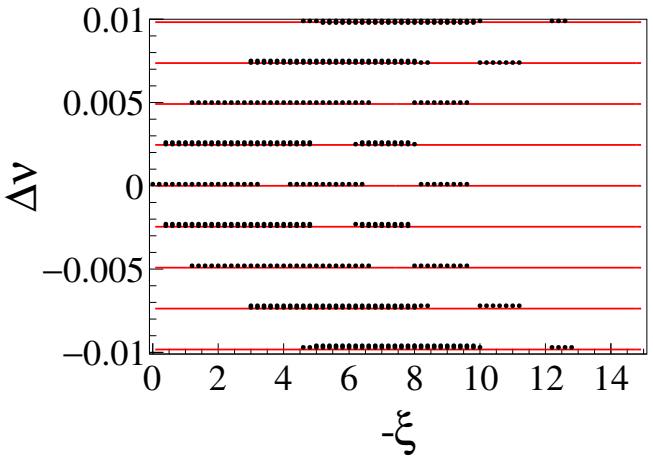

Figure 8.3: Head-tail tune spectra in tracking simulation based on the ABS model with weak space charge force ($N_B = 1.0 \times 10^8$ ppb). The dots indicate only the results for $|a_m| > 0.1$. The red lines represent the frequency shifts calculated by Eq. (5.17) for each head-tail mode in the range of $-4 \leq m \leq 4$.

Figure 8.4b represents the simulations of the relative amplitude $|a_m|$ for the entire bunch in the case of $N_B = 1.0 \times 10^8$ ppb, which are compared with the theoretical results (Eq. (5.36)) in Fig. 8.4a. The theoretical results fairly reproduce the tracking simulations for $N_B = 1.0 \times 10^8$ ppb, backing the reliability of the code with the weak space charge effects. The reduction in the peak value observed in the simulations at higher chromaticity, compared to theoretical results, is caused by the tune spread within the bunch.

8.1.2 Without Indirect Space Charge Force

This subsection deals with the high-intensity cases based on the ABS model without indirect space charge forces ($\Delta\nu_{\mathrm{coh}} = 0$). Equation (5.17) theoretically suggests that the frequency differences identified by the head-tail modes decrease, as the beam intensity increases.

Figure 8.5 represents the simulations illustrating the beam intensity dependence of the tune shift for the respective head-tail modes with fixed chromaticity values of (a) $\xi = -1.5$, (b) $\xi = -6.5$, and (c) $\xi = -12.5$. The red lines represent the frequency shifts calculated by Eq. (5.17) for each head-tail mode from $m = -4$ to 12. The analytical results and the simulations are in good agreement, with the frequency shift degenerating toward high-intensity beams regardless of the chromaticity, following the ABS model, when only the direct space charge effects are taken into account.

Note that Eq. (5.17) suggests that the coherent tune shifts do not depend on the chromaticity. Figure 8.6 shows the simulations of head-tail tune spectra in the ABS

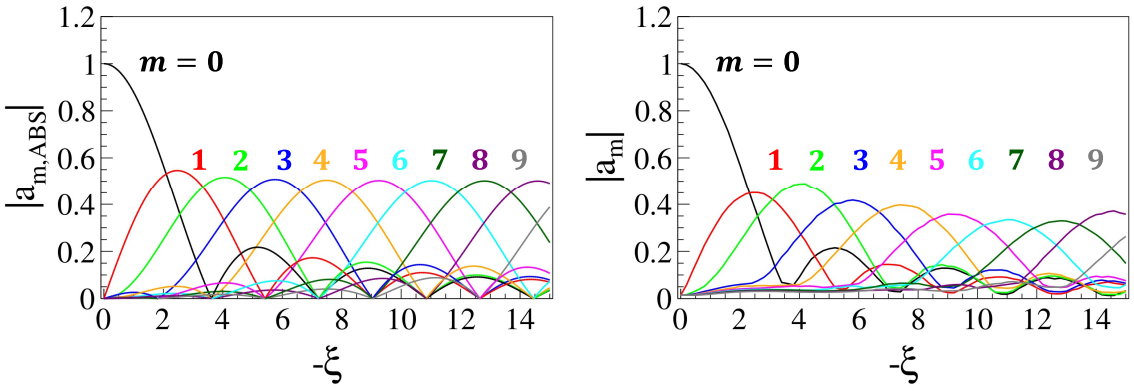

(a) calculated by Eq. (5.36) **(b)** tracking simulation ($N_B = 1.0 \times 10^8$ ppb)

Figure 8.4: Relative amplitudes $|a_m|$ calculated by Eq. (5.36) and tracking simulation based on the ABS model with weak space charge force ($N_B = 1.0 \times 10^8$ ppb). Here, the black, red, green, blue, orange, magenta, cyan, dark green, purple, and gray denote the cases of $m = 0, 1, 2, \cdots 9$, respectively.

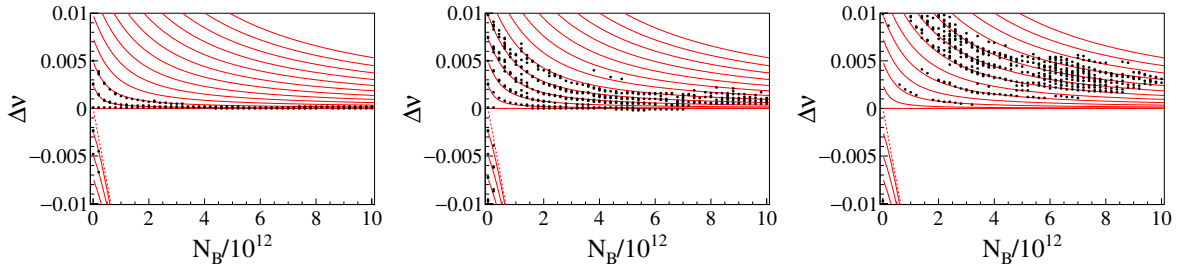

(a) $\xi = -1.5$ **(b)** $\xi = -6.5$ **(c)** $\xi = -12.5$

Figure 8.5: Head-tail tune spectra in the ABS model without indirect space charge effects for various values of chromaticity : (a) $\xi = -1.5$, (b) $\xi = -6.5$, and (c) $\xi = -12.5$. The dots indicate only the results for $|a_m| > 0.1$. The red lines represent the frequency shifts calculated by Eq. (5.17) for each head-tail mode in the range of $-4 \leq m \leq 12$.

model for various beam intensities, where the analytical results calculated using Eq. (5.17) are superimposed on the horizontal lines, revealing the chromaticity dependence of the excited head-tail modes for (a) $N_B = 4.2 \times 10^{12}$ ppb and (b) $N_B = 8.6 \times 10^{12}$ ppb. The frequency shifts remain fixed for the respective beam intensities, even though the chromaticity changes. We can recognize that the higher modes are more strongly excited as the absolute value of the chromaticity increases similar to the weak space charge beams. For example, only modes 0 to 2 can be observed at $\xi = -1.5$, while the modes 3 to 6 appear to be observable at $\xi = -8.0$. The result indicates that Eqs. (8.3) and (8.4) are still valuable for estimating which mode is excited, even for the high-intensity beams with higher chromaticity, although only positive modes are excited in such cases. This excitation pattern, which is consistent with the previous studies [55, 72–75], is reasonable because the coherent tune shift ($\Delta\nu_{\mathrm{coh}} = 0$) must occur for the entire bunch in the high-intensity beams due to the space charge effects.

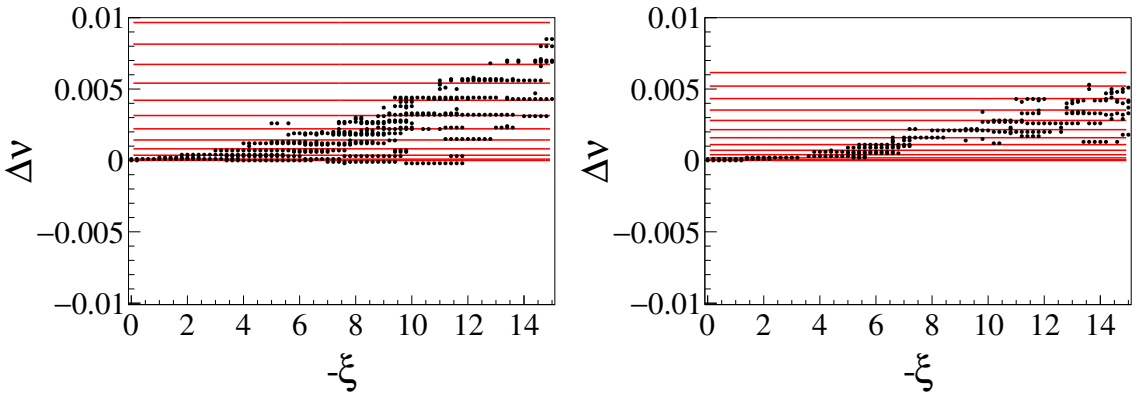

(a) $N_B = 4.2 \times 10^{12}$ ppb **(b)** $N_B = 8.6 \times 10^{12}$ ppb

Figure 8.6: Head-tail tune spectra in the ABS model without indirect space charge effects for various values of intensity : (a) $N_B = 4.2 \times 10^{12}$ ppb and (b) $N_B = 8.6 \times 10^{12}$ ppb. The dots indicate only the results for $|a_m| > 0.1$. The red lines represent the frequency shifts calculated by Eq. (5.17) for each head-tail mode in the range of $0 \leq m \leq 12$.

Figures 8.7a and 8.7b represent the simulations of the relative amplitudes of the entire bunch for $N_B = 4.2 \times 10^{12}$ ppb and 8.6×10^{12} ppb, respectively. In those figures, the black, red, green, blue, orange, magenta, cyan, dark green, dark blue, and gray denote the cases of $m = 0, 1, 2, \cdots 9$, respectively. The comparison between Figs. 8.4 and 8.7 demonstrates that the discrepancy between the theoretical results (which exclude space charge effects) and the simulations becomes more evident as the beam intensity increases, as expected.

Though the frequency shifts converge for the high-intensity beams, making it difficult to distinguish which mode is excited in the simulations, particularly at lower chromaticity where the lower modes are excited, we can identify the excited modes across varying chromaticity, up to the case of $N_B = 4.2 \times 10^{12}$ ppb, where the frequency differences among the respective modes are estimated as Eq. (5.17) for the given beam intensity.

The simulation results demonstrate that the theory accurately predicts the tune shifts because the space charge effects are appropriately considered in the theory, while the

amplitude cannot be done because of the lack of space charge effects. Hence, we conclude that we can evaluate the relative amplitude: a_m, of the respective modes from a theoretical perspective for a beam with $|\Delta\nu_{\text{inc}}| \ll \nu_s$ (refer to Eq. (5.17)). Otherwise, simulation studies are inevitable for an accurate estimate of the beam behaviors.

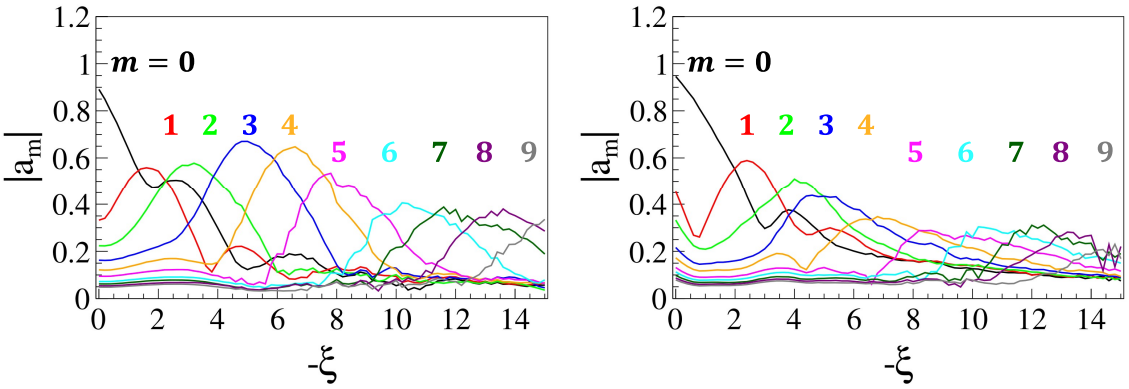

(a) $N_B = 4.2 \times 10^{12}$ ppb **(b)** $N_B = 8.6 \times 10^{12}$ ppb

Figure 8.7: Relative amplitudes $|a_m|$ based on the tracking simulation of the ABS model without indirect space charge effect. Here, the black, red, green, blue, orange, magenta, cyan, dark green, purple, and gray denote the cases of $m = 0, 1, 2, \cdots 9$, respectively.

Up to now, we have dealt with the simulations including the transverse resistive wall impedance discussed in Chapter 5. The simulations suggest that resistive wall impedance does not dominantly affect the intra-bunch motion when no beam instability occurs because some agreement can be observed between the analytical results, which consider only space charge effects, and the simulations that include the wakefield.

To clarify this expectation, let us conduct simulations, neglecting the resistive wall impedance. Figure 8.8 shows the simulation results excluding the wakefield effects for $\xi = -1.5$ and $\xi = -12.5$, which are nearly identical to the results in Figs. 8.5a and 8.5c.

A theoretical estimate of the tune shift due to wakefield offers insight to justify this negligence. The coherent tune shift is given by:

$$\Delta\nu_{\text{coh}} = \Delta\nu_{\text{single}} + \Delta\nu_{\text{multi}} = -0.24 \times 10^{-4} \times N_B/10^{12}, \tag{8.5}$$

where the coherent tune shift for a Gaussian bunch caused by the single-turn wakefield is calculated as

$$\begin{aligned} \Delta\nu_{\text{single}} &= -\mathbf{i}\mathcal{G}\frac{Cec}{16\pi^2\sqrt{\pi}\sigma_z\nu_\beta\beta E_0} N_B Z_{\text{dip,eff}}(\omega_\xi) \\ &= (-0.24 - 0.24\mathbf{i}) \times 10^{-4} \times N_B/10^{12}, \end{aligned} \tag{8.6}$$

and the coherent tune shift of the multi-turn is given by

$$\begin{aligned} \Delta\nu_{\text{multi}} &= -\mathcal{G}\frac{C^2 ec\rho}{4\pi^3\nu_\beta\beta E_0 h_C^3 d_\omega} N_B \sum_{k=1}^{\infty}\sum_{n=0}^{\infty} \exp\left[-\frac{\pi^2\rho k C}{d_\omega^2 Z_0}\left(n+\frac{1}{2}\right)^2 - \mathbf{i}2\pi k\nu_\beta\right] \\ &= (0.016 + 0.018\mathbf{i}) \times 10^{-4} \times N_B/10^{12}, \end{aligned} \tag{8.7}$$

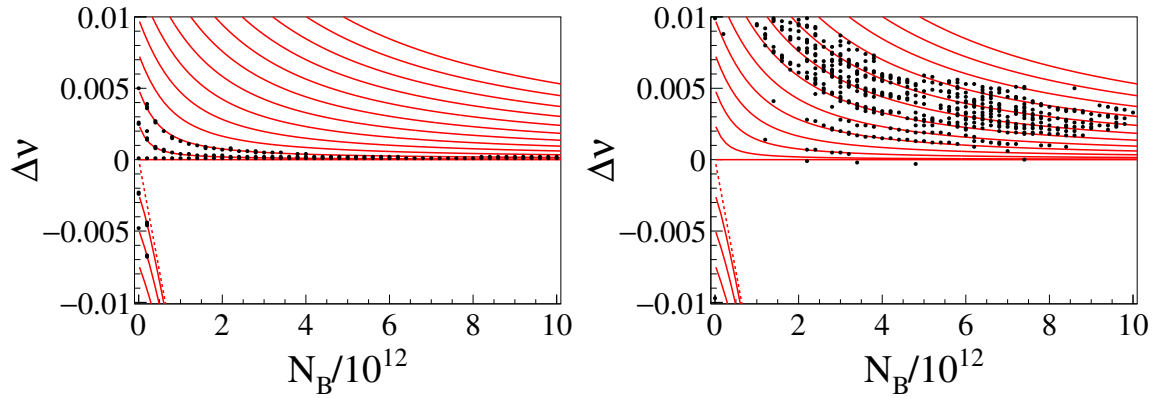

(a) $\xi = -1.5$ **(b)** $\xi = -12.5$

Figure 8.8: Head-tail tune spectra in the ABS model without either indirect space charge effect or transverse wakefield for (a) $\xi = -1.5$ and (b) $\xi = -12.5$. The dots indicate only the results for $|a_m| > 0.1$. The red lines represent the frequency shifts calculated by Eq. (5.17) for each head-tail mode in the range of $-4 \leq m \leq 12$.

with

$$Z_{\mathrm{dip,eff}}(\omega) = \frac{\sum_{p=-\infty}^{\infty} Z_{\mathrm{T1}}^{D}((p+\nu_\beta)\omega_0) h_0((p+\nu_\beta)\omega_0 - \omega)}{\sum_{p=-\infty}^{\infty} h_0((p+\nu_\beta)\omega_0 - \omega)}, \tag{8.8}$$

$$Z_{\mathrm{T1}}^{D}(\omega) = Z_0(\mathrm{sgn}(\omega) - \mathbf{i}) \tanh\left(\sqrt{2\mathbf{i}}\frac{d_\omega}{\delta_{\mathrm{skin}}}\right) \frac{L}{2\pi h_C^3}\delta_{\mathrm{skin}}, \tag{8.9}$$

$\omega_\xi = \omega_0\xi/\eta$ (the definition of chromaticity in Ref. [61] differs from the one used in this thesis), $h_0(\omega) = \exp(-\omega^2\sigma_z^2/c^2)$, and $\delta_{\mathrm{skin}} = \sqrt{2c\rho/Z_0|\omega|}$ [67].

When the resistive wall wakefield from Eq. (6.27) is used as the input parameter, Eq. (8.5) yields a value two orders of magnitude smaller than Eq. (8.2). Thus, we conclude that the theory, accounting only for the direct space charge effect, accurately explains the simulations for the ABS model with resistive wall impedance of the MR, provided no beam instability is triggered and the wakefield-induced tune shift is negligibly smaller than that caused by the space charge forces within the bunch.

8.1.3 With Indirect Space Charge Force

Next, let us include the indirect space charge effects in the ABS model. Figure 8.9 illustrates the excited frequency modes for the same set of chromaticity as in Fig. 8.5, where the analytical lines given by Eq. (5.17) are overwritten from $m = -4$ to 12. We find that the indirect space charge effects cause the significant deformations in the tune shifts of the high-intensity beams. Similar to the case with only the direct space charge considered, as the beam intensity increases, the frequency shifts excited by the respective head-tail modes become degenerate. However, the indirect space charge effect mitigates the mode degeneration of the tune shifts, making it more discernible, as explained by the analytical results in Eq. (5.17). Though only positive modes are excited in the high-intensity beams, this phenomenon is consistent with the previous simulations only including the direct space charge effect because the finite coherent tune shift ($\Delta\nu_{\mathrm{coh}} \neq 0$) must occur for the

entire bunch due to the indirect space charge effect. Even when the indirect space charge is included in simulations, the frequency shift due to the head-tail mode can be sufficiently explained by the theoretical ABS model including the space charge effects.

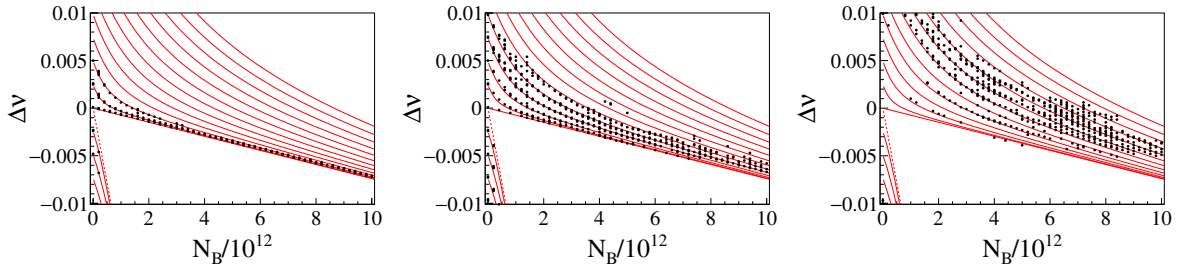

(a) $\xi = -1.5$ **(b)** $\xi = -6.5$ **(c)** $\xi = -12.5$

Figure 8.9: Head-tail tune spectra in the ABS model with indirect space charge effect in addition to the direct space charge effects and the wakefield for various values of chromaticity : (a) $\xi = -1.5$, (b) $\xi = -6.5$, and (c) $\xi = -12.5$. The dots indicate only the results for $|a_m| > 0.1$. The red lines represent the frequency shifts calculated by Eq. (5.17) for each head-tail mode in the range of $-4 \leq m \leq 12$.

As for the chromaticity dependence, Fig. 8.10 illustrates the higher modes can be excited, by increasing the absolute value of the chromaticity, similar to the case, as shown in Fig. 8.5. For reference, the analytical results calculated using Eq. (5.17) are superimposed on the horizontal lines. We can confirm the theoretical prediction that the chromaticity dependence of the tune shift is negligible, even when the indirect space charge effect is considered.

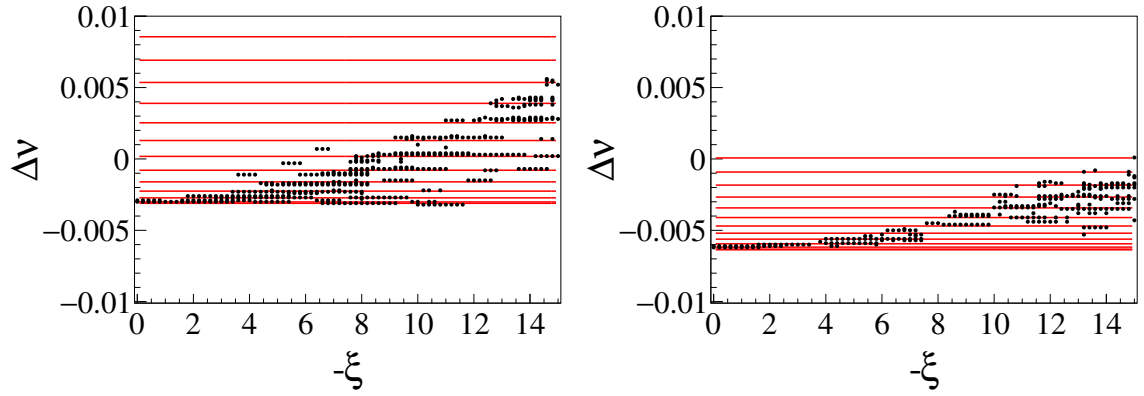

(a) $N_B = 4.2 \times 10^{12}$ ppb **(b)** $N_B = 8.6 \times 10^{12}$ ppb

Figure 8.10: Head-tail tune spectra in the ABS model with indirect space charge effect in addition to the direct space charge effects and the wakefield for various values of intensity : (a) $N_B = 4.2 \times 10^{12}$ ppb and (b) $N_B = 8.6 \times 10^{12}$ ppb. The dots indicate only the results for $|a_m| > 0.1$. The red lines represent the frequency shifts calculated by Eq. (5.17) for each head-tail mode in the range of $0 \leq m \leq 12$.

Similarly to the previous case, let us calculate the relative amplitude of the entire bunch. Figure 8.11 shows the results, including the indirect space charge effect as well as the

direct space charge effect. Compared to Fig. 8.7, which accounts only for the direct space charge effect, there are few noticeable differences between the two. This suggests that when the linear approximations are valid for describing space charge effects, where the chamber radius is significantly larger than the transverse beam size, the relative amplitude remains unaffected by the indirect space charge force.

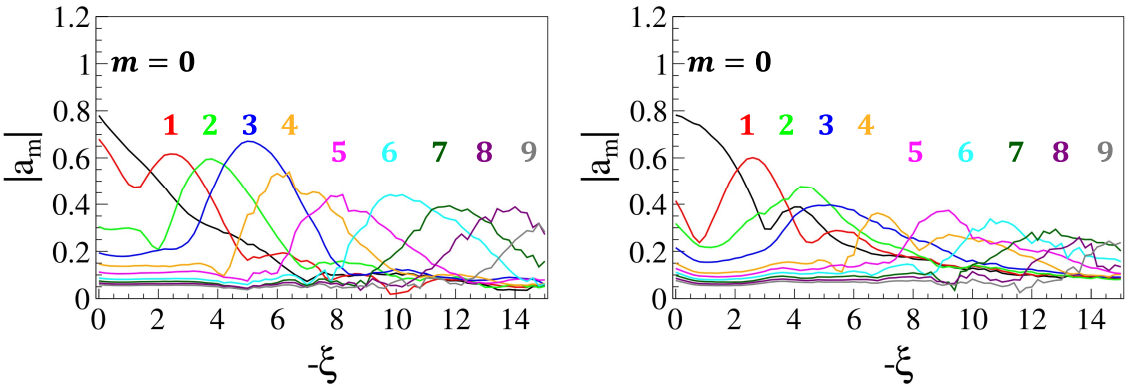

(a) $N_B = 4.2 \times 10^{12}$ ppb **(b)** $N_B = 8.6 \times 10^{12}$ ppb

Figure 8.11: Relative amplitudes $|a_m|$ derived from the tracking simulation of the ABS model with the indirect and direct space charge effects as well as the wakefield effects. Here, the black, red, green, blue, orange, magenta, cyan, dark green, purple, and gray denote the cases of $m = 0, 1, 2, \cdots 9$, respectively.

In conclusion, the theory based on the ABS model predicts the tune shifts, the chromaticity dependence of the spectrum, and the detection of enhancement of modes (but partially) for specified chromaticities in the high-intensity beams where space charge effects are significant, provided the transverse beam size is much smaller than the chamber radius.

The theoretical results, which account for the weak space charge effects, predict the relative amplitude of the entire bunch when $|\Delta\nu_{\text{inc}}| \ll \nu_s$. However, for the high-intensity beams where $|\Delta\nu_{\text{inc}}| > \nu_s$, numerical simulations are necessary to obtain accurate results including the space charge forces.

8.2 Analysis of Gaussian Bunch

8.2.1 Weak Space Charge Force

To cope with a more realistic case, we start focusing on tracking simulations within a Gaussian bunch with weak space charge force under the harmonic potential model and analyze them in the same way as the ABS model.

Figure 8.12 shows the relative amplitude $|\tilde{a}_{m,b}(z)|$ calculated by Eq. (5.58) for various chromaticity ξ. Meanwhile, Fig. 8.13 shows the relative amplitude $|\tilde{a}_m^{(k)}|$ in each segment derived from the tracking simulation with the low-intensity $N_B = 1.0 \times 10^8$ ppb. In those figures, the black, red, green, blue, orange, magenta, cyan, dark green, purple, and gray denote the cases of $m = 0, 1, 2, \cdots 9$, respectively.

We observe that the oscillation amplitudes vary sharply with higher chromaticity for the respective head-tail modes in both the analytical and simulation results. This behavior can be readily understood by modifying Eq. (5.58) as

$$\tilde{a}_{m,b}(z) \simeq \exp\left(\mathbf{i}\chi_\sigma \frac{z}{\sigma_z}\right)(-\mathbf{i})^m \exp\left(-\frac{\chi_\sigma^2}{4}\right) I_{\frac{m}{2}}\left(\frac{\chi_\sigma^2}{4}\right) \cos\left(\chi_\sigma \frac{z}{\sigma_z} - m\frac{\pi}{2}\right), \tag{8.10}$$

as it highlights $|\tilde{a}_{m,b}(z)| \propto |\cos(\chi_\sigma z/\sigma_z - m\pi/2)|$, indicating that the oscillation frequency becomes more pronounced for a fixed head-tail mode as chromaticity increases through χ_σ.

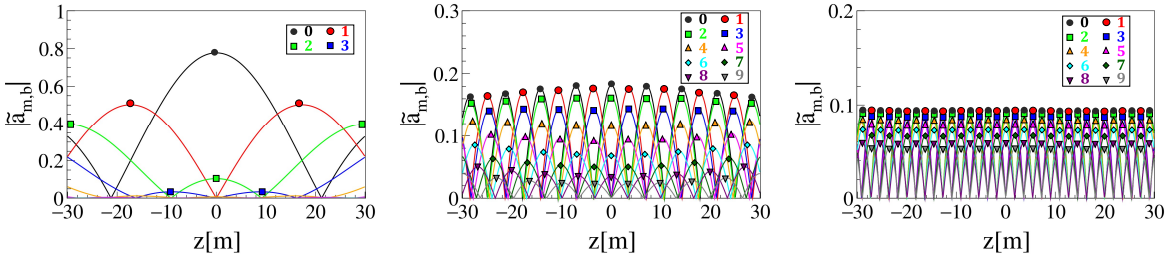

(a) $\xi = -1.5$ **(b)** $\xi = -6.5$ **(c)** $\xi = -12.5$

Figure 8.12: Relative amplitudes $|\tilde{a}_{m,b}(z)|$ calculated by Eq. (5.58) based on the harmonic potential model with weak space charge force. Here, the black, red, green, blue, orange, magenta, cyan, dark green, purple, and gray denote the cases of $m = 0, 1, 2, \cdots 9$, respectively.

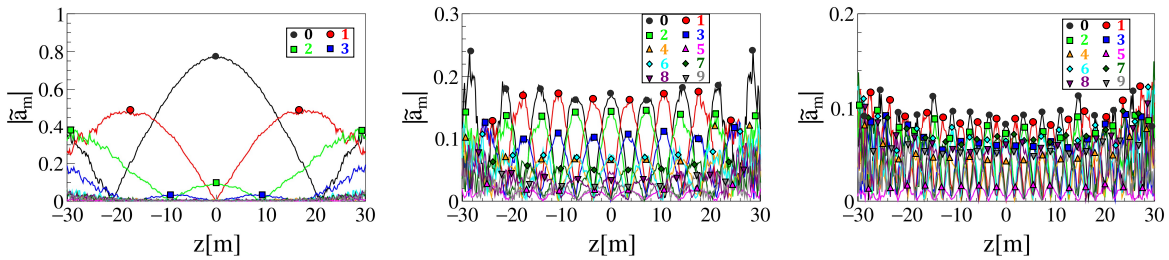

(a) $\xi = -1.5$ **(b)** $\xi = -6.5$ **(c)** $\xi = -12.5$

Figure 8.13: Relative amplitudes $|\tilde{a}_m^{(k)}|$ in tracking simulation based on the harmonic potential model with weak space charge forces. Here, the black, red, green, blue, orange, magenta, cyan, dark green, purple, and gray denote the cases of $m = 0, 1, 2, \cdots 9$, respectively.

The close agreement between the theory and the tracking simulation demonstrates the practical usefulness of the theory at the low-intensity. Conversely, it opens a window for investigating the high-intensity beams with strong space charge effects using our simulation tool.

Figure 8.14 represents the head-tail tune spectra of the harmonic potential model at $N_B = 1.0 \times 10^8$ ppb in the chromaticity range of 0 to -15, revealing the chromaticity dependence of the excited head-tail modes. Unlike the ABS model (see Fig. 8.3), all modes are excited even in the high chromaticity region in the Gaussian bunch model.

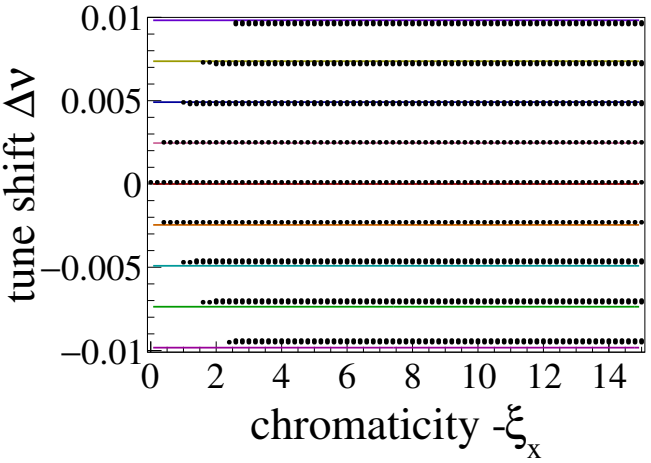

Figure 8.14: Head-tail tune spectra in tracking simulation based on the harmonic potential model with weak space charge force. The dots indicate only the results for $|a_m| > 0.1$. The red lines represent the frequency shifts calculated by Eq. (5.17) for each head-tail mode in the range of $-4 \leq m \leq 4$.

Figure 8.15 compares the relative amplitude $|a_m|$ of the entire bunch for each mode in the case of $N_B = 1.0 \times 10^8$ ppb simulated by the code, with that calculated using the theory (Eq. (5.61)). The theoretical results fairly reproduce the tracking simulations for $N_B = 1.0 \times 10^8$ ppb because the relative amplitude is derived by assuming the space charge effects is negligible. Compared to Fig. 8.4, it is evident that all modes are excited in the higher chromaticity regions for the low-intensity beams, and the specific mode enhancement dependence on the chromaticity disappears in the Gaussian model, which is consistent with the results in Fig. 8.14.

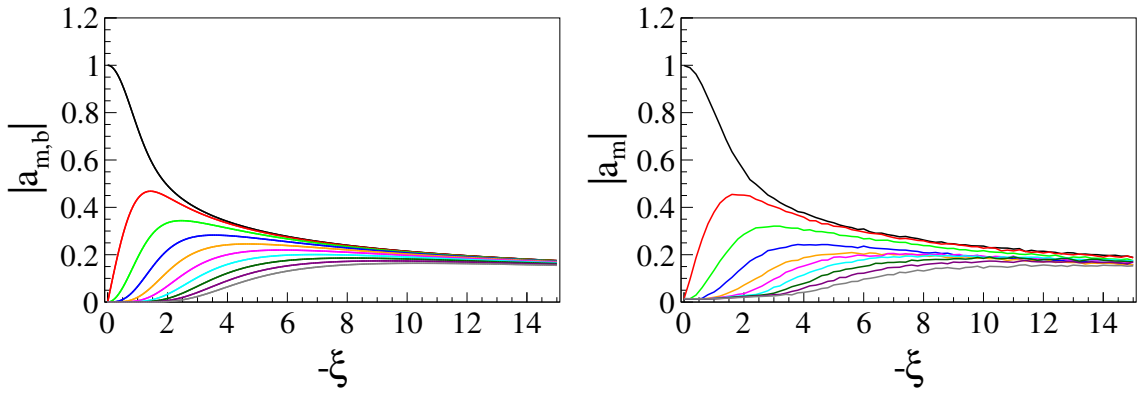

(a) calculated by Eq. (5.61) **(b)** tracking simulation ($N_B = 1.0 \times 10^8$ ppb)

Figure 8.15: Relative amplitudes $|a_m|$ calculated by Eq. (5.61) and tracking simulation of the harmonic potential model with weak space charge forces. Here, the black, red, green, blue, orange, magenta, cyan, dark green, purple, and gray denote the cases of $m = 0, 1, 2, \cdots 9$, respectively.

8.2.2 Without Indirect Space Charge Force

Next, we focus on tracking simulations of Gaussian beams within the harmonic potential model, only including the direct space charge effect. Figure 8.16 shows the simulations for the same set of chromaticity as in Fig. 8.5 with the ABS model. The theoretical results calculated using the ABS model: Eq. (5.17), with the average current matched to the peak current of the Gaussian bunch, are superimposed as solid lines. As a result, it is confirmed that the ABS model can accurately describe the tune shift of the harmonic potential.

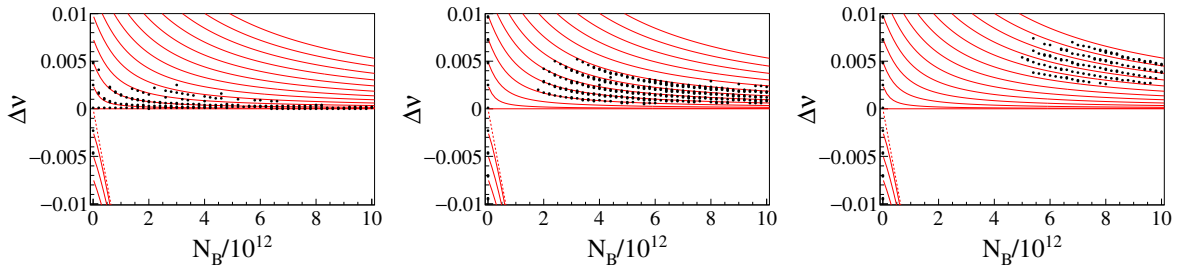

(a) $\xi = -1.5$ **(b)** $\xi = -6.5$ **(c)** $\xi = -12.5$

Figure 8.16: Head-tail tune spectra in the harmonic potential model without indirect space charge effect for various values of chromaticity : (a) $\xi = -1.5$, (b) $\xi = -6.5$, and (c) $\xi = -12.5$. The dots indicate only the results for $|a_m| > 0.1$. The red lines represent the frequency shifts calculated by Eq. (5.17) for each head-tail mode in the range of $-4 \leq m \leq 12$.

Figure 8.17 shows the chromaticity dependence of the excited intra-bunch modes for the cases of (a) $N_B = 4.2 \times 10^{12}$ ppb and (b) $N_B = 8.6 \times 10^{12}$ ppb. For reference, the analytical results calculated using Eq. (5.17) are superimposed on the horizontal lines. The tune shift shows no chromaticity dependence, a feature also observed in the ABS depicted in Fig. 8.6. This behavior carries over to the Gaussian beam in a harmonic potential when the indirect space charge effect is disregarded. However, it is noteworthy that the excited modes are influenced by the choice of chromaticity for the high-intensity beams, contrary to the Gaussian beam with weak space charge forces. For example, only modes 0 to 3 can be excited at $\xi = -1.5$. On the other hand, the modes 4 to 9 appear to be observable at $\xi = -8.0$.

Figure 8.18 illustrates the relative amplitudes $|a_m|$ obtained by the tracking simulation, in which the harmonic potential model is implemented with the indirect space charge effect disregarded. When the beam intensity is $N_B = 8.6 \times 10^{12}$ ppb (as in Fig. 8.18b), the lower modes are degenerate, and the correct relative amplitudes for $m = 1, 2$ could not be obtained in the low chromaticity from the tracking simulation due to insufficient tune resolution. The comparison with the corresponding results for the ABS model, excluding the indirect space charge effects (see Fig. 8.7), shows that the excited modes tend to shift to lower chromaticity values following Eq. (5.61), although the excitation pattern along the chromaticity remains almost the same between the two cases. This demonstrates the limitations of the ABS model in describing the Gaussian beam. Furthermore, while there are no peaks for the respective modes along the chromaticity axis in the weak space charge beam (refer to Fig. 8.15), peaks begin to appear as the space charge effect strengthens.

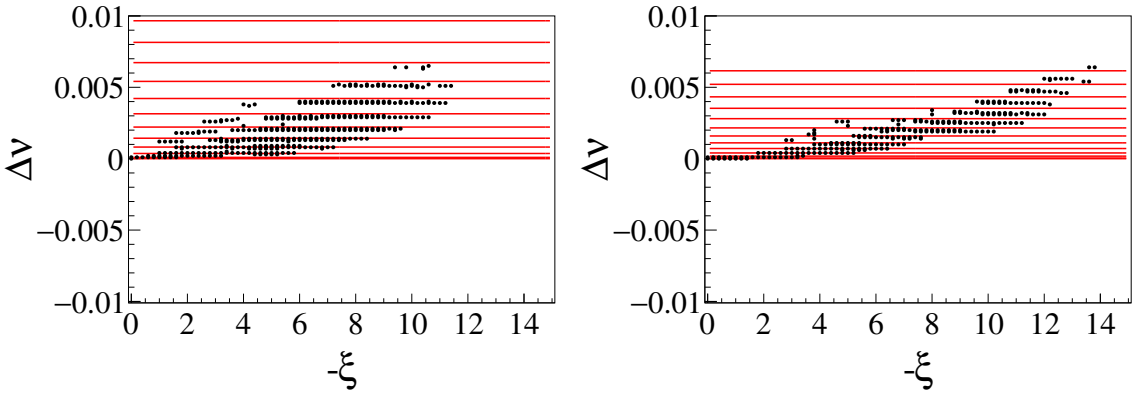

(a) $N_B = 4.2 \times 10^{12}$ ppb **(b)** $N_B = 8.6 \times 10^{12}$ ppb

Figure 8.17: Head-tail tune spectra in the harmonic potential model without indirect space charge effect for various values of intensity : (a) $N_B = 4.2 \times 10^{12}$ ppb and (b) $N_B = 8.6 \times 10^{12}$ ppb. The dots indicate only the results for $|a_m| > 0.1$. The red lines represent the frequency shifts calculated by Eq. (5.17) for each head-tail mode in the range of $0 \leq m \leq 12$.

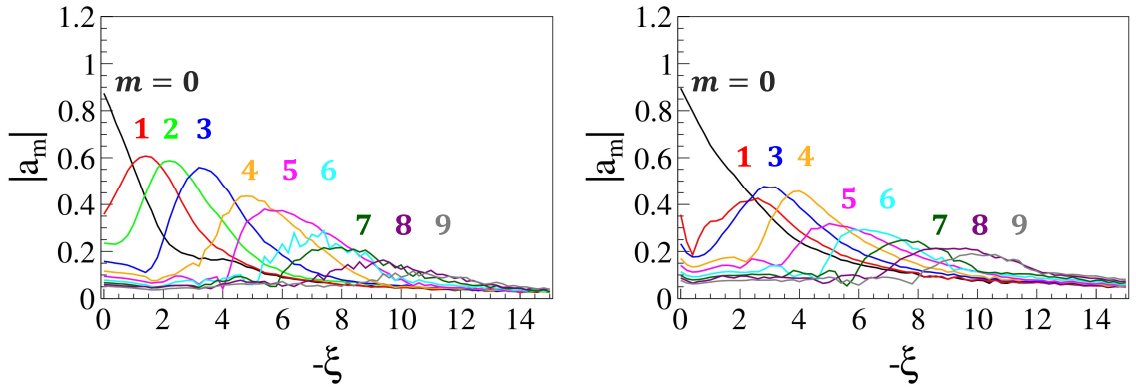

(a) $N_B = 4.2 \times 10^{12}$ ppb **(b)** $N_B = 8.6 \times 10^{12}$ ppb ($m = 1, 2$ is degenerated and only $m = 1$ is shown)

Figure 8.18: Relative amplitudes $|a_m|$ tracking simulation of the harmonic potential model without indirect space charge effect. Here, the black, red, (green,) blue, orange, magenta, cyan, dark green, purple, and gray denote the cases of $m = 0, 1, (2,)3, \cdots 9$, respectively.

Similar to the ABS model, let us compare the theoretical results from Eq. (5.17) with the simulations in the harmonic potential for $\xi = -1.5$ and $\xi = -12.5$. The results are shown in Fig. 8.19. The theoretical results dealing with only the direct space charge effects in the ABS model explain the tune shift up to $N_B = 1.0 \times 10^{13}$ ppb when no instability occurs and the tune shift due to transverse wakefield is negligible.

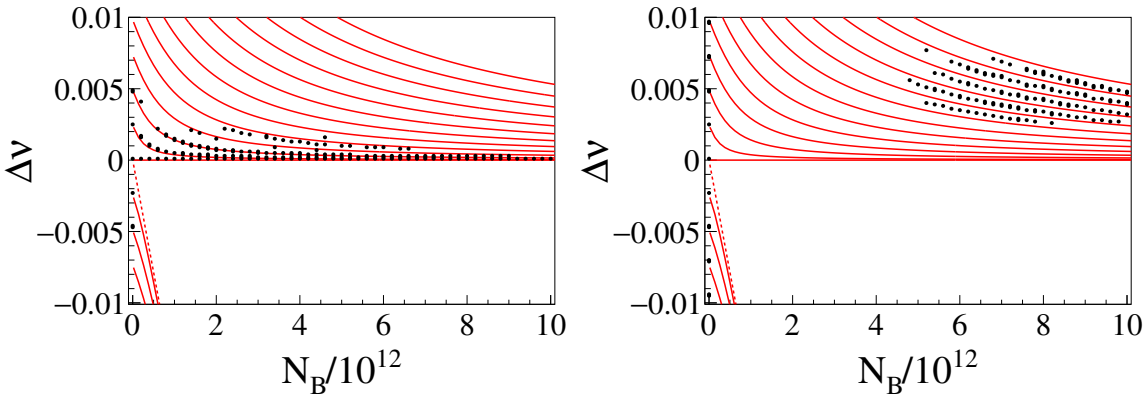

(a) $\xi = -1.5$ **(b)** $\xi = -12.5$

Figure 8.19: Head-tail tune spectra in the harmonic potential model without indirect space charge effect and without transverse wakefield for various values of chromaticity : (a) $\xi = -1.5$ and (b) $\xi = -12.5$. The dots indicate only the results for $|a_m| > 0.1$. The red lines represent the frequency shifts calculated by Eq. (5.17) for each head-tail mode in the range of $-4 \leq m \leq 12$.

8.2.3 With Indirect Space Charge Force

Now, let us consider the Gaussian beam, including all space charge forces. Figure 8.20 shows the intensity dependence of the excited frequency shifts in the bunch for the same set of chromaticity values (ξ) as shown in Fig. 8.9, where the analytical results of Eq. (5.17), based on the ABS model, are superimposed. The indirect space charge effects cause even higher-order head-tail modes to become well separated in the high-intensity beams, even when the chromaticity is large, as observed in the ABS model. However, the degree of separation and the removal of degeneracy in the head-tail modes differ between the Gaussian beam and the ABS model from a quantitative point of view.

The overall behavior of the intensity dependence of the tune shifts can be understood using Eq. (5.17), which incorporates all space charge effects. However, achieving an exact fit with the simulation for the Gaussian bunch model is not expected because the analytical Eq. (5.17) is based on the ABS model, and we need to rely on simulation studies.

Figure 8.21 illustrates the chromaticity dependence of the mode-dependent tune shifts for the high-intensity beams, particularly for (a) $N_B = 4.2 \times 10^{12}$ ppb and (b) $N_B = 8.6 \times 10^{12}$ ppb. The analytical results from Eq. (5.17) are overlaid on the lines in the figures. As shown in Fig. 8.21, the chromaticity dependence of the tune shifts diminishes for the respective beam intensities, as was already observed in Fig. 8.10 for the ABS model cases. Furthermore, we can identify the excitation of specific head-tail modes depending

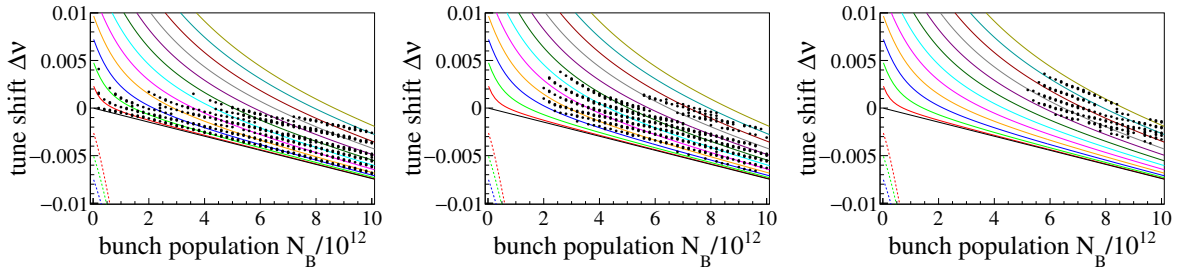

(a) $\xi = -1.5$ **(b)** $\xi = -6.5$ **(c)** $\xi = -12.5$

Figure 8.20: Head-tail tune spectra in the harmonic potential model with indirect space charge effect for various values of chromaticity : (a) $\xi = -1.5$, (b) $\xi = -6.5$, and (c) $\xi = -12.5$. The dots indicate only the results for $|a_m| > 0.1$. The red lines represent the frequency shifts calculated by Eq. (5.17) for each head-tail mode in the range of $-4 \leq m \leq 12$.

on the chromaticity. For example, only modes $m = 0$ to 5 are observable at $\xi = -1.5$, while modes $m = 4$ to 8 appear at $\xi = -8.0$.

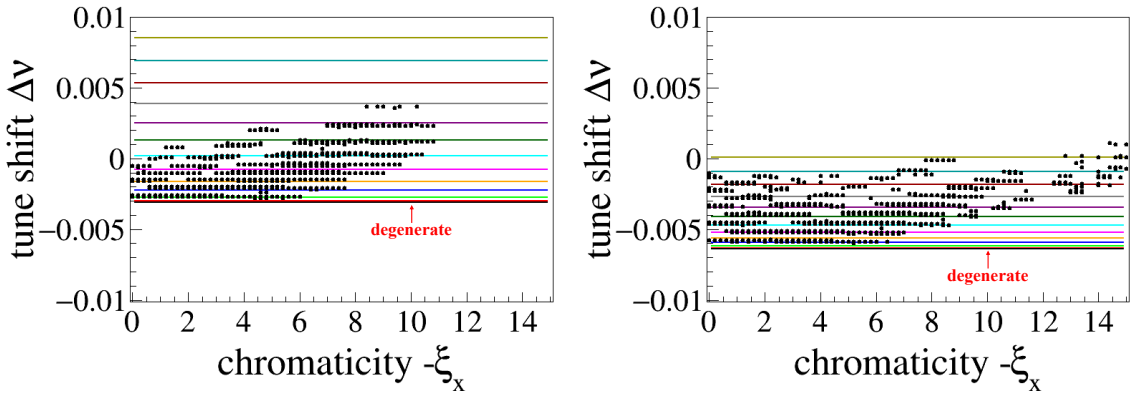

(a) $N_B = 4.2 \times 10^{12}$ ppb **(b)** $N_B = 8.6 \times 10^{12}$ ppb

Figure 8.21: Head-tail tune spectra in the harmonic potential model with indirect space charge effect for various values of intensity : (a) $N_B = 4.2 \times 10^{12}$ ppb and (b) $N_B = 8.6 \times 10^{12}$ ppb. The dots indicate only the results for $|a_m| > 0.1$. The red lines represent the frequency shifts calculated by Eq. (5.17) for each head-tail mode in the range of $0 \leq m \leq 12$.

Figure 8.22 depicts the simulations of the relative amplitudes for the respective head-tail modes for the cases of (a) $N_B = 4.2 \times 10^{12}$ ppb and (b) $N_B = 8.6 \times 10^{12}$ ppb, respectively. In these figures, the black, red, green, blue, orange, magenta, cyan, dark green, purple, and gray curves represent modes $m = 0, 1, 2, \cdots 9$, respectively. The occurrence of these specific excitations can be attributed to the emergence of peaks along the chromaticity axis for the high-intensity beams, as seen in Fig. 8.22. Similar behavior was also observed in Fig. 8.18, which includes only the direct space charge effects. The effects of the indirect space charge in Gaussian beams do not significantly alter the excitation pattern of the head-tail modes under the given chromaticity conditions, similar to the behavior observed in the ABS model.

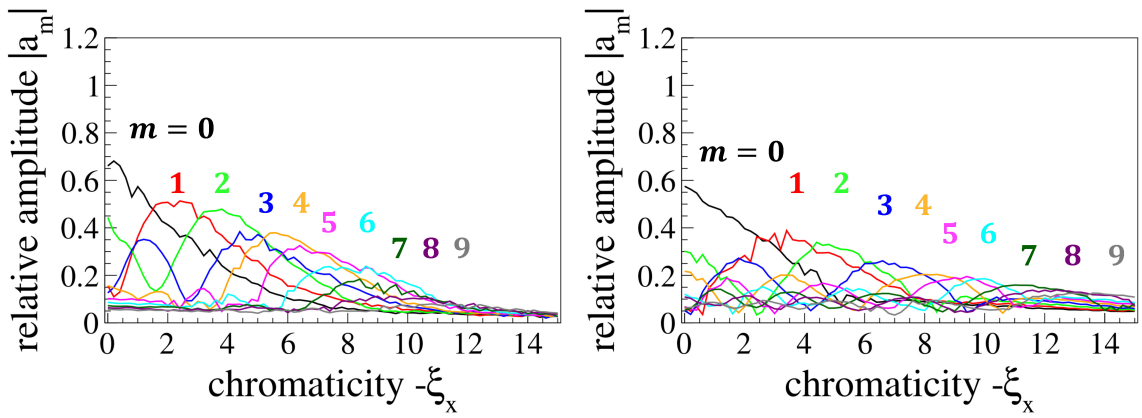

(a) $N_B = 4.2 \times 10^{12}$ ppb **(b)** $N_B = 8.6 \times 10^{12}$ ppb

Figure 8.22: Relative amplitudes $|a_m|$ tracking simulation of the harmonic potential model with indirect space charge effect. Here, the black, red, green, blue, orange, magenta, cyan, dark green, purple, and gray denote the cases of $m = 0, 1, 2, \cdots 9$, respectively.

Finally, Fig. 8.23 summarizes the head-tail frequency shifts from the simulations for four cases: (a) the ABS model without indirect space charge effects, (b) the ABS model including all space charge effects, (c) the harmonic potential model without indirect space charge effects, and (d) the harmonic potential model including all space charge effects.

These figures superimpose the peak positions of each spectrum from Figs. 8.5, 8.9, 8.16, and 8.20 with dots for the chromaticity values $\xi = -1.5, -3.5, -5.5, -6.5, -8.0$, and -12.5, because the frequency shifts due to the head-tail mode are independent of chromaticity, as previously demonstrated. Analytical results from Eq. (5.17) are overlaid in all panels by the solid lines.

The frequency shifts for the harmonic potential model including all space charge effects show the deviations from the analytical results. This discrepancy arises due to the limitations of the current theoretical model, as the formula is derived under the assumption of a square-well potential with an airbag beam, rather than a harmonic potential with a Gaussian bunch.

In conclusion, while Eq. (5.17) provides valuable qualitative insights into the head-tail mode-dependent tune shifts of a high-intensity Gaussian beam, simulation studies are crucial for quantitatively capturing these shifts. This is particularly important for analyzing the impact of the indirect space charge effects on the intensity-dependent tune shifts in the Gaussian beam and the selection of mode excitation patterns, influenced by the direct and indirect space charge effects, under the specified chromaticity.

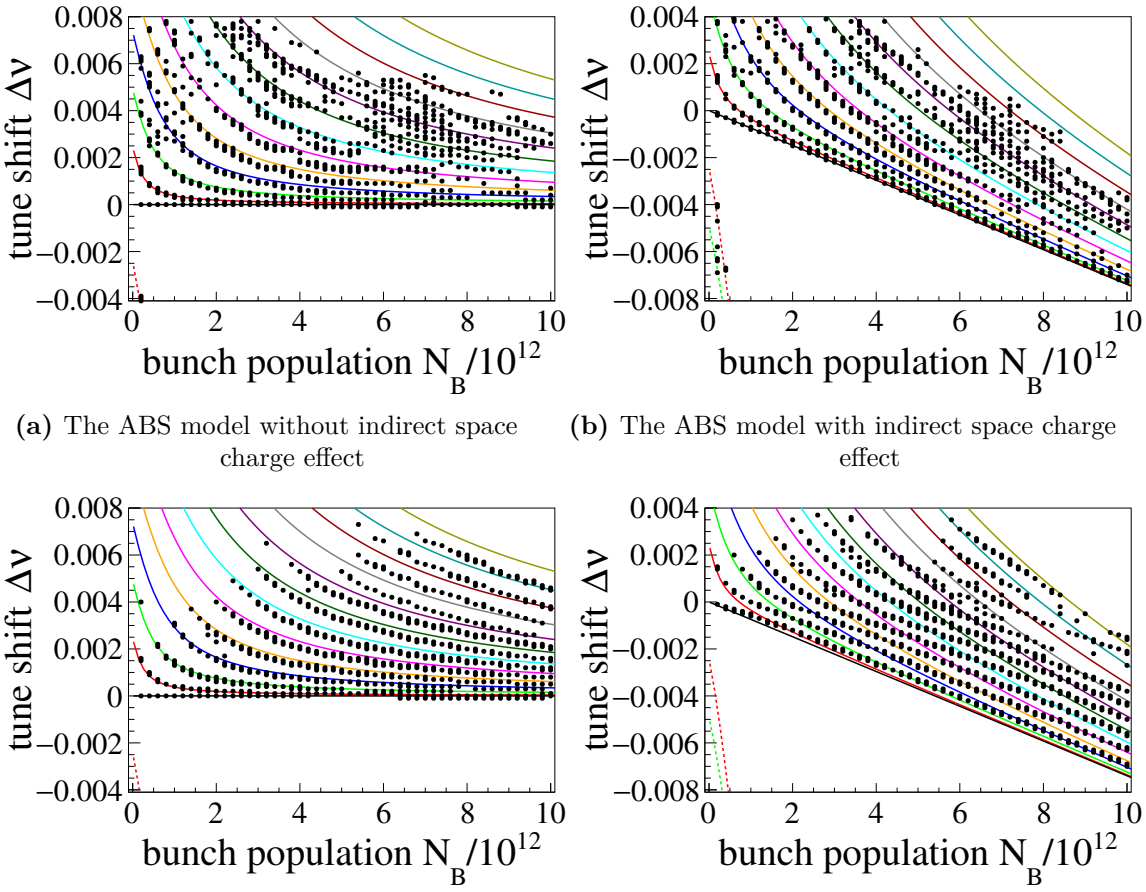

(a) The ABS model without indirect space charge effect

(b) The ABS model with indirect space charge effect

(c) The harmonic potential model without indirect space charge effect

(d) The harmonic potential model with indirect space charge effect

Figure 8.23: The tune shift at which the head-tail tune spectrum reaches its maximum peak in the simulation of the beam intensity parameters in Figs. 8.5, 8.9, 8.16, and 8.20. The dots indicate only the results for $|a_m| > 0.1$. The red lines represent the frequency shifts calculated by Eq. (5.17) for each head-tail mode in the range of $-3 \leq m \leq 12$.

Chapter 9

Comparison with Conventional Study

Up to the previous chapter, we demonstrated through simulations that the head-tail tune shifts are well described by the extended ABS theory in a regime with strong space charge unless beam instabilities are excited. However, for the realistic Gaussian beam, as explained in Sec. 3.5.3, the radial modes may play a crucial role in the beam instabilities such as the TMCI . It is therefore necessary to verify whether our simulation code properly handles these modes. To address this, we perform supplemental simulations in the beam instability regime.

First, to identify the radial modes by comparing the simulations with the theoretical results, we simulate a case where the space charge effect is turned off, leaving only the transverse wakefield, because the theoretical approach is already established in this simplest case. The theoretical results are obtained by using DELPHI [76, 77], a well-established transverse Vlasov solver, with the assumption of the resistive wall impedance given by Eq. (8.9) as its input parameter. The detailed derivation of the Sacherer's integral equation is provided in Appendix C.

The simulations are performed up to the high-intensity beam ($N_B \leq 50 \times 10^{12}$ ppb) to clearly excite the radial modes n_r. Figure 9.1a shows the tune spectra obtained from our simulation and the theoretical outcome for the wakefield-only case with zero chromaticity ($\xi_x = 0$). Black bullet dots denote the simulation results, while the solid and dashed lines represent the theoretical results with the Vlasov solver. The solid lines represent modes with $n_r = 0$, and the dashed lines represent modes with $n_r = 1$. The magenta, green, cyan, orange, red, pink, blue, yellow, and purple denote the outcomes with $m = -4, -3, -2, -1, 0, 1, 2, 3$, and 4, respectively. The simulations reveal that only the head-tail modes $-1 \leq m \leq 1$ are excited in this case. However, as the beam intensity increases, $(m = 0, n_r = 1)$ mode separates from $(m = 0, n_r = 0)$ mode and become identifiable. Furthermore, at a bunch population of $N_B = 28 \times 10^{12}$ ppb, the coupling of $(m = 0, n_r = 0)$ and $(m = -1, n_r = 0)$ modes leads to TMCI. The instability threshold observed in our simulation matches that predicted by the DELPHI. This demonstrates that our simulation code fully reproduces the dynamics of the radial modes.

Figure 9.1b illustrates the case when a large chromaticity ($\xi_x = -8.0$) was introduced to stabilize the beam, where the labeling is the same as in Fig. 9.1a. The simulations reproduce the results by DELPHI, all radial modes are degenerate and merge with the primary head-tail modes, which is consistent with the previous simulations. This indicates that the radial modes no longer play a crucial role in the large chromaticity region where no beam instability is excited.

Having confirmed the code's credibility concerning the wakefield, we then transition to the more physical regime by reintroducing both the direct and indirect space charge effects with the same transverse wakefield. The tune spectrum is shown in Fig. 9.2, with the

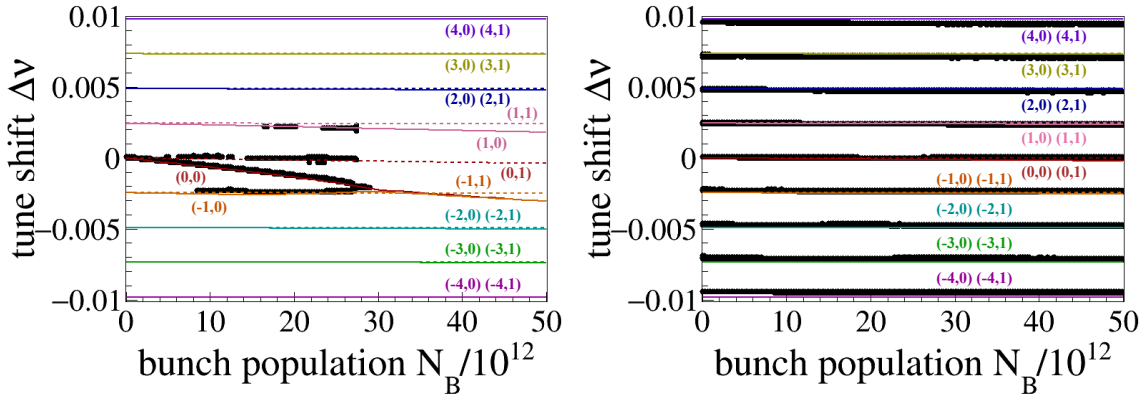

(a) Chromaticity $\xi_x = 0$ **(b)** Chromaticity $\xi_x = -8.0$

Figure 9.1: The tune shift at which the tune spectrum reaches its maximum peak in the simulation with only the transverse wakefield and without space charge effects, compared with the results from the DELPHI Vlasov solver. The pair of numbers on the lines describes the excited mode indices (m, n_r).

contribution from Eq. (8.2) eliminated to clearly show the excitation modes. The higher head-tail modes with $m \geq 0$ are more excited compared to the results in Figs. 9.1a and 9.1b regardless of the choice of chromaticity, with the degeneracy of the radial modes maintained in the case of $\xi_x = -8.0$ (Fig. 9.2b). The spectrum in Fig. 9.2a does not show the clear bifurcation signature of the radial and the head-tail modes, neither TMCI as identified in Fig. 9.1a, indicating the beam instability is suppressed even in the case of $\xi_x = 0$.

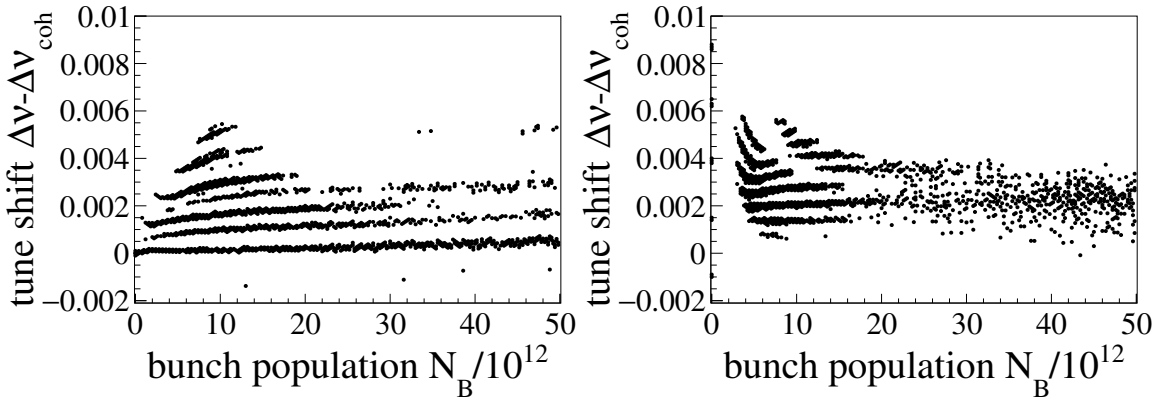

(a) Chromaticity $\xi_x = 0$ **(b)** Chromaticity $\xi_x = -8.0$

Figure 9.2: The tune shift at which the tune spectrum reaches its maximum peak in the simulation with the transverse wakefield, the direct and indirect space charge effects.

Let us examine how the suppression of radial and negative head-tail modes occurs by intentionally changing the ratio, r, of the space charge strength to the wakefield strength, by scaling the horizontal space charge kick (Eq. (6.40)) by a factor r, considering the case of $\xi_x = 0$. The results are shown in Fig. 9.3, where the $(m = 0, n_r = 0)$ mode is

represented by the red bullet. We observe that the higher radial modes and negative head-tail modes gradually disappear as the ratio r (space charge strength) increases, and the higher head-tail modes become more enhanced because they are space charge intrinsic modes explained by the extended ABS theory. This demonstrates that the space charge suppresses TMCI between $(m = 0, n_r = 0)$ and $(m = -1, n_r = 0)$ at $\xi_x = 0$ in Fig. 9.1a by suppressing the negative head-tail modes.

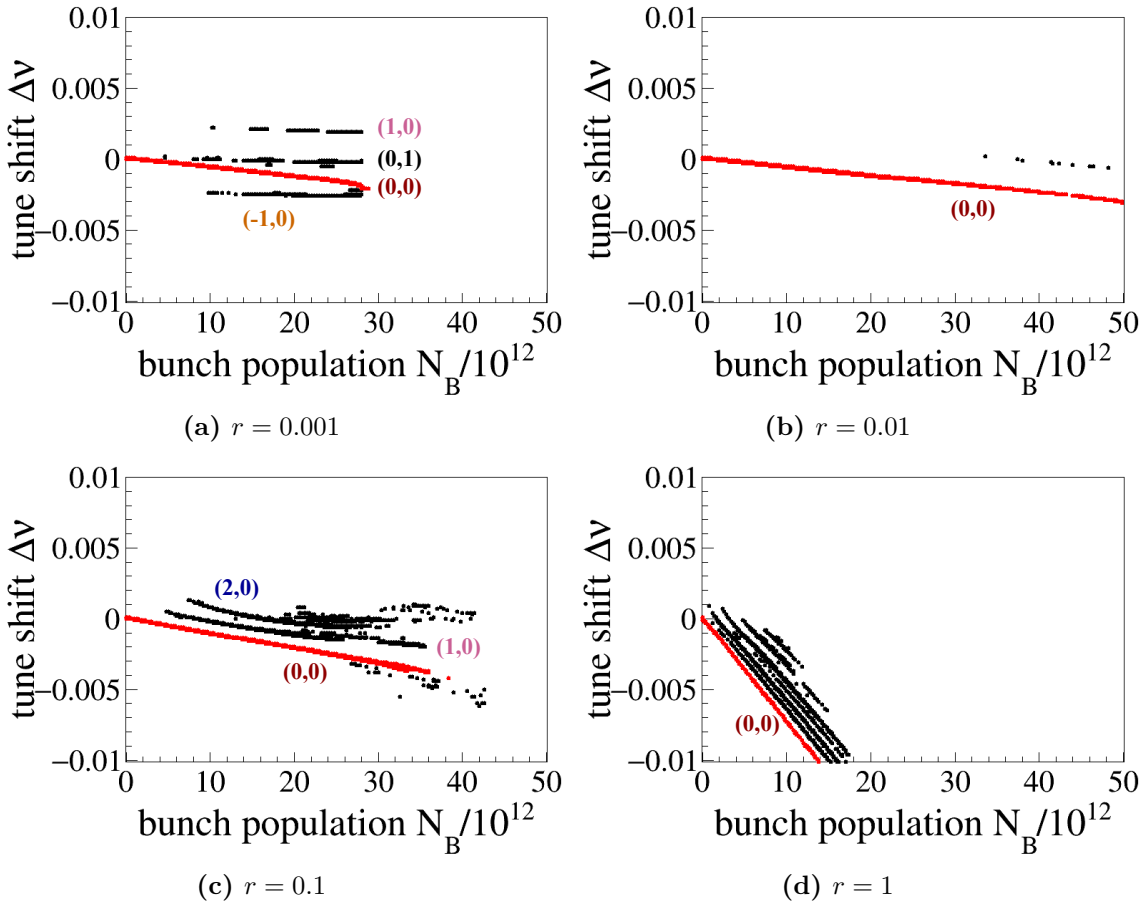

(a) $r = 0.001$ **(b)** $r = 0.01$

(c) $r = 0.1$ **(d)** $r = 1$

Figure 9.3: The tune shift at which the tune spectrum reaches its maximum peak in the simulation with $\xi_x = 0$. The pair of numbers describes the excited mode indices (m, n_r).

Figure 9.4 presents the results with only wakefield effects, wakefield and direct space charge effects, and wakefield with direct and indirect space charge effects, respectively. The simulation reveals that the growth rate with both direct and indirect space charge and wakefield effects (Fig. 9.4c) is milder than that in the case including only wakefield effects (Fig. 9.4a), demonstrating the damping effects due to the indirect space charge force [78, 79]. On the other hand, neglecting the indirect space charge force (Fig. 9.4b) enhance the beam growth rate, compared to the case including only wakefield effects (Fig. 9.4a), which is consistent with another theoretical prediction [80]. In conclusion, our code resolves two different theoretical predictions and highlights the importance of including indirect space charge effects in the simulation.

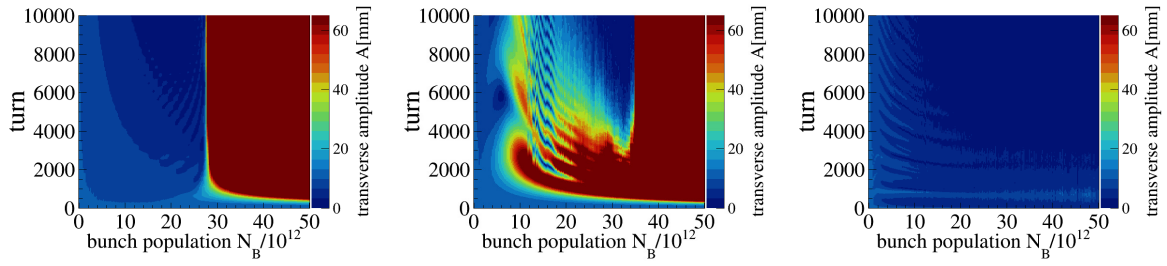

(a) Only the transverse wakefield.

(b) The transverse wakefield and the direct space charge.

(c) The transverse wakefield, the direct and indirect space charge.

Figure 9.4: Transverse amplitude $\overline{A_n}$ scanned by varying beam intensity N_B for the case of chromaticity $\xi_x = 0$.

Chapter 10

Time-Domain Analysis of Simulation Results

Since we have analyzed the frequency spectrum of a Gaussian beam, we will observe how the bunch motions in the Gaussian bunch are affected in the time domain by the space charge effects through the chromaticity, the beam intensity, and the synchrotron period (RF voltage) by the tracking simulation under the storage mode of the J-PARC MR.

10.1 Typical Results of the Simulation

Figure 10.1 shows typical results in the time domain of the tracking simulation for the case of strong space charge ($N_B = 8.6 \times 10^{12}$ ppb) with the chromaticity $\xi_x = -12.5$ and horizontal injection offset $X_0 = 0.01$ m. Figure 10.1a illustrates that the frequency components of the dipole moment $\Delta^{(k)}$, alternately exhibiting high and low-frequency components along the turn. Meanwhile, Fig. 10.1b depicts the oscillatory behavior of the horizontal centroid of the entire bunch, representing the decoherent and recoherent motions of the particles comprising the beam. The comparison between Figs. 10.1a and 10.1b reveals that when the average transverse position indicates decoherence at the N_f turn (or recoherence at the N_{AM} turn), the intra-bunch frequency in Fig. 10.1a reaches its maximum (f_{max}) or minimum, respectively.

For the subsequent analysis, it is necessary to quantitatively define f_{max}, N_f, and N_{AM} from an observation point of view. This is because the frequency components in Fig. 10.1a distribute with intensities, and some oscillation peaks can be observed in Fig. 10.1b, making it challenging to determine these parameters precisely. Since the high-frequency components of the dipole moment are more identifiable in Fig. 10.1a, N_f is defined as the first turn number at which the frequency component reaches its highest value with strongest signal (f_{max}), sweeping from the injection point. Finally, the recoherence period is defined as twice the intra-bunch oscillation period : $N_{\mathrm{AM}} = 2N_f$. In addition, to compare the recoherence period for different synchrotron periods, the normalized recoherence period N_{AM}/N_s is introduced. In the Fig. 10.1 case, we can determine the maximum intra-bunch frequency $f_{\mathrm{max}} = 84.1$ MHz, the intra-bunch oscillation period $N_f = 890$ turn, the recoherence period $N_{\mathrm{AM}} = 1780$ turn, and the normalized recoherence period $N_{\mathrm{AM}}/N_s = 4.3$, respectively.

Figure 10.1c reveals that the dipole moment $|\Delta^{(k)}\sigma_\Delta/q|$ meanders back and forth in the longitudinal direction, with this cycle being equal to N_{AM}.

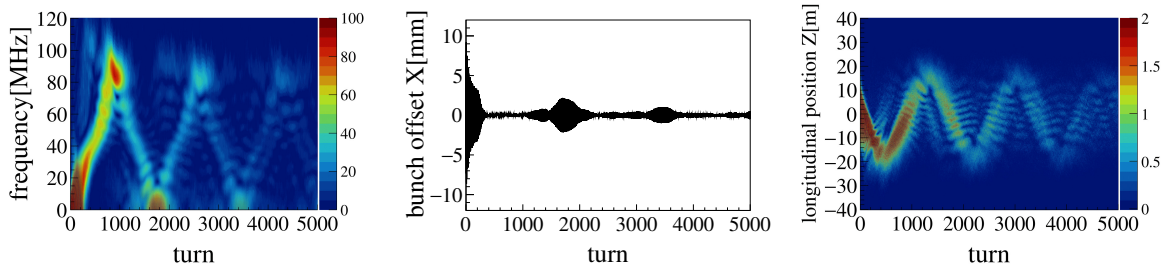

(a) Frequency component of the dipole moment in the bunch

(b) Average of the beam position $\overline{x_n}$

(c) Dipole moment $|\Delta^{(k)}\sigma_\Delta/q|$ in the bunch

Figure 10.1: Transverse bunch motion in the time domain for the chromaticity $\xi_x = -12.5$ and the beam intensity $N_B = 8.6 \times 10^{12}$ ppb.

10.2 Modeling of Head-tail Mode Reflecting Simulation

To interpret the simulation results in Fig. 10.1, the transverse centroid of each segment in the bunch is modeled as

$$\bar{x}(n,z) = X_0 \sum_{m=m_{\min}}^{m_{\max}} \tilde{a}_{m,\mathrm{sc}}(z) \exp\left(-\mathbf{i}2\pi\nu_m n\right), \tag{10.1}$$

where

$$\tilde{a}_{m,\mathrm{sc}}(z) = (-\mathbf{i})^m \exp\left(\mathbf{i}2\pi\frac{\xi_x}{\eta C}z\right) \cos\left(m\left(\tan^{-1}\left(\frac{\pi}{2}\frac{z}{\sigma_z}\right) - \frac{\pi}{2}\right)\right), \tag{10.2}$$

referring to Eq. (5.27). Here, the factor $\pi/2 \times z/\hat{z}$ is replaced with $\tan^{-1}(\pi/2 \times z/\sigma_z)$ in Eq. (10.2). The excitation modes specified by $m_{\min}$ and $m_{\max}$ in Eq. (10.1) are determined by the simulations.

Regarding the tune of the head-tail mode $m \geq 0$, it is assumed to be expressed as

$$\nu_m = \nu_0 + m\Delta\nu, \tag{10.3}$$

with equal intervals of the head-tail modes $\Delta\nu$, based on the simulation results of Fig. 8.23d.

Figure 10.2 shows the dipole moment :

$$\Delta(n,z) = \mathrm{Re}[\bar{x}(n,z)]\rho_z(z), \tag{10.4}$$

its frequency component, and the average of the beam position $X(n) = \mathrm{Re}\left[\int_{-\infty}^{\infty} dz\rho_z(z)\bar{x}(n,z)\right]$ for the parameter set of $\xi_x = -12.5$, $m_{\min} = 5$, $m_{\max} = 9$, $\sigma_z = 10$ m, $\Delta\nu = 0.00057$, $\nu_0 = 21.35$, and $X_0 = 1$ mm. Comparing the results to the tracking simulation (Fig. 10.1), we can observe that the intra-bunch frequency transitions with an interval of N_f between high and low frequencies, the periodic motion occurs at a cycle of $N_{\mathrm{AM}} = 1/\Delta\nu$, and the dipole moment meanders. The analytical model for

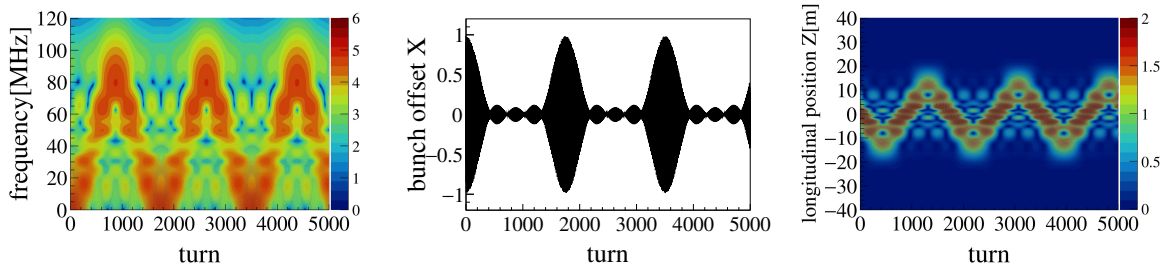

(a) Frequency component of the dipole moment

(b) Average of the beam position $X(n)$

(c) Dipole moment $|\Delta(n,z)|$ in the bunch

Figure 10.2: Transverse bunch motion in the time domain under the condition of $\xi_x = -12.5$, $m_{\min} = 5$, $m_{\max} = 9$.

the simulations reveals that the space charge effects characterize the motions of particles comprising the beam.

To understand the analytical mechanism of this phenomenon, we will extend the upper limit of head-tail mode in Eq. (10.1) to infinity with $m_{\min} = 0$. The transverse centroid of each segment is simplified as

$$\begin{aligned}
&\bar{x}(n,z)/\exp(-i2\pi\nu_0 n) \\
=&X_0 \exp\left(\mathbf{i}2\pi\frac{\xi_x}{\eta C}z\right)\sum_{m=0}^{\infty}\exp\left(-\mathbf{i}m(2\pi\Delta\nu n+\frac{\pi}{2})\right)\cos\left(m\left(\tan^{-1}\left(\frac{\pi}{2}\frac{z}{\sigma_z}\right)-\frac{\pi}{2}\right)\right) \\
=&X_0 \exp\left(\mathbf{i}2\pi\frac{\xi_x}{\eta C}z\right)\frac{1}{2}\left(1+\frac{1}{1+\exp(\mathbf{i}(\tan^{-1}\left(\frac{\pi}{2}\frac{z}{\sigma_z}\right)-2\pi\Delta\nu n))}-\frac{1}{1-\exp(\mathbf{i}(\tan^{-1}\left(\frac{\pi}{2}\frac{z}{\sigma_z}\right)+2\pi\Delta\nu n))}\right)
\end{aligned} \tag{10.5}$$

The last term characterized by $\Delta\nu$ diverges around

$$z=\begin{cases}-\frac{2}{\pi}\sigma_z\tan(2\pi\Delta\nu n), & \text{for } 0<n<\frac{1}{4}N_{\mathrm{AM}},\frac{3}{4}N_{\mathrm{AM}}<n<N_{\mathrm{AM}},\\ +\frac{2}{\pi}\sigma_z\tan(2\pi\Delta\nu n), & \text{for } \frac{1}{4}N_{\mathrm{AM}}<n<\frac{3}{4}N_{\mathrm{AM}},\end{cases} \tag{10.6}$$

in the range of $0 < n < N_{\mathrm{AM}}$, explaining the meandering of the dipole moments along the turn numbers, owing to the space charge effects.

Referring to the derivation of Eq. (4.10), we focus on the phase component of Eq. (10.5) to analyze the dependence of the maximum intra-bunch frequency on chromaticity, including the effects of space charge. First, we calculate $\mathrm{Arg}[\bar{x}(n,z)/\exp(-\mathbf{i}2\pi\nu_0 n)]$ after

substituting $n = N_{\mathrm{AM}}/2$ into Eq. (10.5) for small z, resulting in

$$\begin{aligned}
&\mathrm{Arg}\left[\bar{x}\left(\frac{N_{\mathrm{AM}}}{2}, z\right) / \exp\left(-\mathbf{i}2\pi\nu_0 \frac{N_{\mathrm{AM}}}{2}\right)\right] - 2\pi\frac{\xi_x}{\eta C}z \\
=&\mathrm{Arg}\left[\sum_{m=m_{\min}}^{m_{\max}} \mathbf{i}^m \cos\left(m\left(\tan^{-1}\left(\frac{\pi}{2}\frac{z}{\sigma_z}\right) - \frac{\pi}{2}\right)\right)\right] \\
\simeq&\mathrm{Arg}\left[\sum_{\substack{m_{\min}\le m\le m_{\max} \\ m:\text{even}}} (+1) + \mathbf{i}\sum_{\substack{m_{\min}\le m\le m_{\max} \\ m:\text{odd}}} m\frac{\pi}{2}\frac{z}{\sigma_z}\right].
\end{aligned} \tag{10.7}$$

Here, the second term can be estimated by referring to the condition on $\mathrm{Arg}[\bar{x}(n,z)/\exp(-\mathbf{i}2\pi\nu_0 n)]$ at $n = 0$ for small z, which must be zero due to the very initial condition. As a result, this condition is explicitly expressed by

$$\begin{aligned}
&\mathrm{Arg}[\bar{x}(0,z)/\exp(-\mathbf{i}2\pi\nu_0 0)] - 2\pi\frac{\xi_x}{\eta C}z \\
=&\mathrm{Arg}\left[\sum_{m=m_{\min}}^{m_{\max}} (-\mathbf{i})^m \cos\left(m\left(\tan^{-1}\left(\frac{\pi}{2}\frac{z}{\sigma_z}\right) - \frac{\pi}{2}\right)\right)\right] \\
\simeq&\mathrm{Arg}\left[\sum_{\substack{m_{\min}\le m\le m_{\max} \\ m:\text{even}}} (+1) - \mathbf{i}\sum_{\substack{m_{\min}\le m\le m_{\max} \\ m:\text{odd}}} m\frac{\pi}{2}\frac{z}{\sigma_z}\right].
\end{aligned} \tag{10.8}$$

By combining the complex conjugate of Eq. (10.8) with Eq. (10.7), we derive

$$\mathrm{Arg}\left[\bar{x}\left(\frac{N_{\mathrm{AM}}}{2}, z\right) / \exp\left(-\mathbf{i}2\pi\nu_0 \frac{N_{\mathrm{AM}}}{2}\right)\right] \simeq 4\pi\frac{\xi_x}{\eta C}z. \tag{10.9}$$

Finally, the maximum value of f_{int} at the center of the bunch is given by

$$f_{\max} = f_{\mathrm{int}}\left(\frac{N_{\mathrm{AM}}}{2}\right) \simeq \left|\frac{1}{2\pi}\frac{d}{dt}\left[2\pi\nu_0\frac{N_{\mathrm{AM}}}{2} - 4\pi\frac{\xi_x}{\eta C}z\right]\right| = \left|2f_0\frac{\xi_x}{\eta}\right|, \tag{10.10}$$

which matches Eq. (4.10) in the absence of space charge effects. The validity of this approximate formula including the space charge effect will be discussed in Sec. 11.5.

In the end, the simulations featuring the meandering of the dipole moment, the maximum intra-bunch frequency, and the recoherence of the entire bunch frequency can be qualitatively understood by the analytical model for the given excited head-tail modes $m_{\min}$ and $m_{\max}$ under the chromaticity condition.

10.3 Head-tail Eigenfunction at Gaussian Bunch

In Sec. 10.2, we reconstructed the simulation results using a simplified superposition of head-tail modes with an empirical phase function. To provide a theoretical justification

for the observed waveforms, we refer to the eigenmode analysis of the Vlasov equation for space charge dominated beams developed by Alexahin.

In the regime of strong space charge (SSC), the collective beam dynamics are governed by the Vlasov equation where the space charge force creates a potential well. For a realistic Gaussian longitudinal profile, it is necessary to choose a set of basis functions $\Phi_m(z)$ that are orthogonal with respect to the beam density $\rho(z) \propto \exp(-z^2/2\sigma_z^2)$ serving as the weight function. As derived in Ref. [81–83], the most advantageous choice for such basis functions is constructed by mapping the Legendre polynomials $P_m(u)$ onto the Gaussian profile using the error function:

$$\tilde{a}_{m,\mathrm{sc}}(z) = (-\mathbf{i})^m \exp\left(\mathbf{i}2\pi\frac{\xi_x}{\eta C}z\right)\sqrt{\frac{2m+1}{\sqrt{2\pi}}}P_m\left[\mathrm{erf}\left(\frac{z}{\sqrt{2}\sigma_z}\right)\right]. \tag{10.11}$$

This specific form is mathematically justified because the transformation $u = \mathrm{erf}(z/\sqrt{2}\sigma_z)$ maps the infinite Gaussian tail into the finite interval $[-1, 1]$, allowing the Legendre polynomials to form a complete orthogonal basis weighted by the Gaussian distribution. Furthermore, these functions satisfy the boundary conditions required for the SSC modes, $\Phi'(\pm\infty) = 0$, as established in the theory of head-tail modes for strong space charge.

The meandering behavior of the dipole moment observed in our time-domain simulations (Fig. 10.1) corresponds to the excitation of these specific eigenmodes. The empirical function involving $\tan^{-1}(\pi z/2\sigma_z)$ used in Eq. (10.2) can be understood as an approximation of the rigorous form in Eq. (10.11), as both functions share the same topological property of confining the phase excursion within a finite range despite the infinite bunch extent. Therefore, the simulation results provide strong evidence that the intra-bunch motion in the J-PARC MR under large chromaticity and high intensity is characterized by these Gaussian-SSC eigenmodes defined by Eq. (10.11).

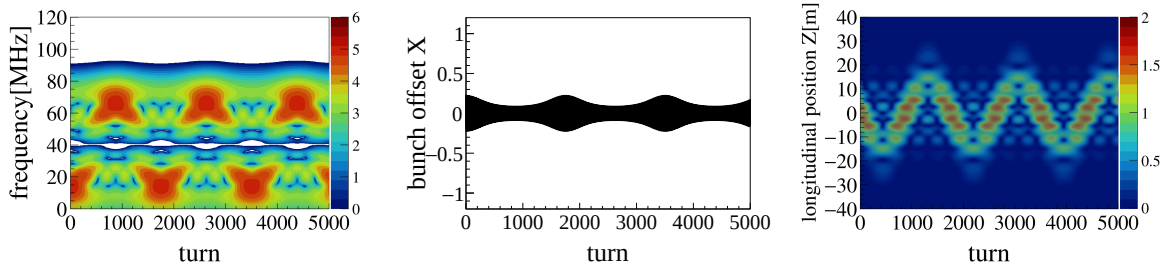

(a) Frequency component of the dipole moment

(b) Average of the beam position $X(n)$

(c) Dipole moment $|\Delta(n, z)|$ in the bunch

Figure 10.3: Transverse bunch motion in the time domain under the condition of $\xi_x = -12.5$, $m_{\min} = 5$, $m_{\max} = 9$, using Eq. (10.11).

While the theoretical eigenmodes defined by Eq. (10.11) reproduce the macroscopic meandering of the dipole moment, a closer inspection of the intra-bunch frequency evolution reveals a subtle discrepancy. In the tracking simulation and the phenomenological $\tan^{-1}$ model (Fig. 10.2), the transition between the uniform oscillation phase and the rapid intra-bunch oscillation phase ($f_{\max}$) appears smooth and continuous. However, when

applying the rigorous $P_m[\mathrm{erf}]$ basis, this frequency transition becomes abrupt and less continuous, despite the correct reproduction of the dipole amplitude cycle.

This behavior can be attributed to the asymptotic properties of the mode functions in the bunch tails. The error function $\mathrm{erf}(z/\sqrt{2}\sigma_z)$ converges to its saturation values exponentially fast ($\propto \exp(-z^2)$), effectively confining the mode oscillation strictly within the bunch core. Mathematically, this corresponds to a hard potential well characteristic of the strong space charge limit, where particles are deeply trapped. In contrast, the phenomenological $\tan^{-1}(z)$ function approaches its limits algebraically ($\propto 1/z$). This soft tail allows the phase information to leak into the peripheral regions of the bunch, creating a smoother interference between the chromaticity phase factor $\exp(i\xi z)$ and the head-tail mode phase.

The smooth transition observed in the tracking simulation suggests that, even under the strong space charge condition in J-PARC MR, the beam dynamics retains a certain degree of softness at the tails, likely due to the mixing driven by synchrotron motion, which is better approximated phenomenologically by the slowly decaying $\tan^{-1}$ function than by the rigorous, yet rigid, SSC eigenmodes. Therefore, while the $P_m[\mathrm{erf}]$ expansion is physically justified for identifying the dominant eigenmodes, the $\tan^{-1}$ model serves as a superior effective model for describing the transient continuity of the intra-bunch frequency in the time domain.

Chapter 11

Experimental Validation with Beam Measurements

In this chapter, we examine the intra-bunch motion predicted by the tracking simulation in the previous chapter by changing the chromaticity, the synchrotron period, and the beam intensity in the storage mode of the J-PARC MR based on beam measurements. We analyze the horizontal centroid of the entire bunch, the dipole moment in the bunch, and its intra-bunch frequency for each turn, when beams are injected into the MR with the horizontal offset of about $X_0 = 5$ mm.

The measurements utilized data from a stripline beam position monitor with a 500 MHz sampling rate. This monitor, comprising two pairs of triangle-shaped electrodes [84], is installed in the J-PARC MR to ensure a wide-band frequency response for the intra-bunch feedback system. The horizontal dipole moment, $\Delta(z)$, along the bunch is obtained by integrating the difference signals from the horizontal electrodes. The horizontal centroid of the entire bunch $\overline{x_n}$ is then calculated by summing all dipole moments in the bunch and multiplying the result by the sensitivity coefficient, 0.046 m, divided by the measured bunch current. For details on this, see Appendix E. In the 3 GeV storage mode with a single bunch, the beam power corresponds to $0.35 \times N_B/10^{12}$ kW for a repetition period of 1.36 s.

The structure of this chapter is organized as follows. Section 11.1 outlines the experimental conditions and the datasets used for the analysis. Section 11.2 presents a typical example of the observed intra-bunch motion to provide a qualitative overview. Subsequently, the simulation predictions are rigorously benchmarked against the measurement results with respect to three key parameters: the synchrotron period in Sec. 11.3, the beam intensity in Sec. 11.4, and the chromaticity in Sec. 11.5.

11.1 Conditions of Measurements

Three sets of measurements were conducted under different machine conditions.

First, we observe the synchrotron tune dependence by scanning the RF voltages $V_{\mathrm{RF}} = 80, 110, 140, 200, 263$ kV, and 400 kV and the beam intensities $N_B = 2.4 \times 10^{12}, 4.2 \times 10^{12}$, and 8.6×10^{12} ppb with the fixed chromaticity $(\xi_x, \xi_y) = (-6.5, -7.4)$ and the betatron tune $(\nu_{\beta,x}, \nu_{\beta,y}) = (21.35, 21.41)$. Table 11.1 summarizes the number of measured shots for the analysis.

Next, we investigate the beam intensity and chromaticity dependences by scanning the protons per bunch $N_B = 1.0 \times 10^{12}, 2.4 \times 10^{12}, 4.2 \times 10^{12}$, and 8.6×10^{12} ppb; and the horizontal chromaticities $\xi_x = -1.5, -7.9$, and -12.5; with the fixed vertical chromaticity

Table 11.1: Number of shots for the analysis of the synchrotron period dependence with the fixed chromaticity $(\xi_x, \xi_y) = (-6.5, -7.4)$ and the betatron tune $(\nu_{\beta,x}, \nu_{\beta,y}) = (21.35, 21.41)$.

N_B[ppb]/10^{12}	2.4	4.2	8.6
$N_s = 340$	3	3	3
$N_s = 410$	3	3	3
$N_s = 480$	-	3	3
$N_s = 570$	-	3	1
$N_s = 650$	-	4	1
$N_s = 760$	3	2	1

$\xi_y = -15$, the betatron tune $(\nu_{\beta,x}, \nu_{\beta,y}) = (21.35, 21.41)$, and the RF voltage $V_{\mathrm{RF}} = 263$ kV equivalent to the synchrotron period $N_s = 410$ turn. For the above two conditions, the measured bunching factor at the injection time was $B_f = 0.017$ for the beam intensity $N_B \leq 4.2 \times 10^{12}$ ppb, and $B_f = 0.022$ for the beam intensity $N_B = 8.6 \times 10^{12}$ ppb.

In the third set of measurements, we scan the beam intensities $N_B = 1.3 \times 10^{11}, 2.5 \times 10^{11}, 5.0 \times 10^{11}, 1.0 \times 10^{12}, 2.4 \times 10^{12}$, and 4.2×10^{12} ppb; and the chromaticities $(\xi_x, \xi_y) = (-5.7, -6.2)$ and $(-3.3, -4.4)$; with the fixed betatron tune $(\nu_{\beta,x}, \nu_{\beta,y}) = (22.30, 20.81)$ and the RF voltage $V_{\mathrm{RF}} = 155$ kV, corresponding to the synchrotron period $N_s = 540$ turn. For this condition, the bunching factor at the injection timing was $B_f = 0.022$ for all beam intensities. Tables 11.2 and 11.3 summarize the number of shots for the analysis, respectively.

Table 11.2: Number of shots for the analysis of the beam intensity and the chromaticity dependences with the fixed betatron tune $(\nu_{\beta,x}, \nu_{\beta,y}) = (21.35, 21.41)$, and the RF voltage $V_{\mathrm{RF}} = 263$ kV.

N_B[ppb]/10^{12}	1.0	2.4	4.2	8.6
$\xi_x = -1.5$	30	30	30	-
$\xi_x = -7.9$	30	30	30	10
$\xi_x = -12.5$	30	30	30	-

Table 11.3: Number of shots for the analysis of the beam intensity and the chromaticity dependences with the fixed betatron tune $(\nu_{\beta,x}, \nu_{\beta,y}) = (22.30, 20.81)$, and the RF voltage $V_{\mathrm{RF}} = 155$ kV.

N_B[ppb]/10^{12}	0.13	0.26	0.52	1.0	2.4	4.2
$\xi_x = -3.3$	3	3	3	3	3	-
$\xi_x = -5.7$	3	3	3	3	3	3

11.2 Typical Results of the Measured Intra-Bunch Motion

Figure 11.1 shows a typical result of the measured intra-bunch motion in the time domain for a beam intensity of ($N_B = 8.6 \times 10^{12}$ ppb) with a chromaticity of $\xi_x = -7.9$. As in the case of the tracking simulation, the frequency components of the dipole moment $|\Delta(z)|$ in Fig. 11.1a reveals an alternation between high-frequency and low-frequency components along the turn. Figure 11.1b shows the oscillatory behavior of the horizontal centroid of the entire bunch, and the level of amplitude represents the decoherence and recoherence motion of the particles that make up the beam. Here, the definitions of $f_{\max}$, N_f, and N_{AM} are the same as those used in the tracking simulation. From the data in Fig.11.1, we determine the maximum bunch frequency to be $f_{\max} = 53.4$ MHz, the bunch oscillation period to be $N_f = 850$ turn, the recoherence period to be $N_{\mathrm{AM}} = 1700$ turn, and the normalized recoherence period to be $N_{\mathrm{AM}}/N_s = 4.1$. From Fig.11.1c, it can be seen that the dipole moment $|\Delta(z)|$ meanders in the longitudinal direction, and that the period is equal to N_{AM}.

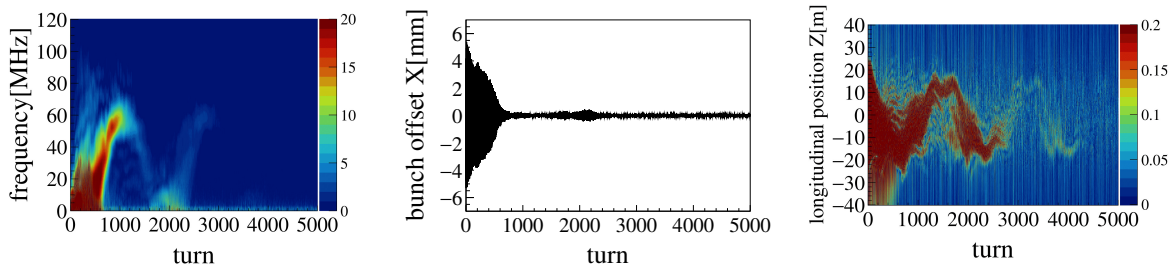

(a) Frequency component of the dipole moment in the bunch

(b) Average of the beam position $\overline{x_n}$

(c) Dipole moment $|\Delta(z)|$ in the bunch

Figure 11.1: Measured transverse bunch motion in the time domain for the chromaticity $\xi_x = -7.9$ and the beam intensity $N_B = 8.6 \times 10^{12}$ ppb and the RF voltage $V_{\mathrm{RF}} = 263$ kV.

Figure 11.2 shows the intra-bunch motion (the dipole moment) observed at the beam measurement by superimposing the trajectories of five consecutive turns at intervals of $N_{\mathrm{AM}}/4$. In the periodic N_{AM}, the oscillation frequency varies between high and low frequencies as mentioned in Fig. 11.1a, and the dipole component oscillates with N_{AM} period between the head and tail as mentioned in Fig. 11.1c.

Figure 11.3 also shows the intra-beam motion (the dipole moment) at $N_{\mathrm{AM}}/2 = N_f$ with various chromaticities. We can directly observe the higher chromaticity excites the higher head-tail modes, as mentioned in Fig. 8.21.

11.3 Synchrotron Period Dependence

This section investigates the dependence of intra-bunch motion on the synchrotron period N_s. By systematically varying the RF voltage, we examine how the longitudinal focusing

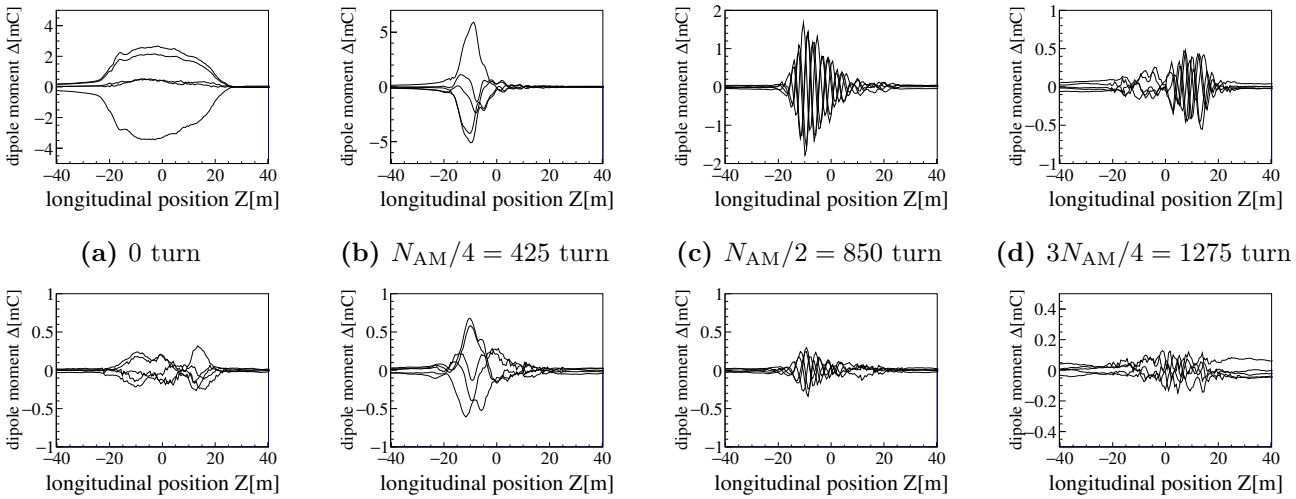

(a) 0 turn **(b)** $N_{\mathrm{AM}}/4 = 425$ turn **(c)** $N_{\mathrm{AM}}/2 = 850$ turn **(d)** $3N_{\mathrm{AM}}/4 = 1275$ turn

(e) $N_{\mathrm{AM}} = 1700$ turn **(f)** $5N_{\mathrm{AM}}/4 = 2125$ turn **(g)** $3N_{\mathrm{AM}}/2 = 2550$ turn **(h)** $7N_{\mathrm{AM}}/4 = 2975$ turn

Figure 11.2: Measured dipole moment $\Delta(z)$ in the bunch at beam measurement for the chromaticity $\xi_x = -7.9$ and the beam intensity $N_B = 8.6 \times 10^{12}$ ppb.

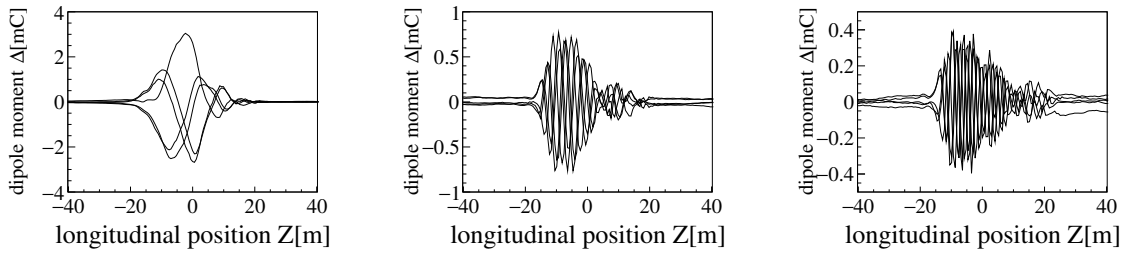

(a) $\xi_x = -1.5$ **(b)** $\xi_x = -7.9$ **(c)** $\xi_x = -12.5$

Figure 11.3: Measured dipole moment $\Delta(z)$ in the bunch for the beam intensity $N_B = 4.2 \times 10^{12}$ ppb and $N_{\mathrm{AM}}/2 = N_f$ turn at beam measurement.

strength influences the recoherence mechanism and compare these observations with the simulation predictions.

11.3.1 Simulation Predictions and Measurement Results

Simulations were performed for various RF voltages corresponding to synchrotron periods from $N_s = 340$ to 760 turns. Specific examples for $\xi_x = -6.5$ and $N_B = 4.2 \times 10^{12}$ ppb are shown in Fig. 11.4. The extracted values for $(f_{\max}, N_{\mathrm{AM}})$ were (43.5 MHz, 1700 turns) for $V_{\mathrm{RF}} = 400$ kV, (39.6 MHz, 1720 turns) for $V_{\mathrm{RF}} = 263$ kV, and (34.2 MHz, 2940 turns) for $V_{\mathrm{RF}} = 110$ kV.

Corresponding measurements were performed under the same parameter set, with the results shown in Fig. 11.5. The measured values for $(f_{\max}, N_{\mathrm{AM}})$ were (43.3 MHz, 1600 turns) for $V_{\mathrm{RF}} = 400$ kV, (45.3 MHz, 2300 turns) for $V_{\mathrm{RF}} = 263$ kV, and (39.8 MHz, 3400 turns) for $V_{\mathrm{RF}} = 110$ kV. The measurements reproduce the key features of the simulation, including the periodic frequency structure and the long recoherence period.

The measured $f_{\max}$ $(39-46$ MHz) and N_{AM}/N_s $(5.2-5.6)$ are comparable to the simulated values of $f_{\max}$ $(34-44$ MHz) and N_{AM}/N_s $(4.2-5.0)$.

11.3.2 Comparison and discussion

Figure 11.6 compares the simulations with the measurements to see the synchrotron period dependence of the maximum intra-bunch frequency $f_{\max}$. No clear dependence on the synchrotron period is observed in the maximum intra-bunch frequency $f_{\max}$ both in the simulations and measurements, which demonstrates no synchrotron tune and beam intensity dependences on the maximum frequency as predicted by Eq. (10.10).

Figure 11.7a represents the simulations to explain the synchrotron period dependence of the normalized recoherence period N_{AM}/N_s. When the space charge effect is stronger ($N_B = 4.2 \times 10^{12}$ and 8.6×10^{12} ppb), the normalized recoherence period stays within the region of $4N_s < N_{\mathrm{AM}} < 5N_s$ even when the synchrotron period is changed. Meanwhile, when the space charge effect is moderate ($N_B = 2.4 \times 10^{12}$ ppb), the normalized recoherence period tends to increase as the synchrotron period increases.

This behavior of the recoherence period can be understood in terms of the head-tail modes analysis. Figure 11.8 shows the head-tail tune spectrum of the relative amplitude a_m, where the synchrotron period is scanned by changing the RF voltage in the tracking simulation. The vertical axis is the head-tail modes tune normalized by the synchrotron tune: $\Delta\nu/\nu_s$. In Figs. 11.8b and 11.8c (in the cases of the strong space charge effect with the respective beam intensities $N_B = 4.2 \times 10^{12}$ and 8.6×10^{12} ppb), we can see that the normalized frequency interval between adjacent head-tail modes is close to a constant of around $0.2 < \Delta\nu/\nu_s < 0.25$, even when the synchrotron period is changed. On the other hand, in Fig. 11.8a (in the case of the moderate space charge effect with the beam intensity $N_B = 2.4 \times 10^{12}$ ppb), the interval dynamically decreases from 0.5 to 0.25 as the synchrotron period increases. As a result, we can conclude that the normalized recoherence period saturates for the higher synchrotron tune due to the space charge effects.

The measured data for the normalized recoherence period N_{AM}/N_s is shown in Fig.

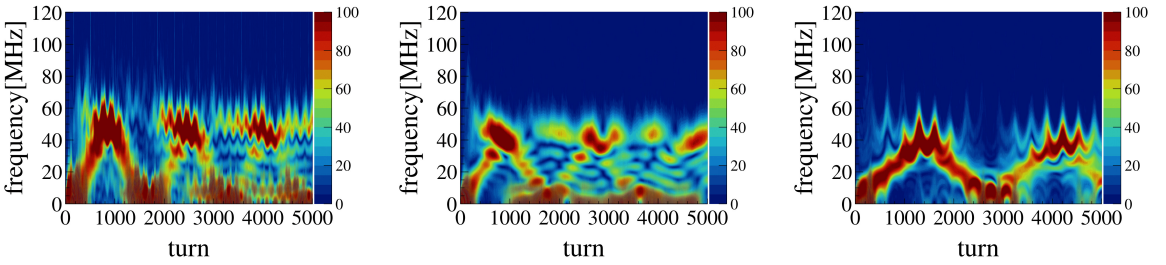

(a) Frequency component of the dipole moment for $V_{\mathrm{RF}} = 400$ kV. $f_{\max} = 43.5$ MHz, $N_{\mathrm{AM}} = 1700$, $N_{\mathrm{AM}}/N_s = 5.0$.

(b) Frequency component of the dipole moment for $V_{\mathrm{RF}} = 263$ kV. $f_{\max} = 39.6$ MHz, $N_{\mathrm{AM}} = 1720$, $N_{\mathrm{AM}}/N_s = 4.2$.

(c) Frequency component of the dipole moment for $V_{\mathrm{RF}} = 110$ kV. $f_{\max} = 34.2$ MHz, $N_{\mathrm{AM}} = 2940$, $N_{\mathrm{AM}}/N_s = 4.5$.

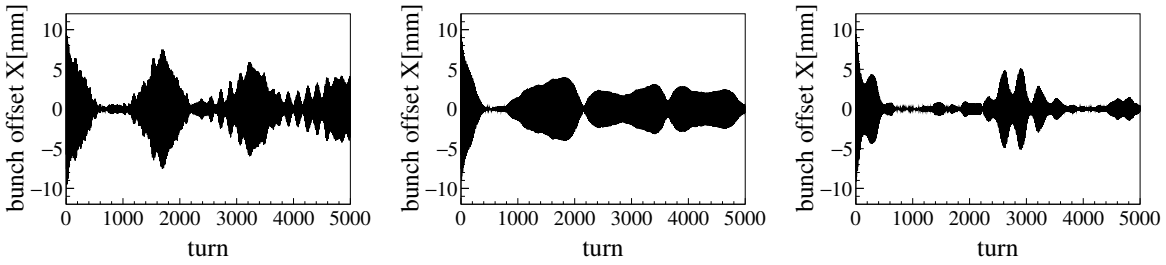

(d) Average of the beam position $\overline{x_n}$ for $V_{\mathrm{RF}} = 400$ kV.

(e) Average of the beam position $\overline{x_n}$ for $V_{\mathrm{RF}} = 263$ kV.

(f) Average of the beam position $\overline{x_n}$ for $V_{\mathrm{RF}} = 110$ kV.

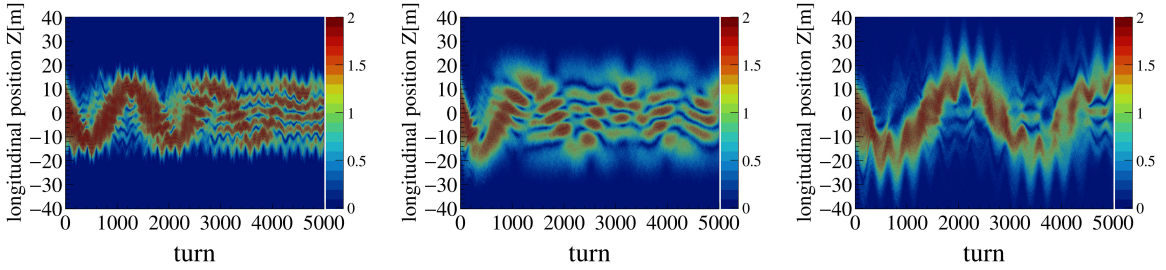

(g) Dipole moment $|\Delta^{(k)}\sigma_\Delta/q|$ in the bunch for $V_{\mathrm{RF}} = 400$ kV.

(h) Dipole moment $|\Delta^{(k)}\sigma_\Delta/q|$ in the bunch for $V_{\mathrm{RF}} = 263$ kV.

(i) Dipole moment $|\Delta^{(k)}\sigma_\Delta/q|$ in the bunch for $V_{\mathrm{RF}} = 110$ kV.

Figure 11.4: Simulations of the transverse bunch motion in the time domain for the RF voltages: $V_{\mathrm{RF}} = 110, 263$, and 400 kV with the chromaticity $\xi_x = -6.5$ and the beam intensity $N_B = 4.2 \times 10^{12}$ ppb.

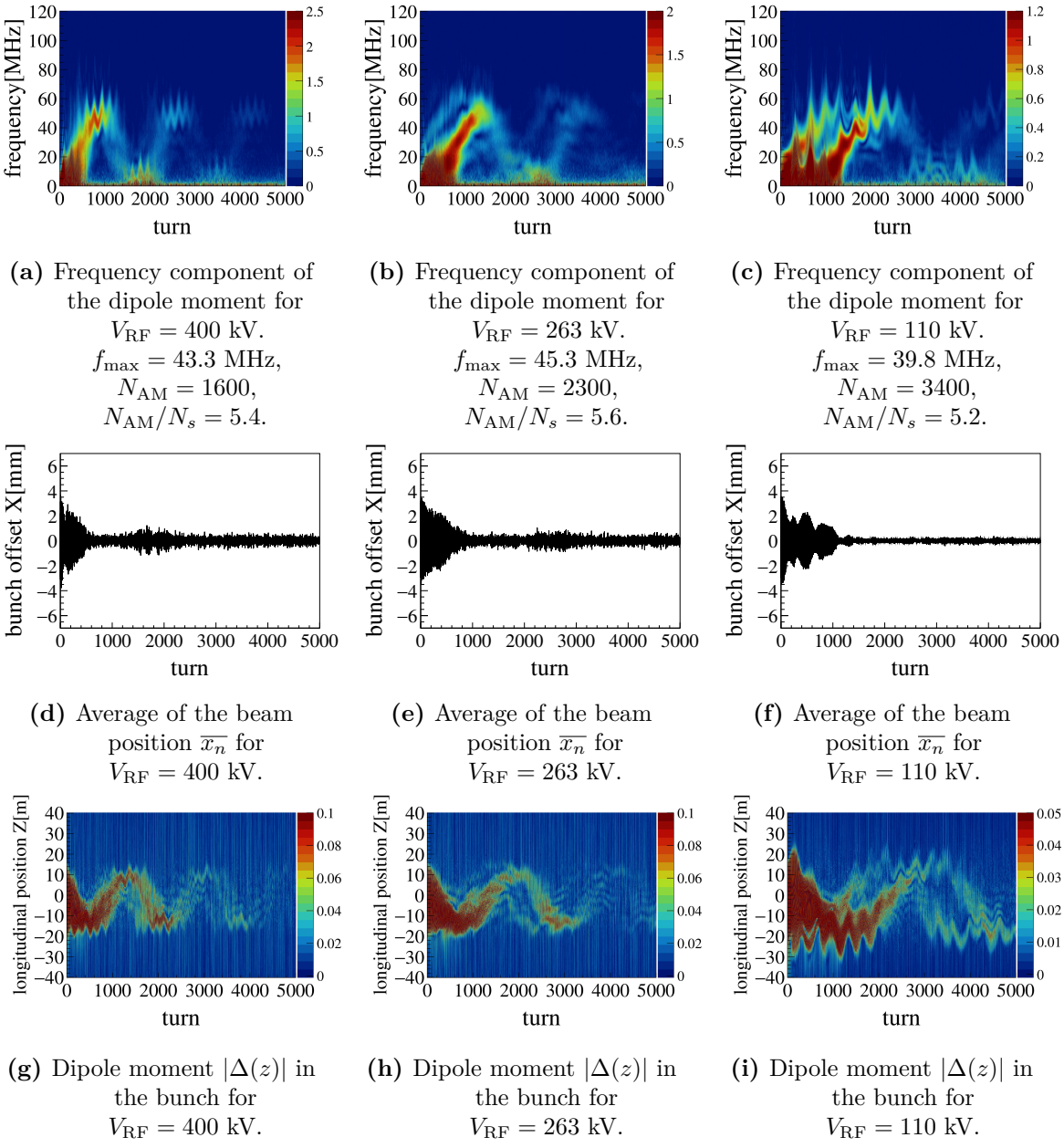

(a) Frequency component of the dipole moment for $V_{\mathrm{RF}} = 400$ kV. $f_{\max} = 43.3$ MHz, $N_{\mathrm{AM}} = 1600$, $N_{\mathrm{AM}}/N_s = 5.4$.

(b) Frequency component of the dipole moment for $V_{\mathrm{RF}} = 263$ kV. $f_{\max} = 45.3$ MHz, $N_{\mathrm{AM}} = 2300$, $N_{\mathrm{AM}}/N_s = 5.6$.

(c) Frequency component of the dipole moment for $V_{\mathrm{RF}} = 110$ kV. $f_{\max} = 39.8$ MHz, $N_{\mathrm{AM}} = 3400$, $N_{\mathrm{AM}}/N_s = 5.2$.

(d) Average of the beam position $\overline{x_n}$ for $V_{\mathrm{RF}} = 400$ kV.

(e) Average of the beam position $\overline{x_n}$ for $V_{\mathrm{RF}} = 263$ kV.

(f) Average of the beam position $\overline{x_n}$ for $V_{\mathrm{RF}} = 110$ kV.

(g) Dipole moment $|\Delta(z)|$ in the bunch for $V_{\mathrm{RF}} = 400$ kV.

(h) Dipole moment $|\Delta(z)|$ in the bunch for $V_{\mathrm{RF}} = 263$ kV.

(i) Dipole moment $|\Delta(z)|$ in the bunch for $V_{\mathrm{RF}} = 110$ kV.

Figure 11.5: Measurements of the transverse bunch motion in the time domain for the RF voltages: $V_{\mathrm{RF}} = 110, 263$, and 400 kV with the chromaticity $\xi_x = -6.5$ and the beam intensity $N_B = 4.2 \times 10^{12}$ ppb.

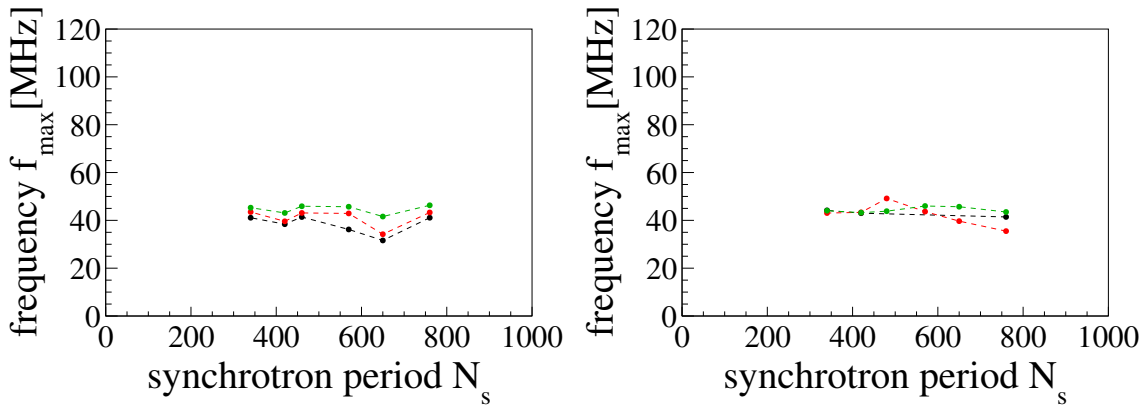

(a) tracking simulation. **(b)** measurment.

Figure 11.6: The maximum intra-bunch frequency $f_{\max}$ for the synchrotron period. Here, the black, red, and green denote the cases of $N_B = 2.4 \times 10^{12}$, 4.2×10^{12}, and 8.6×10^{12} ppb, respectively.

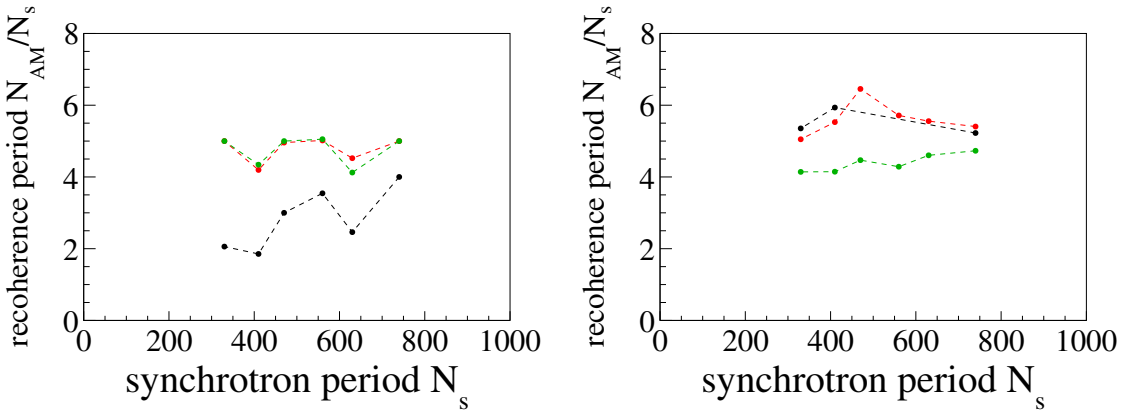

(a) tracking simulation. **(b)** measurement.

Figure 11.7: The normalized recoherence period N_{AM}/N_s for the synchrotron period. Here, the black, red, and green denote the cases of $N_B = 2.4 \times 10^{12}, 4.2 \times 10^{12}$, and 8.6×10^{12} ppb, respectively.

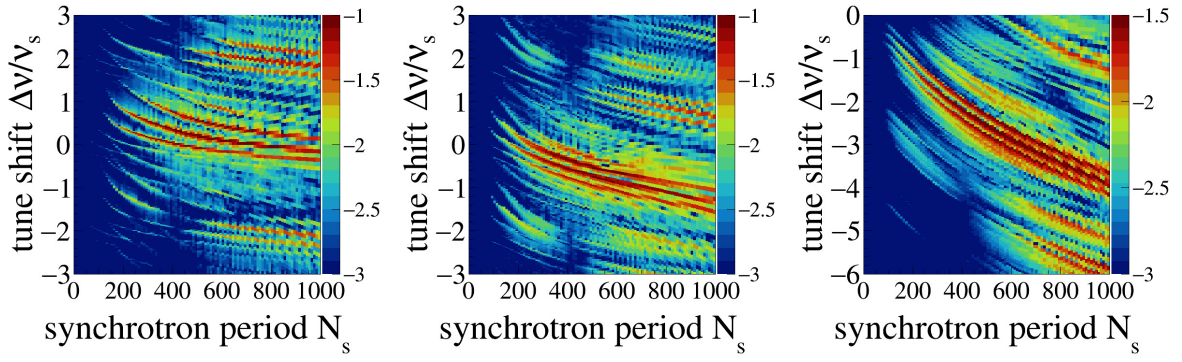

(a) $N_B = 2.4 \times 10^{12}$ ppb **(b)** $N_B = 4.2 \times 10^{12}$ ppb **(c)** $N_B = 8.6 \times 10^{12}$ ppb

Figure 11.8: The simulated spectra of head-tail tune normalized with synchrotron tune $\Delta\nu/\nu_s$ for the synchrotron period obtained by analyzing $\log|a_m|$ of the harmonic model with the indirect space charge effect.

11.7b. The period remains within the range of $4 < N_{\mathrm{AM}}/N_s < 7$ and shows no strong dependence on N_s, consistent with the saturation behavior predicted for high-intensity beams. Interestingly, the data for $N_B = 8.6 \times 10^{12}$ ppb deviates slightly from the lower intensity cases. These measured results indicate that the recoherence period already saturates in the mid-strength region of the space charge, suggesting that the current modeling of the indirect space charge, based on the simplified geometry of the J-PARC MR, overestimates its effect on the intra-bunch motions. Meanwhile, the reason the normalized recoherence period falls below the saturated value for beams with mid-strength space charge is that the injected beam is broadened from the outset due to the large number of N_B. Note, $B_f = 0.017$ for $N_B \leq 4.2 \times 10^{12}$ ppb, but $B_f = 0.022$ for $N_B = 8.6 \times 10^{12}$ ppb in the measurements. Consequently, the effective space charge effect is mitigated in the bunch with $N_B = 8.6 \times 10^{12}$ ppb, leading to a shorter normalized recoherence period compared to the other results.

11.4 Beam Intensity Dependence

Following the analysis of longitudinal dynamics, we proceed to examine the dependence on beam intensity, which is the primary driver of space charge effects. Based on the finding in the previous section that the dependence on the synchrotron period is minimal, data from all three measurement sets are consolidated to evaluate the trends across a wide range of intensities.

11.4.1 Simulation Predictions and Measurement Results

We simulate the beam intensity dependence of intra-bunch motions for a fixed RF voltage $V_{\mathrm{RF}} = 263$ kV and chromaticity. Figure 11.9 shows the simulations of the transverse bunch motion in the time domain for the beam intensity : $N_B = 1.0 \times 10^{12}, 2.4 \times 10^{12}, 4.2 \times 10^{12}$, and 8.6×10^{12} ppb with fixed chromaticity $\xi_x = -8.0$. The extracted values for $(f_{\max}, N_{\mathrm{AM}})$ were (53.3 MHz, 340 turns) for $N_B = 1.0 \times 10^{12}$ ppb, (49.0 MHz, 600 turns) for $N_B = 2.4 \times 10^{12}$ ppb, (51.3 MHz, 1040 turns) for $N_B = 4.2 \times 10^{12}$ ppb, and (53.7 MHz, 1860 turns)

for $N_B = 8.6 \times 10^{12}$ ppb. When the space charge effect is negligible, the recoherence occurs at $N_{\mathrm{AM}} = N_s$ (Chapter 4). However, for the moderate beam intensity in Fig. 11.9e, the recoherence signals weaken due to the betatron tune spread caused by the space charge effects. In contrast, as the beam intensity increases significantly, the strong space charge effects bias the particle distributions within the beam, leading to the reemergence of recoherence, as illustrated in Figs. 11.9g and 11.9h.

Since, we have experimentally confirmed that the synchrotron period does not have a strong effect on the maximum intra-bunch frequency and the normalized recoherence period N_{AM}/N_s in Sec. 11.3.2, we handle the measured data with different synchrotron periods (RF voltages) simultaneously, from now on. Accordingly, we will analyze the beam intensity and the chromaticity dependences after combining the results based on Tables 11.1, 11.2, and 11.3.

Figure 11.10 shows the measurements of the transverse bunch motion in the time domain for the beam intensity : $N_B = 1.0 \times 10^{12}, 2.4 \times 10^{12}, 4.2 \times 10^{12}$, and 8.6×10^{12} ppb with fixed chromaticity $\xi_x = -7.9$, displaying the low to high-intensity beam results in left to right columns. Just as in the simulation predictions, the recoherence signal becomes more visible when the beam intensity increases. The measured values for $(f_{\max}, N_{\mathrm{AM}})$ were (50.5 MHz, 1300 turns) for $N_B = 1.0 \times 10^{12}$ ppb, (52.2 MHz, 2200 turns) for $N_B = 2.4 \times 10^{12}$ ppb, (51.9 MHz, 2100 turns) for $N_B = 4.2 \times 10^{12}$ ppb, and (53.4 MHz, 1700 turns) for $N_B = 8.6 \times 10^{12}$ ppb.

11.4.2 Comparison and discussion

Figure 11.11a shows the simulations of the normalized recoherence period N_{AM}/N_s for the beam intensity, but saturates for the high-intensity regime, regardless of the chromaticity. This feature can be interpreted based on the tune spectrum results shown in Fig. 8.20, similar to the discussion in the Sec. 11.3.2. When the separation of the excited tune shifts across different modes remains nearly identical within the given range of beam intensities, the normalized recoherence period becomes independent of the beam intensity.

For lower chromaticity, the lower head-tail modes are excited, and their degeneration levels rapidly saturate at high beam intensities. In contrast, for higher chromaticity, the higher head-tail modes are excited, and their degeneration levels do not saturate easily, even at high beam intensities (refer to Fig. 8.20).

As a result, achieving saturation of the normalized recoherence period for these beam intensity parameters requires a higher beam intensity in the higher chromaticity condition. From simulation point of view, Fig. 11.11a reveals that, the recoherence period is within $4N_s < N_{\mathrm{AM}} < 5N_s$ for the high-intensity beams. In the J-PARC MR, the recoherence period is expected to lengthen to $1600 < N_{\mathrm{AM}} < 2000$ due to the space charge effects for a beam characterized by the equal intervals of the head-tail modes $\Delta\nu$, within the range of $0.0005 < \Delta\nu < 0.0006$, based on the simulation results of Fig. 8.23d.

Figure 11.11b shows the measurements of the normalized recoherence period for the beam intensity, corresponding to the simulations in Fig. 11.11a. From a measurement perspective, it is difficult to identify N_f, where the highest frequency : $f_{\max}$ appears in the bunch with lower intensity under conditions of lower chromaticity like $\xi_x = -1.5$. From a

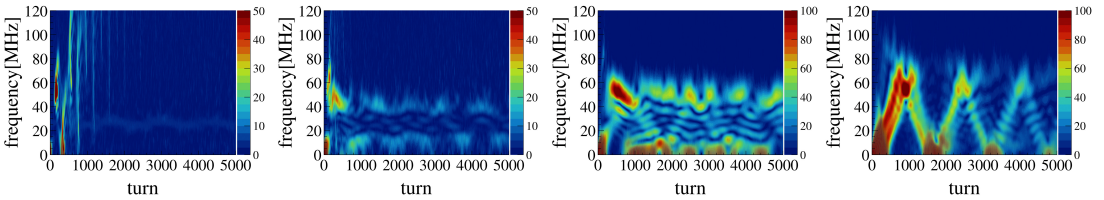

(a) Frequency component of the dipole moment for $N_B = 1.0 \times 10^{12}$ ppb. $f_{\max} =$ 53.3 MHz, $N_{\mathrm{AM}} = 340$, $N_{\mathrm{AM}}/N_s = 0.8$.

(b) Frequency component of the dipole moment for $N_B = 2.4 \times 10^{12}$ ppb. $f_{\max} =$ 49.0 MHz, $N_{\mathrm{AM}} = 600$, $N_{\mathrm{AM}}/N_s = 1.5$.

(c) Frequency component of the dipole moment for $N_B = 4.2 \times 10^{12}$ ppb. $f_{\max} =$ 51.3 MHz, $N_{\mathrm{AM}} = 1040$, $N_{\mathrm{AM}}/N_s = 2.5$.

(d) Frequency component of the dipole moment for $N_B = 8.6 \times 10^{12}$ ppb. $f_{\max} =$ 53.7 MHz, $N_{\mathrm{AM}} = 1860$, $N_{\mathrm{AM}}/N_s = 4.5$.

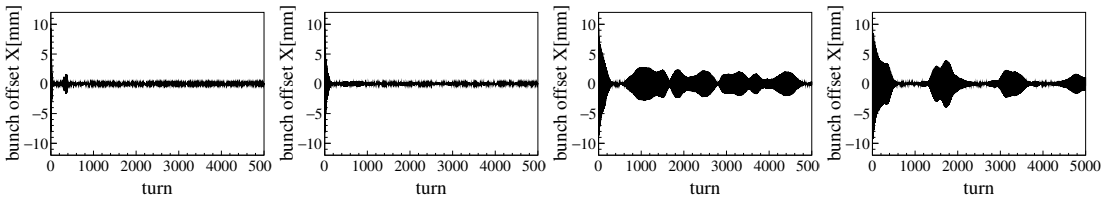

(e) Average of the beam position $\overline{x_n}$ for $N_B = 1.0 \times 10^{12}$ ppb.

(f) Average of the beam position $\overline{x_n}$ for $N_B = 2.4 \times 10^{12}$ ppb.

(g) Average of the beam position $\overline{x_n}$ for $N_B = 4.2 \times 10^{12}$ ppb.

(h) Average of the beam position $\overline{x_n}$ for $N_B = 8.6 \times 10^{12}$ ppb.

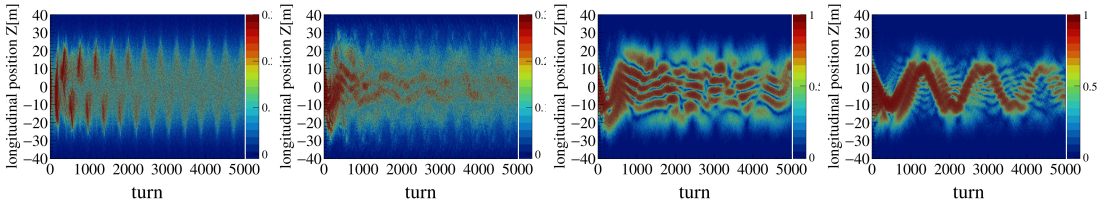

(i) Dipole moment $|\Delta^{(k)}\sigma_\Delta/q|$ in the bunch for $N_B = 1.0 \times 10^{12}$ ppb.

(j) Dipole moment $|\Delta^{(k)}\sigma_\Delta/q|$ in the bunch for $N_B = 2.4 \times 10^{12}$ ppb.

(k) Dipole moment $|\Delta^{(k)}\sigma_\Delta/q|$ in the bunch for $N_B = 4.2 \times 10^{12}$ ppb.

(l) Dipole moment $|\Delta^{(k)}\sigma_\Delta/q|$ in the bunch for $N_B = 8.6 \times 10^{12}$ ppb.

Figure 11.9: Simulation of the transverse bunch motion in the time domain for the beam intensity: $N_B = 1.0 \times 10^{12}, 2.4 \times 10^{12}, 4.2 \times 10^{12}$ and 8.6×10^{12} ppb with the chromaticity $\xi_x = -8.0$, and the RF voltage $V_{\mathrm{RF}} = 263$ kV.

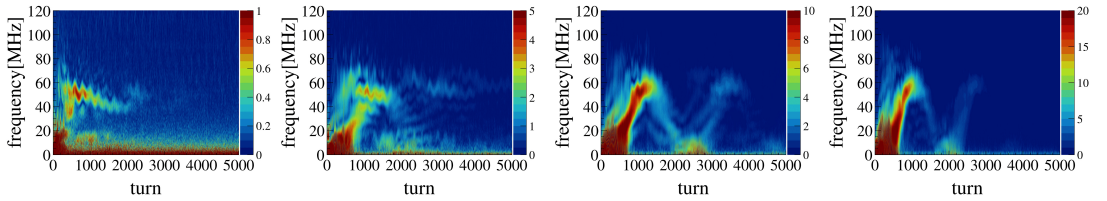

(a) Frequency component of the dipole moment for $N_B = 1.0 \times 10^{12}$ ppb. $f_{\max} = 50.5$ MHz, $N_{\mathrm{AM}} = 1300$, $N_{\mathrm{AM}}/N_s = 3.2$.

(b) Frequency component of the dipole moment for $N_B = 2.4 \times 10^{12}$ ppb. $f_{\max} = 52.2$ MHz, $N_{\mathrm{AM}} = 2200$, $N_{\mathrm{AM}}/N_s = 5.4$.

(c) Frequency component of the dipole moment for $N_B = 4.2 \times 10^{12}$ ppb. $f_{\max} = 51.9$ MHz, $N_{\mathrm{AM}} = 2100$, $N_{\mathrm{AM}}/N_s = 5.1$.

(d) Frequency component of the dipole moment for $N_B = 8.6 \times 10^{12}$ ppb. $f_{\max} = 53.4$ MHz, $N_{\mathrm{AM}} = 1700$, $N_{\mathrm{AM}}/N_s = 4.1$.

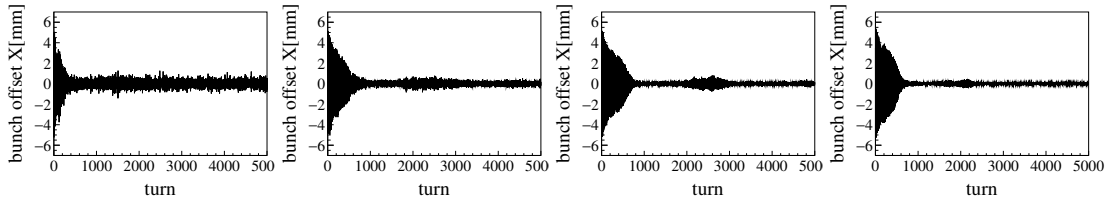

(e) Average of the beam position $\overline{x_n}$ for $N_B = 1.0 \times 10^{12}$ ppb.

(f) Average of the beam position $\overline{x_n}$ for $N_B = 2.4 \times 10^{12}$ ppb.

(g) Average of the beam position $\overline{x_n}$ for $N_B = 4.2 \times 10^{12}$ ppb.

(h) Average of the beam position $\overline{x_n}$ for $N_B = 8.6 \times 10^{12}$ ppb.

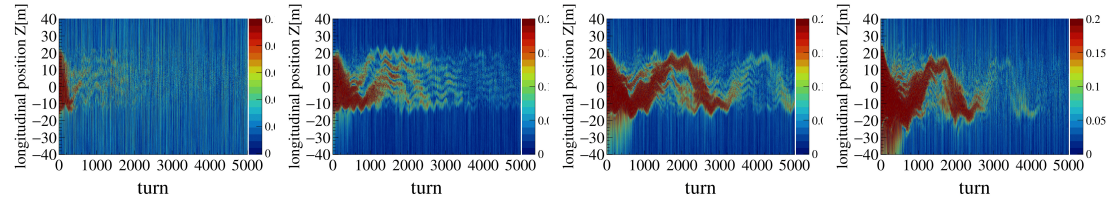

(i) Dipole moment $|\Delta(z)|$ in the bunch for $N_B = 1.0 \times 10^{12}$ ppb.

(j) Dipole moment $|\Delta(z)|$ in the bunch for $N_B = 2.4 \times 10^{12}$ ppb.

(k) Dipole moment $|\Delta(z)|$ in the bunch for $N_B = 4.2 \times 10^{12}$ ppb.

(l) Dipole moment $|\Delta(z)|$ in the bunch for $N_B = 8.6 \times 10^{12}$ ppb.

Figure 11.10: Measurements of the transverse bunch motion in the time domain for the beam intensity: $N_B = 1.0 \times 10^{12}, 2.4 \times 10^{12}, 4.2 \times 10^{12}$, and 8.6×10^{12} ppb with the chromaticity $\xi_x = -7.9$ and the RF voltage $V_{\mathrm{RF}} = 263$ kV.

theoretical viewpoint, this difficulty arises because multiple lower head-tail modes with different mode differences are simultaneously excited in the low-intensity beam at the lower chromaticity setting as explained in Chapter 7. This makes it difficult to define the recoherence period, N_{AM}. As a result, we exclude the measurement point or the case of $N_B = 1.0 \times 10^{12}$ ppb with $\xi_x = -1.5$ in Fig. 11.11b, deeming it unreliable.

The recoherence period appears to approach about $N_{\mathrm{AM}} = N_s$ for the weak beam intensity $N_B = 0.13 \times 10^{12}$ ppb, close to the linear decoherence scenario. As the beam intensity increases, the normalized recoherence period begins to rise, saturates at around $N_B = 2.4 \times 10^{12}$ ppb, and then tends to decrease for higher-intensity beams in the measurements.

More specifically, Fig. 11.11b shows that the saturation number of protons per bunch, at which the normalized recoherence period saturates, depends on the chromaticity. Overall, the saturation number of protons per bunch increases as the chromaticity becomes higher, consistent with the simulation results in Fig. 11.11a.

The decrease in the measured normalized recoherence period in the higher-intensity beams can be attributed to the same reason that explains the drop in normalized recoherence period for the case of $N_B = 8.6 \times 10^{12}$ ppb, as shown in Fig. 11.7b. The longitudinal emittances of the injection beam into the J-PARC MR depend on the beam intensity, which enhances the bunching factor for $N_B = 8.6 \times 10^{12}$ ppb compared to $N_B = 4.2 \times 10^{12}$ ppb. This effect effectively weakens the space charge effect on the bunch, resulting in a shortening of the recoherence period compared to the recoherence period of intermediate-strength beams. As a result, the recoherence period is within the wider range of $4N_s < N_{\mathrm{AM}} < 7N_s$ for the high-intensity and high-chromaticity beams in the measurements, unlike the simulations.

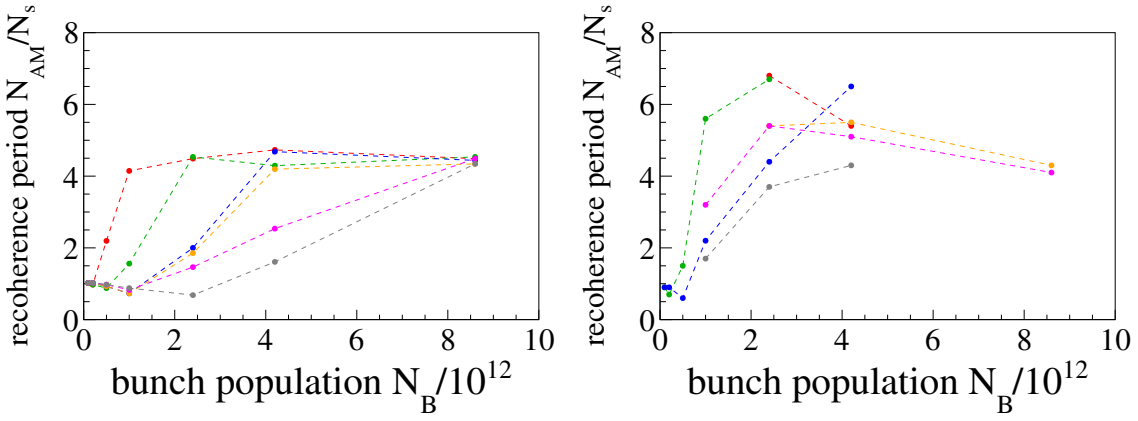

(a) tracking simulation. **(b)** measurement.

Figure 11.11: The normalized recoherence period N_{AM}/N_s with several fixed chromaticities for different beam intensities. Here, the red, green, blue, orange, magenta, and gray in Fig. 11.11a denote the cases of $\xi_x = -1.5, -3.5, -5.5, -6.5, -8.0$, and -12.5, respectively. Here, the red, green, blue, orange, magenta, and gray in Fig. 11.11b denote the cases of $\xi_x = -1.5, -3.3, -5.7, -6.5, -7.9$, and -12.5, respectively.

11.5 Chromaticity Dependence

Finally, this section addresses the dependence on chromaticity. Since chromaticity governs the phase slippage between the head and tail of the bunch, validating its impact on the maximum intra-bunch frequency and the recoherence period is crucial for establishing the reliability of the physical model.

11.5.1 Simulation Predictions and Measurement Results

We simulate the case where the chromaticity is scanned for the parameter set of RF voltage and particles per bunch described in the Sec. 11.4.1. Figure 11.12 shows the transverse bunch motion in the time domain for the chromaticity : $\xi_x = -1.5, -8.0$, and -12.5 with the fixed beam intensity $N_B = 4.2 \times 10^{12}$ ppb. The extracted values for $(f_{\max}, N_{\mathrm{AM}})$ were (53.3 MHz, 340 turns) for $N_B = 1.0 \times 10^{12}$ ppb, (9.5 MHz, 1940 turns) for $\xi_x = -1.5$, (51.3 MHz, 1040 turns) for $\xi_x = -8.0$, and (76.5 MHz, 660 turns) for $\xi_x = -12.5$.

Figure 11.13 shows the measured transverse bunch motion for various chromaticity : $\xi_x = -1.5, -7.9$, and -12.5 with fixed beam intensity $N_B = 4.2 \times 10^{12}$ ppb in the time domain. The measured values for $(f_{\max}, N_{\mathrm{AM}})$ were (10 MHz, 2200 turns) for $\xi_x = -1.5$, (51.9 MHz, 2100 turns) for $\xi_x = -7.9$, and (81.3 MHz, 1800 turns) for $\xi_x = -12.5$.

11.5.2 Comparison and discussion

Figure 11.14a shows the maximum intra-bunch frequency $f_{\max}$ dependence for the chromaticity in the tracking simulation for various beam intensities. Regardless of the space charge effect, the maximum intra-bunch frequency follows $f_{\max} = 6.4|\xi_x|$ MHz (refer to Eq. (10.10) denoted by the black dashed line, identical to Eq. (4.10) derived under the assumption of weak space charge effects.) and is proportional to the chromaticity because all the data points collapse onto a single line.

Figure 11.14b shows the maximum intra-bunch frequency $f_{\max}$ dependence for the chromaticity with the measurement data. The black dashed line represents the analytical result given by Eq. (10.10). We observe the maximum intra-bunch frequency follows the analytical result : $f_{\max} = 6.4|\xi_x|$ MHz. This agreement confirms that the simulations in Fig. 11.14a are in good agreement with the measurement in Fig. 11.14b. In the end, we find that the measurements confirm that space charge effects do not influence the relationship between the maximum intra-bunch frequency and chromaticity, as predicted by the simulations.

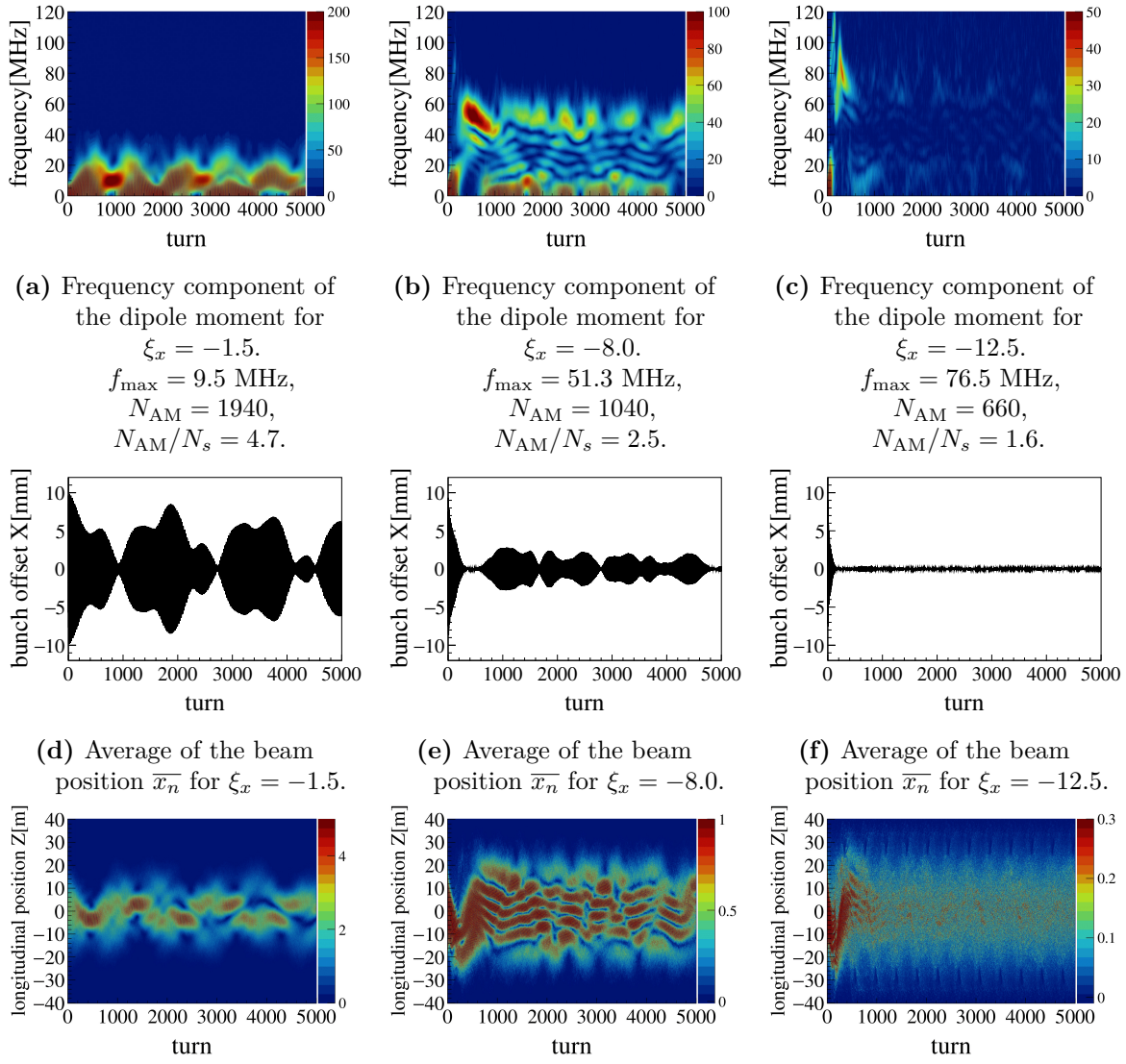

(a) Frequency component of the dipole moment for $\xi_x = -1.5$. $f_{\max} = 9.5$ MHz, $N_{\mathrm{AM}} = 1940$, $N_{\mathrm{AM}}/N_s = 4.7$.

(b) Frequency component of the dipole moment for $\xi_x = -8.0$. $f_{\max} = 51.3$ MHz, $N_{\mathrm{AM}} = 1040$, $N_{\mathrm{AM}}/N_s = 2.5$.

(c) Frequency component of the dipole moment for $\xi_x = -12.5$. $f_{\max} = 76.5$ MHz, $N_{\mathrm{AM}} = 660$, $N_{\mathrm{AM}}/N_s = 1.6$.

(d) Average of the beam position $\overline{x_n}$ for $\xi_x = -1.5$.

(e) Average of the beam position $\overline{x_n}$ for $\xi_x = -8.0$.

(f) Average of the beam position $\overline{x_n}$ for $\xi_x = -12.5$.

(g) Dipole moment $|\Delta^{(k)}\sigma_\Delta/q|$ in the bunch for $\xi_x = -1.5$.

(h) Dipole moment $|\Delta^{(k)}\sigma_\Delta/q|$ in the bunch for $\xi_x = -8.0$.

(i) Dipole moment $|\Delta^{(k)}\sigma_\Delta/q|$ in the bunch for $\xi_x = -12.5$.

Figure 11.12: Simulation of the transverse bunch motion in the time domain for the chromaticity: $\xi_x = -1.5, -8.0$, and -12.5 with the beam intensity $N_B = 4.2 \times 10^{12}$ ppb and the RF voltage $V_{\mathrm{RF}} = 263$ kV.

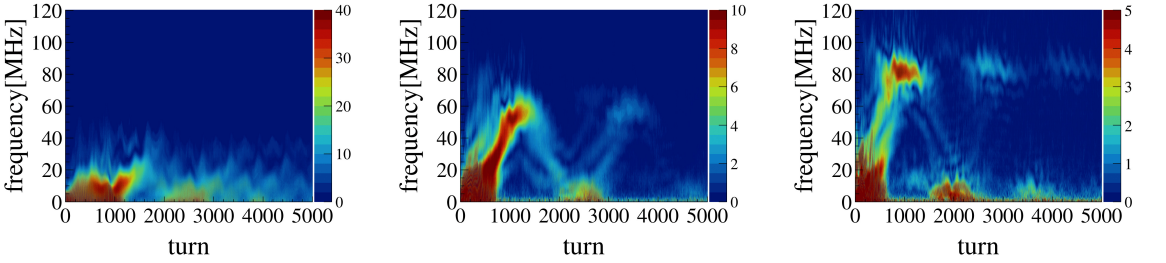

(a) Frequency component of the dipole moment for $\xi_x = -1.5$. $f_{\max} = 10$ MHz, $N_{\mathrm{AM}} = 2200$, $N_{\mathrm{AM}}/N_s = 5.4$.

(b) Frequency component of the dipole moment for $\xi_x = -7.9$. $f_{\max} = 51.9$ MHz, $N_{\mathrm{AM}} = 2100$, $N_{\mathrm{AM}}/N_s = 5.1$.

(c) Frequency component of the dipole moment for $\xi_x = -12.5$. $f_{\max} = 81.3$ MHz, $N_{\mathrm{AM}} = 1800$, $N_{\mathrm{AM}}/N_s = 4.2$.

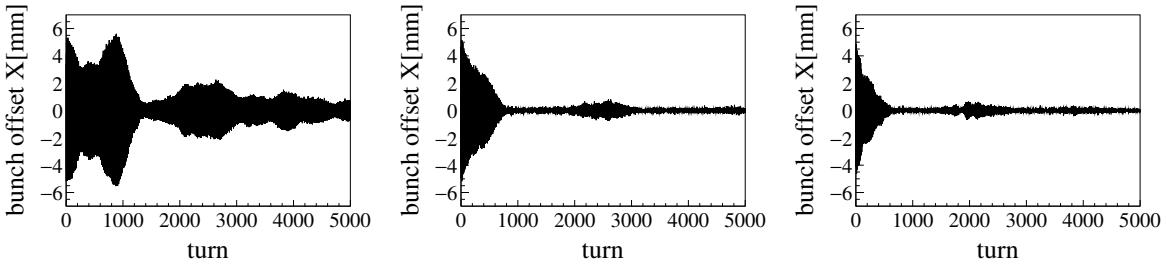

(d) Average of the beam position $\overline{x_n}$ for $\xi_x = -1.5$.

(e) Average of the beam position $\overline{x_n}$ for $\xi_x = -7.9$.

(f) Average of the beam position $\overline{x_n}$ for $\xi_x = -12.5$.

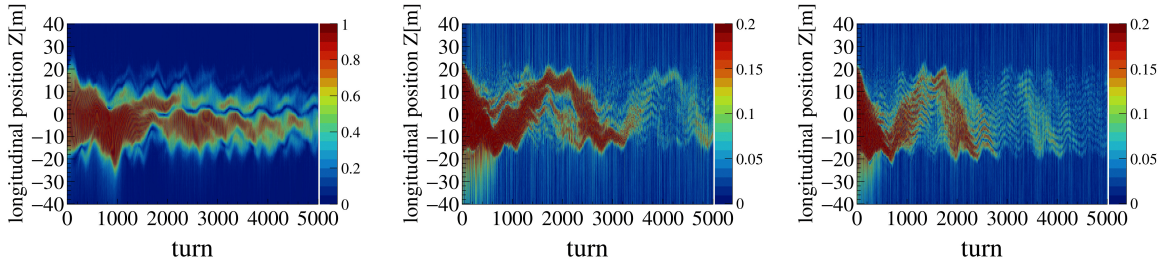

(g) Dipole moment $|\Delta(z)|$ in the bunch for $\xi_x = -1.5$.

(h) Dipole moment $|\Delta(z)|$ in the bunch for $\xi_x = -7.9$.

(i) Dipole moment $|\Delta(z)|$ in the bunch for $\xi_x = -12.5$.

Figure 11.13: Measurements of the transverse bunch motion in the time domain for the chromaticity: $\xi_x = -1.5, -7.9$, and -12.5 with the beam intensity $N_B = 4.2 \times 10^{12}$ ppb and the RF voltage $V_{\mathrm{RF}} = 263$ kV.

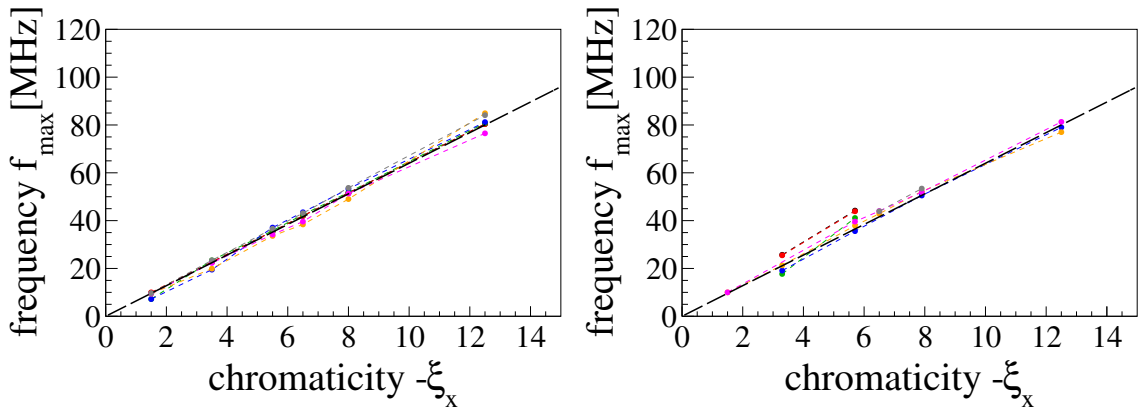

(a) tracking simulation. **(b)** measurement.

Figure 11.14: The maximum intra-bunch frequency $f_{\max}$ with fixed beam intensity for different chromaticities. In Fig. 11.14a, the black, red, green, blue, orange, magenta, and gray denote the cases of $N_B = 1.0 \times 10^{11}, 2.0 \times 10^{11}, 5.0 \times 10^{11}, 1.0 \times 10^{12}, 2.4 \times 10^{12}, 4.2 \times 10^{12}$, and 8.6×10^{12} ppb, respectively. In Fig. 11.14b, the black, red, green, blue, orange, magenta, and gray denote the cases of $N_B = 1.3 \times 10^{11}, 2.6 \times 10^{11}, 5.2 \times 10^{11}, 1.0 \times 10^{12}, 2.4 \times 10^{12}, 4.2 \times 10^{12}$, and 8.6×10^{12} ppb, respectively. The black dashed lines in both figures are the result of Eq. (10.10).

Chapter 12

Conclusion and Outlook

The motivation for this research originates from the necessity for stable operation of high-intensity proton beams in modern accelerator-based experiments. In particular, the pursuit of leptonic CP violation in long-baseline neutrino oscillation experiments demands sustained delivery of high-power proton beams, which places stringent constraints on beam stability in synchrotrons such as the J-PARC MR. Under these conditions, collective effects driven by space charge and wakefield play a central role in limiting the achievable beam intensity. This thesis has addressed these challenges by investigating the fundamental physics of intra-bunch motion in the J-PARC MR and by developing a quantitative framework to understand and control beam instabilities.

To this end, the dynamics of intra-bunch motion were investigated under the influence of direct and indirect space charge forces across a wide range of chromatic phases. By adopting an approach that combines theoretical analysis, numerical simulation, and experimental measurement, a comprehensive physical framework for high-intensity proton beams was established. A macroparticle tracking simulation code was developed to provide a unified treatment of space charge forces and wakefield, and its validity was systematically examined. Notably, the validity range of the linear approximation for space charge was clarified, requiring that the beam size remain sufficiently smaller than the chamber radius. Furthermore, within the stable operating regime of the J-PARC MR, it was determined that neither longitudinal nor transverse impedances are the dominant factors governing the observed beam motion.

A central outcome of this work is the clarification of the distinct roles played by the different components of space charge. Macroparticle simulations demonstrated that direct space charge forces enhance instability by increasing the beam growth rate, whereas indirect space charge forces arising from image currents act to suppress instability by shifting coherent mode frequencies. This distinction resolves previously conflicting predictions regarding beam stability in the presence of space charge. The reliability of the simulation framework was further confirmed by reproducing instability thresholds consistent with the Vlasov solver DELPHI in the absence of space charge.

From a theoretical perspective, the ABS model was re-established and extended to describe realistic Gaussian bunches confined in a harmonic potential. This extended framework provides physical insight into the simulation results, particularly describing the mechanisms underlying mode-dependent tune shifts and the extension of the recoherence time. The agreement between theory and simulation in the weak space charge regime supports the validity of applying the numerical framework to the strong space charge regime relevant for high-intensity operation.

Detailed analysis revealed that while Gaussian bunches typically excite all head-tail modes when space charge is neglected, the inclusion of strong space charge effects alters this

behavior. The indirect space charge effect mitigates the degeneration of head-tail modes, allowing higher-order modes to dominate at large chromaticity. This mechanism explains the observed nonlinear saturation of the recoherence period at high beam intensities: as the head-tail mode spectrum becomes distinct and harder to degenerate, further increases in beam intensity no longer lead to extended recoherence times.

These findings were validated through comparison with beam measurements at the J-PARC MR. Although variations in the injection beam emittance modulated the absolute recoherence time by changing the effective space charge strength, the simulations quantitatively reproduced the observed nonlinear saturation trend. Furthermore, the study confirmed that the linear relationship between the maximum intra-bunch oscillation frequency and chromaticity remains robust even under strong space charge conditions, reinforcing the applicability of standard diagnostic techniques in high-intensity beams.

In conclusion, this thesis establishes a quantitative and experimentally validated framework for understanding intra-bunch dynamics in high-intensity proton synchrotrons dominated by space charge effects. By clarifying the mechanisms governing instability thresholds, mode coupling, and recoherence behavior, this work provides a solid physical basis for achieving stable high-power beam operation. The finding that high-frequency components rise with increasing beam intensity is particularly relevant for the design of active mitigation systems. These results directly support ongoing and future upgrades of the J-PARC MR, where reliable operation at increased beam power is a critical requirement. More broadly, the framework and findings presented herein contribute to the realization of high-intensity neutrino beams for long-baseline neutrino experiments, including T2K and Hyper-Kamiokande, and are applicable to the design and operation of future MW-class proton accelerators.

References

[1] M. Benedikt, P. Collier, V. Mertens, J. Poole, and K. Schindl. LHC Design Report, volume III: The LHC injector chain. Technical report, 2004.

[2] L. J. Laslett. On intensity limitations imposed by transverse space-charge effects in circular particle accelerators. In *Proceedings of the 1963 Summer Study on Storage Rings, Accelerators and Experimentation at Super-High Energies, eConf C630610*, pages 324–367, 1963.

[3] G Rumolo, F Ruggiero, and F Zimmermann. Simulation of the electron-cloud build up and its consequences on heat load, beam stability, and diagnostics. *Physical Review Special Topics-Accelerators and Beams*, 4(1):012801, 2001.

[4] Takashi Asami, Hideaki Hotchi, Susumu Igarashi, Tadashi Koseki, Yoichi Sato, Noboru Yamamoto, and Takaaki Yasui. Precise evaluation of time-varying quadrupole field errors through closed-orbit measurements in the J-PARC main ring. *Physical Review Accelerators and Beams*, 28(1):012801, 2025.

[5] Shoji Nagamiya. Introduction to J-PARC. *Progress of Theoretical and Experimental Physics*, 2012(1):02B001, 2012.

[6] Y Yamazaki. The JAERI-KEK Joint Project for the High-Intensity Proton Accelerator, J-PARC. In *Proceedings of the 2003 Particle Accelerator Conference*, volume 1, pages 576–580. IEEE, 2003.

[7] 山崎良成. J-PARC 加速器夜話 (J-PARC 加速器スキーム選択の経緯). **加速器**, 21 (4):345–351, 2025.

[8] Fujio Naito. J-PARC accelerator status. *Nuclear and particle physics proceedings*, 273:181–187, 2016.

[9] E Cicek, K Futatsukawa, T Miyao, S Mizobata, N Hayashi, A Miura, and K Moriya. Implementation of an advanced mtca.4-based digitizer for monitoring comb-like beam at the j-parc linac.

[10] Masanori Ikegami. Beam commissioning and operation of the J-PARC linac. *Progress of Theoretical and Experimental Physics*, 2012(1):02B002, 2012.

[11] 森下卓俊. J-PARC リニアックの運転状況と出力増強に向けた検討. **加速器**, 21(4): 288–296, 2025.

[12] H Hotchi, M Kinsho, K Hasegawa, N Hayashi, Y Hikichi, S Hiroki, J Kamiya, K Kanazawa, M Kawase, F Noda, et al. Beam commissioning of the 3-GeV rapid cycling synchrotron of the Japan Proton Accelerator Research Complex. *Physical Review Special Topics—Accelerators and Beams*, 12(4):040402, 2009.

[13] H Hotchi, H Harada, N Hayashi, S Kato, M Kinsho, K Okabe, PK Saha, Y Shobuda, F Tamura, N Tani, et al. Achievement of a low-loss 1-MW beam operation in the

3-GeV rapid cycling synchrotron of the Japan Proton Accelerator Research Complex. *Physical Review Accelerators and Beams*, 20(6):060402, 2017.

[14] 山本風海. J-PARC 速い繰り返しの 3 GeV シンクロトロンにおける 1 MW 連続運転と 1 MW 超ビーム加速に向けた検討. **加速器**, 21(4):297–304, 2025.

[15] 發知英明, 原田寛之, 岡部晃大, 菖蒲田義博, 田村文彦, 吉本政弘, et al. J-PARC RCS におけるビーム力学的研究とビーム損失の低減. **加速器**, 16(2):109–118, 2019.

[16] T. Koseki et al. Beam commissioning and operation of the J-PARC main ring synchrotron. *Progress of Theoretical and Experimental Physics*, 2012(1):02B004, 2012.

[17] H Hotchi, Y Sato, et al. Progress of Beam Power Upgrade in J-PARC Main Ring. *Proc. IPAC*, pages 1124–1127, 2025.

[18] S. Igarashi et al. Accelerator design for 1.3 MW beam power operation of the J-PARC main ring. *Progress of Theoretical and Experimental Physics*, 2021(3):033G01, 2021.

[19] S. Igarashi et al. High-power beam operation at J-PARC. In *Proceedings of the 61st ICFA Advanced Beam Dynamics Workshop on High-Intensity and High-Brightness Hadron Beams*, pages 147–152, Daejeon, Korea, 2018.

[20] T. Koseki et al. Upgrade plan of J-PARC MR-toward 1.3 MW beam power. In *Proceedings of the 9th International Particle Accelerator Conference*, pages 966–969, Vancouver, BC, Canada, 2018.

[21] T. Yasui. J-PARC MR operation with the high repetition rate upgrade. In *Proceedings of the 14th International Particle Accelerator Conference*, pages 1294–1298, Venice, Italy, 2023.

[22] T. Yasui, S. Igarashi, Y. Sato, and H. Hotchi. First Result of the High Repetition Operation in J-PARC MR. In *Proceedings of the 23rd International Workshop on Neutrinos from Accelerators*, volume 8, page 23, Salt Lake City, UT, USA, 2023.

[23] 五十嵐進. J-PARC 主リングのビームパワー増強. **加速器**, 21(4):305–313, 2025.

[24] Takuya Sugimoto, Kuanjun Fan, Koji Ishii, Hiroshi Matsumoto, et al. Upgrade of the injection kicker system for J-PARC main ring. *Proc. IPAC*, pages 526–528, 2014.

[25] Yuichi Morita, Yoshinori Kurimoto, Kazuki Miura, Daichi Naito, Ryu Sagawa, Tetsushi Shimogawa, and Tatsuya Yoshino. Capacitor bank of power supply for J-PARC MR main magnets. *Nuclear Instruments and Methods in Physics Research Section A: Accelerators, Spectrometers, Detectors and Associated Equipment*, 901: 156–163, 2018.

[26] Tetsushi Shimogawa, Yoshinori Kurimoto, Yuichi Morita, Kazuki Miura, and Daichi Naito. A control system of new magnet power converter for J-PARC main ring upgrade. *IEEE Transactions on Nuclear Science*, 66(7):1236–1241, 2019.

[27] Kiyomi Seiya, K Hara, K Hasegawa, M Nomura, C Ohmori, H Okita, T Shimada, Y Sugiyama, F Tamura, M Yamamoto, et al. RF system upgrade for 1.3 MW operation of J-PARC main ring. *Proc. IPAC*, 24:19–24, 2024.

[28] Masashi Shirakata, Jumpei Takano, and Kotomi Kadowaki. Beam collimator system which consists of seven units in J-PARC main ring. In *Proceedings of the 19th annual meeting of Particle Accelerator Society of Japan*, pages 756–760, 2022.

[29] MJ Shirakata, S Igarashi, K Ishii, Y Sato, J Takano, and Scandic Triangeln Hotel. New arrangement of collimators of J-PARC main ring. *Proc. HB2016, Malmö, Sweden, THAM4Y01*, pages 543–547, 2016.

[30] Tatsunobu Shibata, Koji Ishii, T Sugimoto, Hiroshi Matsumoto, and K Fan. The development of a new low field septum magnet system for fast extraction in main ring of J-PARC. In *Journal of Physics: Conference Series*, volume 1067, page 052020. IOP Publishing, 2018.

[31] Tatsunobu Shibata, Koji Ishii, Takuya Sugimoto, Noriyuki Matsumoto, Hiroshi Matsumoto, and Kuanjun Fan. The new high field septum magnets for upgrading of fast extraction in MR of J-PARC. In *Proceedings of the 3rd J-PARC Symposium (J-PARC2019)*, page 011034, 2021.

[32] Soma Iwata, Koji Ishii, Tatsunobu Shibata, and Tomohiro Takayanagi. Solutions for manufacturing defects of the new septum magnets using for fast extraction in J-PARC main ring. In *Proceedings of the 20th annual meeting of Particle Accelerator Society of Japan*, pages 539–544, 2023.

[33] Takuro Kimura, Norihiko Kamikubota, Kenichi Sato, Shuei Yamada, Koji Ishii, Tatsunobu Shibata, and Takuya Sugimoto. Development of a ms-Abort System via J-PARC MR-MPS. In *Proceedings of the 15th annual meeting of Particle Accelerator Society of Japan*, pages 609–612, 2018.

[34] T Toyama, Y Hashimoto, K Hanamura, S Hatakeyama, M Okada, and M Tejima. Performance and upgrade of BPMs at the J-PARC MR. *Proc. IBIC' 12*, pages 107–111, 2012.

[35] Yoshinori Kurimoto and Keigo Nakamura. Development and applications of a multi-purpose digital controller with a System-on-Chip FPGA for accelerators. *Nuclear Instruments and Methods in Physics Research Section A: Accelerators, Spectrometers, Detectors and Associated Equipment*, 840:160–167, 2016.

[36] Takeshi Toyama, K Satou, S Hatakeyama, and Tokai JAEA. Recovery and check of the switching relay in the BPMs in the J-PARC MR. *Proc. IPAC'23*, pages 4706–4709.

[37] 外山毅. J-PARC 加速器のビーム結合インピーダンスの影響と対策. **加速器**, 21(4): 314–322, 2025.

[38] Shuichiro Hatakeyama, Takeshi Toyama, and Masaki Tejima. A system for monitoring of the transverse injection error and betatron tune in j-parc mr, 2007.

[39] Hiroyuki Sako, S Hiroki, H Takahashi, K Yamamoto, and H Ikeda. An application for beam profile reconstruction with multi-wire profile monitors at J-PARC RCS. In *TUPC092, this conference*, 2008.

[40] Kiwamu Sato, Yoshinori Hashimoto, Yoichi Sato, Susumu Igarashi, Tadashi Koseki,

and E Hamada. Multi-Ribbon Profile Monitor for high power proton beam at J-PARC MR abort line. In *Journal of Physics: Conference Series*, volume 1350, page 012152. IOP Publishing, 2019.

[41] Takeshi Toyama, D Arakawa, Y Hashimoto, S Lee, T Miura, Suguru Muto, N Hayashi, R Toyokawa, and Junichi Kishiro. Beam diagnostics for the J-PARC main ring synchrotron. In *Proceedings of the 2005 Particle Accelerator Conference*, pages 958–960. IEEE, 2005.

[42] Takeshi Toyama, D Arakawa, M Arinaga, K HanamuraC, H HaradaB, Y Hashimoto, S HatakeyamaC, N Hayashi, S Hiramatsu, S IgarashiA, et al. Beam diagnostics at the first beam commissioning of the J-PARC MR. *Proceedings of PAC09, Vancouver, BC, Canada*, 2009.

[43] Yoshinori Hashimoto, Shigenori HiramatsuA, Dai ArakawaA, Mitsuhiro ArinagaA, Masaki TejimaA, and Takeshi ToyamaA. Characteristics of a DCCT for the J-PARC main ring. In *Proceedings of the 8th annual meeting of Particle Accelerator Society of Japan*, pages 5–5, 2011.

[44] Y Ohmori et al. A calibration method for beam DCCT of J-PARC main ring. In *Proceedings of the 8th annual meeting of Particle Accelerator Society of Japan*, pages 4–4, 2011.

[45] 小林隆. J-PARC におけるビーム利用研究. **加速器**, 21(4):272–278, 2025.

[46] POT & Power over Entire T2K History: https://t2k.org/docs/plotsx/frequentlyupdated/Beam/2025-03-18/. .

[47] K Abe, N Abgrall, H Aihara, Y Ajima, JB Albert, D Allan, P-A Amaudruz, C Andreopoulos, B Andrieu, MD Anerella, et al. The T2K experiment. *Nuclear Instruments and Methods in Physics Research Section A: Accelerators, Spectrometers, Detectors and Associated Equipment*, 659(1):106–135, 2011.

[48] K. Abe et al. Updated T2K measurements of muon neutrino and antineutrino disappearance using 3.6×10^{21} protons on target. *Physical Review D*, 108(7):072011, 2023.

[49] K. Abe et al. Indication of electron neutrino appearance from an accelerator-produced off-axis muon neutrino beam. *Physical Review Letters*, 107(4):041801, 2011.

[50] K. Abe et al. Observation of electron neutrino appearance in a muon neutrino beam. *Physical Review Letters*, 112(6):061802, 2014.

[51] K. Abe et al. Constraint on the matter-antimatter symmetry-violating phase in neutrino oscillations. *Nature*, 580(7803):339–344, 2020.

[52] K Abe, H Aihara, A Ajmi, C Alt, C Andreopoulos, M Antonova, S Aoki, Y Asada, Y Ashida, A Atherton, et al. J-PARC neutrino beamline upgrade technical design report. 2019.

[53] Tatsushi Nakamoto, Norio Higashi, Toru Ogitsu, Akio Terashima, Yasuo Ajima, Michael Anerella, Ramesh Gupta, Hisashi Hattori, Tadashi Ichihara, Yosuke Iwamoto, et al. Design of superconducting combined function magnets for the 50 GeV proton

beam line for the J-PARC neutrino experiment. *IEEE transactions on applied superconductivity*, 14(2):616–619, 2004.

[54] J Gareyte and F Sacherer. Head-tail type instabilities in the cern ps and booster. Technical report, CERN-MPS-DL-74-4, 1974.

[55] V. Kornilov and O. Boine-Frankenheim. Transverse decoherence and coherent spectra in long bunches with space charge. *Physical Review Special Topics-Accelerators and Beams*, 15(11):114201, 2012.

[56] R. E. Meller, A. W. Chao, J. M. Peterson, S. G. Peggs, and M. Furman. Decoherence of kicked beams. Technical Report SSC-N-360, 1987.

[57] I. Karpov, V. Kornilov, and O. Boine-Frankenheim. Early transverse decoherence of bunches with space charge. 19(12):124201, 2016.

[58] I. Karpov. *Damping of coherent oscillations in intense ion beams*. PhD thesis, Darmstadt, Tech. U., 2017.

[59] M. Blaskiewicz. Fast head-tail instability with space charge. *Physical Review Special Topics-Accelerators and Beams*, 1(4):044201, 1998.

[60] K. Y. Ng. *Physics of Intensity Dependent Beam Instabilities*. World Scientific, Singapore, 2002.

[61] A. W. Chao. *Physics of Collective Beam Instabilities in High Energy Accelerators*. John Wiley & Sons, Inc., New York, 1993.

[62] M. Abramowitz and I. A. Stegun. Handbook of Mathematical Functions With Formulas, Graphs, and Mathematical Tables. 1974.

[63] G. L. Sabbi. Simulation of single-bunch collective effects in LEP by linear expansion of the distribution moments. Technical Report CERN SL/95-25(AP), 1995.

[64] G. L. Sabbi. TRISIM user's guide. Technical Report CERN SL/94-73(AP), 1994.

[65] K. L. F. Bane and M. Sands. The short-range resistive wall wakefields. Technical Report SLAC/AP-87, Stanford Linear Accelerator Center, Stanford University, Stanford, CA, USA, 1991.

[66] N. Yoshimura, T. Toyama, Y. Shobuda, T. Nakamura, K. Omi, A. Kobayashi, M. Okada, Y. Sato, and T. Nakaya. Study on simulation code for transverse instabilities for the J-PARC MR. In *Proceedings of the 20th Annual Meeting of the Particle Accelerator Society of Japan*, pages 260–264, 2023, (Japanese).

[67] Y. Shobuda and K. Yokoya. Resistive wall impedance and tune shift for a chamber with a finite thickness. *Physical Review E*, 66(5):056501, 2002.

[68] K. Yokoya. Resistive wall impedance of beam pipes of general cross section. *Particle Accelerators*, 41:221–248, 1993.

[69] R. L. Gluckstern, J. van Zeijts, and B. Zotter. Coupling impedance of beam pipes of general cross section. *Physical Review E*, 47(1):656, 1993.

[70] A. Kobayashi, T. Toyama, Y. Sato, S. Igarashi, M. Yoshii, and Y. Sugiyama. The investigation on the time structure of the wake field at the J-PARC MR. In *Proceedings of the 16th Annual Meeting of the Particle Accelerator Society of Japan*, pages 223–227, 2019, (Japanese).

[71] I. M. Kapchinskij and V. V. Vladimirskij. Limitations of proton beam current in a strong focusing linear accelerator associated with the beam space charge. In *Proceedings of the International Conference on High Energy Accelerators and Instrumentation*, page 274, 1959.

[72] V. Kornilov and O. Boine-Frankenheim. Head-tail instability and Landau damping in bunches with space charge. *Physical Review Special Topics-Accelerators and Beams*, 13(11):114201, 2010.

[73] R. Singh, O. Boine-Frankenheim, O. Chorniy, P. Forck, R. Haseitl, W. Kaufmann, P. Kowina, K. Lang, and T. Weiland. Interpretation of transverse tune spectra in a heavy-ion synchrotron at high intensities. *Physical Review Special Topics-Accelerators and Beams*, 16(3):034201, 2013.

[74] V. Kornilov and O. Boine-Frankenheim. Simulation studies & code validation for the head-tail instability with space charge. In *Proceedings of the 10th International Computational Accelerator Physics Conference*, volume San Francisco, CA, USA, pages 58–63, 2010.

[75] O. Boine-Frankenheim and V. Kornilov. Transverse Schottky noise spectrum for bunches with space charge. *Physical Review Special Topics-Accelerators and Beams*, 12(11):114201, 2009.

[76] N. Mounet. DELPHI: An analytic Vlasov Solver for impedance-driven modes. Technical Report CERN Technical Report No. CERN-ACC-SLIDES-2014-0066, 2014.

[77] N. Mounet. Direct Vlasov solvers. arXiv preprint arXiv:2006.09080, 2020.

[78] Y. Shobuda, Y. H. Chin, P. K. Saha, H. Hotchi, H. Harada, Y. Irie, F. Tamura, N. Tani, T. Toyama, Y. Watanabe, et al. Theoretical elucidation of space charge effects on the coupled-bunch instability at the 3 GeV rapid cycling synchrotron at the Japan Proton Accelerator Research Complex. *Progress of Theoretical and Experimental Physics*, 2017(1):013G01, 2017.

[79] P. K. Saha, Y. Shobuda, H. Hotchi, H. Harada, N. Hayashi, M. Kinsho, F. Tamura, N. Tani, M. Yamamoto, Y. Watanabe, et al. Simulation, measurement, and mitigation of beam instability caused by the kicker impedance in the 3-GeV rapid cycling synchrotron at the Japan Proton Accelerator Research Complex. *Physical Review Accelerators and Beams*, 21(2):024203, 2018.

[80] A. Burov. Convective instabilities of bunched beams with space charge. *Physical Review Accelerators and Beams*, 22(3):034202, 2019.

[81] Y Alexahin, A Burov, and V Shiltsev. Landau damping with electron lenses in space-charge dominated beams. *Journal of Instrumentation*, 16(03):P03046, 2021.

[82] Alexey Burov. Head-tail modes for strong space charge. *Physical Review Special Topics—Accelerators and Beams*, 12(4):044202, 2009.

[83] A Burov. Erratum: Head-tail modes for strong space charge. *Physical Review Special Topics—Accelerators and Beams*, 12(10), 2009.

[84] Y. Shobuda, Y. H. Chin, K. Takata, T. Toyama, and K. Nakamura. Triangle and concave pentagon electrodes for an improved broadband frequency response of stripline beam position monitors. *Physical Review Accelerators and Beams*, 19(2): 021003, 2016.

[85] Junichi Odagiri, Sakae Araki, Kazuro Furukawa, N Kamikubota, A Kiyomichi, H Nakagawa, and TT Nakamura. Application of EPICS on F3RP61 to accelerator control. In *Proceedings of the 6th Annual Meeting of Particle Accelerator Society of Japan, Tokai*, pages 916–918, 2009.

[86] T Iitsuka, S Motohashi, M Takagi, and S Yoshida. Virtual IO controllers at J-PARC MR using Xen. 2011.

[87] N Kamikubota, N Yamamoto, H Nakagawa, S Yamada, KC Sato, T Katoh, J Odagiri, N Kikuzawa, Y Kato, M Kawase, et al. J-PARC control toward future reliable operation. *Proc. ICALEPCS' 11*, pages 378–381, 2011.

[88] Norihiko Kamikubota, S Yamada, KC Sato, N Yamamoto, T Iitsuka, T Aoyama, S Yoshida, and H Nemoto. Operation experience and migration of I/O controllers for J-PARC main ring. *Proceedings of PCaPAC in Campinas, Brazil*, 2016.

[89] Fumio Hiroki, Hiroshi Yoshikawa, Y Takeuchi, and K Kudo. Personnel protection system in J-PARC linac. In *Proceedings of the 1st Annual Meeting of Particle Accelerator Society of Japan,(August 4-6, 2004) p*, volume 159, 2004.

[90] J Chiba, K Furukawa, N Kamikubota, T Katoh, H Nakagawa, K Niki, J Odagiri, Y Takeuchi, N Yamamoto KEK M Furuse, Y Kato, et al. Present status of the J-PARC control system. In *ICALEPCS*, volume 3, pages 1–5, 2003.

[91] H Nakagawa, A Akiyama, Y Kato, and JI Odagiri. The accelerator protection system based on embedded EPICS for J-PARC. *Proceedings of ICALEPCS2009, Kobe*, 2009.

[92] Ken Sakashita, Megan Friend, K Nakayoshi, S Yamasu, and Y Koshio. Upgrade of the machine protection system toward 1.3 MW operation of the j-PARC neutrino beamline. In *Proceedings of the 7th International Beam Instrumentation Conference, IBIC 2018*, pages 18–21. Joint Accelerator Conferences Website (JACoW), 2018.

[93] KC Sato, T Kimura, S Yamada, N Kamikubota, and Noboru Yamamoto. The software-based machine protection system using EPICS in J-PARC MR. In *17th International Conference on Accelerator and Large Experimental Physics Control Systems (ICALEPCS'19), New York, NY, USA, 05-11 October 2019*, pages 1418–1420. JACOW Publishing, Geneva, Switzerland, 2020.

[94] Fumihiko Tamura and JAERI Hiroshi Yoshikawa. J-PARC timing system. *Extraction*, 10(500μs):20ms, 2003.

[95] Tadahiko Katoh, K Furukawa, N Kamikubota, H Nakagawa, J Odagiri, G Shen, N Takeuchi, N Yamamoto, M Yoshii, H Sakaki, et al. Present status of the J-PARC control system. In *Proceedings of the 2005 Particle Accelerator Conference*, pages 302–304. IEEE, 2005.

[96] Fumihiko Tamura, Yasuyuki Sugiyama, Masahito Yoshii, and Masatsugu Ryoshi. Development of next-generation LLRF control system for J-PARC rapid cycling synchrotron. *IEEE Transactions on Nuclear Science*, 66(7):1242–1248, 2019.

[97] Takao Kato, M Ikegami, Sheng Wang, and Shinian Fu. Beam study with RF choppers in the MEBT of the J-PARC proton linac. In *Proceedings of the 2003 Particle Accelerator Conference*, volume 3, pages 1455–1457. IEEE, 2003.

[98] Sheng Wang, Shinian Fu, and Takao Kato. The development and beam test of an RF chopper system for J-PARC. *Nuclear Instruments and Methods in Physics Research Section A: Accelerators, Spectrometers, Detectors and Associated Equipment*, 547 (2-3):302–312, 2005.

[99] PK Saha, M Yoshimoto, S Hatakeyama, H Hotchi, H Harada, F Tamura, K Yamamoto, Y Yamazaki, M Kinsho, and Y Irie. First measurement and online monitoring of the stripper foil thinning and pinhole formation to achieve a longer foil lifetime in high-intensity accelerators. *Physical Review Accelerators and Beams*, 23(8):082801, 2020.

[100] Kazami Yamamoto and Shinichi Kato. Effect of injection energy on residual dose around the charge exchange foil. *Physical Review Special Topics—Accelerators and Beams*, 15(12):120401, 2012.

[101] H Hotchi, H Harada, N Hayashi, M Kinsho, PK Saha, Y Shobuda, F Tamura, K Yamamoto, M Yamamoto, M Yoshimoto, et al. Beam loss reduction by injection painting in the 3-GeV rapid cycling synchrotron of the Japan Proton Accelerator Research Complex. *Physical Review Special Topics—Accelerators and Beams*, 15(4): 040402, 2012.

[102] Fumihiko Tamura, Masanobu Yamamoto, Masahito Yoshii, Chihiro Ohmori, Masahiro Nomura, Alexander Schnase, Makoto Toda, Hiromitsu Suzuki, Taihei Shimada, Keigo Hara, et al. Longitudinal painting with large amplitude second harmonic rf voltages in the rapid cycling synchrotron of the Japan Proton Accelerator Research Complex. *Physical Review Special Topics—Accelerators and Beams*, 12(4): 041001, 2009.

[103] N Tani, T Adachi, S Igarashi, Y Watanabe, H Someya, H Sato, and J Kishiro. Design of RCS magnets for J-PARC 3-GeV synchrotron. *IEEE Transactions on Applied superconductivity*, 14(2):409–412, 2004.

[104] Chihiro Ohmori, Eizi Ezura, Keigo Hara, Katsushi Hasegawa, Yasuhiro Makida, Ryotaro Muto, Masahiro Nomura, Toru Ogitsu, Taihei Shimada, Alexander Schnase, et al. Development of a high gradient rf system using a nanocrystalline soft magnetic alloy. *Physical Review Special Topics—Accelerators and Beams*, 16(11):112002, 2013.

[105] Fumihiko Tamura, Masanobu Yamamoto, Chihiro Ohmori, Alexander Schnase,

Masahito Yoshii, Masahiro Nomura, Makoto Toda, Taihei Shimada, Keigo Hara, and Katsushi Hasegawa. Multiharmonic rf feedforward system for beam loading compensation in wide-band cavities of a rapid cycling synchrotron. *Physical Review Special Topics—Accelerators and Beams*, 14(5):051004, 2011.

[106] Kazami Yamamoto, Takeo Shibata, Norio Ogiwara, and Michikazu Kinsho. Secondary electron emission yields from the J-PARC RCS vacuum components. *Vacuum*, 81 (6):788–792, 2007.

[107] Junichiro Kamiya, Tomohiro Takayanagi, and Masao Watanabe. Performance of extraction kicker magnet in a rapid cycling synchrotron. *Physical Review Special Topics—Accelerators and Beams*, 12(7):072401, 2009.

[108] Susumu Sato, T Tomisawa, H Akikawa, Akira Ueno, S Lee, Z Igarashi, M Ikegami, T Toyama, and N Kamikubota. Developments of the calibation tools for beam position monitor at J-PARC linac. In *Proceedings of the 2005 Particle Accelerator Conference*, pages 2777–2779. IEEE, 2005.

[109] Akihiko Miura, Nobuo Ouchi, Hidetomo Oguri, Kazuo Hasegawa, Tomoaki Miyao, and Masanori Ikegami. Design and delivery of beam monitors for the energy-upgraded linac in J-PARC. *Journal of the Korean Physical Society*, 66(3):364–372, 2015.

[110] Naoki Hayashi, S Hiroki, J Kishiro, Y Teruyama, R Toyokawa, D Arakawa, S Lee, T Miura, and T Toyama. Development of the beam diagnostics system for the J-PARC Rapid-Cycling Synchrotron. In *Proceedings of the 2005 Particle Accelerator Conference*, pages 299–301. IEEE, 2005.

[111] N Hayashi, S Hiroki, R Saeki, R Toyokawa, K Yamamoto, D Arakawa, S Hiramatsu, S Lee, K Satou, M Tejima, et al. The beam position monitor system of the J-PARC RCS. In *Proceedings of EPAC*, pages 1128–1130, 2008.

[112] N Hayashi, M Kawase, S Hatakeyama, S Hiroki, R Saeki, H Takahashi, Y Teruyama, R Toyokawa, D Arakawa, S Hiramatsu, et al. Beam position monitor system of J-PARC RCS. *Nuclear Instruments and Methods in Physics Research Section A: Accelerators, Spectrometers, Detectors and Associated Equipment*, 677:94–106, 2012.

[113] Akihiko Miura, J Tamura, Y Liu, and T Miyao. Bunch shape monitor development in J-PARC linac. In *Journal of Physics: Conference Series*, volume 874, page 012080. IOP Publishing, 2017.

[114] Susumu Igarashi, DA Arakawa, Yoshinori Hashimoto, M Tejima, Takeshi Toyama, Kotoku Hanamura, and MELCO SC. Flying Wire Beam Profile Monitors at the J-PARC MR. *Proceedings of IBIC2012, Tsukuba, Japan*, 2012.

[115] Yoshinori Hashimoto, Y Sato, T Toyama, T Mitsuhashi, T Nakamura, Masaki Tejima, M Uota, and H Sakai. Development of a profile monitor using OTR and fluorescence for injected beams in J-PARC main ring. *Proc. IBIC2021, Pohang, Rep of Korea*, pages 263–267, 2021.

[116] Kenichirou Satou, N Hayashi, S Lee, and Takeshi Toyama. A prototype of residual gas ionization profile monitor for J-PARC RCS. *EPAC 2006*, (1):1163–1165, 2006.

[117] Yoshinori Sato, Keizo Agari, Erina Hirose, Masaharu Ieiri, Youichi Igarashi, Susumu Inaba, Yoji Katoh, Michifumi Minakawa, Hiroyuki Noumi, Masatoshi Saito, et al. Development of residual gas ionization profile monitor for high intensity proton beams. In *IEEE Nuclear Science Symposium Conference Record, 2005*, volume 2, pages 1043–1046. IEEE, 2005.

[118] Seishu Lee, M Tanaka, T Toyama, and J Kishiro. The beam loss monitor system of the J-PARC linac, 3GeV RCS and 50GeV MR. *Signal [AU]*, 20:25, 2004.

[119] Kenichirou Satou, Takeshi Toyama, Norihiko Kamikubota, Shuei Yamada, and Susumu Yoshida. Development of wide dynamic range beam loss monitor system for J-PARC main ring. In *Journal of Physics: Conference Series*, volume 874, page 012087. IOP Publishing, 2017.

[120] Fujio Maekawa, Masahide Harada, Kenichi Oikawa, Makoto Teshigawara, Tetsuya Kai, Shin-ichiro Meigo, Motoki Ooi, Shinichi Sakamoto, Hiroshi Takada, Masatoshi Futakawa, et al. First neutron production utilizing J-PARC pulsed spallation neutron source JSNS and neutronic performance demonstrated. *Nuclear Instruments and Methods in Physics Research Section A: Accelerators, Spectrometers, Detectors and Associated Equipment*, 620(2-3):159–165, 2010.

[121] Kenji Nakajima, Yukinobu Kawakita, Shinichi Itoh, Jun Abe, Kazuya Aizawa, Hiroyuki Aoki, Hitoshi Endo, Masaki Fujita, Kenichi Funakoshi, Wu Gong, et al. Materials and life science experimental facility (MLF) at the Japan proton accelerator research complex II: neutron scattering instruments. *Quantum Beam Science*, 1(3): 9, 2017.

[122] K Oikawa, F Maekawa, M Harada, T Kai, S Meigo, Y Kasugai, M Ooi, K Sakai, M Teshigawara, S Hasegawa, et al. Design and application of NOBORU—NeutrOn Beam line for observation and research use at J-PARC. *Nuclear Instruments and Methods in Physics Research Section A: Accelerators, Spectrometers, Detectors and Associated Equipment*, 589(2):310–317, 2008.

[123] 牧村俊助, 的場史朗, and 河村成肇. J-PARC MLF ミュオン生成標的. **加速器**, 18(4): 202–209, 2022.

[124] Y Miyake, K Nishiyama, N Kawamura, P Strasser, S Makimura, A Koda, K Shimomura, H Fujimori, K Nakahara, R Kadono, et al. J-PARC muon source, muse. *Nuclear Instruments and Methods in Physics Research Section A: Accelerators, Spectrometers, Detectors and Associated Equipment*, 600(1):22–24, 2009.

[125] Ryosuke Kadono and Yasuhiro Miyake. MUSE, the goddess of muons, and her future. *Reports on Progress in Physics*, 75(2):026302, 2012.

[126] Yasuhiro Miyake, Koichiro Shimomura, Naritoshi Kawamura, Patrick Strasser, Akihiko Koda, Shunsuke Makimura, Hiroshi Fujimori, Yutaka Ikedo, Kazutaka Nakahara, Soshi Takeshita, et al. J-parc muon facility, muse. *Physics Procedia*, 30: 46–49, 2012.

[127] Hiromi Iinuma et al. New approach to the Muon g-2 and EDM experiment at J-PARC. In *Journal of Physics: Conference Series*, volume 295, page 012032, 2011.

[128] Tsutomu Mibe et al. Measurement of muon g-2 and EDM with an ultra-cold muon beam at J-PARC. *Nuclear Physics B-Proceedings Supplements*, 218(1):242–246, 2011.

[129] Toshiyuki Takahashi, Satoshi Adachi, Michelangelo Agnello, Kanae Aoki, Osamu Araoka, Bernd Bassalleck, Elena Botta, Stefania Bufalino, Nobuyuki Chiga, Petr Evtoukhovitch, et al. "Beam and SKS spectrometers at the K1.8 beam line. *Progress of Theoretical and Experimental Physics*, 2012(1):02B010, 2012.

[130] JK Ahn, B Beckford, M Campbell, SH Chen, J Comfort, K Dona, MS Farrington, K Hanai, N Hara, H Haraguchi, et al. Study of the KL $\rightarrow \pi\ 0\ \nu\ \nu^{-}$ Decay at the J-PARC KOTO Experiment. *Physical review letters*, 126(12):121801, 2021.

[131] Yoshitaka Kuno. A search for muon-to-electron conversion at J-PARC: The COMET experiment. *Progress of Theoretical and Experimental Physics*, 2013(2):022C01, 2013.

[132] COMET collaboration, R Abramishvili, G Adamov, RR Akhmetshin, A Allin, JC Angélique, V Anishchik, M Aoki, D Aznabayev, I Bagaturia, et al. COMET Phase-I technical design report. *Progress of Theoretical and Experimental Physics*, 2020(3):033C01, 2020.

[133] T Nakadaira. The graphite target for J-PARC neutrino beam-line. *Journal of Radioanalytical and Nuclear Chemistry*, 305(3):777–782, 2015.

[134] A. K. Ichikawa. Design concept of the magnetic horn system for the T2K neutrino beam. *Nuclear Instruments and Methods in Physics Research Section A: Accelerators, Spectrometers, Detectors and Associated Equipment*, 690:27–33, 2012.

[135] Y. Ashida, M. Friend, A. K. Ichikawa, T. Ishida, H. Kubo, K. G. Nakamura, K. Sakashita, and W. Uno. A new electron-multiplier-tube-based beam monitor for muon monitoring at the T2K experiment. *Progress of Theoretical and Experimental Physics*, 2018(10):103H01, 2018.

[136] T. Honjo, Y. Ashida, O. F. Auersperg-Castell, M. Friend, I. Heitkamp, A. K. Ichikawa, M. Ishitsuka, N. Izumi, S. Kasama, S. Kashiwagi, et al. Performance evaluation of electron multiplier tubes as a high-intensity muon beam monitor of accelerator neutrino experiments. *Progress of Theoretical and Experimental Physics*, 2024(12):123H01, 2024.

[137] Matsuoka K., Ichikawa A., Kubo H., Maruyama T., Murakami A., Nakaya T., and Yokoyama M. Development and production of the ionization chamber for the T2K muon monitor. *Nuclear Instruments and Methods in Physics Research Section A: Accelerators, Spectrometers, Detectors and Associated Equipment*, 623(1):385–387, 2010.

[138] K Matsuoka, A. K. Ichikawa, H. Kubo, K. Maeda, T. Maruyama, C. Matsumura, A. Murakami, T. Nakaya, K. Nishikawa, T. Ozaki, et al. Design and performance of the muon monitor for the T2K neutrino oscillation experiment. *Nuclear Instruments and Methods in Physics Research Section A: Accelerators, Spectrometers, Detectors and Associated Equipment*, 624(3):591–600, 2010.

[139] K. Abe, N. Abgrall, Y. Ajima, H. Aihara, J. B. Albert, C. Andreopoulos, B. Andrieu, M. D. Anerella, S. Aoki, O. Araoka, et al. Measurements of the T2K neutrino beam properties using the INGRID on-axis near detector. *Nuclear Instruments and Methods in Physics Research Section A: Accelerators, Spectrometers, Detectors and Associated Equipment*, 694:211–223, 2012.

[140] M. Barranco Luque, M. Calvetti, L. Dumps, C. Girard, H. Hoffmann, G. Maurin, L. Naumann, J. Perez, G. Piano Mortari, A. Placci, P. Queru, M. Rijssenbeek, C. Rubbia, B. Sadoulet, and C. Tao. The construction of the central detector for an experiment at the CERN p-p collider. *Nuclear Instruments and Methods*, 176(1): 175–180, 1980.

[141] P-A Amaudruz, M. Barbi, D. Bishop, N. Braam, D. G. Brook-Roberge, S. Giffin, S. Gomi, P. Gumplinger, K. Hamano, N. C. Hastings, et al. The T2K fine-grained detectors. *Nuclear Instruments and Methods in Physics Research Section A: Accelerators, Spectrometers, Detectors and Associated Equipment*, 696(22):1–31, 2012.

[142] Nicolas Abgrall, B. Andrieu, P. Baron, P. Bene, V. Berardi, J. Beucher, P. Birney, F. Blaszczyk, Alain Blondel, C. Bojechko, et al. Time projection chambers for the T2K near detectors. *Nuclear Instruments and Methods in Physics Research Section A: Accelerators, Spectrometers, Detectors and Associated Equipment*, 637(1):25–46, 2011.

[143] A Korzenev, F Barao, S Bordoni, D Breton, F Cadoux, Y Favre, M Khabibullin, A Khotyantsev, Y Kudenko, T Lux, et al. A 4π time-of-flight detector for the ND280/T2K upgrade. *Journal of Instrumentation*, 17(01):P01016, 2022.

[144] D. Allan, C. Andreopoulos, C. Angelsen, G. J. Barker, G. Barr, S. Bentham, I. Bertram, S. Boyd, K. Briggs, R. G. Calland, et al. The electromagnetic calorimeter for the T2K near detector ND280. *Journal of Instrumentation*, 8(10):P10019, 2013.

[145] S. Aoki, G. Barr, M. Batkiewicz, J. Błocki, J. D. Brinson, W. Coleman, A. Dąbrowska, I. Danko, M. Dziewiecki, B. Ellison, et al. The T2K side muon range detector (SMRD). *Nuclear Instruments and Methods in Physics Research Section A: Accelerators, Spectrometers, Detectors and Associated Equipment*, 698:135–146, 2013.

[146] K. Abe, H. Aihara, A. Ajmi, C. Andreopoulos, M. Antonova, S. Aoki, Y. Asada, Y. Ashida, A. Atherton, E. Atkin, et al. T2K ND280 Upgrade–Technical Design Report. *arXiv preprint arXiv:1901.03750*, 2019.

[147] K Abe, R Akutsu, A Ali, C Alt, J Amey, C Andreopoulos, L Anthony, M Antonova, S Aoki, A Ariga, et al. Measurement of the muon neutrino charged-current single $\pi+$ production on hydrocarbon using the T2K off-axis near detector ND280. *Physical Review D*, 101(1):012007, 2020.

[148] K Abe, N Akhlaq, R Akutsu, A Ali, C Alt, C Andreopoulos, L Anthony, M Antonova, S Aoki, A Ariga, et al. Measurements of ν^- μ and ν^- $\mu+$ ν μ charged-current cross-sections without detected pions or protons on water and hydrocarbon at a mean anti-neutrino energy of 0.86 GeV. *Progress of Theoretical and Experimental Physics*, 2021(4):043C01, 2021.

[149] T Fukuda, S Aoki, S Cao, N Chikuma, Y Fukuzawa, M Gonin, T Hayashino, Y Hayato, A Hiramoto, F Hosomi, et al. First neutrino event detection with nuclear emulsion at J-PARC neutrino beamline. *Progress of Theoretical and Experimental Physics*, 2017(6):063C02, 2017.

[150] T. Odagawa, Y. Suzuki, T. Fukuda, T. Kikawa, M. Komatsu, T. Nakaya, O. Sato, H. Shibuya, and K. Yasutome. Momentum reconstruction of charged particles using multiple Coulomb scatterings in a nuclear emulsion detector. *Progress of Theoretical and Experimental Physics*, 2022(11):113H01, 2022.

[151] C. Campagnari, S. Cho, S. Choi, S. Chung, M. Citron, A. De Roeck, M. Gastal, S. Ha, A. Haas, C. S. Hill, et al. Design and Mechanical Integration of Scintillation Modules for SUB-Millicharge ExperimenT (SUBMET). 2025.

[152] K. Abe et al. Hyper-Kamiokande design report. 2018.

[153] T2K and beyond: https://t2k-experiment.org/beyond-t2k/. .

[154] Y. Itow, T. Kajita, K. Kaneyuki, M. Shiozawa, Y. Totsuka, Y. Hayato, T. Ishida, T. Ishii, T. Kobayashi, T. Maruyama, et al. The JHF-Kamioka neutrino project. 2001.

[155] S Fukuda, Y Fukuda, Takashi Hayakawa, E Ichihara, Masaki Ishitsuka, Y Itow, T Kajita, J Kameda, K Kaneyuki, Shunsuke Kasuga, et al. The Super-Kamiokande detector. *Nuclear Instruments and Methods in Physics Research Section A: Accelerators, Spectrometers, Detectors and Associated Equipment*, 501(2):418–462, 2003.

[156] K Abe, C Bronner, Y Hayato, K Hiraide, M Ikeda, S Imaizumi, J Kameda, Y Kanemura, Y Kataoka, S Miki, et al. First gadolinium loading to Super-Kamiokande. *Nuclear Instruments and Methods in Physics Research Section A: Accelerators, Spectrometers, Detectors and Associated Equipment*, 1027:166248, 2022.

[157] Shota Izumiyama, Hyper-Kamiokande Collaboration, et al. Evaluation of neutron tagging performance in the Hyper-Kamiokande experiment. In *Journal of Physics: Conference Series*, volume 2156, page 012204. IOP Publishing, 2021.

[158] B. Zotter. Tune shifts of excentric beams in elliptic vacuum chambers. *IEEE Transactions on Nuclear Science*, 22(3):1451–1455, 1975.

[159] Nobuyuki Yoshimura, Takeshi Toyama, and Yoshihiro Shobuda. Space charge effects on the intrabunch motion under large chromaticity at the main ring in the Japan Proton Accelerator Research Complex. *Physical Review Accelerators and Beams*, 28 (10):101003, 2025.

[160] K. Nakamura. T2K 実験ニュートリノビーム増強のための J-PARC MR Intra-bunch Feedback System の開発, 2014.

Appendix A

Applications of Accelerators in Science

Although originally developed for fundamental research in particle physics, particle accelerator technologies have become essential tools across a wide range of scientific and industrial disciplines. The societal and economic impact of accelerator-based science now extends into materials science, chemistry, biology, and medical science. Facilities in Japan, including KEK, J-PARC, and Super Photon ring-8 GeV (SPring-8), demonstrate the broad applicability of these technologies.

One major application is the generation of synchrotron radiation. When high-energy electron beams travel through magnetic fields in circular accelerators, they emit intense, collimated radiation ranging from infrared to hard X-rays. This radiation allows the analysis of atomic structures and electronic properties of matter. Facilities such as the Photon Factory (PF) at KEK operate multiple beamlines supporting X-ray diffraction, spectroscopy, and imaging techniques. At SPring-8 and the newly commissioned NanoTerasu, synchrotron radiation is enhanced using insertion devices such as undulators and wigglers. These magnetic structures induce periodic electron trajectories, thereby increasing brightness and tunability. Undulators produce quasi-monochromatic X-rays suitable for high-resolution measurements, while wigglers generate high-intensity broadband radiation. The combination enables flexible, high-flux beams optimized for diverse experimental needs.

In the life sciences, synchrotron-based X-ray crystallography is the primary method for determining three-dimensional protein structures. This technique was used to rapidly analyze SARS-CoV-2 proteins, contributing to vaccine and drug development. In materials research, synchrotron X-rays allow the analysis of crystal structure, electronic states, and real-time chemical processes, supporting advances in battery design, catalysis, and semiconductor development.

Neutron scattering provides a complementary probe. At J-PARC's MLF, neutrons are generated through spallation by bombarding heavy-metal targets with high-intensity proton beams. Neutrons penetrate deeply and interact with atomic nuclei, enabling the detection of light elements and magnetic order. This makes them effective for studying hydrogen storage materials, lithium-ion batteries, fuel cells, and quantum magnetic systems. In biological contexts, neutron scattering reveals the structure and dynamics of proteins and membranes in solution.

Muon science is supported at J-PARC's MUon Science Establishment (MUSE). Muons, generated with spin polarization, are implanted into samples to probe local magnetic fields. The spin precession of muons, detected via their decay products, provides sensitive magnetic field measurements through Muon Spin Rotation/Relaxation/Resonance (μSR).

This method is used to investigate superconductors, novel magnetic materials, and strongly correlated electron systems. Muonic atoms formed via muon capture also enable non-destructive elemental analysis for cultural heritage artifacts and industrial components.

In medical applications, particle therapy using protons or carbon ions is employed for highly targeted cancer treatment. These charged particles deposit most of their energy near the end of their range, a phenomenon known as the Bragg peak, allowing precise irradiation of tumors with minimal exposure to surrounding healthy tissue. This improves therapeutic outcomes and reduces side effects. Ongoing development of compact and cost-efficient accelerator systems continues to expand clinical access to this treatment modality.

Appendix B

J-PARC Facility Overview

B.1 Control and Safety Systems

B.1.1 Control System

The J-PARC control system is a large-scale distributed architecture built on the Experimental Physics and Industrial Control System (EPICS) framework, integrating a variety of front-end controllers and high-level applications.

Common Infrastructure

The J-PARC control network is a dedicated, independent network for control purposes, completely separated from the office Local Area Network (LAN) used for research operations by a firewall and Demilitarized Zone (DMZ). Fiber optic cables are deployed in a star configuration from the Central Control Building (CCB) to each facility. Furthermore, Virtual Local Area Network (VLAN) technology logically divides the network by facility (LI, RCS, MR, MLF, HD, NU, CCB), minimizing the impact of failures through this design.

The server cluster has transitioned from physical blade servers to general-purpose rack-mount servers, with Kernel-based Virtual Machine (KVM) virtualization technology fully implemented across the board. This enables efficient resource utilization and live migration in the event of server failure. The software environment is systematically updated; the current standard OS is Alma Linux 9, and the EPICS version is 7.0.7. The Graphical User Interface (GUI) used by operators is the high-performance integrated development environment Control System Studio (CSS), which is the standard.

Input/Output Controller

The Input/Output Controller (IOC), at the forefront of equipment control, has evolved from legacy VME systems into more efficient and diverse forms. At J-PARC today, the following three types are the mainstays in operation:

Programmable Logic Controller (PLC)-IOC: This configuration utilizes the Central Processing Unit (CPU) module of a PLC running the Linux OS as the IOC. It allows direct control of the PLC's robust I/O modules from EPICS and is widely adopted for many field devices.

Virtual Input/Output Controller (VIOC): A virtual IOC running on a server without physical hardware. It is used for controlling devices over networks and software-based tasks like system monitoring, significantly reducing costs and physical space requirements.

"Saba-Taro" IOC: An IOC utilizing commercially available small fanless servers, offering performance surpassing VME-IOCs at a lower cost. It is being increasingly adopted as the primary replacement for obsolete VME-IOCs. [85–88]

Interlock System / Timing System

In high-intensity accelerators like J-PARC, the Machine Protection System (MPS) to prevent beam-induced equipment damage and unwanted activation, the Personal Protection System (PPS) to ensure worker safety, and the timing system are critically important.

PPS is designed with human safety as the top priority. To ensure reliability, it is independent from the accelerator control system and is built using a highly reliable, redundant PLC system, not computers. [89]

MPS is a system that rapidly and safely shuts down the accelerator when an abnormality occurs in any equipment during beam delivery. In addition to conventional hardwired signals, MPS employs two advanced mechanisms. Soft-MPS: A software-based mechanism utilizing EPICS network information. It is used to incorporate complex operating conditions (such as beam intensity or bunch number of bunch) into interlocks that cannot be achieved with hardware signals, and to rapidly implement emergency safety measures. High-Speed FPGA Interlock: On the neutrino beamline, a dedicated module called "PAPILLON," equipped with an FPGA, is installed to prevent damage when the beam deviates from the target. It processes signals from the beam profile monitor in real-time at the microsecond level and immediately halts the beam upon detecting an anomaly. [90–93]

The ability of J-PARC's three accelerators to operate synchronously with nanosecond precision is made possible by a high-accuracy timing system. The current system is being upgraded to a next-generation system utilizing FPGAs and high-speed serial communication technology. This consolidation allows the three signals—clock, trigger, and control code—previously transmitted separately via three optical cables, to be integrated into a single optical cable. This simplifies wiring and enhances noise immunity. [94, 95]

B.1.2 Custom Application System

The latest control technologies are utilized in various applications to maximize accelerator performance.

Low Level RF (LLRF) Control: In RCS and MR, the Micro Telecommunications Computing Architecture - Enhancements for Rear I/O and Precision Timing (MTCA.4) platform, suited for high-speed, high-capacity data processing, is employed to compensate for beam loading, a challenge in enhancing beam intensity. On this foundation, an advanced control method called "Multi-Harmonic Vector RF Voltage Control Feedback" is implemented, enabling stable acceleration of high-intensity beams.

Power Supply Control: For the main magnet power supply in RCS, the legacy control system was replaced with a compact integrated control unit featuring System on a Chip (SoC) FPGAs. Additionally, the application of machine learning is being explored for adjusting the complex current waveform patterns of the paint bump power supply, with expectations for future automation and optimization. [96]

B.2 Description of the LINAC

B.2.1 Ion Source

At the Ion Source (IS), which serves as the starting point for acceleration, negative hydrogen ions (H^-) are generated and extracted at an energy of 50 keV.

The IS is an RF-driven source based on a proven design from the Spallation Neutron Source (SNS) in the United States, utilizing an internal antenna customized for J-PARC to generate hydrogen plasma. The plasma is confined within a cylindrical stainless steel chamber by an 18-pole cusp magnetic field created by permanent magnets.

To dramatically improve the efficiency of H^-ion generation, a small amount of cesium is introduced as vapor from an oven. This lowers the work function of the molybdenum plasma electrode surface, which enhances H^-production. This method is clean, as it avoids impurities that can arise from the thermal decomposition of cesium compounds, and a single 2.5 g load of cesium is sufficient for over a year of operation. To protect the newly formed H^-ions from being destroyed by high-energy electrons within the plasma, a rod filter magnet is used to create a magnetic field that prevents these electrons from reaching the extraction area.

Additionally, a sophisticated dual-RF system is employed to ensure stable plasma ignition and beam extraction. First, a weak, Continuous-Wave (CW) 30 MHz RF pulse (under 50 W) generates a low-density "seed" plasma. Then, synchronized with the beam extraction timing, the main high-power 2 MHz RF pulse is applied to produce the high-density plasma required. This stabilization technique enables the stable supply of a 60 mA beam for more than one year.

B.2.2 Linac

Radio Frequency Quadrupole Linac

RFQ accelerates negative hydrogen ions $H^-$from 50 keV to 3 MeV. The RFQ focuses the beam with four electrodes while accelerating it in the direction of travel using a special "corrugated" structure on the electrode surface. Its most distinctive feature is its ability to continuously convert the beam supplied from the ion source into small bunches with a greater efficiency of 90%, enabling efficient acceleration in the subsequent accelerator.

Drift Tube Linac / Separated-type Drift Tube Linac

The beam emitted from the RFQ is accelerated to 50 MeV in the DTL and then to 181 MeV in the SDTL. The frequency of 324 MHz has the advantage of increasing the number of beam bunches and reducing space charge effects, but it also poses the challenge of reducing the diameter of the drift tubes installed inside the accelerating cavities. At J-PARC, an ultra-compact quadrupole magnet with an internal cooling channel was developed and put into practical use by employing a technique that alternates plating and polishing (Periodic Reverse (PR) copper electroforming), thereby resolving this issue.

Annular Coupled Structure Linac

ACS raises the energy from 181 MeV to the target of 400 MeV. As energy increases, structures such as DTL experience a decrease in acceleration efficiency, so a more efficient structure called a "coupled-cavity structure" is required. At J-PARC, after comparing several candidates (the US SCS type and the Russian DAW type), ACS was adopted because it has good symmetry of the acceleration electric field and minimal degradation of beam quality. The RF frequency used in the ACS is 972 MHz, three times higher than in the preceding stage. The higher frequency allows the high-frequency source, the klystron, to be compact and easier to handle. The ACS consists of a total of 21 modules, with each module's length varying as the beam speed increases. However, to keep costs down, the numerous cells (the smallest unit of acceleration) within each module are all designed to be the same length.

B.2.3 MEBT1: Chopper

Between the RFQ, the initial acceleration stage of the J-PARC linear accelerator, and the next stage, the DTL, there is a Medium Energy Beam Transport-1 (MEBT1). This system includes two buncher cavities for shaping the beam and one beam chopper, which plays an extremely important role.

The duration of the macro-pulses sent from the linear accelerator is about 500 μs, which is relatively long, while the time it takes for the beam to complete one revolution in the circular accelerator RCS is about 1.63 μs, which is extremely short. If the beam is continuously injected without any intervention, the entire RCS ring would become filled with the beam. However, the RCS RF acceleration system accelerates particles using a sinusoidal electric field, so only a small portion of particles whose timing aligns with the wave can be accepted and accelerated. Particles whose timing does not align are not accelerated and scattered throughout the ring, resulting in significant beam loss.

The beam chopper operates in sync with the RCS's standby frequency, kicking out only the beams that cannot be accepted by the RCS at the incorrect timing. These unwanted beams are safely processed by colliding with a carbon-made block called a "scraper." This process leaves only the portion of the original macro-pulse that can be accepted by the RCS, forming an intermediate-pulse sequence.

Additionally, this system allows for free adjustment of the beam intensity sent downstream without altering any operating conditions of the linear accelerator itself (such as ion source output). Specifically, it is possible to change the length of the intermediate-pulses or to skip some intermediate-pulses (e.g., switching from two-bunch operation to one-bunch operation of the RCS). This extremely flexible intensity adjustment function is routinely utilized in experimental operations requiring various conditions and in accelerator adjustment operations, and it is an important technology supporting the stable operation of J-PARC.

In beam tests, when generating a beam with large macro-pulses and small intermediate-pulses, attention must be paid to the temperature resistance of the scraper. In other words, when changing the beam intensity while maintaining the macro-pulse length, there is also a lower limit to the intensity. [97, 98]

B.2.4 L3BT: Debuncher

The LINAC to 3GeV Beam Transport (L3BT) connecting the linear accelerator and the RCS is equipped with two debuncher cavities. The main purpose of these cavities is to minimize the momentum spread of the beam before it enters the RCS. This is achieved by converting the energy fluctuations of the beam into a spread in the length of the beam bunch (phase spread) through "rotation in the longitudinal phase space." At J-PARC, this system using two debuncher with separated functions is employed. The upstream cavity minimizes the momentum jitter of the beam coming from the linear accelerator, while the downstream cavity adjusts the momentum spread of the entire beam. This two-stage system allows flexible adjustment of energy spread without compromising jitter correction performance. This is important for suppressing (longitudinal) space charge effects in high-intensity beams.

B.2.5 L3BT: Scraper

To meet the requirement specification of 99.9% unnormalized emittance at the RCS injection point being 6πmmmrad or less, the L3BT is equipped with a lateral scraper system using a charge exchange method to remove the beam halo. Only the halo portion passes through the carbon foil, causing the original hydrogen negative ions (H^-) to lose electrons and transform into protons (H^+). The beam core and halo have opposite charge signs, so they are separated in opposite directions by bending magnets and safely guided to a dedicated beam dump.

This scraper section consists of four basic units called FODO cells repeated four times, with a total of eight scrapers installed, four in the horizontal direction and four in the vertical direction. The period length of the FODO cell is 8 meters, with a phase advance of approximately 45 degrees per cell. As a result, the beam cross-section is shaped into an octagon in phase space in both the horizontal and vertical directions, enabling a highly clean beam to be delivered to the RCS.

B.3 Description of the RCS

B.3.1 Lattice Design

The RCS lattice employs the FODO-type structure, which is the basic configuration for stabilizing beams. This arrangement alternates quadrupole magnets (F) that focus the beam with quadrupole magnets (D) that defocus it. In RCS, the basic unit is a cell known as DOFO. The ring has a three-fold symmetrical structure, and this one-third unit is referred to as a superperiod. One superperiod consists of two arc modules (parts that bend the beam) and one straight module. This straight module is designed so that the momentum dispersion is zero, making it an ideal location for installing important equipment that requires precise operation, such as beam injection/extraction devices and acceleration cavities.

The most ingenious aspect of the RCS lattice design is the inclusion of "Missing-Bend Cells" (cells without a bending magnet) in the arc modules. In this cell, the momentum

dispersion becomes locally very large, about 6 m. This property is utilized to install a sextupole magnet at this location. The sextupole magnet plays a role in efficiently correcting chromaticity, thereby enhancing beam stability. Additionally, as a result of this lattice design with large dispersion, the transition energy is set to a very high value of 10.8 GeV. Since the RCS accelerates the beam only up to 3 GeV, the beam does not pass through this troublesome energy region during operation. Passing through the transition energy region is difficult to control and causes beam instability, but this design fundamentally avoids this issue, significantly contributing to stable beam acceleration and reduced losses.

B.3.2 Beam Injection

In order to accumulate a large number of particles in the ring, the RCS uses a multi-turn injection method, which employs two important techniques: charge exchange injection scheme and painting injection scheme.

Charge Exchange Injection

Just before the beam enters the ring, it passes through an extremely thin carbon foil with a thickness of approximately 300 $\mu g/cm^2$, stripping both electrons and converting them into protons (H^+). The protons (positively charged particles) circulating inside the ring and the incoming beam (negatively charged particles) are deflected in opposite directions by the same magnetic field. This property allows the incoming beam to be merged with the circulating beam without affecting the orbit of the circulating beam, enabling particles to be accumulated repeatedly at the same location. This allows us to circumvent the constraints of Liouville's theorem and dramatically increase particle density. If we attempt to inject a proton beam, it would bend in the same direction as the circulating beam, making such accumulation impossible in principle.

We create a localized bump orbit within the ring using shift bump electromagnets, merge the H^-beam at the apex of the bump, and perform charge exchange using carbon foil installed there. During charge exchange, 99.6% become protons, while a small portion becomes neutral hydrogen (H^0) with only one electron stripped, or unconverted H^-. These would otherwise exit the orbit and irradiate the device, so they are all converted to protons using dedicated second and third foils and safely directed to the beam disposal line. [99, 100]

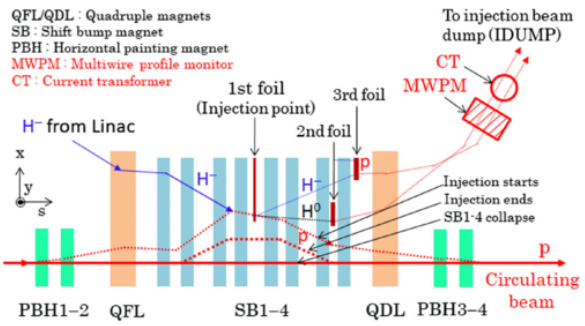

Figure B.1: Schematic of the RCS injection section and stripper foil position. [99]

Painting Injection

In high-density beams, the space charge effect becomes stronger, leading to serious instability in the beam. A technique to mitigate this is called painting injection. This method involves sweeping the beam across the acceptance region rather than continuously overlapping it at the same point in phase space. This intentionally widens the beam, reducing charge density and weakening repulsive forces. In RCS, painting is performed in both the transverse and longitudinal directions.

Transverse painting controls the spread of the beam in the horizontal and vertical directions. In the horizontal plane, four paint bump magnets installed within the ring are used to temporally change the orbit of the circulating beam, so that the injected beam, which initially follows a fixed orbit, is distributed across different positions of the moving circular orbit. In the vertical plane, two paint bump magnets installed on the injection line gradually change the injection angle over time, further broadening the distribution. By combining these horizontal and vertical painting methods, advanced control of the transverse beam profile is achieved; for instance, correlated painting can produce a nearly square cross-section, while anti-correlated painting results in an elliptical distribution.

Longitudinal painting controls the spread of the beam's momentum direction. This is achieved by slightly varying the frequency of the RF acceleration cavity used for acceleration during the injection beam.

In (MR/RCS) RF group jargon, the setting with longitudinal painting enabled and the second harmonic enabled in RCS is referred to as "Ari-Ari(both enabled)." The opposite is called "Nashi-Nashi (both disabled)." This adjustment is particularly applied to reduce the peak current of the bunch. [101, 102]

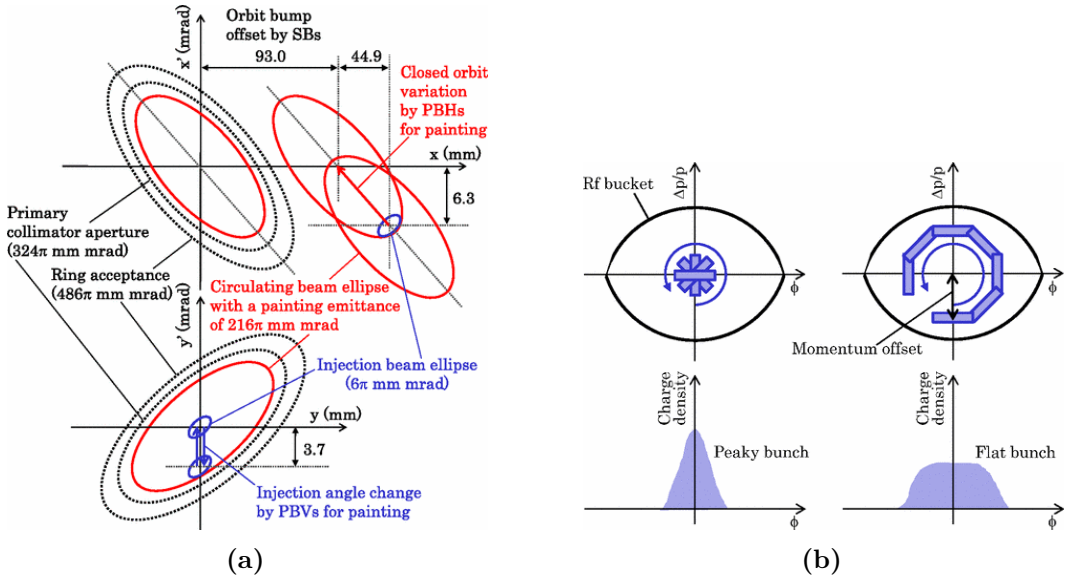

Figure B.2: (a) Schematic of injection painting in transverse plane. The upper panel shows the horizontal phase space, and the lower panel shows the vertical phase space. (b) Schematic of longitudinal painting without (left) and with (right) momentum offset. Squares represent injection bunches from the LINAC. [101]

Strategies and Challenges

At J-PARC, the "RCS method" was adopted, in which the H^- beam is injected into the RCS at 400 MeV and then accelerated to 3 GeV within the ring to increase the beam power. This is because the MR requires beams with higher energy, and it is more efficient for the RCS, which serves as a booster, to pre-accelerate the energy, thereby optimizing the overall facility. This is because if the energy of the H^- beam is increased too much, electrons are stripped off due to the Lorentz force, resulting in an energy limit (about 1.3 GeV) for charged particle injection. Additionally, having a margin in the beam loss rate at injection is another advantage.

The RCS is an accelerator that handles high-intensity beams, making it highly susceptible to nonlinear forces such as space charge effects and fringe magnetic fields leaking from the ends of large-bore electromagnets. Painting is a powerful method for mitigating space charge effects, but since it intentionally widens the beam, improper use may actually increase beam loss due to nonlinear forces. Finding the optimal operating parameters is not straightforward and requires a meticulous adjustment process that involves thoroughly understanding the behavior of single particles at low beam intensities, gradually increasing the beam intensity while investigating each effect, and exploring optimization—a process that involves significant research elements.

B.3.3 Electromagnetic System

The RCS electromagnetic system consists mainly of 24 bending magnets (1 family) that create the beam trajectory, 60 quadrupole magnets (7 families) that converge the beam, and 18 sextupole magnets (3 families) that correct chromatic aberration, as well as numerous other magnets such as 54 steering magnets for trajectory correction. In order to accelerate high-intensity beams, it is necessary to increase the beam size to suppress particle repulsion, which in turn requires a very large aperture for the magnets (bore diameter of 410 mm for quadrupole magnets) and advanced technology along with large power supplies.

Rapid Cycle Compatibility

All electromagnets in the RCS must change the strength of their magnetic fields at a rapid cycle of 25 Hz. This rapid change causes eddy currents to occur within metal components, leading to energy loss due to heat generation and magnetic field disruption. To overcome this challenge, the following innovative measures have been implemented in the RCS electromagnets.

Instead of conventional hollow copper conductors, a special conductor consisting of multiple aluminum strands twisted together around a stainless steel cooling water pipe has been developed and adopted. This eliminates eddy current generation pathways and significantly reduces losses.

The core of the electromagnet is constructed by laminating electrically insulated silicon steel plates with a thickness of 0.5 mm, suppressing eddy currents within the core. Grooves at the magnetic pole tips: Fine slits are provided at the ends of the magnetic poles of the bending magnets and quadrupole magnets, where eddy currents have a particularly significant impact.

Efficient Supply and Precise Control of High Power

Generating and changing high-speed, powerful magnetic fields requires a massive amount of power, but RCS employs a highly energy-efficient resonant power supply. An AC magnetic field is superimposed on a DC magnetic field corresponding to the intermediate energy. One power supply for the bending magnets and seven power supplies for the quadrupole magnets each form a resonant circuit with a choke transformer and capacitor, and excite the electromagnets with sine waves in synchronized timing.

In particular, in the 3GeV region, the effects of magnetic saturation in the core become significant. To address this, the current of the seven families of quadrupole magnets is individually controlled in response to changes in the magnetic field of the reference bending magnet, enabling precise tracking of magnetic field shifts.

Minimizing Manufacturing and Installation Errors

To achieve an ideal accelerator, it is necessary to minimize the slight performance variations (manufacturing errors) of each electromagnet and the misalignment (installation errors) of their installation positions.

In the RCS, the magnetic fields of all main electromagnets were precisely measured in advance to identify individual differences. We then used a technique called "shuffling" to determine the optimal placement within the ring so that these errors cancel each other out. By pairing bending magnets with similar error tendencies at positions on the ring that are π out of phase, we have minimized COD. We have implemented similar measures for quadrupole magnets to minimize beta function modulation.

Through precise alignment work, the electromagnets were installed with extremely high accuracy, with positional errors of ± 0.1 mm or less and rotational errors of ± 0.1 mrad or less. As a result, the influence of installation errors on the beam is kept to a minimum.

Additionally, to correct orbital deviations, 26 small bipolar correction magnets are arranged horizontally and vertically adjacent to the quadrupole magnets, with BPMs installed in the gaps to precisely measure the beam position. [103]

B.3.4 Radio Frequency Cavity

In RCS, the RF frequency is varied from 1.23 MHz at injection to 1.67 MHz at extraction to accommodate changes in beam velocity due to acceleration. To address this issue, J-PARC has adopted an RF cavity equipped with a MA.

In conventional proton synchrotrons, ferrite material was used in the acceleration cavities, and the resonance frequency of the cavities was adjusted by applying an external bias magnetic field to control the permeability. However, J-PARC has focused on MA, represented by FINEMET, and is maximizing its excellent properties. MA offers two major advantages over conventional ferrite. First, MA has a higher saturation magnetic flux density than ferrite and is more heat-resistant, enabling the injection of larger RF power. This has allowed J-PARC to achieve an acceleration gradient of over 20 kV/m, significantly exceeding the previous limit of approximately 10 kV/m. Second, MA cavities

have an extremely low Q-factor (Q=2 in RCS). This means that the cavity responds not only to a specific frequency but also across a very wide frequency band.

This low Q-factor characteristic brings two distinct advantages to RCS's RF system. The complex tuning control feedback required in conventional ferrite cavities to adjust the frequency in accordance with acceleration is no longer necessary. Since the cavity's inherent wide frequency band (0.9 MHz to 3.4 MHz) covers all necessary frequency sweeps, the LLRF system can be simplified, achieving high stability and reproducibility. With an extremely wide bandwidth of Q=2, RCS can drive both the fundamental wave for accelerating the beam and the second harmonic wave for shaping the bunch and mitigating space charge effects simultaneously with a single cavity. Adding a separate cavity dedicated to the second harmonic wave would increase the ring length and require additional acceleration voltage. For the RCS, which achieves high-intensity beams in a limited space, this dual harmonic operation is an indispensable technology.

Currently, 12 MA cavities are installed in the RCS, each capable of generating a maximum acceleration voltage of 45 kV, totaling approximately 500 kV across the system. The entire system consists of MA cavities, high-frequency amplifiers using high-power vacuum tubes (tetrodes), and an LLRF control system. The LLRF at J-PARC is an advanced system where all circuits are digitally configured. Since the RF frequency is low (several MHz), RF signals can be directly A/D converted, eliminating the need for mixers and enabling reproducible control. Direct Digital Synthesis (DDS) technology enables the precise and stable direct generation of RF signals with multiple harmonics. This LLRF system precisely controls the RF frequency, voltage, and phase based on signals from various monitors. Frequency control: Feedback from dR BPM. Phase control: Feedback from FCT monitors. Voltage control: Feedback from voltage monitors in each cavity (Auto Voltage Control (AVC)). Waveform observation: Signals from the WCM are used for observing bunch waveforms and beam loading compensation via RF feedforward (FF). The "mountain plot," which displays WCM waveforms side by side for each revolution, is a highly effective tool for visualizing the vertical behavior of the beam. [104, 105]

B.3.5 Vacuum Chamber

In RCS, titanium is used in the straight sections of the accelerator vacuum chamber where there are no electromagnets, as it has low gas release and is less prone to radiation. On the other hand, in areas where bending magnets and quadrupole magnets are installed, alumina ceramics, which are insulators, are used to avoid the effects of heat generation and multipole components of magnetic fields caused by eddy currents. However, ceramics cannot confine the RF frequency wakefield generated by the beam itself, allowing them to leak outward. Additionally, they cannot serve as a path for the image currents necessary for stable beam operation. To address this issue, RCS has applied copper plates in stripline patterns to the outer surface of the ceramic chamber using an electroforming process. This serves as an RF shield while also functioning as a path for image currents, thereby suppressing resistive wall impedance. This combination of ceramic chamber and RF shield technology is a unique and essential element for achieving stable high-intensity beam acceleration in the RCS. This technology has been applied not only to the main electromagnet section but also to chambers with complex shapes in the beam injection

section and has been implemented in practical applications. [106]

B.3.6 Beam Extraction

Proton beams accelerated from RCS to 3 GeV are extracted using a method called FX. This method involves extracting all of the beam bunches (in the case of RCS, up to two bunches) circulating in the ring to the outside of the ring in a single revolution. This process is performed in two stages using kicker magnets and septum magnets.

First, 8 kicker magnets, capable of generating powerful magnetic fields in a very short time, operate simultaneously to impart a sharp angle (kick) of about 17 mrad to the circulating beam.

The beam, which has been kicked and shifted outward, is guided to 3 septum magnets installed downstream. The septum magnets bend the beam by another 288 mrad, completely separating it from the orbit that continues to circle the ring and sending the beam to the next transport line. [107]

B.4 Description of the Beam Diagnosis System

B.4.1 Beam Positon Monitor

BPM at LINAC

The 102 BPMs installed in the LI serve as the cornerstone for trajectory monitoring and calibration, ensuring the stable delivery of high-quality beams to the downstream RCS. Their most critical role is minimizing beam loss, which is key to high-intensity operation. To achieve this, they non-destructively monitor the beam center trajectory with high precision, to within approximately 100 μm. Moreover, these monitors are multifunctional, not merely monitoring position. Their signals are also utilized for diverse beam diagnostics, including evaluating momentum spread, estimating emittance, and adjusting acceleration phase.

Unlike the electrostatic induction type commonly used in ring accelerators, all BPMs in the LI are of the 4-stripline type. This is because they offer high sensitivity to RF and are well-suited for measuring beam timing and phase information. To ensure mechanical positional accuracy, all detectors are mounted directly inside the quadrupole magnets or on their yokes. Furthermore, as the beam accelerates, increasing in energy and size, the BPM aperture is progressively enlarged from approximately 24 mm at the MEBT1 to 180 mm at the L3BT terminus.

Signal processing employs the Log-Ratio method, which achieves both a wide dynamic range and high-speed response. This enables measurements with high positional resolution of 0.1 mm or less, ranging from low-intensity beams (5 mA) during beam tuning to high-intensity beams (50 mA) during rated operation. Signals are transmitted via long cables from detectors within the tunnel and processed by electronic circuits on the ground.

To meet the high measurement accuracy requirement of approximately 100 μm, the BPM undergoes two stages of precise calibration. First, prior to installation, wires carrying RF

signals are scanned within the BPM on a test bench to map the relationship between physical position and electrical response (bench calibration). Second, after installation, the actual beam is used to precisely align the electrical center of the BPM with the magnetic center of the quadrupole magnet in which it is mounted. This latter process, called Beam Based Calibration (BBC), enables calibration with an accuracy of less than 50 μm, overcoming mechanical installation errors. This high-precision calibration is the foundational technology supporting stable beam transport from the LI to the RCS. [108, 109]

BPM at RCS

The 54 BPMs installed in the RCS are the most critical diagnostic devices for reliably capturing the high-intensity beam with its intense intensity fluctuations and stabilizing its trajectory. The most important role of the BPM is to precisely measure and correct the COD. In the RCS, high measurement accuracy in the order of 0.1 mm is achieved through methods such as wire calibration, and this high-precision trajectory information supports stable beam operation. Beyond COD measurement, the BPMs also enable turn-by-turn tracking of beam behavior during injection and direct observation of bunch waveforms. They thus serve as indispensable diagnostic tools for detailed beam tuning and performance enhancement.

The BPMs in the RCS employ a wideband, highly linear electrostatic diagonal-cut electrode design. Its design incorporates numerous innovations to withstand the harsh RCS specific environment of 25Hz rapid-cycle operation and extreme space constraints. The most significant feature is that, to save space, the majority of the BPM detectors are integrated inside the steering electromagnets. To minimize equipment radioactivity and facilitate maintenance, lightweight titanium with low residual radioactivity is used for key materials. To avoid the effects of the fluctuating 25Hz magnetic field, the detector body features a thin-walled structure with ribs designed to withstand vacuum forces. The support frame incorporates insulation and slits as eddy current countermeasures. For areas requiring particularly large openings, such as the beam entrance, a special large rectangular-section BPM with a 610mm diameter bellows has been developed and installed.

To stably transmit the beam signal with its varying frequency, an impedance matching transformer is placed near the detector. This also offers the advantage of attenuating the signal strength to 1/7 while improving noise immunity, protecting the downstream electronic circuits from the high-intensity beam. In the analog section of the signal processing circuit, relays switch between amplifiers and attenuators to handle large beam intensity fluctuations, ensuring the A/D converter's input range is always utilized effectively. The faint signals captured by the detector are transmitted via cables over 100 meters long and processed by the ground-based signal processing unit. The signal is digitized by a 14-bit, 40 MS/s ADC. An FPGA handles control, while a 600 MHz DSP performs data analysis. The DSP's powerful computational capability enables FFT processing of up to 4096 points, allowing precise position calculation with high frequency resolution. Although the 54 signal processing units are distributed across three rooms, they are connected via a shared memory network called Reflect Memory. This synchronizes all BPM data and timing information in real time, enabling coordinated operation across the entire system. [110–112]

B.4.2 Beam Profile Monitor

Wire Scanner Monitor (destructive, LI)

To accurately measure the beam profile, a total of 36 Wire Scanner Monitors (WSMs) are installed at various points along the LI. The WSM measures the profile by stretching two wires across a frame tilted 45 degrees relative to the drive unit and crossing them with the beam in increments of 0.1 mm using a stepper motor. When the H^-beam accelerated by the LI collides with the wire, electrons from the H^-beam are captured by the wire, generating a current signal proportional to the beam intensity at that position. By recording this signal along with the wire's position, the beam's cross-sectional shape is reconstructed. The wire material has been optimized based on the balance between beam energy and thermal load. Currently, Carbon NanoTube (CNT) wires are used at the thermally most demanding 3 MeV point, while tungsten wires are used elsewhere.

Bunch Shape Monitor (destructive, LI)

Beyond Standard Model (BSM) is a critical diagnostic device in a linear accelerator for measuring the longitudinal bunch shape of the beam. It plays a vital role in adjusting longitudinal matching to smoothly transfer the beam to subsequent RCS, particularly in the low-energy region where space charge effects strongly influence the beam.

The BSM applies the principle of streak cameras. First, probes such as wires or graphite are inserted along the beamline. When the beam strikes the probe, secondary electrons with the same temporal structure as the beam are generated. These secondary electrons are extracted using a high voltage of approximately -10kV and transported to the RF deflector. In the RF deflector, a high-frequency electric field synchronized with the linac's accelerating RF is applied. This modulates the temporal distribution of the secondary electrons into a lateral spatial distribution. By measuring this spatially spread electron distribution on a screen, the original beam's longitudinal profile is reconstructed.

BSM is installed in the MEBT1, the most critical matching section for transferring the beam from the RFQ to the DTL. The beam in this section is low-energy (3 MeV) and high-intensity (approximately 60 mA), resulting in extremely severe thermal loading on the target. The initially adopted tungsten wire frequently broke. This problem was overcome by developing and introducing High-Oriented Pyrolytic Graphite (HOPG) as the target. It is currently the only BSM achieving stable beam measurement and beam parameter calculation.

BSMs are also installed in the ACS section and L3BT, but they have not yet reached beam parameter measurement capability and development continues. [113]

Flying Wire Monitor (destructive, MR)

Flying Wire Monitor (FWM) is a highly reliable diagnostic instrument developed to accurately measure the transverse profile of beams in MR. Its primary role is to sample the beam cross-section non-stationarily without compromising the stability of high-intensity beams. It is particularly used for beam adjustment during injection, diagnosing mismatches, and observing beam shape changes due to resonance during acceleration.

The FWM measurement principle consists of the following steps. First, an extremely fine carbon fiber wire, approximately 7 μm in diameter, is injected into the beam at a high speed of 5 m/s and made to cross it. When beam particles collide with the wire, secondary particles are generated through this interaction. These secondary particles are detected by a scintillator and Photomultiplier Tube (PMT) placed outside the vacuum chamber, converting the light signal into an electrical signal. By correlating the precise position information of the wire with the signal intensity detected at that position, the beam's transverse profile is reconstructed.

The primary advantage is the ability to directly measure the profile of a high-intensity beam while minimizing its impact, achieved by passing the beam through an extremely fine wire at high speed. However, because the wire physically crosses the beam, it is not a completely non-destructive monitor. Furthermore, measurement is limited to the instant of the sweep, making it unsuitable for continuous observation.

Two FWMs are independently installed. Over long-term operation, there have been almost no wire breakage incidents, demonstrating extremely high reliability in the high-intensity beam environment. Among J-PARC's diverse array of monitors, the FWM plays a complementary role to the MRPM, which enables continuous monitoring by leveraging its characteristics, and the Optical Transition Radiation (OTR)/fluorescence (FL) monitor, which simultaneously captures the beam core and halo. [114]

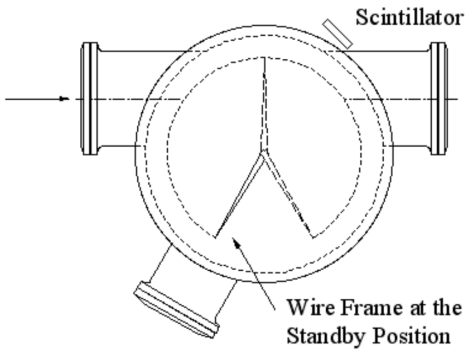

Figure B.3: Schematic of flying wire monitor. [114]

Optical Transition Radiation/Fluorescence Monitor, (destructive,3-50BT, MR)

OTR/FL monitor is a high-performance two-dimensional beam profile monitor that combines two phenomena: OTR and FL. Its most significant feature is its extremely wide dynamic range, reaching 10^6, enabling simultaneous two-dimensional imaging of both the intense beam core and the extremely faint beam halo spreading around it.

This capability is achieved through a dual-screen method that skillfully utilizes two different types of screens. First, the intense core portion is captured using the faint but fast-responding OTR emitted from a thin titanium foil at the beam center.Next, four alumina screens positioned around it measure the much brighter FL emitted by halo particles colliding, capturing the low-intensity halo portion. Combining these two images allows the entire beam profile to be shown with high precision within a single image.

To capture this faint light, the monitor incorporates various technical innovations. Light generated at the target is transferred to the camera using an Offner optical system with extremely high light collection efficiency. Finally, the transferred light is amplified by an Image Intensifier (I.I.) and imaged by a high-sensitivity Complementary Metal Oxide Semiconductor (CMOS) camera.

The OTR/FL monitor installed in the 3-50BT contributes to optimizing beam cuts with the collimator and selecting beam conditions by directly diagnosing the beam halo in two dimensions. Based on this proven performance, plans are currently underway to install a new OTR/FL monitor inside the MR. [115]

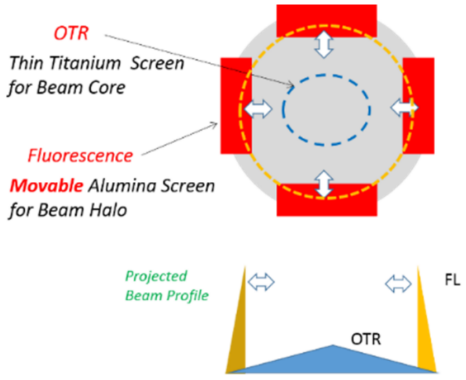

Figure B.4: Schematic of optical transition radiation/fluorescence monitor. [115]

Residual Gas Ionization Profile Monitor (nondestructive, RCS, MR)

The Residual Gas Ionization Profile Monitor (IPM) is used to measure transverse profiles in RCS and MR. The IPM's most significant feature is its ability to continuously measure the profile of the circulating beam in a completely non-destructive manner, without affecting the beam at all. Its principle utilizes the minute residual gas remaining inside the vacuum chamber. The density distribution of the ion-electron pairs generated when the beam ionizes this residual gas is proportional to the beam's charge density distribution. These generated charged particles are transported to the detector by an externally applied electric field. The beam's one-dimensional profile is then reconstructed from their arrival position and number. The IPM primarily consists of electrodes to generate the electric field, a MicroChannel Plate (MCP) to amplify the signal, and a multi-strip anode to detect the amplified signal as positional information. The MCP has an amplification factor of approximately 1 million, enabling it to reliably capture weak signals. Due to its non-destructive and continuous measurement characteristics, the IPM is an indispensable tool not only for emittance measurement but also for matching adjustments of the incident beam. Particularly in RCS, which employs painting injection where the beam is superimposed layer by layer, the IPM is essential for monitoring the turn-by-turn formation of the distribution.

The IPM can be switched to collect either positively charged ions or electrons. When collecting positively charged ions, the configuration is relatively simple. However, during high-intensity beam operation, the ion trajectory is bent by the beam's own space charge forces, causing profile distortion. Therefore, it is primarily used for measuring low-intensity

adjustment beams. Electrons, being very light, are strongly affected by space charge forces. However, by applying a guide field parallel to the electric field and transporting electrons while winding them along magnetic field lines, accurate profile measurements become possible. This guide field employs a special design using a 3-pole wiggler magnet, ensuring the overall kick applied to the beam is zero to avoid affecting the main beam. [116, 117]

B.4.3 Beam Current Monitor

Slow Current Transformer (LI, RCS)

The primary purpose of the SCT is to accurately measure beam intensity. It is specifically designed to suppress droop (waveform sag) in long beam pulses, such as the 500μs pulse in LI or the 20ms pulse in RCS, ensuring the entire pulse intensity is accurately captured. LI employs an active-type CT that enhances low-frequency response using a preamplifier. It boasts a coil winding of 50 turns, achieving a sag of less than 3% and a high measurement accuracy of less than 0.1 mA for a 500μs pulse width. RCS uses a more advanced feedback-type CT as the SCT. This CT dramatically extends the time constant to approximately 20 seconds using a feedback circuit to measure intensity during the extremely long acceleration time of 20ms.

Fast Current Transformer (LI, RCS, MR)

The primary purpose of the FCT is to precisely measure the temporal position (phase) of the bunch. To achieve this, the coil turns are minimized (1 turn in LI), enabling nanosecond-level fast response and a wide bandwidth reaching 180 MHz. In the LI, it serves two critical roles. One is to compare the bunch phase with the reference signal from the accelerating RF. The other is to measure the signal arrival time difference between two FCTs (Time of Flight (ToF)) and calculate the beam energy with high resolution of less than 0.1%. RCS and MR are indispensable as sensors for the RF phase feedback system, detecting the phase of the beam circulating the ring and correcting the phase of the RF accelerating cavities in real time. Additionally, in MR, they are also used to provide timing information for the fast extraction kicker.

B.4.4 Beam Loss Monitor

Beam Loss Monitor (BLM) is an indispensable device for the stable operation and safety of J-PARC. It detects secondary particles (neutrons and gamma rays) generated when off-orbit particles strike accelerator components, contributing to equipment protection, activation reduction, and beam tuning. Its most critical role is its integration with the MPS; if a beam loss exceeds a set threshold, the BLM instantly triggers the MPS to initiate an emergency beam stop, thereby preventing equipment damage and excessive activation.

Plastic Scintillator (LI, RCS)

This detector amplifies the scintillation light generated when radiation strikes the plastic using a PMT. Its key feature is a time resolution on the nanosecond scale, roughly an order

of magnitude better than the Proportional-type BLM (PBLM). Leveraging this high-speed response, it serves a specialized role not for general machine protection like the MPS, but as a detailed diagnostic tool for beam tuning. They are strategically placed in parts of the LI and concentrated in high-loss areas of the RCS, such as injection, extraction, and collimator sections, to enable detailed analysis of the temporal structure of beam loss during tuning.

Proportional Chamber (LI, RCS, MR)

The primary detector used across all three of J-PARC's accelerators is the gas-filled PBLM. It operates by amplifying electrons—produced by the ionization of a fill gas (99% Ar + 1% CO2) by radiation–via a Townsend avalanche under high voltage. This design combines high radiation hardness with high sensitivity and a fast response time on the order of microseconds. In the LI, they are placed between every accelerating cavity, while in the RCS and MR, they are installed on every quadrupole magnet stand, forming a wide-area network for comprehensive loss monitoring across the entire accelerator. Leveraging its fast response time (100 ns), the PBLM serves as the primary trigger for the MPS. However, it faces a fundamental challenge: under conditions of extremely high loss rates, the detector gain drops due to space charge effects, leading to an underestimation of the loss magnitude.

Air Ionization Chamber (MR)

Air Ionization Chamber (AIC) is a unique and robust detector that uses the air inside the accelerator tunnel as its ionization medium within a special coaxial cable structure. As it operates without gas amplification, its sensitivity is low, but it maintains excellent linearity up to extremely high radiation doses. Its primary drawback is a relatively slow response time on the millisecond scale. This detector is deployed exclusively in the MR to complement the PBLM by providing an accurate measurement of large, integrated losses where the PBLM would underestimate. This combination allows the MR to achieve a vast measurement dynamic range of 10^4 to 10^5. [118, 119]

B.5 Description of the Experimental Facility

B.5.1 Material and Life Science Experimental Facility

The MLF is a multi-purpose facility that utilizes a 1 MW pulsed proton beam supplied by the RCS to generate two quantum beams - neutrons and muons — and advances cutting-edge research across diverse fields including materials science, life sciences, and particle and nuclear physics. The MLF is equipped with 21 neutron beamlines and 4 muon beamlines. It also hosts the JSNS^2 experiment, which searches for sterile neutrinos.

Beam Transport

3GeV to Neutron Facility Beam Transport (3NBT) is the facility that transports the proton beam accelerated in the RCS through the airspace above the MR to the Japan Spallation Neutron Source (JSNS) target in the MLF. It uses an octupole magnet to flatten the beam transverse.

JSNS

When a 3 GeV proton beam strikes a mercury target, nuclear spallation reactions generate a large number of neutrons. These neutrons are decelerated to low energies suitable for neutron scattering experiments by three moderators filled with liquid hydrogen (20 K). The moderators consist of a coupled type (high intensity, low resolution), an uncoupled type (medium intensity, medium resolution), and a poisoned uncoupled type (low intensity, high resolution), selected according to the experimental purpose. Furthermore, the target area is surrounded by reflectors, efficiently guiding the generated neutrons into the moderators. [120–123]

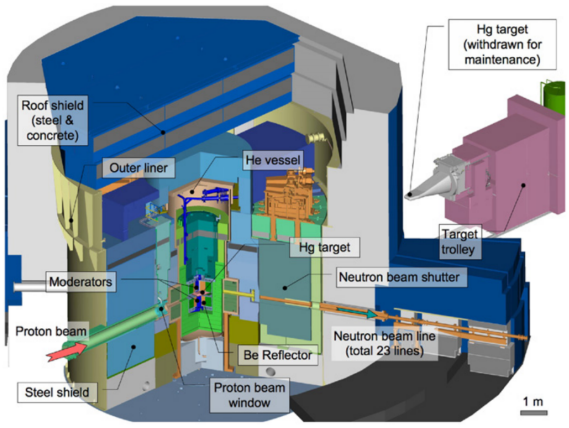

Figure B.5: Schematic of the JSNS. [120]

MUSE

30 m upstream of JSNS, MUSE receives a portion (about 5%) of the proton beam from the RCS. This beam strikes a 20 mm thick rotating graphite target. The collision produces pions, which decay to create muons. [124–126]

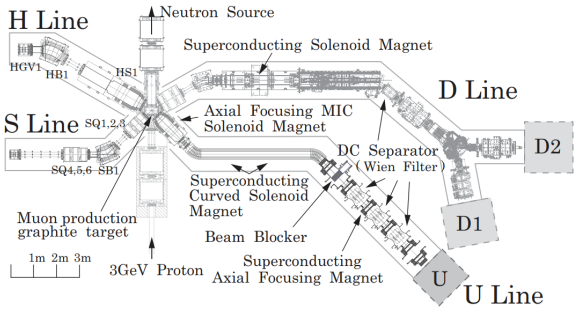

Figure B.6: Schematic of the MUSE. [126]

D-Line(Decay/Surface Muon Beam Line): D-line is a versatile beamline capable of supplying both high-energy decay muons (positive and negative) and low-energy surface muons (positive only). It utilizes a super-conducting solenoid magnet that operated for approximately 30 years at the KEK Tsukuba Campus, ensuring high reliability. This 6-meter-long solenoid with a 5-tesla magnetic field efficiently captures and decays pions

in flight, generating high-intensity high-energy muons (up to 120 MeV/c). Muon characteristic X-rays emitted when negative pions are captured by atoms possess energies approximately 200 times higher than those from ordinary atoms, making them valuable for non-destructive elemental analysis.

U-Line(Ultra Slow Muon Beam Line): U-line is a beamline capable of supplying Ultra-Slow Muons (USMs) with uniform energy. This is achieved by irradiating a high-intensity surface muon beam onto a high-temperature tungsten target, emitting muonium ions, and then stripping electrons from them using pulsed lasers. The USM beam features low energy, low emittance, and a short time distribution. The μSR spectrometer is installed in the U1A area. In the U1B area, plans are underway to reaccelerate the USM to 5 MeV using a compact AVF cyclotron, enabling the realization of a transmission muon microscope.

S-Line(Surface Muon Beam Line): S-line is a beamline specialized for physical property experiments using the μSR method. It employs large-aperture quadrupole electromagnets and efficiently transports surface muons to the experimental area. The μSR spectrometer is installed in the S1 area and is used for numerous user experiments. In the S2 area, precision measurements of muonium's 1s-2s transition are conducted.

H-Line(High Momentum Muon Beam Line): H-line is a dedicated beamline for large-scale fundamental physics experiments aimed at exploring BSM. Designed to supply high-flux muon beams, it meets the demand for high statistics. In the H1 area, Muonium Spectroscopy Experiment Using Microwave (MuSEUM) experiment conducts ultra-precise measurement of the HyperFine Structure (HFS) of muonium, while the DeeMe experiment searches for $\mu - e$ conversion. In the H2 area and the extension building, g-2/EDM experiment is progressing to measure the muon anomalous magnetic moment (g-2) and Electric Dipole Moment (EDM) with the world's highest precision. [127, 128]

B.5.2 Hadron Experimental Facility

Hadron Experiment Facility is a cutting-edge research center that utilizes the proton beam supplied from the MR to explore fundamental mysteries in particle and nuclear physics. The beam extracted from the MR passes through a branching point called the switchyard, where it is distributed to multiple beamlines with different characteristics and transported to each experimental area.

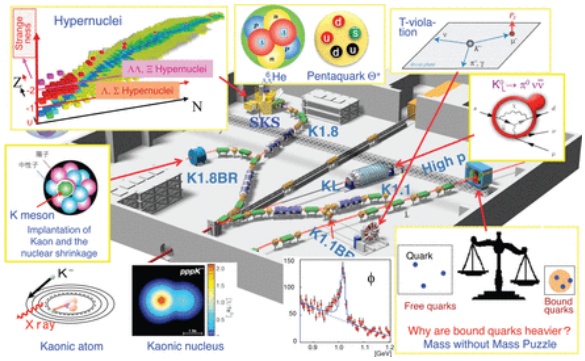

Figure B.7: Schematic of the Hadron Experimental Facility. [5]

Switchyard: The switchyard is the branching area that distributes the proton beam supplied by the SX from the MR to each beamline of the hadron experiment facility. Here, using the Lambertson magnet, a very small portion of the beam halo (about $10^{-3} - 10^{-4}$) is carved off and directed to the B-line, while the remaining bulk is passed through to the A-line.

A-Line: A-line is the main beamline of the Hadron Experiment Facility, irradiating the secondary particle production target (T1). When the proton beam collides with the pure gold T1 target, diverse secondary particles such as kaon and pion are produced and sent to the secondary beamlines (K1.8, K1.8BR, KL). Specifically, the KL beamline hosts the KOTO experiment, which investigates the rare decays of the K_L. [129, 130]

B-Line(High-p Beam Line): The B-line is a high-momentum beamline designed to directly utilize the 30 GeV proton beam.

C-Line: C-line is a dedicated beamline for the Coherent Muon to Electron Transition (COMET) experiment, which studies $\mu - e$ transitions. The MR accelerator operates at 8 GeV with a 9.6-second cycle time, and beam extraction takes approximately 0.5 seconds. [131, 132]

B.5.3 Neutrino Experimental Facility

Target Station

The Target Station at the J-PARC Neutrino Experiment Facility is the core component for generating neutrino beams from the proton beam. The main equipment is housed within a massive vacuum vessel filled with helium gas at atmospheric pressure, surrounded by thousands of tons of cast iron blocks and concrete for radiation shielding. Due to the high radiation environment, the equipment is designed for remote operation to enable replacement and maintenance.

Target: This is a graphite rod-shaped target measuring 90 cm in length and 2.6 cm in diameter. Colliding a 30 GeV proton beam with it produces large quantities of parent particles for neutrinos, such as pions and kaons. The heat generated by the proton beam collision is cooled by helium gas flowing between the target and its sleeve. The use of helium cooling instead of water cooling offers the advantages of avoiding instantaneous pressure increases in the water and enabling operation at higher temperatures (operating center temperature above 700°C) where radiation damage to the graphite is reduced. [133]

Electromagnetic Horn: Three pulsed electromagnets efficiently focus the charged pion mesons generated at the target along the beam path. By applying a high-current pulse of 320 kA synchronized with the proton beam timing, they generate a powerful toroidal magnetic field of up to 2.1 T. This field bends the pions' trajectories toward the beam axis, significantly enhancing the neutrino beam intensity. By reversing the polarity of the current flowing through the electromagnetic horn, it is possible to select whether to focus positive pions or negative pions. This enables the generation of either a neutrino beam or an antineutrino beam. [134]

Decay Volume: This approximately 100-meter-long cavity allows pions, focused by an electromagnetic horn, to decay into muon neutrinos and muon particles while traveling

through it. The desired neutrino beam is formed during this flight through the space.

Beam Dump: This device, installed at the very end of the decay volume, consists of a massive graphite block and a water-cooled iron shield. All protons that pass through the target, along with any pion mesons that did not decay, are absorbed and stopped here. Replacement after operation is not anticipated; it is designed to continuously absorb the entire beam power throughout the facility's operational lifetime.

MUon MONitor (MUMON): MUMON is a detector essential for the stable operation of the T2K experiment, monitoring the intensity and profile of the muon beam in real time for each beam bunch. Directly measuring neutrinos themselves requires statistical processing of a large number of events, making it difficult to know the instantaneous beam state. Therefore, MUMON measures muons produced simultaneously with neutrinos when pions decay. It is the only detector capable of measuring the muon profile for each proton beam bunch. This indirect measurement enables the immediate detection of beam anomalies and provides feedback to the accelerator operation. Installed in a pit behind a massive beam dump, MUMON detects high-energy muons with momenta exceeding 5 GeV/c that have passed through the beam dump. To ensure reliability and robustness, MUMON consists of two independent detector types: a silicon PIN photodiode (Si) and an ion chamber (IC). Each of these detectors features a sensor array arranged in a 7×7 grid, with a sensor spacing of 25 cm, covering a total area of 1.5 m square. It is designed for stable, long-term operation even in high radiation environments. It can measure the center position of the muon beam with an accuracy of 2.3 cm, equivalent to 0.28 mrad when converted to a neutrino beam. It also monitors beam intensity stability with a resolution of less than 3%. [135–138]

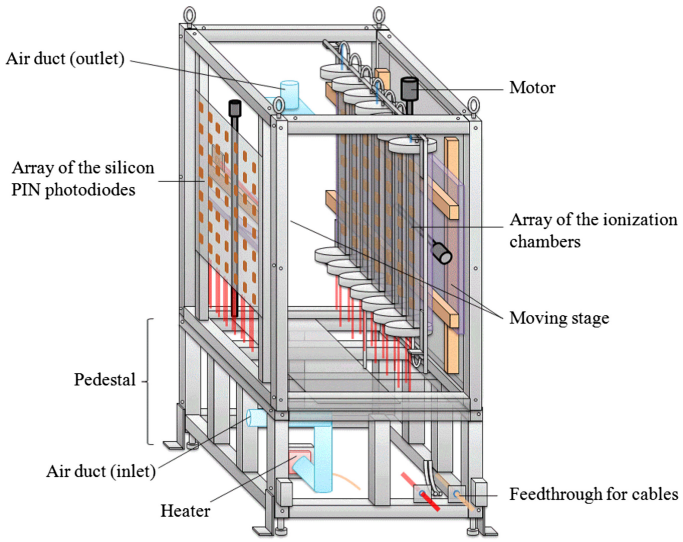

Figure B.8: Schematic of the muon monitor. [138]

Near Detectors (ND)

The near detectors are installed in an underground hall 280 meters downstream from the neutrino target. Its primary purpose is to precisely measure the characteristics of the neutrino beam before it reaches Far Detectors (FDs) and undergoes oscillation. The

data obtained here serves as a crucial benchmark for improving the accuracy of neutrino oscillation analysis by comparing it with results from distant observations. The detector group is broadly categorized into on-axis detectors, which monitor along the beam's central axis, and off-axis detectors, which observe at positions offset from the beam's central axis at the same angle as SK and Hyper-Kamiokande (HK).

Interactive Neutrino GRID (INGRID): As an on-axis detector, it monitors the stability of the neutrino beam's intensity and direction. Detector modules with a sandwich structure, alternating layers of iron and scintillator, are arranged in a cross configuration, with 7 modules horizontally and 7 vertically surrounding the beam axis. The neutrino beam axis passes through the center of the cross, enabling monitoring of the beam center with an accuracy of 0.1 mrad. [139]

(a) (b)

Figure B.9: Schematic of the (a) INGRID detector and (b) INGRID module's interior and exterior.[47]

Near Detector at 280m (ND280): This is the main detector of the off-axis detector, observing at the same 2.5-degree off-axis angle as FDs. It precisely measures the neutrino beam flux and energy distribution before oscillation, the fraction of ν_e in the neutrino beam, and the neutrino reaction cross-section. Multiple subdetectors are housed within the 0.2 T dipole magnet used in the UA1 experiment. [140] Applying a magnetic field enables precise measurement of the momentum and charge of charged particles produced in neutrino reactions. SuperFGD (Fine Grained Detector) [141] is a new main detector composed of approximately 2 million 1 cm^3 scintillator cubes, capable of capturing particle tracks with high precision in three dimensions. High Angle Time Projection Chamber (HATPC) [142] is positioned above and below SuperFGD, capturing the tracks of particles scattered over a wide angle. ToF (Time-of-Flight) [143] surrounds these detectors, helping to identify particles based on their flight time. Additionally, conventional TPCs, the Electromagnetic CALorimeter (ECAL) [144], and the Side Muon Range Detector (SMRD) [145] function as an integrated system. [146]

WAGASCI (WAter Grid And SCintillator detector) complex: This is a group of detectors that perform observations at an off-axis angle of 1.5 degrees. Specifically, it aims to reduce systematic errors in oscillation analysis by measuring neutrino reactions using the same water target as the distant detectors. It consists of the Baby-MIND (Magnetized Iron Neutrino Detector), Wall-MRD (Wall Muon Range Detector), and Proton Module, centered around the WAGASCI module, which features a grid-like arrangement of water and scintillators. [147, 148]

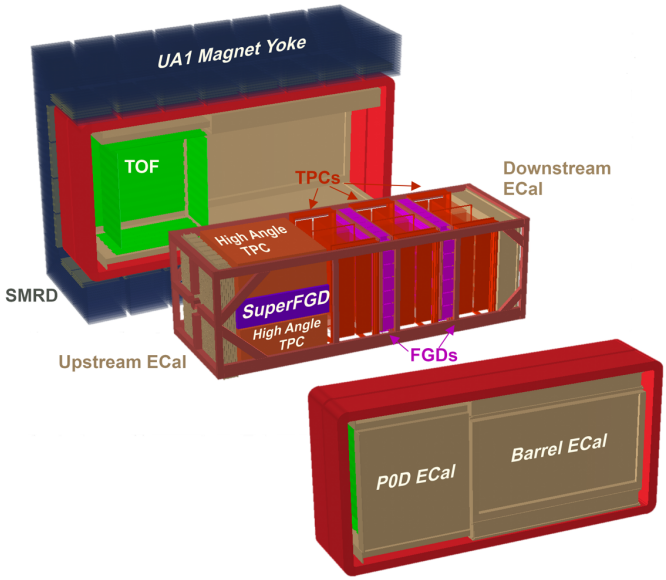

Figure B.10: Schematic of the ND280 [146]

NINJA (Neutrino Interaction research with Nuclear emulsion and J-PARC Accelerator): Using detectors placed within the WAGASCI complex, it aims to improve the accuracy of neutrino reaction models using nuclear emulsion. [149, 150]

SUBMET (SUB-Millicharge ExperimenT): This is not a neutrino experiment, but it is installed in the same ND280 pit and searches for dark matter candidate particles. It attempts to detect χ_s that may be produced by neutrino target using a scintillator. [151]

Intermediate Detector

Intermediate Water Cherenkov Detector (IWCD) is a new water Cherenkov detector planned for installation about 850 meters downstream from the neutrino production target at J-PARC. The detector consists of a tank 13 meters high and 9 meters in diameter, filled with 600 tons of gadolinium-doped water. The primary objective of IWCD is to measure neutrino reaction cross-sections with high precision at each energy level, addressing the major source of systematic error in the HK experiment. The key feature of IWCD is its ability to move the entire detector vertically within a shaft approximately 40m deep. This allows the off-axis angle of the neutrino beam to be varied from 1ř to 4ř. Changing the off-axis angle alters the observed neutrino energy distribution, enabling the acquisition of neutrino reaction data across a wide range of energies. Combining these data allows the reproduction of any energy distribution and the precise measurement of energy dependence. The detector employs approximately 400 multi-photomultiplier tubes (mPMTs), enabling it to capture the ring patterns of Cherenkov light with higher resolution than conventional large 50cm-diameter PMTs. This is expected to improve the positional resolution of reaction locations. [152]

Far Detectors (FD)

SK is one of the world's largest water Cherenkov detectors, installed 1,000 meters underground at the Kamioka Mine in Gifu Prefecture, approximately 295 km from J-PARC.

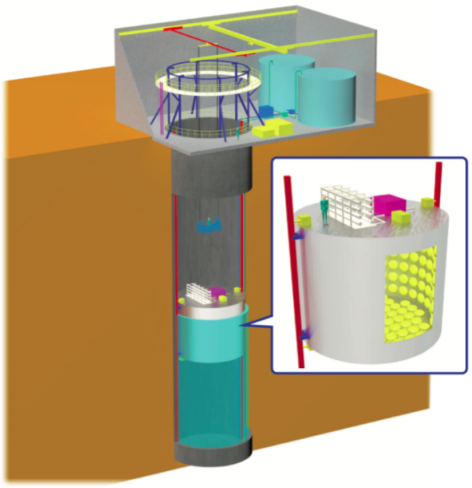

Figure B.11: Schematic of the intermediate water cherenkov detector. [153]

It stores 50,000 tons of water in a massive cylindrical tank measuring 39 meters in diameter and 41 meters in height, serving as the far detector for the T2K experiment to observe neutrino oscillation phenomena. The detector is optically divided into two layers: the Inner Detector (ID) and the Outer Detector (OD). The ID is the main detector for observing neutrino interactions, with about 11,000 PMTs of 50cm diameter installed on its inner wall. It captures Cherenkov light emitted by charged particles produced when neutrinos interact with atomic nuclei in the water. The OD surrounds the ID with a water layer approximately 2 meters thick and houses about 2,000 PMTs with a diameter of 20 cm. It serves to identify and remove background events originating externally, such as cosmic-ray muons. A major feature of SK is its ability to identify neutrino types with high precision based on the ring patterns of the observed Cherenkov light. Muons originating from muon neutrinos produce rings with sharp outlines, whereas electrons from electron neutrinos generate electromagnetic showers, resulting in rings with blurred outlines. This characteristic allows muons and electrons to be distinguished with 99% accuracy, enabling determination of whether muon neutrinos sent from J-PARC have transformed into electron neutrinos. Since 2020, gadolinium has been added to the ultra-pure water within the detector, enabling observations as SK-Gd. Gadolinium possesses the property of capturing neutrons extremely efficiently. This significantly improves the detection efficiency of neutrons emitted simultaneously when antineutrinos released from supernova explosions interact with water, thereby enhancing sensitivity to faint neutrino signals from space. [154–156]

HK is the next-generation, ultra-large water Cherenkov detector currently under construction as the successor to SK, aiming to begin observations in 2027. It will fill a cylindrical tank measuring 68 meters in diameter and 71 meters in height with 250,000 tons of water, achieving an effective volume approximately eight times that of SK. This increase in size will dramatically improve neutrino detection sensitivity. While sharing SK's two-layer structure, the inner tank will house 20,000 newly developed high-performance 50cm-diameter PMTs. This will enhance its light detection capability. HK will function as a distant detector receiving the powerful neutrino beam from J-PARC, which will be upgraded to 1.3 MW. This will advance the T2K experiment, aiming to discover CP

symmetry violation in neutrinos. [152]

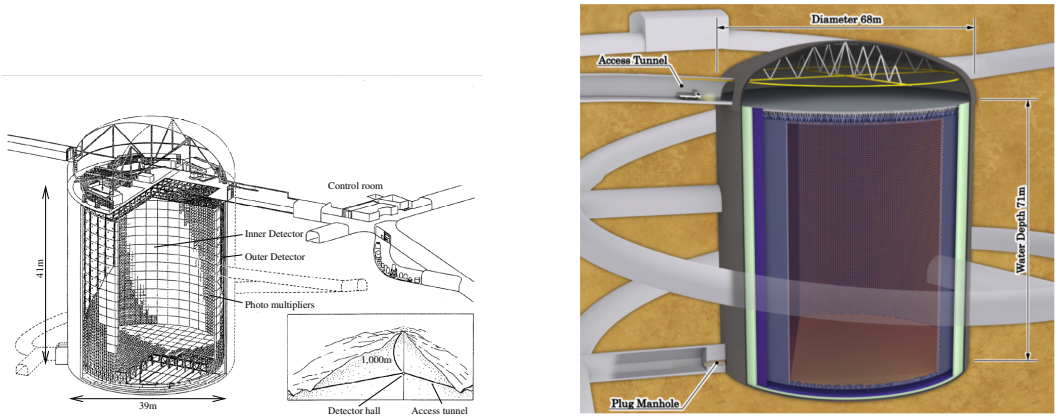

(a) **(b)**

Figure B.12: Schematic of (a) Super-Kamiokande detector [154] and (b) the HK detector. [157]

Appendix C

Vlasov Formalism for Head-Tail Modes

C.1 Sacherer's Integral Equation

We summarize the Vlasov formalism for transverse collective single-bunch head-tail modes in devices with linear chromaticity. The derivation is valid in the ultrarelativistic limit ($\beta \approx 1$). The particle distribution Ψ is described in the four-dimensional phase space (x, p_x, z, δ). The Vlasov equation is given by:

$$\frac{d\Psi}{ds} = \frac{\partial\Psi}{\partial s} + x'\frac{\partial\Psi}{\partial x} + p'x\frac{\partial\Psi}{\partial p_x} + z'\frac{\partial\Psi}{\partial z} + \delta'\frac{\partial\Psi}{\partial\delta} = 0. \tag{C.1}$$

The transverse and longitudinal equations of motion for a single particle and their respective derivatives are given by:

$$\begin{aligned} x' &= p_x, \\ p'x &= -\left(\frac{\omega\beta}{c}\right)^2 x + \frac{1}{E_0}F_x(z,s), \\ z' &= -\eta\delta, \\ \delta' &= \frac{1}{\eta}\left(\frac{\omega_s}{c}\right)^2 z. \end{aligned}$$

Note that ω_s represents the synchrotron oscillation frequency. Using the single-particle equations of motion and transforming to polar coordinates:

$$\begin{aligned} (x, p_x) &= \left(q\cos\theta, -\frac{\omega\beta}{c}q\sin\theta\right), \\ (z, \delta) &= \left(r\cos\phi, \frac{\omega_s}{\eta c}r\sin\phi\right). \end{aligned}$$

The Vlasov equation, including a linear chromaticity term ξ, becomes:

$$\frac{\partial\Psi}{\partial s} + \frac{\omega_\beta}{c}(1+\xi\delta)\frac{\partial\Psi}{\partial\theta} + \frac{\omega_s}{c}\frac{\partial\Psi}{\partial\phi} - \frac{c\omega_\beta F_x}{E_0}\left(\sin\theta\frac{\partial\Psi}{\partial q} + \frac{\cos\theta}{q}\frac{\partial\Psi}{\partial\theta}\right) = 0. \tag{C.2}$$

We describe the distribution as the sum of a stationary solution Ψ_0 and a small perturbation Ψ_1 oscillating at a complex coherent frequency Ω:

$$\Psi = \Psi_0 + \Psi_1 e^{-i\Omega s/c} = f_0(q)g_0(r) + f_1(q,\theta)g_1(r,\phi)e^{-i\Omega s/c}. \tag{C.3}$$

Here, f_0 and g_0 are the stationary transverse and longitudinal distributions, respectively. $f_1(q,\theta)$ and $g_1(r,\phi)$ represent the transverse and longitudinal structures of the coherent mode.

We linearize the Vlasov equation (Eq. (C.1)) by inserting the perturbation (Eq. (C.3)). For the transverse structure, we assume the Rigid Dipole Mode, where the bunch oscillates as a whole:

$$f_1(q,\theta) = -Df'0(q)e^{i\theta}, \tag{C.4}$$

where D is the dipole moment. Substituting the perturbation (Eq. (C.3)) and the rigid-dipole ansatz (Eq. (C.4)) into the Vlasov equation (Eq. (C.2)), and applying the Rotating Wave Approximation (retaining only terms $\propto e^{i\theta}$), we obtain a simplified Vlasov equation that depends only on the longitudinal coordinates:

$$\left[i(\Omega - \omega\beta(1+\xi\delta))g_1 - \omega_s\frac{\partial g_1}{\partial\phi}\right] De^{-i\Omega s/c} + i\frac{c^2}{2E_0}\omega_\beta F_x g_0 = 0. \tag{C.5}$$

The wake force F_x is itself generated by the perturbation. In the frequency domain, it is expressed using the transverse impedance $Z_T(\omega)$ and the longitudinal charge density spectrum $\tilde{\rho}_1(\omega)$:

$$F_x = iD\frac{e^2\omega_0^2}{4\pi^2 c}e^{-i\Omega s/c}\sum_p \tilde{\rho}1(\omega')Z_T(\omega')e^{i\omega' z/c}, \tag{C.6}$$

where $\omega' = p\omega_0 + \Omega$. Substituting the force (Eq. (C.6)) into the simplified Vlasov equation (Eq. (C.5)) and using $z = r\cos\phi$ yields the Vlasov-Wakefield equation, which governs the self-consistent motion of the longitudinal perturbation g_1:

$$i(\Omega - \omega\beta(1+\xi\delta))g_1 - \omega_s\frac{\partial g_1}{\partial\phi} = \frac{ce^2\omega_0^2}{8\pi^2 E_0\omega_\beta}g_0\sum_p \tilde{\rho}1(\omega')Z_T(\omega')e^{i\omega' r\cos\phi/c}. \tag{C.7}$$

To solve this equation, we introduce Sacherer's Ansatz for the longitudinal perturbation g_1:

$$g_1(r,\phi) = e^{i(\omega\xi/c)r\cos\phi}\sum_m \alpha_m R_m(r)e^{im\phi}, \tag{C.8}$$

where $\omega_\xi = \xi\omega_\beta/\eta$. The exponential factor is chosen to approximately cancel the chromatic term $\xi\delta$ in the Vlasov equation. The charge density spectrum $\tilde{\rho}_1$ is defined as the projection of g_1:

$$\tilde{\rho}_1(\omega') = \frac{\omega_s}{\eta c}\int rdr\int d\phi e^{-i\omega' r\cos\phi/c}g_1(r,\phi). \tag{C.9}$$

We now follow two paths to create a self-consistent equation:

Path 1: Express $\tilde{\rho}_1$ in terms of R_m Substitute the g_1 Ansatz (Eq. (C.8)) into the definition of $\tilde{\rho}_1$ (Eq. (C.9)) and integrate over ϕ using the integral definition of the Bessel function J_m:

$$\tilde{\rho}1(\omega') = 2\pi\frac{\omega_s}{\eta c}\int rdr\sum_m \alpha_m R_m(r)i^{-m}J_m\left(\frac{\omega'-\omega\xi}{c}r\right). \tag{C.10}$$

Path 2: Express R_l in terms of $\tilde{\rho}_1$ Substitute the g_1 Ansatz (Eq. (C.8)) into the Vlasov-Wakefield equation (Eq. (C.7)). The left-hand side simplifies due to the choice of the

Ansatz:

$$\sum_m i(\Omega - \omega_\beta - m\omega_s)\alpha_m R_m(r)e^{im\phi} \approx \frac{ce^2\omega_0^2}{8\pi^2 E_0\omega_\beta} g_0 \sum_p \tilde{\rho}1(\omega')Z_T(\omega')e^{i(\omega'-\omega\xi)r\cos\phi/c}. \quad \text{(C.11)}$$

We now apply the Fourier transform $\int d\phi e^{-il\phi}$ to both sides. The left side isolates the $m = l$ term due to orthogonality. The right side yields a Bessel function J_l. This gives:

$$(\Omega - \omega_\beta - l\omega_s)\alpha_l R_l(r) = -i\frac{ce^2\omega_0^2}{8\pi^2 E_0\omega_\beta} i^l g_0(r) \sum_p \tilde{\rho}1(\omega')Z_T(\omega')J_l\left(\frac{\omega'-\omega\xi}{c}r\right). \quad \text{(C.12)}$$

Final Step: Sacherer's Integral Equation Finally, we substitute the expression for $\tilde{\rho}_1$ (Eq. (C.10)) into (Eq. (C.12)) to eliminate $\tilde{\rho}_1$. This yields a self-consistent integral equation for the radial mode functions $R_l(r)$:

$$(\Omega-\omega_\beta-l\omega_s)\alpha_l R_l(r) = -i\frac{e^2\omega_0^2\omega_s}{4\pi E_0\omega_\beta\eta} g_0(r) \sum_{l'} \int \tilde{r}d\tilde{r}\alpha_{l'}R_{l'}(\tilde{r})i^{l-l'} \sum_p Z_T(\omega')J_l\left(\frac{\omega'-\omega_\xi}{c}r\right)J_{l'}\left(\frac{\omega'-\omega_\xi}{c}\tilde{r}\right) \quad \text{(C.13)}$$

This is (transverse) Sacherer's integral equation. Here, we approximate $\Omega \approx \omega_\beta + l\omega_s$ in the impedance term, redefining $\omega' = p\omega_0 + \omega_\beta + l\omega_s$.

C.2 General Solution Method

The Sacherer integral equation (Eq. (C.13)) derived in Appendix C.1 is the exact equation relating the coherent frequency Ω and the mode distribution $R_l(r)$. However, this is in the form of an integral equation, making it difficult to solve analytically or directly determine Ω as it stands. Therefore, we consider transforming this equation into an eigenvalue problem for a matrix that can be solved numerically.

First, we define a basis function for expanding the unknown radial function $R_l(r)$. We define a weight function $W(r)$ proportional to the steady-state radial distribution $g_0(r)$. We introduce a normalized orthogonal basis $f_k(r)$ orthogonal to this weight function $W(r)$ (where $k = 0, 1, 2, \ldots$ is the index of radial modes):

$$\int rdrW(r)f_k(r)f_{k'}(r) = \delta_{kk'}. \quad \text{(C.14)}$$

Next, we expand the solution $\alpha_l R_l(r)$ using this orthogonal function basis $f_k(r)$:

$$\alpha_l R_l(r) = W(r)\sum_k a_{lk}f_k(r). \quad \text{(C.15)}$$

Here, a_{lk} is the expansion coefficient representing the mode amplitude for azimuthal mode l and radial mode k. Substitute this expansion (Eq. (C.15)) into both sides of Sacherer's integral equation Eq. (C.13). Then, multiply both sides by $f_k(r)$ and perform the integration of $\int rdr$.

$$(\Omega - \omega_\beta - l\omega_s)a_{lk} = \sum_{l',k'} M_{(lk),(l'k')}a_{l'k'}. \quad \text{(C.16)}$$

The eigenvalue problem (Eq. (C.16)) is precisely the eigenvalue problem for a matrix whose eigenvalues are Ω:

$$[(\Omega - \omega_\beta - l\omega_s)\mathbf{I} - \mathbf{M}]\mathbf{a} = 0. \tag{C.17}$$

Here, $\mathbf{a}$ is a vector composed of coefficients a_{lk}, $\mathbf{I}$ is the identity matrix, and $\mathbf{M}$ is the coupling matrix. Here, the element $M_{(lk),(l'k')}$ of the matrix $\mathbf{M}$ is the coupling coefficient indicating how strongly modes (l,k) and (l',k') are coupled via impedance Z_T. The elements of this matrix $\mathbf{M}$ are obtained by evaluating the integral on the right-hand side of Eq. (C.13):

$$M_{(lk),(l'k')} = -i\frac{e^2\omega_0^2\omega_s}{4\pi E_0\omega_\beta\eta}C_W\sum_p Z_T(\omega')i^{l-l'}\tilde{\lambda}lk(\omega'-\omega\xi)\tilde{\lambda}l'k'(\omega'-\omega\xi). \tag{C.18}$$

Here, C_W is the normalization constant for $g_0(r) = C_W W(r)$, and $\tilde{\lambda}_{lk}$ is the form factor for mode (l,k):

$$\tilde{\lambda}lk(\omega) = \int rdrW(r)f_k(r)J_l\left(\frac{\omega r}{c}\right). \tag{C.19}$$

This is a spectrum showing how much the spatial distribution $W(r)f_k(r)$ of mode (l,k) overlaps with the wave of frequency ω (the Bessel function $J_l(\omega r/c)$). The condition for this equation to have non-trivial solutions (where $\mathbf{a} \neq 0$) is that the determinant of the coefficient matrix is zero:

$$\det[(\Omega - \omega\beta - l\omega_s)\delta_{ll'}\delta_{kk'} - M_{(lk),(l'k')}] = 0. \tag{C.20}$$

Solving Sacherer's integral equation reduces to constructing this coupling matrix $\mathbf{M}$ (typically truncated to finite dimensions k,l) and numerically determining its eigenvalues Ω. This constitutes the standard solution method in Sacherer theory.

C.3 Air-Bag Model

The general solution method (matrix form) presented in Appendix C.2 is rigorous but difficult to understand in terms of its physical meaning. Therefore, we consider the most simplified "Air-bag model", where the particle distribution of the beam is concentrated only at the maximum amplitude end $\hat{r}$ in the longitudinal direction. In the airbag model, the steady-state distribution $g_0(r)$ is described as a delta function that only takes values at the bunch edge $\hat{r}$:

$$g_0(r) = C_0\delta(r-\hat{r}). \tag{C.21}$$

Here, C_0 is the normalization constant. Since the steady-state distribution exists only at $r = \hat{r}$, perturbation is possible only there. Therefore, the unknown radial function $R_l(r)$ must also be a delta function of the same form:

$$R_l(r) = \delta(r-\hat{r}). \tag{C.22}$$

Note: Since the coefficient α_l carries the amplitude of the mode, the normalization constant for $R_l(r)$ is set to 1.

Substitute these definitions (Eqs. (C.21), (C.22)) into Sacherer's integral equation (Eq. (C.13)). Let N_B denote the number of particles in the bunch. Rewriting the normalization

constant $C_0\hat{r} = N_B\eta c/(2\pi\omega_s)$ (which follows from the definition of $g_0(r)$), we ultimately obtain the following equation:

$$(\Omega - \omega_\beta - l\omega_s)\alpha_l = -i\frac{N_B c e^2\omega_0^2}{8\pi^2 E_0\omega_\beta}\sum_{l'}\alpha_{l'}i^{l-l'}\sum_p Z_T(\omega')J_l\left(\frac{\omega'-\omega_\xi}{c}\hat{r}\right)J_{l'}\left(\frac{\omega'-\omega_\xi}{c}\hat{r}\right). \tag{C.23}$$

Applying the assumption that interactions between modes are neglected (i.e., treating the mode coupling term for $l \neq l'$ as zero) yields the following simplified dispersion relation, which directly provides the coherent frequency Ω for each mode l:

$$\Omega - \omega_\beta - l\omega_s = -i\frac{N_B c e^2\omega_0^2}{8\pi^2 E_0\omega_\beta}\sum_p Z_T(\omega')J_l^2\left(\frac{\omega'-\omega_\xi}{c}\hat{r}\right). \tag{C.24}$$

This equation shows that the coherent frequency shift for mode l (left-hand side) is determined by the overlap between the impedance Z_T and the shape of that mode (J_l^2). Instability analysis reduces to evaluating the imaginary part of the right-hand side of this equation (the instability growth rate).

C.4 Gaussian Distribution

For a Gaussian bunch distribution, the radial functions are given by:

$$g_0(\tau) = e^{-b\tau^2}\sum_k g_k L_k^0(\alpha\tau^2), \tag{C.25}$$

$$R_m(\tau) = \left(\frac{\tau}{\tau_b}\right)^{|l|}e^{-b\tau^2}\sum_n a_{mn}L_n^{|m|}(a\tau^2). \tag{C.26}$$

Here, L_n^m denotes the generalized Laguerre polynomials. Under this assumption, the DELPHI simulation performs the calculations.

C.5 Sinusoidal Model

As in Appendix C.4, we assume that only the diagonal elements ($l' = l$ and $k' = k$) of the matrix $\mathbf{M}$ contribute to instability, and that the off-diagonal elements (mode coupling terms) can be neglected. Applying this approximation to (Eq. (C.16)) yields:

$$\Omega - \omega_\beta - l\omega_s = M_{(lk),(lk)}. \tag{C.27}$$

In the definition of the matrix $\mathbf{M}$ (Eq. (C.18)), setting $l' = l, k' = k$ yields:

$$M_{(lk),(lk)} = -i\frac{e^2\omega_0^2\omega_s}{4\pi E_0\omega_\beta\eta}C_W\sum_p Z_T(\omega')|\tilde{\lambda}lk(\omega'-\omega\xi)|^2. \tag{C.28}$$

The general solution method (matrix form) presented in Appendix C.4 is rigorous but complex, while the airbag model is simple but unrealistic. Sacherer proposed a more realistic and practical approximate solution method. Instead of solving the exact radial

function $R_l(r)$ (or its basis $f_k(r)$), we assume that the shape $\lambda_{m1}(\tau)$ (where τ is the time coordinate within the bunch) of the lowest-order radial mode ($k = 1$), which is most prone to instability, can be approximated by the following simple sinusoidal functions:

$$\lambda_{m1}(\tau) \propto \begin{cases} \cos\left((m+1)\pi\frac{\tau}{\tau_L}\right) & (m = 0, 2, \dots \text{ even mode}) \\ \sin\left((m+1)\pi\frac{\tau}{\tau_L}\right) & (m = 1, 3, \dots \text{ odd mode}) \end{cases} \tag{C.29}$$

Here, τ_L is the total length of the bunch. The crucial point of this assumption is that mode m has m nodes except at the two ends of the bunch. This assumption is theoretically justified by the fact that, when assuming a "water-bag distribution" ($g_0(r) \propto$ const.), the linear density projected onto the vertical axis, its exact solution (Bessel function), can be very well approximated by a sine wave.

The greatest advantage of this sine wave mode assumption (Eq. (C.29)) is that it allows the instability growth rate to be evaluated directly, without explicitly solving integral equations or performing matrix calculations. By applying the Fourier transform to the assumed mode shape $\lambda_{m1}(\tau)$, we can analytically compute the power spectrum $h_m(\omega) = |\tilde{\lambda}_{m1}(\omega)|^2$ for that mode. This Fourier transform can be performed analytically and is given by:

$$h_m(\omega) \propto \frac{1 + (-1)^m \cos(\omega\tau_L)}{[(\omega\tau_L/\pi)^2 - (m+1)^2]^2}. \tag{C.30}$$

Substituting this result into the Eq. (C.27) for the coherent frequency Ω, which neglects mode coupling, enables the derivation of a practical formula for calculating the instability growth rate:

$$\Omega - \omega_\beta - l\omega_s = -i\frac{1}{1+|l|}\frac{e^2\omega_0^2\omega_s}{4\pi E_0\omega_\beta\eta}C_W\frac{\sum_p Z_T(\omega')h_m(\omega' - \omega_\xi)}{\sum_p h_m(\omega' - \omega_\xi)}. \tag{C.31}$$

Appendix D

Space Charge Effects in the Elliptical Chamber

In this appendix, we derive the electromagnetic fields produced by a beam with an elliptical cross-section inside a conductive elliptical vacuum chamber, which forms the basis of the space charge model in Sec. 6.4.

D.1 Potential in the Rest Frame

Let us consider an elliptical chamber with a major axis $2h_{E_x} = 2f\cosh u_0$ and a minor axis $2h_{E_y} = 2f\sinh u_0$, where $f = \sqrt{h_{E_x}^2 - h_{E_y}^2}$ is the focal distance. The scalar potential $\bar{\Phi}$ at position (x, y) induced by a point charge at (x_s, y_s) in the beam's rest frame is given by [158]:

$$\bar{\Phi}(x, y, x_s, y_s) = -\frac{\bar{\lambda}}{4\pi\epsilon_0}\log\left|\frac{D_s^x}{D_s}\frac{CD_s - C_sD}{CD_s^x - C_s^xD}\frac{C - C_s}{D + D_s}\frac{C - C_s^x}{D + D_s^x}\right|. \tag{D.1}$$

Here, the functions S, C, D are defined using Jacobian elliptic functions $\mathrm{sn}, \mathrm{cn}, \mathrm{dn}$ with modulus k:

$$\begin{aligned} S &= \mathrm{sn}(u(\zeta), k), \\ C &= \mathrm{cn}(u(\zeta), k), \\ D &= \mathrm{dn}(u(\zeta), k), \end{aligned} \tag{D.2}$$

where $\zeta = x + iy$. The argument $u(\zeta)$ relates to the coordinate via conformal mapping:

$$u(\zeta) = \frac{2K(k)}{\pi}\cos^{-1}\frac{\zeta}{f}, \tag{D.3}$$

where $K(k)$ is the complete elliptic integral of the first kind. The subscript s denotes the functions evaluated at source coordinates $\zeta_s = x_s + iy_s$, and the superscript x denotes the complex conjugate ($S^x = S(\bar{\zeta})$).

D.2 Electric Field in the Laboratory Frame

The electric field E_x^0 in the laboratory frame is obtained from the potential $\Phi = \gamma\bar{\Phi}$. By differentiating the potential, we obtain:

$$\begin{aligned} E_x^0 &= -\frac{\partial\Phi}{\partial x} \\ &= \frac{\lambda}{4\pi\epsilon_0}\frac{KS}{\pi W}\left[\frac{D}{C-C_1}+\frac{D}{C-C_1^x}-\frac{Ck^2}{D+D_1}-\frac{Ck^2}{D+D_1^x}+\frac{DD_1-C_1Ck^2}{CD_1-C_1D}-\frac{DD_1^x-C_1^xCk^2}{CD_1^x-C_1^xD}\right] \\ &+\frac{\lambda}{4\pi\epsilon_0}\frac{KS^x}{\pi W^x}\left[\frac{D^x}{C^x-C_1^x}+\frac{D^x}{C^x-C_1}-\frac{C^xk^2}{D^x+D_1^x}-\frac{C^xk^2}{D^x+D_1}+\frac{D^xD_1^x-C_1^xC^xk^2}{C^xD_1^x-C_1^xD^x}-\frac{D^xD_1-C_1C^xk^2}{C^xD_1-C_1D^x}\right], \end{aligned} \tag{D.4}$$

where $W = \sqrt{f^2-\zeta^2}$.

D.3 Approximation for Small Beam Size

Assuming the beam size is sufficiently smaller than the chamber dimensions ($a_x, a_y \ll h_{E_x}, h_{E_y}$), we can expand the image field components using a Taylor series. The indirect electric field $E_{x,\mathrm{im}}^0$ on the horizontal axis ($y = 0$) is approximated as:

$$E_{x,\mathrm{im}}^0 = \frac{\lambda}{2\pi\epsilon_0}(A_1x_s + A_2x + \dots). \tag{D.5}$$

The expansion coefficients A_1 through A_4 depend on the chamber geometry:

$$\begin{aligned} A_1 &= \frac{1}{6f^2}\left(1-\frac{4(1-2k^2)K^2}{\pi^2}\right), \\ A_2 &= \frac{1}{6f^2}\left(2-\frac{4(2-k^2)K^2}{\pi^2}\right). \end{aligned} \tag{D.6}$$

For a cylindrical limit ($h_{E_x} \to h_{E_y} = h_C$), these converge to $A_1 \to 1/h_C^2$ and $A_2 \to 0$.

By integrating these fields over the elliptical beam distribution $I(x_s, y_s)$, we derive the final expressions for the direct and indirect electric forces used in Eq. (6.39). For a detailed derivation including the magnetic field term, refer to [159].

Appendix E

Reconstruction of Intra-bunch Beam Position from BPM Signals

In this appendix, we describe how we reconstructed beam position information from the voltage data obtained from the BPM in J-PARC MR, as described in Chapter 11.

E.1 Hardware Configuration and Signal Acquisition

In the J-PARC MR, the IBFB system utilizes dedicated BPMs, such as the tapered-electrode BPM or stripline BPM located downstream of the neutrino/abort branch point. These monitors are designed to have a wide bandwidth to capture the fast internal motion of the bunches.

The output signals from the BPM electrodes are sampled at a rate 64 times the accelerating RF frequency ($64 \times f_{RF}$). This high-speed sampling allows each RF bucket to be divided into 64 longitudinal "slices," enabling the system to resolve the intra-bunch structure with a resolution of approximately several nanoseconds.

E.2 Position Calculation Algorithm

The transverse beam position within each slice is reconstructed using the four electrode signals. For a given transverse plane (horizontal or vertical), the difference (Δ) and sum (Σ) signals are derived from the opposite electrodes (e.g., V_A and V_B):

$$\Sigma = V_A + V_B \tag{E.1}$$

$$\Delta = V_A - V_B \tag{E.2}$$

The signals are integrated over the duration of each slice after correcting for linear offsets. The transverse position x is then calculated by the ratio of the integrated difference signal to the integrated sum signal, multiplied by a sensitivity coefficient κ (determined by the BPM geometry; $\kappa = 46$ mm [160]):

$$x[mm] = \kappa \frac{\int \Delta dt}{\int \Sigma dt} \tag{E.3}$$

By normalizing the difference signal with the sum signal, the reconstructed position becomes independent of the beam intensity, allowing for pure displacement measurements.

In regions where the beam intensity (Σ) is low, such as the bunch head and tail, the position calculation becomes susceptible to noise and misalignment due to cable transmission characteristics. To mitigate this, apply a threshold to the Σ signal and perform integration in the region around the signal center where the signal-to-noise ratio is sufficient.

E.3 Extraction of Intra-bunch Motion

To analyze instabilities such as head-tail modes, the dipole moment within the bunch $\Delta(z)$ is often used instead of the displacement of the entire bunch. The dipole moment is defined as the product of the bunch current (charge density λ) and the position x:

$$\Delta(z) = \lambda(z)x(z) \tag{E.4}$$

This quantity represents the transverse distribution of the bunch's charge center.

E.4 Digital Filtering for Feedback

The reconstructed position signals contain not only the instability components but also the closed orbit and other low-frequency noise. The IBFB processor applies a digital FIR filter (typically a 4-tap filter) to these signals. This filtering stage isolates the betatron oscillation components, which are then used to calculate the necessary kick strength to be applied by the stripline kickers in the feedback loop.

List of Acronyms

μSR Muon Spin Rotation/Relaxation/Resonance.

3-50BT 3GeV to 50GeV Beam Transport.

3NBT 3GeV to Neutron Facility Beam Transport.

ABH Air-Bag Harmonic.

ABS Air-Bag Square-well.

AC Alternating Current.

ACS Annular Coupled Structure Linac.

ADC Analog to Digital Converter.

AIC Air Ionization Chamber.

AVC Auto Voltage Control.

BBA Beam Based Alignment.

BBC Beam Based Calibration.

BBGC Beam Based Gain Calibration.

BLM Beam Loss Monitor.

BPM Beam Position Monitor.

BPMC Beam Position Monitor Circuit.

BSM Beyond Standard Model.

BxB Bunch-by-Bunch.

BxBFB bunch-by-bunch feedback.

CCB Central Control Building.

CERN European Organization for Nuclear Research.

CMOS Complementary Metal Oxide Semiconductor.

CNT Carbon NanoTube.

COD Closed Orbit Distortion.

COMET Coherent Muon to Electron Transition.

CP Charge-Parity.

CPU Central Processing Unit.

CSS Control System Studio.

CT Current Transformer.

CW Continuous-Wave.

DC Direct Current.

DCCT DC Current Transformer.

DDS Direct Digital Synthesis.

DM Dark Matter.

DMZ Demilitarized Zone.

DSP Digital Signal Processor.

DTL Drift Tube Linac.

EDM Electric Dipole Moment.

EPICS Experimental Physics and Industrial Control System.

FCT Fast Current Transformer.

FD Far Detector.

FF feedforward.

FFT Fast Fourier Transform.

FL fluorescence.

FPGA Field-Programmable Gate Array.

FWM Flying Wire Monitor.

FX Fast Extraction.

g-2 anomalous magnetic moment.

GUI Graphical User Interface.

HD Hadron Experimental Facility.

HFS HyperFine Structure.

HK Hyper-Kamiokande.

HOM Higher-Order Mode.

HOPG High-Oriented Pyrolytic Graphite.

I.I. Image Intensifier.

ID Inner Detector.

IOC Input/Output Controller.

IPM Residual Gas Ionization Profile Monitor.

IS Ion Source.

IWCD Intermediate Water Cherenkov Detector.

J-PARC Japan Proton Accelerator Research Complex.

JAEA Japan Atomic Energy Agency.

JSNS Japan Spallation Neutron Source.

KEK High Energy Accelerator Research Organization.

KVM Kernel-based Virtual Machine.

L3BT LINAC to 3GeV Beam Transport.

LAN Local Area Network.

LHC Large Hadron Collider.

LI LInear accelerator.

linac linear accelerator.

LLRF Low Level RF.

MA Magnetic Alloy.

MCP MicroChannel Plate.

MEBT1 Medium Energy Beam Transport-1.

MLF Materials and Life Science Experimental Facility.

mPMT multi-photomultiplier tube.

MPS Machine Protection System.

MR Main Ring.

MRPM Multi-Ribbon Profile Monitor.

MTCA.4 Micro Telecommunications Computing Architecture - Enhancements for Rear I/O and Precision Timing.

MUMON MUon MONitor.

MUSE MUon Science Establishment.

MuSEUM Muonium Spectroscopy Experiment Using Microwave.

MWPM Multi-Wire Profile Monitor.

NU Neutrino Experimental Facility.

OD Outer Detector.

OTR Optical Transition Radiation.

PBLM Proportional-type BLM.

PF Photon Factory.

PLC Programmable Logic Controller.

PMT Photomultiplier Tube.

POT Protons On Target.

ppb proton per bunch.

PPS Personal Protection System.

PR Periodic Reverse.

PS Power Supply.

RCS Rapid-Cycle Synchrotron.

RF Radio Frequency.

RFQ Radio Frequency Quadruple Linac.

SCFM Superconducting Composite Function Magnet.

SCT Slow Current Transformer.

SDTL Separated-type Drift Tube Linac.

SEY Secondary Electron Yield.

SK Super-Kamiokande.

SM Standard Model.

SNS Spallation Neutron Source.

SoC System on a Chip.

SPring-8 Super Photon ring-8 GeV.

SUSY Supersymmetry.

SX Slow Extraction.

T2K Tokai to Kamioka.

TMCI Transverse Mode Coupling Instability.

ToF Time of Flight.

USM Ultra-Slow Muon.

VIOC Virtual Input/Output Controller.

VLAN Virtual Local Area Network.

WCM Wall Current Monitor.

WSM Wire Scanner Monitor.

List of Symbols

$a_{m,\mathrm{ABH}}$ Relative amplitude in the ABH model

$a_{m,\mathrm{ABS}}$ Relative amplitude in the ABS model

$\bar{\lambda}$ Charge line density in the rest frame

$\bar{\Phi}$ Scalar potential in the rest frame

$\bar{x}$ Horizontal centroid of each segment

$\bar{x}(n,z)$ Transverse centroid

β Lorentz beta

β_x Average value of the beta function along the ring

χ_σ rms chromatic phase

χ_b Chromatic phase

χ_{ABH} Chromatic phase in the ABH model

χ_{ABS} Chromatic phase in the ABS model

$\Delta\nu$ Tune interval between the head-tail modes

$\Delta\nu_x, \Delta\nu_{\pm,k}$ Eigenvalue of the head-tail mode

ΔT Advance time per step

δ Longitudinal momentum deviation

$\Delta\nu_{\mathrm{multi}}$ Coherent tune shift caused by the multi-turn wake

$\Delta\nu_{\mathrm{single}}$ Coherent tune shift caused by the single-turn wake

$\Delta^{(k)}$ Dipole moment in k-th segment

δ_0 Momentum deviation of ABS model

Δ_n Dipole moment of the respective bunch

δ_u, δ_d Momentum deviation of each stream

δ_{skin} Skin depth

ϵ_0 Vacuum permittivity

ϵ_1 Incoherent electric image coefficient

ϵ_2 Incoherent magnetic image coefficient

ϵ_x Unnormalized rms horizontal emittance

η Slippage factor

$f_{\mathrm{int}}(n)$ Intra-bunch frequency

$f_{\max}$ Maximum value of intra-bunch frequency $f_{int}(n)$

γ Lorentz gamma

$\hat{\lambda}$ Peak line density of electrical charges

$\hat{T_n}$ Time at the n-th step

$\hat{z}$ Half bunch length of ABS and ABH model

λ Charge line density in the laboratory frame

$\lambda^{(k)}$ Charge density in k-th segment

$\mathcal{G}$ Geometrical factor

N_{AM} Recoherence time

N_{particle} Number of macroparticles in the bunch

ν_0 Bare batatron tune

ν_m Head-tail mode frequency

ν_s Bare synchrotron tune

$\nu_{\beta,x}$ Horizontal bare betatron tune

$\Delta\nu_{\mathrm{coh}}$ Coherent tune shift from the indirect space charge

$\Delta\nu_{\mathrm{inc}}$ Incoherent tune shift from the direct space charge

ω_ξ Chromatic frequency

$\overline{A_n}$ Transverse amplitude (Courant-Snyder invariant)

$\overline{x_n}$ Transverse centroid of the entire bunch

Φ Scalar potential in the laboratory frame

ϕ Betatron phase advance

ϕ_u, ϕ_d Betatron phase advance of each stream

q_{sc} Space charge parameter

ρ Resistivity of the resistive wall chamber

σ_Δ Segment length

σ_δ rms momentum deviation

σ_x rms horizontal beam size

σ_z rms longitudinal beam size

$\sigma_{x'}$ rms horizontal beam divergence

$\tilde{a}_{m,\mathrm{ABS}}(z)$ Relative amplitude in the ABS model in each segment

θ Synchrotron phase

θ_0 Synchrotron initial phase

$\tilde{a}_{m,\mathrm{sc}}(z)$ Relative amplitude in the head-tail mode modeling in each segment

$\tilde{a}_{m,b}(z)$ Relative amplitude for the Gaussian beam in each segment

V_{RF} RF voltage

$W_{\mathrm{T1}}(s)$ Horizontal resistive wall wake

ξ_1 Coherent electric image coefficient

ξ_2 Coherent magnetic image coefficient

ξ_x Horizontal chromaticity

$Z_{\mathrm{dip,eff}}$ Transverse effective impedance

Z^D_{T1} Transverse impedance

$A(n)$ Amplitude of betatron oscillation

A_m Head-tail mode coefficient

a_x, a_y Horizontal and vertical beam sizes

A_z Vector potential in the laboratory frame

$a_{m,b}$ Relative amplitude for the Gaussian beam

B_f Bunching factor

C Circumference of the ring

c Light velocity

d_ω Finite thickness of the resistive wall chamber

e Electric charge

$E^0_{x,\mathrm{DS}}, E^0_{x,\mathrm{im}}$ E^0_x excited by the direct and indirect space charge

E_0 Total energy

E^0_x Horizontal component of the electric field excited by the point charge in the laboratory frame

$E_{x,\mathrm{DS}}$ Superposition of the horizontal component of the electric field by the direct space charge

$E_{x,\mathrm{im}}$ Superposition of the horizontal component of the electric field by the indirect space charge

F Filling factor of the elliptical chambers along the ring

f Half distance between the two focal points

f_0 Revolution frequency

F_B Filling factor of the bending magnet along the ring

F_x^{ele} Electric contributions to the Lorentz force

F_x^{mag} Magnetic contributions to the Lorentz force

F_{beam} Space charge force and wakefield

g Half distance between the magnetic pole surfaces of parallel plates placed perpendicularly to the vertical axis

h Harmonic number

h_0 Power spectrum of the Gaussian zero azimuthal bunch mode

h_C Radius of the cylindrical conductive chamber

h_{Ex}, h_{Ey} Major horizontal and minor vertical axis of the elliptical conductive chamber

i Macroparticle number index

$I(x, y)$ Region occupied by the beam on the transverse plane

k Eigenmode number index

L Length of the resistive wall chamber

m Head-tail mode number index

m_{max} Highest mode in the head-tail mode modeling

m_{min} Lowest mode in the head-tail mode modeling

n Simulation step number index

$N^{(k)}$ Number of macroparticles in k-th segment

N_λ Number of times the resistive wall is summed

N_B Bunch population

N_f Decoherence time

n_r Radial mode

N_s Synchrotron period

q Allocated charge for one macroparticle

r Ratio of the space charge strength to the wake strength

r_p Classical particle radius of the proton

s Path length

$S_i^{(k)}$ Shape function

T_0 Revolution period

$V(N_\lambda)$ Sum of the resistive wall impedance up to N_λ

x Horizontal position

x'	Horizontal position derivative with respect to path length
$X(n)$	Transverse centroid of the entire bunch
$x^{(k)}$	Transverse centroid in k-th segment
X_0	Horizontal offset position at injection
x_u, x_d	Transverse position of each stream
z	Longitudinal position
$z^{(k)}$	Longitudinal position in k-th segment
Z_0	Impedance of free space
z_b	Full bunch length

List of Figures

2.1 Schematic layout of the J-PARC accelerators and experimental facilities. [5] 17
2.2 Schematic of beam time structure. [8]. 18
2.3 Schematic of thinning process (currently implemented with 128 segments) . 18
2.4 Schematic of the Rapid-Cycling Synchrotron, where the red text correspond to the beam diagnostics equipment. [12] 20
2.5 Schematic of the Main Ring, the Hadron Experimental Facility, and the Neutrino Experimental Facility. [16] 21
2.6 (a) Beam intensity (red) and kinetic energy (blue) during the 954 kW FX beam study. (b) Beam intensity (red) and spill structure (blue) during the 100 kW SX beam study. [17] 22
2.7 Schematic of the MR injection section. [24] 23
2.8 Distribution of beam loss monitor signals during high-power beam operation at 1×10^{14} ppp. Signal sensitivity in the blue region is 24 times that in the red region. [16] 25
2.9 Schematic of installed dump core [18] 25
2.10 (a) Schematic of the FX septum magnet (SM). (b) Photo of the high-field SM. [32] 26
2.11 (a) Schematic of the BPM of J-PARC MR. [36] (b) Schematic of the signal processing for the BPM of J-PARC MR. [38] 28
2.12 (a) Schematic of the multi-ribbon profile monitor. (b) Profing results of MR ABT-MRPM. [40] 29
2.13 History of delivered proton count to the T2K experiment. [46] 31
2.14 Schematic of the neutrino beamline. [47] 32

3.1 Tune diagram with resonance lines ($0 < \nu_x < 0.5, 0 < \nu_y < 0.5$) 37
3.2 Conceptual illustration of the wakefield mechanism. (Top) Analogy using a boat's wake to demonstrate causality, where the disturbance affects only the trailing region. (Bottom) Schematic of electromagnetic wakefield induced by a particle bunch in a vacuum chamber. The graph shows the source particle, the wakefield function $G(z - z')$, and the resulting cumulative total wakefield potential $W(z)$. 42
3.3 Real (solid blue line) and imaginary (dashed red line) parts of the transverse resonator impedance as a function of frequency ratio ω/ω_r 45

3.4 Signal patterns of head-tail modes ($m = 0, 1, 2$) for different chromatic phases χ. The rows display signals at specific turns ($k = 0, 4$) and the superposition of multiple turns ($k = 0$ to 5). (a) represents zero chromaticity ($\chi = 0$), showing standing waves. (b) and (c) represent non-zero chromaticity ($\chi = 5, 9$ rad), showing the traveling wave characteristics driven by the head-tail phase shift.[54] 48

5.1 Schematic representations of the longitudinal phase space distributions for the three models discussed in this chapter. (a) ABS Model: Particles are concentrated at the bunch edges ($\pm\hat{z}$) and move freely within a square-well potential. (b) ABH Model: Particles are distributed on a ring trajectory (Air-Bag) under a harmonic potential, executing synchrotron oscillation. (c) Gaussian Bunch: Particles are distributed according to a Gaussian profile within a harmonic potential. 55

6.1 Longitudinal resistive wall wakefield potential divided by the total charge of bunch for σ=2.72 m. 70
6.2 Theoretical result of synchrotron tune deviation due to the potential $U'(\phi)$ (red line) and the simulation results (point) in the case of $N_B = 3 \times 10^{14}$ ppb and $\sigma_z = 2.72$ m. 71
6.3 Sum of multi-turn wakes for different N_λ(left) and the deviation from the analytical estimate with infinite N_λ(right). 73

7.1 Transverse amplitude $\overline{A_n}$ scanned by varying the number of macroparticles N_{particle}. 78
7.2 The result of tracking simulation scanned by varying time steps relative to the revolution time $T_0/\Delta T$. 78
7.3 Transverse amplitude $\overline{A_n}$ with constant wakefield by varying the size of the mesh that divides the bunch longitudinally as $C/(h\sigma_\Delta)$. 79
7.4 Transverse amplitudes of the bunch oscillation calculated by Eq. (4.12) and tracking simulations for $V_{\text{RF}} = 110$kV(blue), $V_{\text{RF}} = 263$kV(black), and $V_{\text{RF}} = 400$kV(red). 79
7.5 Transverse amplitudes of the bunch oscillation calculated by Eq. (4.12) and tracking simulations for $\xi = -1$ (black), $\xi = -2$ (red), $\xi = -3$ (blue), and $\xi = -8$ (green). 80
7.6 The dipole moment $|\Delta^{(k)}\sigma_\Delta/q|$ in the bunch by the tracking simulations. . 80
7.7 Frequency components of the dipole moment in the bunch by the tracking simulations. 81
7.8 The simulations (dots) and the theoretical results by Eq. (4.10) (red line) of the maximum intra-bunch frequency $f_{\max}$ for each chromaticity condition. 81

8.1 Analytical results of relative amplitudes $|\tilde{a}_{m,\text{ABS}}(z)|$ calculated by Eq. (5.27) based on the ABS model with weak space charge force. Here, the black, red, green, blue, orange, magenta, cyan, dark green, purple, and gray denote the cases of $m = 0, 1, 2, \cdots 9$, respectively. 83

8.2 Relative amplitudes $|\tilde{a}_m^{(k)}|$ in tracking simulation based on the ABS model with weak space charge force ($N_B = 1.0 \times 10^8$ ppb). Here, the black, red, green, blue, orange, magenta, cyan, dark green, purple, and gray denote the cases of $m = 0, 1, 2, \cdots 9$, respectively. 83
8.3 Head-tail tune spectra in tracking simulation based on the ABS model with weak space charge force ($N_B = 1.0 \times 10^8$ ppb). The dots indicate only the results for $|a_m| > 0.1$. The red lines represent the frequency shifts calculated by Eq. (5.17) for each head-tail mode in the range of $-4 \leq m \leq 4$. 84
8.4 Relative amplitudes $|a_m|$ calculated by Eq. (5.36) and tracking simulation based on the ABS model with weak space charge force ($N_B = 1.0 \times 10^8$ ppb). Here, the black, red, green, blue, orange, magenta, cyan, dark green, purple, and gray denote the cases of $m = 0, 1, 2, \cdots 9$, respectively. 85
8.5 Head-tail tune spectra in the ABS model without indirect space charge effects for various values of chromaticity : (a) $\xi = -1.5$, (b) $\xi = -6.5$, and (c) $\xi = -12.5$. The dots indicate only the results for $|a_m| > 0.1$. The red lines represent the frequency shifts calculated by Eq. (5.17) for each head-tail mode in the range of $-4 \leq m \leq 12$. 85
8.6 Head-tail tune spectra in the ABS model without indirect space charge effects for various values of intensity : (a) $N_B = 4.2 \times 10^{12}$ ppb and (b) $N_B = 8.6 \times 10^{12}$ ppb. The dots indicate only the results for $|a_m| > 0.1$. The red lines represent the frequency shifts calculated by Eq. (5.17) for each head-tail mode in the range of $0 \leq m \leq 12$. 86
8.7 Relative amplitudes $|a_m|$ based on the tracking simulation of the ABS model without indirect space charge effect. Here, the black, red, green, blue, orange, magenta, cyan, dark green, purple, and gray denote the cases of $m = 0, 1, 2, \cdots 9$, respectively. 87
8.8 Head-tail tune spectra in the ABS model without either indirect space charge effect or transverse wakefield for (a) $\xi = -1.5$ and (b) $\xi = -12.5$. The dots indicate only the results for $|a_m| > 0.1$. The red lines represent the frequency shifts calculated by Eq. (5.17) for each head-tail mode in the range of $-4 \leq m \leq 12$. 88
8.9 Head-tail tune spectra in the ABS model with indirect space charge effect in addition to the direct space charge effects and the wakefield for various values of chromaticity : (a) $\xi = -1.5$, (b) $\xi = -6.5$, and (c) $\xi = -12.5$. The dots indicate only the results for $|a_m| > 0.1$. The red lines represent the frequency shifts calculated by Eq. (5.17) for each head-tail mode in the range of $-4 \leq m \leq 12$. 89
8.10 Head-tail tune spectra in the ABS model with indirect space charge effect in addition to the direct space charge effects and the wakefield for various values of intensity : (a) $N_B = 4.2 \times 10^{12}$ ppb and (b) $N_B = 8.6 \times 10^{12}$ ppb. The dots indicate only the results for $|a_m| > 0.1$. The red lines represent the frequency shifts calculated by Eq. (5.17) for each head-tail mode in the range of $0 \leq m \leq 12$. 89

8.11 Relative amplitudes $|a_m|$ derived from the tracking simulation of the ABS model with the indirect and direct space charge effects as well as the wakefield effects. Here, the black, red, green, blue, orange, magenta, cyan, dark green, purple, and gray denote the cases of $m = 0, 1, 2, \cdots 9$, respectively. 90
8.12 Relative amplitudes $|\tilde{a}_{m,b}(z)|$ calculated by Eq. (5.58) based on the harmonic potential model with weak space charge force. Here, the black, red, green, blue, orange, magenta, cyan, dark green, purple, and gray denote the cases of $m = 0, 1, 2, \cdots 9$, respectively. 91
8.13 Relative amplitudes $|\tilde{a}_m^{(k)}|$ in tracking simulation based on the harmonic potential model with weak space charge forces. Here, the black, red, green, blue, orange, magenta, cyan, dark green, purple, and gray denote the cases of $m = 0, 1, 2, \cdots 9$, respectively. 91
8.14 Head-tail tune spectra in tracking simulation based on the harmonic potential model with weak space charge force. The dots indicate only the results for $|a_m| > 0.1$. The red lines represent the frequency shifts calculated by Eq. (5.17) for each head-tail mode in the range of $-4 \leq m \leq 4$. 92
8.15 Relative amplitudes $|a_m|$ calculated by Eq. (5.61) and tracking simulation of the harmonic potential model with weak space charge forces. Here, the black, red, green, blue, orange, magenta, cyan, dark green, purple, and gray denote the cases of $m = 0, 1, 2, \cdots 9$, respectively. 92
8.16 Head-tail tune spectra in the harmonic potential model without indirect space charge effect for various values of chromaticity : (a) $\xi = -1.5$, (b) $\xi = -6.5$, and (c) $\xi = -12.5$. The dots indicate only the results for $|a_m| > 0.1$. The red lines represent the frequency shifts calculated by Eq. (5.17) for each head-tail mode in the range of $-4 \leq m \leq 12$. 93
8.17 Head-tail tune spectra in the harmonic potential model without indirect space charge effect for various values of intensity : (a) $N_B = 4.2 \times 10^{12}$ ppb and (b) $N_B = 8.6 \times 10^{12}$ ppb. The dots indicate only the results for $|a_m| > 0.1$. The red lines represent the frequency shifts calculated by Eq. (5.17) for each head-tail mode in the range of $0 \leq m \leq 12$. 94
8.18 Relative amplitudes $|a_m|$ tracking simulation of the harmonic potential model without indirect space charge effect. Here, the black, red, (green,) blue, orange, magenta, cyan, dark green, purple, and gray denote the cases of $m = 0, 1, (2,) 3, \cdots 9$, respectively. 94
8.19 Head-tail tune spectra in the harmonic potential model without indirect space charge effect and without transverse wakefield for various values of chromaticity : (a) $\xi = -1.5$ and (b) $\xi = -12.5$. The dots indicate only the results for $|a_m| > 0.1$. The red lines represent the frequency shifts calculated by Eq. (5.17) for each head-tail mode in the range of $-4 \leq m \leq 12$. 95
8.20 Head-tail tune spectra in the harmonic potential model with indirect space charge effect for various values of chromaticity : (a) $\xi = -1.5$, (b) $\xi = -6.5$, and (c) $\xi = -12.5$. The dots indicate only the results for $|a_m| > 0.1$. The red lines represent the frequency shifts calculated by Eq. (5.17) for each head-tail mode in the range of $-4 \leq m \leq 12$. 96

8.21 Head-tail tune spectra in the harmonic potential model with indirect space charge effect for various values of intensity : (a) $N_B = 4.2 \times 10^{12}$ ppb and (b) $N_B = 8.6 \times 10^{12}$ ppb. The dots indicate only the results for $|a_m| > 0.1$. The red lines represent the frequency shifts calculated by Eq. (5.17) for each head-tail mode in the range of $0 \leq m \leq 12$. 96
8.22 Relative amplitudes $|a_m|$ tracking simulation of the harmonic potential model with indirect space charge effect. Here, the black, red, green, blue, orange, magenta, cyan, dark green, purple, and gray denote the cases of $m = 0, 1, 2, \cdots 9$, respectively. 97
8.23 The tune shift at which the head-tail tune spectrum reaches its maximum peak in the simulation of the beam intensity parameters in Figs. 8.5, 8.9, 8.16, and 8.20. The dots indicate only the results for $|a_m| > 0.1$. The red lines represent the frequency shifts calculated by Eq. (5.17) for each head-tail mode in the range of $-3 \leq m \leq 12$. 98

9.1 The tune shift at which the tune spectrum reaches its maximum peak in the simulation with only the transverse wakefield and without space charge effects, compared with the results from the DELPHI Vlasov solver. The pair of numbers on the lines describes the excited mode indices (m, n_r). . . 100
9.2 The tune shift at which the tune spectrum reaches its maximum peak in the simulation with the transverse wakefield, the direct and indirect space charge effects. 100
9.3 The tune shift at which the tune spectrum reaches its maximum peak in the simulation with $\xi_x = 0$. The pair of numbers describes the excited mode indices (m, n_r). 101
9.4 Transverse amplitude $\overline{A_n}$ scanned by varying beam intensity N_B for the case of chromaticity $\xi_x = 0$. 102

10.1 Transverse bunch motion in the time domain for the chromaticity $\xi_x = -12.5$ and the beam intensity $N_B = 8.6 \times 10^{12}$ ppb. 104
10.2 Transverse bunch motion in the time domain under the condition of $\xi_x = -12.5$, $m_{\min} = 5$, $m_{\max} = 9$. 105
10.3 Transverse bunch motion in the time domain under the condition of $\xi_x = -12.5$, $m_{\min} = 5$, $m_{\max} = 9$, using Eq. (10.11). 107

11.1 Measured transverse bunch motion in the time domain for the chromaticity $\xi_x = -7.9$ and the beam intensity $N_B = 8.6 \times 10^{12}$ ppb and the RF voltage $V_{\mathrm{RF}} = 263$ kV. 111
11.2 Measured dipole moment $\Delta(z)$ in the bunch at beam measurement for the chromaticity $\xi_x = -7.9$ and the beam intensity $N_B = 8.6 \times 10^{12}$ ppb. . . . 112
11.3 Measured dipole moment $\Delta(z)$ in the bunch for the beam intensity $N_B = 4.2 \times 10^{12}$ ppb and $N_{\mathrm{AM}}/2 = N_f$ turn at beam measurement. 112
11.4 Simulations of the transverse bunch motion in the time domain for the RF voltages: $V_{\mathrm{RF}} = 110, 263$, and 400 kV with the chromaticity $\xi_x = -6.5$ and the beam intensity $N_B = 4.2 \times 10^{12}$ ppb. 114

11.5 Measurements of the transverse bunch motion in the time domain for the RF voltages: $V_{\rm RF} = 110, 263$, and 400 kV with the chromaticity $\xi_x = -6.5$ and the beam intensity $N_B = 4.2 \times 10^{12}$ ppb. 115
11.6 The maximum intra-bunch frequency $f_{\rm max}$ for the synchrotron period. Here, the black, red, and green denote the cases of $N_B = 2.4 \times 10^{12}$, 4.2×10^{12}, and 8.6×10^{12} ppb, respectively. 116
11.7 The normalized recoherence period $N_{\rm AM}/N_s$ for the synchrotron period. Here, the black, red, and green denote the cases of $N_B = 2.4 \times 10^{12}, 4.2 \times 10^{12}$, and 8.6×10^{12} ppb, respectively. 116
11.8 The simulated spectra of head-tail tune normalized with synchrotron tune $\Delta\nu/\nu_s$ for the synchrotron period obtained by analyzing $\log|a_m|$ of the harmonic model with the indirect space charge effect. 117
11.9 Simulation of the transverse bunch motion in the time domain for the beam intensity: $N_B = 1.0 \times 10^{12}, 2.4 \times 10^{12}, 4.2 \times 10^{12}$ and 8.6×10^{12} ppb with the chromaticity $\xi_x = -8.0$, and the RF voltage $V_{\rm RF} = 263$ kV. 119
11.10 Measurements of the transverse bunch motion in the time domain for the beam intensity: $N_B = 1.0 \times 10^{12}, 2.4 \times 10^{12}, 4.2 \times 10^{12}$, and 8.6×10^{12} ppb with the chromaticity $\xi_x = -7.9$ and the RF voltage $V_{\rm RF} = 263$ kV. 120
11.11 The normalized recoherence period $N_{\rm AM}/N_s$ with several fixed chromaticities for different beam intensities. Here, the red, green, blue, orange, magenta, and gray in Fig. 11.11a denote the cases of $\xi_x = -1.5, -3.5, -5.5, -6.5, -8.0$, and -12.5, respectively. Here, the red, green, blue, orange, magenta, and gray in Fig. 11.11b denote the cases of $\xi_x = -1.5, -3.3, -5.7, -6.5, -7.9$, and -12.5, respectively. 121
11.12 Simulation of the transverse bunch motion in the time domain for the chromaticity: $\xi_x = -1.5, -8.0$, and -12.5 with the beam intensity $N_B = 4.2 \times 10^{12}$ ppb and the RF voltage $V_{\rm RF} = 263$ kV. 123
11.13 Measurements of the transverse bunch motion in the time domain for the chromaticity: $\xi_x = -1.5, -7.9$, and -12.5 with the beam intensity $N_B = 4.2 \times 10^{12}$ ppb and the RF voltage $V_{\rm RF} = 263$ kV. 124
11.14 The maximum intra-bunch frequency $f_{\rm max}$ with fixed beam intensity for different chromaticities. In Fig. 11.14a, the black, red, green, blue, orange, magenta, and gray denote the cases of $N_B = 1.0 \times 10^{11}, 2.0 \times 10^{11}, 5.0 \times 10^{11}, 1.0 \times 10^{12}, 2.4 \times 10^{12}, 4.2 \times 10^{12}$, and 8.6×10^{12} ppb, respectively. In Fig. 11.14b, the black, red, green, blue, orange, magenta, and gray denote the cases of $N_B = 1.3 \times 10^{11}, 2.6 \times 10^{11}, 5.2 \times 10^{11}, 1.0 \times 10^{12}, 2.4 \times 10^{12}, 4.2 \times 10^{12}$, and 8.6×10^{12} ppb, respectively. The black dashed lines in both figures are the result of Eq. (10.10). 125

B.1 Schematic of the RCS injection section and stripper foil position. [99] . . . 148
B.2 (a) Schematic of injection painting in transverse plane. The upper panel shows the horizontal phase space, and the lower panel shows the vertical phase space. (b) Schematic of longitudinal painting without (left) and with (right) momentum offset. Squares represent injection bunches from the LINAC. [101] 149
B.3 Schematic of flying wire monitor. [114] 156

B.4 Schematic of optical transition radiation/fluorescence monitor. [115] 157
B.5 Schematic of the JSNS. [120] 160
B.6 Schematic of the MUSE. [126] 160
B.7 Schematic of the Hadron Experimental Facility. [5] 161
B.8 Schematic of the muon monitor. [138] 163
B.9 Schematic of the (a) INGRID detector and (b) INGRID module's interior and exterior.[47] 164
B.10 Schematic of the ND280 [146] 165
B.11 Schematic of the intermediate water cherenkov detector. [153] 166
B.12 Schematic of (a) Super-Kamiokande detector [154] and (b) the HK detector. [157] 167

List of Tables

2.1 LI parameter [10, 11] . . . 19
2.2 RCS parameter [12] . . . 20
2.3 MR parameter [16] . . . 22

11.1 Number of shots for the analysis of the synchrotron period dependence with the fixed chromaticity $(\xi_x, \xi_y) = (-6.5, -7.4)$ and the betatron tune $(\nu_{\beta,x}, \nu_{\beta,y}) = (21.35, 21.41)$. . . . 110
11.2 Number of shots for the analysis of the beam intensity and the chromaticity dependences with the fixed betatron tune $(\nu_{\beta,x}, \nu_{\beta,y}) = (21.35, 21.41)$, and the RF voltage $V_{\mathrm{RF}} = 263$ kV. . . . 110
11.3 Number of shots for the analysis of the beam intensity and the chromaticity dependences with the fixed betatron tune $(\nu_{\beta,x}, \nu_{\beta,y}) = (22.30, 20.81)$, and the RF voltage $V_{\mathrm{RF}} = 155$ kV. . . . 110